

Developing a New Synthesis Strategy for Fe-N-C Catalysts for the Oxygen Reduction Reaction in Proton-Exchange-Membrane Fuel Cells



TECHNISCHE
UNIVERSITÄT
DARMSTADT



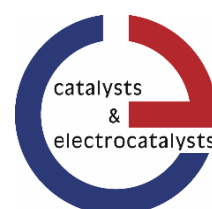
Graduate School of
**Energy Science
and Engineering**

Vom Fachbereich Chemie
der Technischen Universität Darmstadt

zur Erlangung des Grades
Doctor rerum naturalium
(Dr. rer. nat.)

Dissertation
von Markus Christopher Kübler

Erstgutachterin: Prof. Dr. Ulrike I. Kramm
Zweitgutachterin: Prof. Dr. Barbara Albert
Darmstadt 2021



Kübler, Markus: Developing a New Synthesis Strategy for Fe-N-C Catalysts for the Oxygen Reduction Reaction in Proton-Exchange-Membrane Fuel Cells

Darmstadt, Technische Universität Darmstadt

Jahr der Veröffentlichung der Dissertation auf TUprints: 2021

Tag der Einreichung: 18. Mai 2021

Tag der mündlichen Prüfung: 05. Juli 2021

Veröffentlicht unter CC BY-SA 4.0 International <https://creativecommons.org/licenses/>

Erklärungen laut Promotionsordnung

§8 Abs. 1 lit. c PromO

Ich versichere hiermit, dass die elektronische Version meiner Dissertation mit der schriftlichen Version übereinstimmt und für die Durchführung des Promotionsverfahrens vorliegt.

§8 Abs. 1 lit. d PromO

Ich versichere hiermit, dass zu einem vorherigen Zeitpunkt noch keine Promotion versucht wurde und zu keinem früheren Zeitpunkt an einer in- oder ausländischen Hochschule eingereicht wurde. In diesem Fall sind nähere Angaben über Zeitpunkt, Hochschule, Dissertationsthema und Ergebnis dieses Versuchs mitzuteilen.

§9 Abs. 1 PromO

Ich versichere hiermit, dass die vorliegende Dissertation selbstständig und nur unter Verwendung der angegebenen Quellen verfasst wurde.

§9 Abs. 2 PromO

Die Arbeit hat bisher noch nicht zu Prüfungszwecken gedient.

Darmstadt, 18.05.2021

Markus Christopher Kübler

Abstract

Within this work, a new synthesis method for a Fe-N-C catalyst is developed. Fe-N-C catalysts are considered promising materials for the replacement of expensive Pt and catalyze the oxygen reduction reaction (ORR) on the cathode inside proton-exchange-membrane fuel cells (PEMFCs). This work briefly summarizes the standpoint of current PEMFC technology and provides a detailed overview on the to this day reported synthesis methods and applied precursors for Fe-N-C catalysts. One major concern with the synthesis of Fe-N-C catalysts is that for a high performance often complex precursors like porphyrins or zeolitic imidazolate frameworks (ZIFs) are used. These precursors are expensive or not well suited for a scale-up [1-3]. Here, a new method is presented which is based on a cheap and simple polypyrrole precursor which at the same time yields catalysts with a high fuel cell performance. Important parameters for the new preparation method are systematically investigated and useful insights, for instance on the influence of the iron salt precursor, a bimetallic iron and manganese approach, the heat-treatment temperature, or the effectiveness of the acid leaching, are presented. The final catalyst of this work is compared to the best-off performing Fe-N-C catalysts reported in literature. Further, the overall preparation method is briefly discussed with respect to its scale-up practicability by comparing the individual synthesis steps to the to this day commercially most advanced Fe-N-C catalysts.

Acknowledgements

This thesis was done at the *Technische Universität Darmstadt* with financial support by the *Bundesministerium für Bildung und Forschung* (BMBF) within the research group *Catalyst and Electrocatalysts* of Prof. Dr. Ulrike I. Kramm.

I highly acknowledge that I was given the opportunity to perform this work within the group of Prof. Dr. Ulrike I. Kramm as well as her support as supervisor and an inspiring example of scientific excellence.

I furthermore thank Prof. Dr. Barbara Albert, Prof. Dr. Peter Strasser, Prof. Dr. Rolf Schäfer and Prof. Dr. Bastian Etzold for their invested time and scientific feedback as the second reviewer and examiners of this thesis.

During the course of this work, several colleagues and students assisted with lab work and characterization of my catalyst samples. I am very thankful for their support and for all the great discussions within our working group.

Janik Scharf, Pascal Theis and Niels Kubitzka supported me during their time as research assistant and student intern with the preparation of numerous catalysts and with the MEA fabrication process. I thank Lingmei Ni and Stephan Wagner for the Mössbauer characterization. Especially Stephan Wagner for the profound discussions on the general topic of Fe-N-C catalyst structure during his beam times. I would also like to thank Stephen Paul, David Wallace and Lingmei Ni for conducting the BET and the Raman measurements for me. I appreciate the cooperative work with Valdislav Gridin, who is working on different stabilizations strategies of the here developed catalyst and who provided me the data for the comparability tests.

I am very thankful for the support and love of my family over all the years. To both of my parents and my older brothers who inspired me as a positive role model on the way. I am also very grateful for the love and emotional support from Carolin.

Table of Contents

Abstract	i
Acknowledgements	ii
Table of Contents	iii
List of Tables	v
List of Figures	vii
List of Abbreviations	xiv
List of Symbols	xix
1 Introduction and the Broader Context	1
2 Aim and Outline of this Work	5
3 Fuel Cells Background Information and Current Scientific Knowledge	9
3.1 Proton-Exchange-Membrane Fuel Cells (PEMFCs)	9
3.2 Current Cost Status and Goals for the Automotive Fuel Cell Industry	21
4 Non-Precious Metal-Based ORR Catalysts	29
4.1 Non-Precious Metal Based Catalysts: Enormous Potential of Cost Reduction	29
4.2 Instability of Me-N-C Catalysts	31
4.3 Structure and Active Site of Me-N-C Catalysts	35
5 Literature Review on Synthesis of Non-Precious Metal Based ORR Catalysts	38
6 Experimental Part	66
6.1 Remark on the ⁵⁷ Fe-Mössbauer Analysis in this Work	74
7 Results and Discussion on Surface Functionalized Multi-Walled Carbon Nanotubes as Non-Precious Metal Oxygen Reduction Catalysts	75
7.1 Background and Motivation on MWCNT Based ORR Catalysts	76
7.2 Synthesis Method and Prepared MWCNT Catalysts	77
7.3 Structural Characterization	78
7.4 Electrochemical Experiments	82
7.5 Summary and Conclusions on MWCNTs Based Fe-N-C Catalyst	88
8 Results and Discussion on the Synthesis of Polypyrrole Based Me-N-C Catalyst	90
8.1 The Concept and the Preparation Process	91
8.2 On the Influence of Methyl Orange During the Synthesis of Polypyrrole-Based Fe-N-C Catalysts	93
8.2.1 Prepared Catalysts for Investigating the Influence of Methyl Orange	93

8.2.2 Structural Characterizations	95
8.2.3 Electrochemical Experiments	101
8.2.4 Brief Summary on the Influence of Methyl Orange	104
8.3 On the Influence of the Fe-Precursor Salt	105
8.3.1 Prepared Catalysts and Investigated Fe-Precursors	105
8.3.2 Structural Characterizations	106
8.3.3 Electrochemical Experiments	110
8.3.4 Brief Summary on the Influence of Different Iron Salts	112
8.4 Optimization of a Mn-Fe-precursor Mixture	113
8.4.1 Prepared Catalysts and Investigated Iron/Manganese-Precursors	113
8.4.2 Structural Characterizations	114
8.4.3 Electrochemical Experiments	117
8.4.4 Brief Summary on the Influence of Different Fe/Mn Salts	122
8.5 Variation of the Temperature during the Synthesis of Polypyrrole-Based Me-N-C Catalysts	123
8.5.1 Catalysts Prepared with Varying Duration of the Second Heat Treatment	123
8.5.2 Catalysts Prepared with Varying Temperature of the First Heat-Treatment	127
8.6 Increasing the Acid Leaching of Inorganic Metal Species	134
8.7 The Influence of Doping Agents on Polypyrrole based Me-N-C Catalysts	140
8.8 Summary of Key Findings and Systematic Comparison of the Most Relevant Catalysts	146
9 Comparison to Best-Off Materials	149
10 Summary and Outlook	152
11 References	156
12 Appendix	I

List of Tables

Table 1: Forecasted penalties resulting from exceeding CO ₂ emission target values for car manufactures in the EU [17].	3
Table 2: Overview of addressed topics related to Fe-N-C catalyst synthesis and investigated approach of solution within the different chapters of this thesis.	6
Table 3: Key data of the PEMFC stack of the Toyota Mirai Model [106].	22
Table 4: Current status and ultimate technology targets considering cost and durability of PEMFC systems for the application in LDVs and MDVs [19, 20].	23
Table 5: Key data of the state-of-the-art PEMFC stack published by U.S. DOE in 2018 [20].	24
Table 6: Precursor and individual synthesis steps cost of the U.S. DOE's 2018 state-of-the-art cathode catalyst, d-PtCo/HSC-f with respect to the annual production rate of a 80 kW _{net} system [20].	25
Table 7: Cathode catalyst costs per 80 kW _{net} system in dependence of the production rate for U.S. DOE's 2018 Pt-based catalyst d-PtCo-HSAC-f and NPM based catalyst from Pajarito Powders PANI-C-Fe [20, 142].	30
Table 8: Small organic molecules which have been applied as N-precursors to synthesize Me-N-C catalysts (monomers of polymer-based precursors are not included).	45
Table 9: Overview of conducting or non-conducting polymers that have been used as precursors for the synthesis of Me-N-C catalysts.	54
Table 10: Overview of all catalysts which were investigated within this thesis.	68
Table 11: Overview of fuel cell measurements and catalyst loadings.	73
Table 12: Overview of investigated MWCNTs based FeNC catalyst materials.	78
Table 13: Overview of investigated catalyst materials comparing common PPy to nanotube PPy and investigating the influence of methyl orange.	93
Table 14: Mössbauer parameters and iron species assignment.	98
Table 15: Correlation of relative methyl orange content of the polypyrrole nanotube precursor to the BET surface area of the final catalyst and the maximum power output during PEMFC tests.	103
Table 16: Summary of prepared Fe-N-C catalysts based on different iron salt precursors.	105
Table 17: Overview of catalyst materials that underwent a second heat treatment and further investigations during PEMFC testing.	106
Table 18: Mössbauer parameters and assignment of iron species for the polypyrrole-methyl orange-based catalysts which were prepared with different iron salts.	109
Table 19: Overview of prepared Fe, Mn and Fe + Mn based polypyrrole-methyl orange catalysts.	114
Table 20: Fe, Mn-Catalysts prepared without a second heat treatment and with a varying total duration time of the second heat treatment.	124
Table 21: Fe and Mn-based polypyrrole-methyl orange catalysts prepared at 800 °C and 1000 °C.	128
Table 22: Fe and Mn-based polypyrrole-methyl orange catalysts prepared at 1000 °C with a different acid leaching step.	135
Table 23: Catalysts prepared from FeCl ₃ /KMnO ₄ polypyrrole mixtures. The polypyrrole is doped with different organic compounds.	141
Table 24: Chapters of this thesis by addressed problem of Fe-N-C catalyst preparation and provided solution.	146

Table 25: Key-parameters for the catalysts Cat A - E.

148

Table 26: Comparison of the so-far published best performing non-precious metal-based ORR catalyst during PEMFC tests in H₂-air.

149

List of Figures

- Figure 1: Annual global fossil fuel carbon emissions by individual contributors (a) and the average global temperature correlating with the atmospheric CO₂ concentration (b) [5-7]. 1
- Figure 2: Change in greenhouse gas emissions of the EU by sector, normalized to the emissions of the year 1990, figure taken from the European Environment Agency [14]. 2
- Figure 3: Field of application for BEVs, FCEVs and synthetic fuel based transport solutions in respect to weight and average mileage per trip demand, figure taken from [18]. 4
- Figure 4: Delivered fuel cell power per year with respect to the type of fuel cell. PEMFC, AFC and DMFC are highlighted because the developed catalysts of this work could be applied within these fuel cells [34]. 9
- Figure 5: Left: schematic drawing of a PEMFC's layout giving the different parts, right: the half-cell and overall cell reactions [35]. 10
- Figure 6: PEMFC polarization curve giving the cell voltage versus the current density; the different regions of the irreversible voltage losses are caused by mixed potential, activation loss, ohmic resistance and mass transport limitations. Figure adapted from [36]. 11
- Figure 7: Different designs and geometries of flow plates: parallel flow-channel (a), parallel-serpentine flow-channel (b), pillar flow-channel (c) [40], Honda FXC Clarity wave flow-channel with cooling technology (d) [41], Toyota Mirai 3D fine-mesh flow-field (e) [42] and graphene foam flow field (f) [43]. 12
- Figure 8: Location of the GDL between flow field and catalyst layer inside the PEMFC (a) [52] and artificially colored SEM image giving the cross section of a GDL highlighting macroporous carbon fiber layer (blue) and microporous carbon black layer (red) [60]. 13
- Figure 9: Chemical structure of Nafion™ showing the different possible compositions influenced by the values of the parameters x, y, n and m (a) [63], cluster network model proposed for hydrated PFSA membranes [64] (b) and structure and length of the side chain from different PFSA copolymers [65]. 14
- Figure 10: Composition of the cathode catalyst layer (CCL) showing binder, catalyst particles and catalyst support. Transport of reactants and products is illustrated by the interaction of the CCL with the membrane and the microporous layer (MPL) [74]. 15
- Figure 11: Illustration of the over-potentials for the redox reaction pairs HOR/HER and ORR/OER of Pt [75]. 16
- Figure 12: 3D Visualizations (segmented tomograms) of Pt particle deposited on or in different carbon supports (HSC vs Vulcan) [93] (a) and impact of the carbon support on the fuel cell performance [94] (b). 17
- Figure 13: Controlled pore size and depth allows for good O₂ and H⁺ mass transport properties, whereas at the same time the catalytically active Pt-surface is protected from ionomer adsorption [96]. 18
- Figure 14: Influence of the ionomer content inside the catalyst layer; low ionomer contents show low mass transport resistances and low proton conductivities, high ionomer contents show high mass transport resistances and high proton conductivities, a balanced ionomer content is needed to fit both needs [97]. 19
- Figure 15: Catalyst particles covered with conventional ionomer (a) and a backbone modified ionomer possessing a higher O₂ permeability (b) [22]. 19
- Figure 16: The Coulomb interactions between ionomer and nitrogen functional groups of the support lead to uniformly dispersed ionomer inside the catalyst layer [97]. 19

Figure 17: Reaction pathways of Ce(IV)O ₂ quenching radical oxygen species [101].	20
Figure 18: Development of the cost for a 80 kW _{net} PEMFC system since 2006 [19].	21
Figure 19: FC performance difference of a PtCo catalyst and a Pt catalyst. Even with lower total Pt loading the PtCo catalyst shows higher current densities [94].	22
Figure 20: Voltage loss of U.S. DOE's 2018 PEMFC system operating at 2 A cm ⁻² or 3 A cm ⁻² (a) and state-of-the-art PEMFC stack costs in relation to the yearly production rate (b) [19, 21].	24
Figure 21: Mined platinum in tons by the year 2019 with respect to country and worldwide [23].	26
Figure 22: Impact of fuel cell vehicles on platinum demand, study performed 2013 by Roland Berger [112].	27
Figure 23: Effect of MEA power density of the PANI-C-Fe catalyst based MEA (LANL) on the fuel cell stack costs [142].	31
Figure 24: Pourbaix diagram of iron, showing the thermodynamic instability of iron under PEMFC conditions [154].	33
Figure 25: The impact of soaking a Nafion TM membrane in Fe ²⁺ containing solution: Severe performance loss in the polarization curve [160].	34
Figure 26: Ball-stick-model of the active site of an Me-N-C catalyst, showing the geometric structure of an MeN ₄ center embedded in carbon [174].	36
Figure 27: Iron nanoparticle surrounded by a highly graphitized carbon layer which protects the iron from dissolution during acid treatments but not from electrochemical leaching during PEMFC operation.	37
Figure 28: Asymmetric volcano plot relating ORR activity to the redox potential of the MeN ₄ complex and the O ₂ binding energy, the type of transition metal Me takes great action in governing these parameters [203].	40
Figure 29: a) H ₂ O ₂ formation and b) ORR activity of different Me-N-C catalysts in O ₂ saturated H ₂ SO ₄ solution (pH = 1, 1500 rpm, 0.96 mg cm ⁻² catalyst disc loading) and c) H ₂ O ₂ oxidoreduction in 9 mM H ₂ O ₂ (pH = 1, N ₂ saturated, 1500 rpm, 0.4 mg cm ⁻²) [207].	41
Figure 30: Change of nitrogen composition a), total nitrogen content and ORR current density b) with respect to the nominal Fe loading of the precursor mixture of a carbon black, melamine, Fe(Ac) ₂ catalyst system [220].	43
Figure 31: Ball-and-stick model illustrating the chemical structure of Me-phthalocyanine a) and Me-porphyrin b), the hydrogen atoms can be replaced by different substitutes [232].	44
Figure 32: Synthesis steps of the silica-based sacrificial synthesis method (SSM) [270].	49
Figure 33: Local coordination environment of the transition metal inside the ZIF (a), hierarchical structure of the ZIF (b) and proposed formation of active sites by Ma et al. (c) [315].	50
Figure 34: Correlating PEMFC activity (a) and stability (b) of NH ₃ treated carbon black FeTMPPCl catalysts with the NH ₃ concentration of the gas feed. Activity is increased at the costs of stability [26].	52
Figure 35: Schematic overview of the synthesis process of a PANI-Me-C catalysts, comprising the steps of mixing the oxidized carbon support with the monomer solution and polymerization agents (A + B), heat-treatment and acid leaching (C+D) [140].	58
Figure 36: Polymerization of aniline related monomers but with an additional N-functional group, the new side chains of the polymers are in red circles and have a high affinity to Fe-ions [346].	59

- Figure 37: Schematic preparation of hollow PPy spheres from mesoporous SCMS, FeCl₃ and pyrrole vapor (a), final catalyst after pyrolysis SEM image (b) and HR-TEM image revealing uniform particle size and shape (c) [354]. 60
- Figure 38: Schematic synthesis route applying NaCl crystals as readily dissolvable hard-template for the synthesis of a PPy-based Fe-N-C catalyst (a) and TEM pictures of the material after pyrolysis showing a disordered honeycomb-like structure [353]. 61
- Figure 39: Diagram of the synthesis of a stabilized PAN based ORR catalyst (a), PEMFC polarization curve under O₂ and air (b) and retention of initial current density at 0.8 V (c), PEMFC experiment conditions: cathode loading 3.3 mg cm⁻², anode loading 0.2 mg_{Pt} cm⁻², H₂ and air 0.2 MPa, cell temperature 80 °C and Nafion® NR211 membrane [143]. 62
- Figure 40: PANI-Fe-C catalysts prepared with different carbon supports, comparison of RRDE activity (a), RRDE selectivity (b), fuel cell activity (c) and fuel cell stability (d) [409]. 64
- Figure 41: Co-PPy-C catalysts prepared following two different sequences resulting in different surface exposed carbon phases (a) and the respective fuel cell polarization curve and stability tests [412]. 65
- Figure 42: Cover image of Energy Technology featuring the results of chapter 7 on surface functionalized multi-walled carbon nanotubes as non-precious metal oxygen reduction catalysts [413]. 75
- Figure 43: TEM picture of a MWCNT consisting of several coaxially arranged graphene sheets rolled into a cylinder. 76
- Figure 44: Schematic presentation of the different synthesis steps and assumed coordination of Fe-phen. 77
- Figure 45: TEM pictures of pristine MWCNTs before (a, b) and after pyrolysis together with Fe(Ac)₂, phenanthroline and sulphur (c-j). Unmodified MWCNTs (c, d), pyridinic functionalized (e, f), unmodified but mixed with amino-indazole (g, h) and indazolic functionalized (i, j). 78
- Figure 46: Overview of the N₂ sorption experiments and resulting BET surface areas for MWCNT-based catalysts. 80
- Figure 47: Mössbauer spectra of the catalysts FeNC (a), FeNC_{pyr} (b) and FeNC_{ind} (c) and quadrupole splitting versus isomer shift (d). 81
- Figure 48: ORR polarization curves (A) and respective H₂O₂ yield (B) for the different MWCNT catalysts recorded with a sweep rate of 10 mV s⁻¹ in O₂ saturated 0.1 M H₂SO₄, a rotation rate of 1500 rpm and a loading of 0.8 mg cm⁻². 82
- Figure 49: Initial ORR sweep (solid) and after performing 10,000 scans ranging from 0 to 1.2 V in N₂ saturated 0.1 M H₂SO₄ with a sweep rate of 500 mV s⁻¹ (hollow) for the different MWCNT catalysts (a-d). 83
- Figure 50: DEMS experiments showing LSV scans under N₂ saturated atmosphere at 23 °C (left) and 60 °C (right), electrochemical output (upper) and ion current $m/z = 44$ detected with the mass spectrometer (lower). 84
- Figure 51: Outcome of the PEMFC tests showing the cell voltage versus current density for the MWCNTs-based catalysts (experiment conditions: H₂-O₂, cathode loading 1.7 mg cm⁻², N212 membrane, 1 bar gauge back pressure, 0.2 L min⁻¹ oxidant and fuel flow, 81 °C, 96 % humidity). 86
- Figure 52: Short PEMFC stability test of MWCNTs based Fe-N-C catalysts performed at a constant potential of 600 mV, showing the measured absolute current density a) and the remaining current density in percent b) (experiment conditions: H₂-O₂, cathode loading 1.7 mg cm⁻², 86

N212 membrane, 1 bar gauge back pressure, 0.2 L min ⁻¹ oxidant and fuel flow, 81 °C, 96 % humidity).	87
Figure 53: Oxidative polymerization of pyrrole monomer to polypyrrole in the presence of FeCl ₃ (A) and FeCl ₃ + methyl orange (B).	91
Figure 54: Schematic synthesis process of polypyrrole (PPy) nanotube based ORR catalyst.	91
Figure 55: Acidic RDE polarization curve of a polypyrrole Fe-N-C catalyst and a polypyrrole nanotube Fe-N-C catalyst in O ₂ saturated electrolyte (experiment conditions: 10 mV s ⁻¹ , 1500 rpm, 0.5 mg _{Catalyst} cm ⁻²).	92
Figure 56: TEM photographs of the two polypyrrole C-N precursors possessing either no specific morphology (b) or showing a nanotube morphology (a), the respective catalyst resulting after pyrolysis are given below (c-j).	95
Figure 57: Bar-graphs are presenting the results of the N ₂ sorption experiments for catalysts prepared from different polypyrrole precursors.	96
Figure 58: Mössbauer spectra of catalysts prepared from different PPy precursors and from different polypyrrole methyl orange nanotubes.	97
Figure 59: Raman spectra obtained after pyrolysis at different temperatures for polypyrrole (a), polypyrrole-methyl orange nanotubes (b), polypyrrole and Fe-precursor mixture (c) and polypyrrole-methyl orange nanotubes and Fe-precursor mixture (d).	99
Figure 60: Reductive scans of the polarization curves obtained in 0.1 M H ₂ SO ₄ saturated with O ₂ , rotation rate of 1500 rpm, 10 mV s ⁻¹ and a disc loading of 0.5 mg cm ⁻² . The disc current density is given in a) and the H ₂ O ₂ yield in b).	101
Figure 61: Polarization curves of prepared catalysts in O ₂ saturated 0.1 M H ₂ SO ₄ obtained with a rotation rate of 1500 rpm, a sweep rate of 10 mV s ⁻¹ and a disc loading of 0.5 mg cm ⁻² , disc currents density a) and H ₂ O ₂ yield calculated from the measured ring currents b).	102
Figure 62: PEMFC polarization curves of different polypyrrole catalysts, voltage against current density (a) and voltage against power density (b). (experiment conditions: H ₂ -O ₂ , cathode loading 2.1 - 3.3 mg cm ⁻² , N212 membrane, 1 bar gauge back pressure, 0.2 L min ⁻¹ oxidant and fuel flow, 80 °C, 96 % humidity).	103
Figure 63: TEM images of polypyrrole-methyl orange nanotubes after pyrolyzation with different iron salts.	106
Figure 64: BET surface areas of polypyrrole methyl orange nanotube catalysts prepared from different iron salts (a) and BET surface areas after a second heat treatment and with varying iron salt content (b).	107
Figure 65: Mössbauer spectra of polypyrrole methyl orange nanotube catalysts prepared with different iron salts.	108
Figure 66: ORR polarization curves a) and respective H ₂ O ₂ yields b) for the catalysts prepared from different iron precursors recorded with a sweep rate of 10 mV s ⁻¹ in O ₂ saturated 0.1 M H ₂ SO ₄ a rotation rate of 1500 rpm and a disc loading of 0.5 mg cm ⁻² .	110
Figure 67: PEMFC polarization curves of polypyrrole-methyl orange catalysts prepared with different iron salts, voltage against current density (a) and voltage against power density (b). (experiment conditions: H ₂ -O ₂ , cathode loading 3.3 - 3.4 mg cm ⁻² , N212 membrane, 1 bar gauge back pressure, 0.2 L min ⁻¹ oxidant and fuel flow, 80 °C, 96 % humidity).	111
Figure 68: PEMFC polarization curves of polypyrrole-methyl orange catalysts prepared with different iron salts and with altering iron salts amounts after a second heat treatment, voltage against current density (a) and voltage against power density (b). (experiment conditions: H ₂ -O ₂ ,	

- cathode loading $3.2 - 3.4 \text{ mg cm}^{-2}$, N212 membrane, 1 bar gauge back pressure, 0.2 L min^{-1} oxidant and fuel flow, $80 \text{ }^\circ\text{C}$, 96 % humidity). 112
- Figure 69: TEM pictures of polypyrrole-methyl orange-based catalysts prepared with different Fe, Mn or Fe + Mn salts. The catalyst in the lower right was prepared with a different amount of transition metal salts. 115
- Figure 70: BET surface areas for Fe, Mn and Fe/Mn-based Me-N-C catalysts obtained from N_2 sorption experiments. 115
- Figure 71: ORR polarization curves (a) and respective H_2O_2 yields (b) for the catalysts prepared from different iron, manganese and iron + manganese precursors recorded with a sweep rate of 10 mV s^{-1} in O_2 saturated $0.1 \text{ M H}_2\text{SO}_4$, a rotation rate of 1500 rpm and a disc loading of 0.5 mg cm^{-2} . 117
- Figure 72: ORR polarization curves (a) and respective H_2O_2 yields (b) for the catalysts prepared from either $\text{Fe}(\text{Ac})_2$ or $\text{Mn}(\text{Ac})_2$ recorded with a sweep rate of 10 mV s^{-1} in O_2 saturated $0.1 \text{ M H}_2\text{SO}_4$, a rotation rate of 1500 rpm and a disc loading of 0.5 mg cm^{-2} . 118
- Figure 73: PEMFC polarization curves of different Fe, Mn polypyrrole-methyl orange catalysts, voltage against current density (a) and voltage against power density (b). (experiment conditions: $\text{H}_2\text{-O}_2$, cathode loading $2.8 - 3.4 \text{ mg cm}^{-2}$, N212 membrane, 1 bar gauge back pressure, 0.2 L min^{-1} oxidant and fuel flow, $80 \text{ }^\circ\text{C}$, 96 % humidity). 119
- Figure 74: PEMFC stability tests of catalysts that were prepared from Fe, Mn or Fe + Mn salts. The durability tests are performed at a constant potential of 600 mV. (experiment conditions: $\text{H}_2\text{-O}_2$, cathode loading $2.8 - 3.4 \text{ mg cm}^{-2}$, N212 membrane, 1 bar gauge back pressure, 0.2 L min^{-1} oxidant and fuel flow, $80 \text{ }^\circ\text{C}$, 96 % humidity). 120
- Figure 75: PEMFC polarization curves of different $\text{FeCl}_3 + \text{KMnO}_4$ based polypyrrole-methyl orange catalysts after a second heat treatment with altering Fe to Mn-salt ratio and amounts, voltage against current density (a) and voltage against power density (b). (experiment conditions: $\text{H}_2\text{-O}_2$, cathode loading $3.2 - 3.3 \text{ mg cm}^{-2}$, N212 membrane, 1 bar gauge back pressure, 0.2 L min^{-1} oxidant and fuel flow, $80 \text{ }^\circ\text{C}$, 96 % humidity). 121
- Figure 76: PEMFC stability tests of $\text{FeCl}_3 + \text{KMnO}_4$ based polypyrrole-methyl orange catalysts after a second heat treatment with altering Fe to Mn-salt ratio and amounts, performed at a constant potential of 600 mV. (experiment conditions: $\text{H}_2\text{-O}_2$, cathode loading $3.2 - 3.3 \text{ mg cm}^{-2}$, N212 membrane, 1 bar gauge back pressure, 0.2 L min^{-1} oxidant and fuel flow, $80 \text{ }^\circ\text{C}$, 96 % humidity). 121
- Figure 77: Specific BET surface area obtained from N_2 sorption measurements for catalysts that underwent different second heat treatment duration times and the initial catalyst that was treated once. 125
- Figure 78: PEMFC performance of catalysts that underwent no second heat treatment or a second heat treatment with a varying duration time. (experiment conditions: $\text{H}_2\text{-O}_2$, cathode loading $3.3 - 3.7 \text{ mg cm}^{-2}$, N212 membrane, 1 bar gauge back pressure, 0.2 L min^{-1} oxidant and fuel flow, $80 \text{ }^\circ\text{C}$, 96 % humidity). 125
- Figure 79: PEMFC stability tests of catalysts that underwent no second heat treatment or a second heat treatment with a varying duration time. The durability tests are performed at a constant potential of 600 mV. (experiment conditions: $\text{H}_2\text{-O}_2$, cathode loading $3.3 - 3.7 \text{ mg cm}^{-2}$, N212 membrane, 1 bar gauge back pressure, 0.2 L min^{-1} oxidant and fuel flow, $80 \text{ }^\circ\text{C}$, 96 % humidity). 127
- Figure 80: BET surface areas obtained from N_2 sorption measurements for two $\text{FeCl}_3/\text{KMnO}_4$, polypyrrole-methyl orange-based catalysts that differ only in the absolute temperature of their first heat treatment. 129

Figure 81: TEM photographs of FeCl ₃ /KMnO ₄ , polypyrrole-methyl orange-based catalysts prepared at 800 °C (left) or 1000 °C (right).	129
Figure 82: Mössbauer spectra of catalysts which were prepared at different temperatures.	130
Figure 83: PEMFC polarization curves of catalysts that are prepared at different temperatures during the first heat treatment. (experiment conditions: H ₂ -O ₂ , cathode loading 3.4 - 3.6 mg cm ⁻² , N212 membrane, 1 bar gauge back pressure, 0.2 L min ⁻¹ oxidant and fuel flow, 80 °C, 96 % humidity).	131
Figure 84: PEMFC stability tests of catalysts that that are prepared at different temperatures during the first heat treatment. The durability tests are performed at a constant potential of 600 mV. (experiment conditions: H ₂ -O ₂ , cathode loading 3.4 - 3.6 mg cm ⁻² , N212 membrane, 1 bar gauge back pressure, 0.2 L min ⁻¹ oxidant and fuel flow, 80 °C, 96 % humidity).	132
Figure 85: PEMFC polarization curves of catalysts that are prepared at different temperatures during the first heat treatment. (experiment conditions: H ₂ -air, cathode loading 3.4 - 3.6 mg cm ⁻² , N212 membrane, 1 bar gauge back pressure, 0.2 L min ⁻¹ oxidant and fuel flow, 80 °C, 96 % humidity).	133
Figure 86: PEMFC stability tests of catalysts that that are prepared at different temperatures during the first heat treatment. The durability tests are performed at a constant potential of 600 mV. (experiment conditions: H ₂ -air, cathode loading 3.4 - 3.6 mg cm ⁻² , N212 membrane, 1 bar gauge back pressure, 0.2 L min ⁻¹ oxidant and fuel flow, 80 °C, 96 % humidity).	133
Figure 87: BET surface areas obtained from N ₂ sorption measurements for two FeCl ₃ /KMnO ₄ , polypyrrole-methyl orange-based catalysts prepared with a normal acid leaching C-PPy-1000 and with an isopropanol acid leaching C-PPy-1000-IsoAL.	135
Figure 88: TEM photographs of FeCl ₃ /KMnO ₄ polypyrrole-methyl orange catalysts that are prepared at 1000 °C but with a different acid leaching, upper (red box) pictures of catalysts that underwent a 2 M HCl acid leaching and lower (blue box) pictures of catalyst that was acid leached with 2 M HCl + isopropanol.	136
Figure 89: Influence of the acid leaching procedure on the ⁵⁷ Fe-Mössbauer spectra of polypyrrole catalysts.	137
Figure 90: PEMFC polarization curves of catalysts that are prepared at different temperatures during the first heat treatment. (experiment conditions: H ₂ -air, cathode loading 3.2 - 3.5 mg cm ⁻² , N212 membrane, 1 bar gauge back pressure, 0.2 Lmin ⁻¹ oxidant and fuel flow, 80 °C, 96 % humidity).	138
Figure 91: PEMFC stability tests of a FeCl ₃ /KMnO ₄ polypyrrole-methyl orange catalyst that was prepared with a common 2M HCl acid treatment and of the same catalyst prepared with a 2 M HCl + isopropanol acid treatment. The durability tests are performed at a constant potential of 500 mV. (experiment conditions: H ₂ -air, cathode loading 3.2 - 3.5 mg cm ⁻² , N212 membrane, 1 bar gauge back pressure, 0.2 L min ⁻¹ oxidant and fuel flow, 80 °C, 96 % humidity).	139
Figure 92: Lewis-structure and name of the as doping agents investigated compounds for the preparation of polypyrrole-based catalysts.	140
Figure 93: TEM photographs of different polypyrrole based catalysts. Upper pictures show catalyst obtained from polypyrrole-methyl orange, C-PPy-MO and lower pictures gives C-PPy-CT2R a catalyst prepared from polypyrrole-Chromotrop©2R.	142
Figure 94: TEM photographs of different polypyrrole based catalysts. Upper pictures show catalyst obtained from polypyrrole-toluenesulfonic acid, C-PPy-TSA, middle pictures show the catalyst synthesized with polypyrrole- naphthalenedisulfonic acid and lower pictures gives C-PPy-SA a catalyst prepared from polypyrrole-sulfanilic acid.	143

-
- Figure 95: BET surface area obtained from N₂ sorption experiments for catalysts which are synthesized from different polypyrrole + organic molecule precursors. 143
- Figure 96: PEMFC polarization curves of catalysts that are prepared from differently doped polypyrrole. (experiment conditions: H₂-air, cathode loading 3.5 - 3.7 mg cm⁻², N212 membrane, 1 bar gauge back pressure, 0.2 L min⁻¹ oxidant and fuel flow, 80 °C, 96 % humidity). 144
- Figure 97: PEMFC polarization curves of catalysts that are prepared from differently doped polypyrrole. (experiment conditions: H₂-air, cathode loading 2.7 mg cm⁻², N212 membrane, 1 bar gauge back pressure, 0.2 L min⁻¹ oxidant and fuel flow, 80 °C, 96 % humidity). 145
- Figure 98: Polarization curve of catalysts A - E, (experiment conditions: H₂-air, cathode loading 3.3 - 3.9 mg cm⁻², N212 membrane, 1 bar gauge back pressure, 0.2 L min⁻¹ oxidant and fuel flow, 80 °C, 96 % humidity). 148
- Figure 99: 50-hour Stability test of catalysts A - E. (experiment conditions: H₂-air, cathode loading 3.3 - 3.9 mg cm⁻², N212 membrane, 1 bar gauge back pressure, 0.2 L min⁻¹ oxidant and fuel flow, 80 °C, 96 % humidity, 500 mV constant potential). 148
- Figure 100: Schematic representation of the particular synthesis steps for the process of making different non-precious metal-based ORR catalysts. Approach developed by Pajarito Powder (left, blue), Nisshinbo Holdings Inc. (middle, green) and the method presented in this work (right, red). 151

List of Abbreviations

aapyr	4-aminoantipyrine
ACL	anode catalyst layer
AFC	alkaline fuel cell
AL	acid leaching
APS	ammonium peroxydisulfate
ATZC	3-amino-1,2,4-triazole-5-carboxylic acid
B	boron
BET	Brunauer-Emmett-Teller
BEV	battery electrical vehicle
bidpiz	bi-dipyrido[3,2-a:2',3'-c] phenazine
bis-Me-Im	2,20-bis(4,5-dimethylimidazole)
BOP	balance of plant
BoT	beginning of test
BP	2,2-bipyridine
CA	cyanamide
CB	carbon black
CCL	cathode catalyst layer
CDIAC	Carbon Dioxide Information Analysis Center
CeO ₂	cerium(IV) oxide
CH ₃ CN	acetonitrile
CNT	carbon nanotube
Co	cobalt
CO ₂	carbon dioxide
COR	carbon oxidation reaction
CoTMPP	5,10,15,20-Tetrakis(4-methoxyphenyl)-21H,23H-porphine cobalt(II)
Cr	chromium
Cu	copper
CV	cyclic voltammetry
DABCO	1,4-diazabicyclo [2.2.2] octane
DBSNa	sodium dodecylbenzene sulfonate
DCDA	dicyandiamide
DEMS	differential electrochemical mass spectrometry
DFMA	design for manufacturing & assembly
DFT	density functional theory

DMF	N,N-dimethylformamide
DMFC	direct methanol fuel cell
DPTZ	3,6-di-2- pyridyl-1,2,4,5-tetrazine
e ⁻	electron
EBIT	earnings before interests and taxes
EDA	ethylenediamine
EDTA	ethylenediaminetetraacetic acid
EoT	end of test
EU	European Union
EW	equivalent weight
EXAFS	extended x-ray absorption fine structure
F	fluorine
FC	fuel cell
FCEV	fuel cell electrical vehicle
Fe	iron
Fe(Ac) ₂	iron acetate
Fe(C ₂ O ₄)	iron oxalate
Fe(CN) ₆	iron cyanide
Fe(NO ₃) ₃	iron nitrate
Fe(OH) ₂	iron hydroxide
Fe(SCN) ₃	iron thiocyanate
Fe ₃ O ₄	iron oxide
FeCl ₂	iron (II) chloride
FeCl ₃	iron (III) chloride
Fe-N-C	iron-nitrogen-carbon
Fe(Ox)	iron oxalate
FePc	iron phthalocyanine
FeSO ₄	iron sulfate
FeTMPPCl	5,10,15,20-Tetrakis(4-methoxyphenyl)-21H,23H-porphine iron(III) chloride
GDL	gas diffusion layer
GDP	gross domestic product
GGA	generalized gradient approximation
Gly	glycine
H ₂	hydrogen molecule
H ₂ O	water

H ₂ O ₂	hydrogen peroxide
H ₂ SO ₄	sulfuric acid
HAADF-STEM	high-angle annular dark-field scanning transmission electron microscopy
HCl	hydrogen chloride
HF	hydrogen fluoride
HNO ₃	nitric acid
HSAC	high surface area carbon
ICP-MS	inductively coupled plasma mass spectrometry
ICV	internal combustion engine
IEC	ion exchange capacity
IrO ₂	iridium oxide
LANL	Los Alamos National Laboratory Institute
LDA	local density approximation
LDV	light duty vehicle
MBZ	mebendazol
MCFC	molten carbonate fuel cell
MDV	medium duty vehicle
MEA	membrane electrode assembly
Mel	melamine
Me-N-C	metal-nitrogen-carbon
MFR	melamine formaldehyde resin
Mn	manganese
MnCl ₂	manganese chloride
MOF	metal organic framework
MPL	microporous layer
MS	Mössbauer spectroscopy
MSAC	medium surface area carbon
MWCNT	multi-walled carbon nanotube
N	nitrogen
NA	nitroaniline
NaCl	sodium chloride
NCB	sicarbazin
NH ₃	ammonia
Ni	nickel
NP	nanoparticle

O	oxygen
O ₂	oxygen molecule
OA	oxalic acid
OER	oxygen evolution reaction
ONP	organic nitrogen precursor
ORR	oxygen reduction reaction
P	phosphor
P-2-ABI	poly-2-aminobenzimidazole
P3MTh	Poly-3-methylthiophene
PAFC	phosphoric acid fuel cell
PAN	poly acryl nitrile
PANI	poly aniline
p-BDA	p-phenylenediamine
PDA	poly-dopamine
p-DAP	poly-diaminopyridine
PEDOT:PSS	poly-(3,4-ethylenedioxythiophene) polystyrene sulfonate
PEI	poly-ethylenimine
PEMFC	proton exchange membrane fuel cell
PFSA	perfluorosulfonic acid
PGM	platinum group metal
phen	1,10-phenanthroline
PI	polyindole
PmPDA	poly- <i>m</i> -phenylenediamine
Ppy	poly pyrrole
Pt	platinum
PTCDA	perylenetetra-carboxylic-dianhydride
PTFE	poly(tetraflouro ethylene)
PTh	polythiophene
PTPT	poly-(2,4,6-tripyrrol-1,3,5-triazine)
Pur	purine
PVESF	perfluoriated vinyl ether sulfonyl fluoride
PVP	polyvinylpyrrolidone
Pyr-COOH	2-pyrazinecarboxylic acid
RDE	rotating disc electrode
RDS	rate determining step

rGO	reduced graphene oxide
RHE	reversible hydrogen electrode
ROS	radical oxygen species
RRDE	rotating ring disc electrode
S	sulfur
SCMS	silica core mesoporous shell
SGB	sulfaguanidin
SOFC	solid oxide fuel cell
SSM	sacrificial support method
TAPP	5,10,15,20-(tetra-4-aminophenyl)porphyrin
TEM	transmission electron microscopy
TFE	tetrafluoroethylene
TGA	thermogravimetric analysis
THF	tetrahydrofuran
TiO ₂	titan dioxide
TOF	turn over frequency
ToF-SIMS	time-of-flight secondary ion mass spectrometry
TPA	terephthalic acid
TPTZ	2,4,6-tri(2-pyridyl)-s-triazine
TsOH	p-toluenesulfonic acid
TsONa	p-toluenesulfonic acid
U.S. DOE	United States Department of Energy
V	vanadium
XANES	x-ray absorption near-edge structure spectroscopy
XPS	x-ray photoelectron spectroscopy
XRD	x-ray diffraction
ZIF	zeolitic imidazole framework
Zn	zinc
Zn(NO ₃) ₃	zinc nitrate

List of Symbols

Symbol	Name of Symbol	Dimension
$E_{1/2}$	half wave potential	V
E_{cell}	cell potential	V
$E_{iR\text{-corr}}$	iR -corrected potential	V
E_{onset}	onset potential	V
e	elementary charge	A s
ε	Faradaic efficiency	%
E_{theo}	Nernstian potential	V
η	overpotential	V
$\eta_{\text{act,c}}$	cathodic activation overpotential	V
$\eta_{\text{conc,c}}$	cathodic concentration overpotential	V
η_{Ω}	Ohmic loss	V
F	Faraday's constant	A s mol ⁻¹
i	current	A
i_{D}	ring current	A
i_{R}	ring current	A
j_0	exchange current density	A m ⁻²
$j_{\text{diff,lim}}$	diffusion limited current density	A m ⁻²
j_{kin}	kinetic current density	A m ⁻²
j_{rel}	relative current density	%
n	amount	
N_{A}	Avogadro's constant	
n_{e}	number of electrons	
N_{eff}	collection efficiency	%
n_{m}	monolayer capacity	mV s ⁻¹
v	sweep rate	V s ⁻¹
OCV	open circuit voltage	V
p	equilibrium pressure	bar
p/p_0	relative pressure	
p_0	saturation pressure	bar
Q	electric charge	A s
R	universal gas constant	J mol ⁻¹ K ⁻¹
R	resistance	Ω

R_{Ω}	Ohmic resistance	Ω
T	temperature	K
ν	kinematic viscosity	$\text{m}^2 \text{s}^{-1}$
W_{el}	electrical work	J

1 Introduction and the Broader Context

The Climate Challenge

During the last centuries, in combination with other important discoveries the utilization of fossil-based energy carriers played a major role in the proceeding of mankind. A growing world population and an increasing gross domestic product (GDP) lead to a growth in the demand of these energy carriers [4]. The main product of the combustion of fossil fuels is CO₂ (and H₂O). As a consequence, the annual emissions caused by the combustion of fossil fuels is increasing, this is illustrated in **Figure 1 a)** with the data provided from the Carbon Dioxide Information Analysis Center (CDIAC) [5, 6]. For the concentration of atmospheric CO₂, a positive correlation with the global temperature is found as given in **Figure 1 b)** by the data obtained from the Earth Policy Institute in Washington, D.C., USA [7]. Hence, it has been pointed out by many researchers that the excessive utilization of fossil fuels has an influence on the global climate, leading to severe ecological damages [8-12].

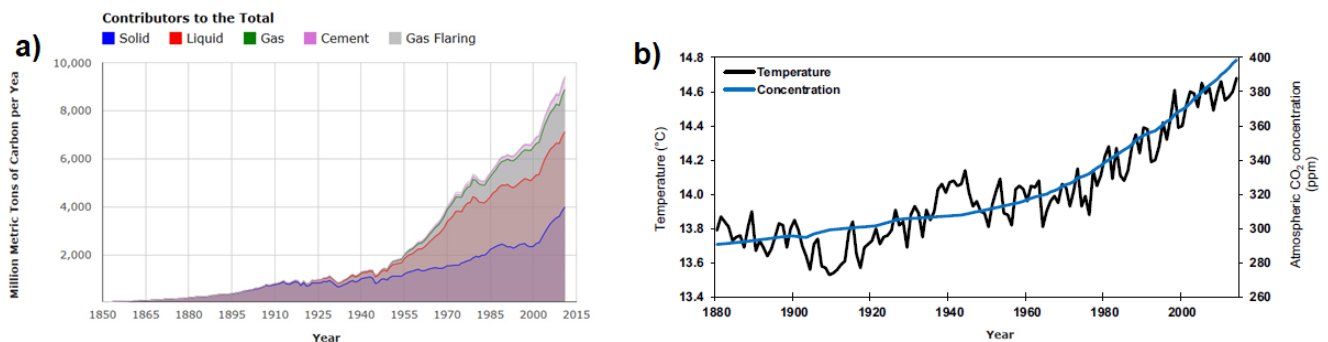


Figure 1: Annual global fossil fuel carbon emissions by individual contributors (a) and the average global temperature correlating with the atmospheric CO₂ concentration (b) [5-7].

The causality of anthropogenic greenhouse gas emissions and climate change, as well as the significance of associated ecological, economical and health problems that comes along with this change, are also recognized in society and by political decision-makers. This is why recently the European Union (EU) intensified efforts in climate policy by the communication of the so-called "European Green Deal". The regarding communication paper from the European Commission states that "The atmosphere is warming and the climate is changing with each passing year. [...] The European Green Deal [...] aims to transform the EU into a fair and prosperous society, with a modern, resource-efficient and competitive economy where there are **no net emissions of greenhouse gases in 2050 and where economic growth is decoupled from resource use.**" [13]. To reach the ambition of zero net greenhouse gas emission in 2050, substantial challenges in politics, economics and also science still remain.

Amongst other technologies, hydrogen driven fuel cells are considered to play a major role in the transition from the use of fossil fuel-based energy to renewable energy. A fuel cell is an electrochemical power converter which utilizes the energy stored in chemical bonds by turning it directly into electrical power. In the case of the hydrogen driven fuel cells, the energy is taken from the hydrogen-hydrogen bond of the H₂ molecule. The reaction product of this energy transition is obtained after the combination of the hydrogen with oxygen (from air) producing pure water. If fed with "green" hydrogen, i.e. hydrogen generated for instance from water splitting powered by renewable electricity like solar or wind, no greenhouse gases are emitted during this process. Because of their high technology readiness level, the so-called proton-exchange-membrane fuel cells (PEMFCs) are of particular interest for the application in the transport and mobility sector, as well as for stationary applications.

The Special Case of the Transport Sector and the Problem of Car Manufactures

The transport sector is responsible for almost a quarter of EU's greenhouse gas emissions. The issue related to greenhouse gas emission from the transport sector is illustrated in **Figure 2**. Since 1990 the emissions of all other sectors have seen a decline whereas the emissions from the transport sector increased [14].

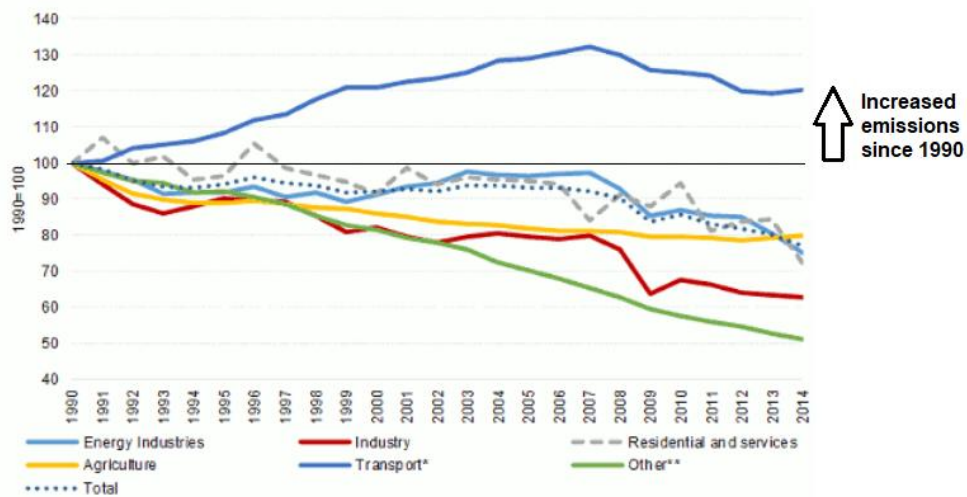


Figure 2: Change in greenhouse gas emissions of the EU by sector, normalized to the emissions of the year 1990, figure taken from the European Environment Agency [14].

In 2014, road transport alone contributed with more than 70 % to the emissions from the transport sector [14]. Likewise in 2014, the EU passed a regulation considering the target average CO₂ emissions of new passenger cars [15]. The regulation demands new passenger cars in average not to exceed the emission of 95 g_{CO2}/km from 2021 onwards [16]. In detail the target value is also depending on the weight of the vehicle and is calculated according to:

$$95 \frac{g_{CO_2}}{km} + 0.0457 \text{ (average weight of vehicle sold - 1.372 kg)}$$

Car manufactures face a penalty of 95 € per gram CO₂ and per vehicle above this limit. In 2018 the average CO₂ emission of new passenger cars in the EU was reported with 120.4 g_{CO2}/km. Which is still 126 % of the upcoming target value and has only slightly changed since 2014 when 123.4 g_{CO2}/km were reported. A study conducted by the PA Consulting Group predicts the financial penalties for car manufactures to account for 14,655 billion Euro in 2021 [17]. For some manufactures the scenario penalty even exceeds the earnings. Details on the target value and the forecasted penalty for each car manufacture are shown in **Table 1**.

Table 1: Forecasted penalties resulting from exceeding CO₂ emission target values for car manufactures in the EU [17].

Car maker	2018 [g _{CO2} /km]	2021 target [g _{CO2} /km]	2021 forecast [g _{CO2} /km]	Penalty [million €]	Penalty [% of EBIT 2018]
Volkswagen	121.1	96.6	109.3	4,504	32.4
Daimler	130.4	103.1	114.1	997	9.0
Fiat-Chrysler	125.4	92.8	119.8	2,461	49.5
BMW	123.6	102.5	110.1	754	8.3
Renault-Nissan-Mitsubishi	108.2	92.9	97.8	1,057	12.4
Mazda	134.8	94.9	123.6	877	115.7
Honda	126.8	94	119.2	322	5.5
Toyota	100.9	94.9	95.1	18	0.1
Volvo	129.5	108.5	119.8	382	27.6
Hyundai-Kia	118.9	93.4	101.1	797	28.9
PSA	113.9	91.6	95.6	938	21.3
Jaguar-Land-Rover	151.5	130.6	135	93	404.3
Ford	122.7	96.6	109.3	1,456	39.0
Average or Sum	123.7	99.4	111.5	14,655	58.0

Based on the numbers in **Table 1**, it is obvious that for the majority of car makers the forecasted penalties are a matter of financial survival. Following 2021 the target values for average CO₂ emissions are even lower. In 2025, 80.8 g_{CO2}/km and in 2030 59.4 g_{CO2}/km have to be reached, respectively [17]. Considering that 1 liter of petrol converts to 2,330 g of CO₂ and 1 liter of diesel to 2,640 g, the average fuel consumption must diminish to 2.6 liter per 100 km of petrol fuel and 2.3 liter per 100 km of diesel by 2030. By selling vehicles powered by internal combustion engines (ICV) only, manufacturers cannot reach these targets.

Conclusion

Alternative propulsion techniques become inevitable. Primarily, these alternative techniques are represented by battery electrical vehicles (BEVs) and fuel cell electrical vehicles (FCEVs). Whereas at the moment BEVs have an advantage in market penetration, both BEVs and FCEVs have unique characteristics which makes either BEVs or FCEVs better suited in respect to the demands governed by the field of application [18]. As illustrated in **Figure 3**, the deployment of FCEVs is beneficial for the transport sectors demanding a higher range and greater weights. As it is the case for medium and large cars, busses, trucks and trains. Contrary, BEVs are better suited for urban mobility applications, as they provide less range in a smaller and lighter vehicle. Higher energy densities are required for planes or passenger ships and can be achieved with synthetic fuels.

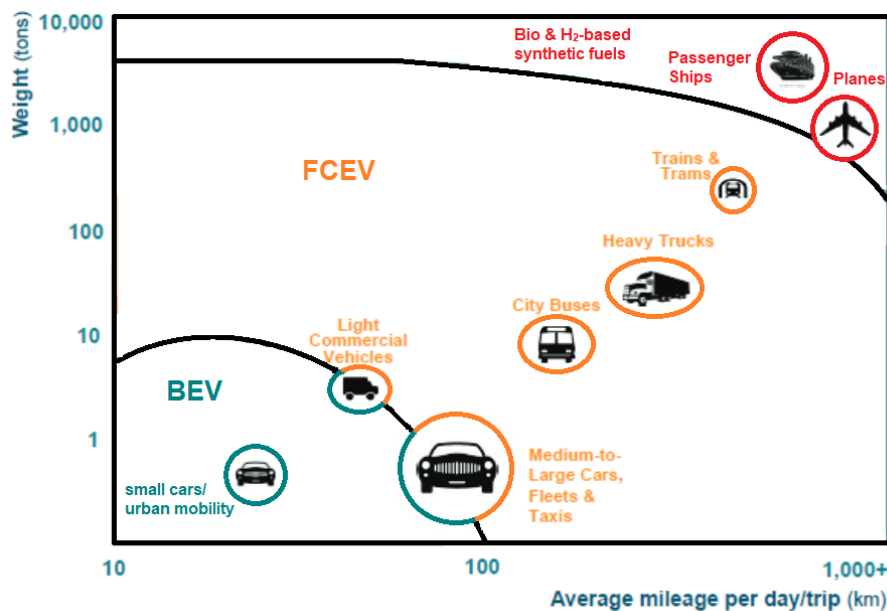


Figure 3: Field of application for BEVs, FCEVs and synthetic fuel based transport solutions in respect to weight and average mileage per trip demand, figure taken from [18].

Summarizing the preceding facts about the relation of anthropogenic greenhouse gas emissions, climate change, climate policy and the upcoming challenges, the future transport sector faces, an urgent need for reliable and economically affordable alternative driven power sources.

2 Aim and Outline of this Work

Aim of this Work

For the successful decarbonization of the transport sector there is an urgent need for alternatively driven power devices. Especially with respect to heavy duty and long-range applications, PEMFCs are among the most promising devices that can fulfill this need. Still, there are different challenges for this technology that have to be addressed. A major one are the high costs which are mainly caused by the usage of Pt-based catalysts. Especially for the cathodic ORR, where great amounts of the expensive precious metal are required to compensate for the sluggish reaction kinetics.

Over the last decades, PEMFC technology made significant progress. Stack costs of an 80 kW_{net} system (one passenger car) were reduced from 140 \$ kW_{net}⁻¹ in 2006 to only 46 \$ kW_{net}⁻¹ in 2018 (production rate 500,000 systems per year) [19]. Thereby, the Pt demand was lowered to ~10 g per vehicle [20]. Still, major challenges remain. The ultimate cost target reported by the U.S. Department of Energy (U.S. DOE) is 30 \$ kW_{net}⁻¹ [19, 20]. Currently, over 40 % of fuel cell stack costs are caused by the Pt-based catalysts [19, 21]. Researchers from General Motors concluded that when "*Considering both the cost to consumer and the supply–demand relation in the precious metal market, a stretch target of 6 g_{Pt} per vehicle appears appropriate.* [22]" However, costs are not the only reason that are associated with usage of Pt in fuel cells. The criticality becomes obvious when one considers that 92 % of all Pt is mined in just three countries (South Africa, Russia and Zimbabwe) [23]. In total, five major drawbacks in relation with the use of Pt-based fuel cell catalysts can be identified (see end of chapter 3.2).

This thesis faces the mentioned problems by developing a new synthesis route for a so-called Fe-N-C oxygen reduction reaction (ORR) catalyst. These catalysts are based on cheap and earth abundant elements such as Fe, N and C. So far, Fe-N-C catalysts still need to improve in activity and stability. Poor volumetric activity, low-active site density and an unfortunate trade-off relation between activity and stability limit their application. However, the potential of replacing scarce Pt with a cheap transition metal could become a game changer for the PEMFC technology.

The preparation of a Fe-N-C catalyst is a complex and multi-step process in that way that there are several synthesis parameters which contribute to either activity, stability or both, sometimes in a contrary fashion. Therefore, precise understanding, balancing or even "fine-tuning" of these parameters is necessary to reach fuel cell performance targets. This thesis addresses drawbacks that were associated with previous Fe-N-C catalyst synthesis. The most successful findings of this work have been submitted for a patent application [24].

Outline of this Work

Table 2 shows the topics of Fe-N-C catalyst synthesis that were addressed within the different chapters of this work.

Table 2: Overview of addressed topics related to Fe-N-C catalyst synthesis and investigated approach of solution within the different chapters of this thesis.

Key-word/ Chapter + page	Problem Addressed	Approach
Preliminary Experiments Chapter 7, page: 75	Low stability caused by amorphous carbon phases.	Highly graphitized carbon nanotubes as primary carbon source.
Simple C,N-Precursor Chapter 8.1/8.2, page: 91	Expensive C, N precursors due to complex structure (e.g. ZIF-8 or porphyrins).	Doped polypyrrole (PPy) as simple C, N precursor.
Iron Precursors Chapter 8.3, page: 105	Low activity due to inhomogeneous iron site composition.	Find the best-suited iron salt precursor for specific PPy.
Iron-Manganese Precursors Chapter 8.4, page: 113	Low activity but higher stability reported for manganese catalysts.	Investigate possible synergetic effect of iron (high activity) and manganese (high stability).
Heat-Treatment and Stability Chapter 8.5, page: 123	Low stability caused by amorphous carbon phases.	Optimize heat-treatment temperature.
Inorganic Side-Phases Chapter 8.6, page: 134	Catalysts can contain inorganic iron, even after acid leaching.	Refine the leaching procedure.
Doping Agents Chapter 8.7, page: 140	Low mass transport due to unfavorable catalyst particle morphology and high catalyst loadings.	Examine the effect of doping agent on morphology.

Preliminary experiments, chapter 7: During the course of this thesis two different approaches have been developed. The first synthesis is based on surface functionalized carbon nanotubes (CNTs). This catalyst showed very high ORR activity and stability under rotating disc electrode (RDE) conditions. However, these results could not be transferred to the fuel cell testing level. Learning from the drawbacks of this first approach, a second synthesis based on doped polypyrrole was developed.

Main part of the thesis, chapter 8: This chapter deals with a new synthesis approach based on doped polypyrrole and represents the main part of this thesis.

Simple C, N precursor, chapter 8.1/8.2: Previous catalysts that showed high fuel cell performance are often based on complex and thus expensive C, N precursors such as ZIF-8 or porphyrins [25, 26]. Contrary, simple precursors like polypyrrole or polyvinylpyrrolidone show low performances [27-30].

This problem is address in chapter 8.1/8.2 by doping a simple polypyrrole precursor with a low-cost organic molecule.

Iron precursor, chapter 8.3: During the heat treatment of Fe-N-C catalyst synthesis the molecular FeN_xC_y active sites are formed simultaneously with other inorganic iron side phases such as iron nanoparticles or iron carbides. Often the fraction of active sites underweights the fraction of iron side phases resulting in low active catalyst. The approach presented in chapter 8.3 targets the type of iron salt, the latter plays a crucial role on this parameter. Different iron salts are investigated in combination with the doped polypyrrole precursor.

Iron-manganese precursors, chapter 8.4: So-far in acidic media, iron based Fe-N-C catalyst showed the highest ORR activity, whereas other transition metals, in particular manganese, show better stability [31]. In chapter 8.4 synergetic effects of a bimetallic iron- and manganese-based catalysts are investigated, with the aim of obtaining a good stability (Mn) while maintaining a high activity (Fe).

Heat-treatment and stability, chapter 8.5: Among others, one of the main degradation paths that is discussed for Fe-N-C catalysts is carbon corrosion. Previous catalysts often show a highly disordered and amorphous carbon structure, latter eases the terms of carbon corrosion induced degradation processes [32]. This issue is addressed in chapter 8.5 by investigating the relation between heat-treatment temperature and stability for the developed doped polypyrrole catalyst.

Inorganic side-phases, chapter 8.6: Usually, Fe-N-C catalysts are subjected to an acid leaching step after the heat treatment. In principle this step should remove all inorganic iron side phases from the catalyst. However, because inorganic iron is often shielded by carbon, Fe-N-C catalyst in reality contain high amounts of inorganic phases even after a leaching step. Inorganic iron can leach out during fuel cell operation, this leads to severe MEA damage [33]. In chapter 8.6 a leaching method is presented which significantly improves the leaching of side phases whereas the active sites stay intact.

Doping agents, chapter 8.7: To compensate for low volumetric activity of Fe-N-C catalysts, high loadings are applied during fuel cell application. However, high cathode catalyst layer loadings lead to severe performance losses due to mass transport issues. With respect to this matter, the morphology of the catalyst particles as well as their size play an important role on this. Chapter 8.7 investigates the influence of different doping agents on the morphology of the catalyst particles with the aim of improving performance in the mass transport limited regime of the fuel cell polarization curve.

A short summary is given in chapter 8.8 by providing fuel cell tests for the best performing catalyst of each chapter under comparable operation conditions. The performance of the final catalyst of this work is compared with the "best-off" values reported in literature in chapter 9. Likewise, the

practicability of the developed synthesis process is briefly discussed in chapter 9. A comprehensive summary and an outlook are provided in chapter 10. Further information and an evaluation of the reproducibility of the synthesis is found in the appendix.

3 Fuel Cells Background Information and Current Scientific Knowledge

This chapter provides background information for this work. The aim is to draw a detailed picture on the current development standpoint of fuel cell technology in general. Even so this work is focused on the development of a cathode catalyst, a brief overview of all components of a fuel cell will be given following. This is because the dimensions of the individual parts influence each other. Meaning for an overall success of the fuel cell technology a comprehensive understanding and balancing of all components together is needed. This holds true especially when one considers the costs. As an example: even so Fe-N-C catalysts are significantly cheaper than Pt/C catalysts, the overall stack costs of a PEMFC system might increase when implementing a Fe-N-C catalyst. The power density of Fe-N-C catalysts is usually much lower compared to Pt/C catalysts. This requires a greater cell area in order to reach the same power output, meaning more membranes, bipolar plates etc., this drives the costs. This subject will be discussed in more detail later in chapter 3.2.

3.1 Proton-Exchange-Membrane Fuel Cells (PEMFCs)

A fuel cell is an electrochemical power source which utilizes the energy stored in chemical bonds by converting it directly into electrical power. There are different types of fuel cells, utilizing different fuels or operating at different conditions like temperature or pH-value. The most important types of fuel cells are the proton-exchange-membrane fuel cell (PEMFC), the alkaline fuel cell (AFC), the direct methanol fuel cell (DMFC), the solid-oxide fuel cell (SOFC), the phosphoric acid fuel cell (PAFC) and the molten-carbonate fuel cell (MCFC). **Figure 4** gives the annually delivered fuel cell power in megawatt [34]. Among the different types of fuel cells, the PEMFC dominates the fuel cell market. This is because of the high development grade and readiness level of the PEMFC technology. The non-precious metal-based ORR catalyst that is developed in this work could be used in PEMFCs, AFCs or DMFCs. This thesis will focus on the PEMFC as it is the most widely adopted technology.

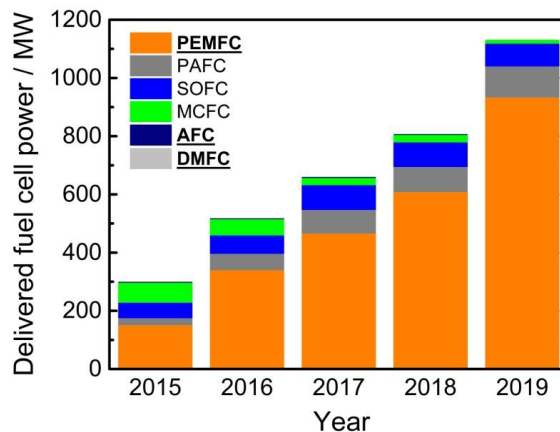


Figure 4: Delivered fuel cell power per year with respect to the type of fuel cell. PEMFC, AFC and DMFC are highlighted because the developed catalysts of this work could be applied within these fuel cells [34].

General PEMFC Setup and Reaction Equations

Figure 5 gives a schematic drawing of a PEMFC showing its different components [35]. The different components of the fuel cell are arranged in a sandwich-like way with the electrolyte membrane in the centre. The occurring chemical reactions are displayed on the right-hand side of Figure 5. Briefly, during operation H₂ gas is delivered to the anode where it is oxidized by the anode catalyst giving hydrogen ions and electrons. The hydrogen ions are migrating through the electrolyte (membrane) whereas the electrons are forced through an external circuit to the cathode side. Here, with the help of the cathode catalyst, the electrons and the hydrogen ions combine with oxygen which is provided by the cathode gas flow to form pure water (and heat). The developed catalyst of this work is applied inside the cathode catalyst layer (CCL), it is highlighted red. For an isothermal operation of the fuel cell, the products water and heat need to be removed continuously.

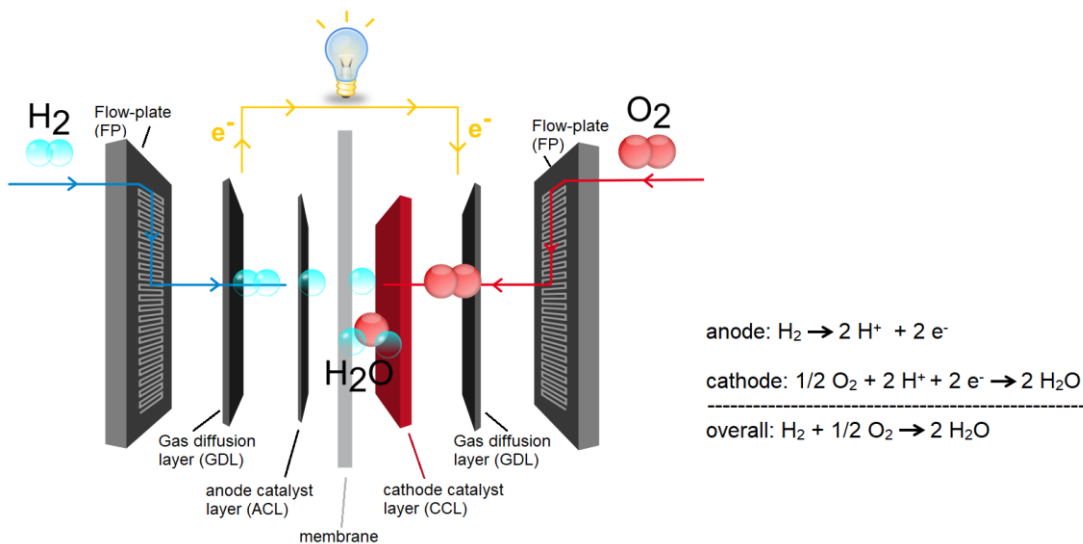


Figure 5: Left: schematic drawing of a PEMFC's layout giving the different parts, right: the half-cell and overall cell reactions [35].

Polarization Curve of the PEMFC

The performance of a fuel cell is often visualized by its voltage versus current density response, the so-called polarization curve. Due to specific irreversible losses, the cell voltage decreases with an increasing current density. Figure 6 shows the typical course of a PEMFC polarization curve [36].

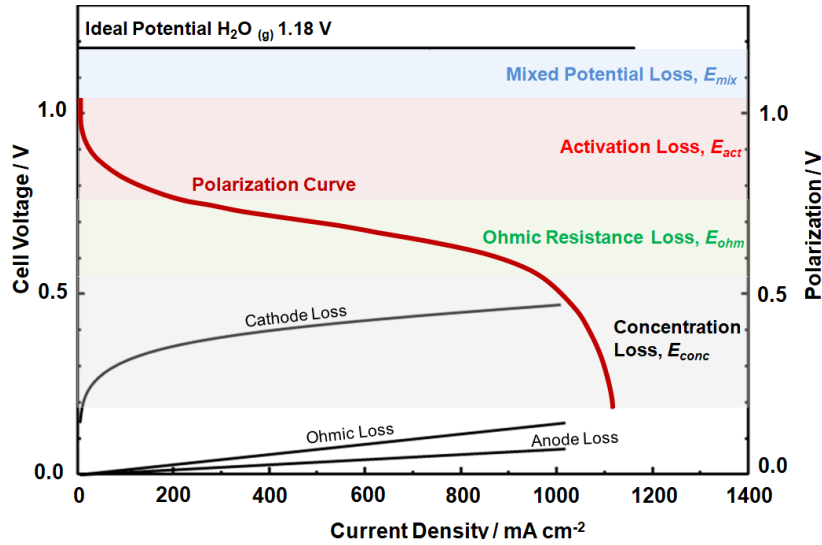


Figure 6: PEMFC polarization curve giving the cell voltage versus the current density; the different regions of the irreversible voltage losses are caused by mixed potential, activation loss, ohmic resistance and mass transport limitations. Figure adapted from [36].

The actual cell voltage V_{cell} at a given current density is expressed as the ideal (reversible) voltage E_{ideal}^0 minus the mixed potential loss E_{mix} , the activation loss E_{act} , the ohmic resistance loss E_{ohm} and the concentration loss E_{conc} :

$$V_{cell} = E_{ideal}^0 - E_{act} - E_{mix} - E_{ohm} - E_{conc} \quad (1)$$

Mixed potential losses E_{mix} are caused by fuel crossover through the membrane, electronic conduction through the membrane (electronic short) and oxidation of catalyst and electrode materials as a result of the fuel crossover. The effects of the mixed potential are strongly depending on the thickness of the electrolyte membrane and the tightness of the sealing gasket. In general, the open circuit is lowered by values of 5 -10 mV whereas during fuel cell operation, the current density is only affected to minor degrees causing current density losses of a few milliamperes. The activation losses E_{act} are caused by the energy barrier which needs to be overcome to drive the cell reactions (ORR and HOR). It is mainly a function of temperature, pressure and the concentration of hydrogen and oxygen. The main part of this loss is caused by the sluggish ORR kinetics at the cathode. This behavior is explained later in **Figure 11**. Hence, improved ORR catalysts are urgently needed to improve the overall performances of PEMFCs. The Ohmic resistance E_{ohm} which is considerably visible for medium current density ranges is resulting in a linear voltage loss because it follows the Ohmic law. Smaller parts of this voltage decay are caused by electronic resistance of the fuel cell components. The electrons must travel through the catalyst layer, the gas-diffusion-layer, the flow fields and the cables to the load. Still, the majority of the Ohmic resistance loss is caused by the proton conductivity through the electrolyte. The resistance of proton conductivity is much greater than that of electron conduction due to the higher mass of

protons. Concentration losses E_{conc} usually occur at higher current densities, respectively lower cell potentials. In this region of the polarization curve the reaction rate exceeds the rate at which the reactants are delivered, or the product (water) is removed. Hence, mass transport properties become the limiting step.

Flow Plates/Bipolar Plates

At the outer ends of the PEMFC the flow plates or bipolar plates are positioned. The tasks of these plates are [37]:

- delivering and distributing the gas flows
- fixing the cell by bringing mechanical stability
- separating individual cells of a stack
- carrying the current away from the cell
- facilitating the heat management.

Depending on the application type of the PEMFC, the flow plates are manufactured from different materials, such as steel, stainless steel, titanium, titanium alloys, electrographite, polymer-carbon-/ or polymer-metal-composites [37-39]. A variety of different designs and geometries of flow plates have been realized, some important ones are given in **Figure 7** [39].

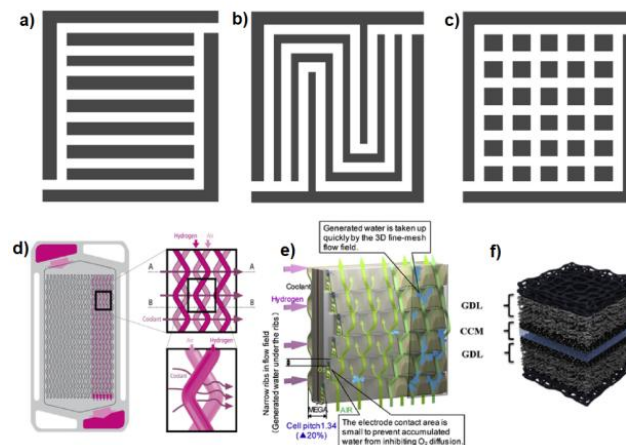


Figure 7: Different designs and geometries of flow plates: parallel flow-channel (a), parallel-serpentine flow-channel (b), pillar flow-channel (c) [40], Honda FXC Clarity wave flow-channel with cooling technology (d) [41], Toyota Mirai 3D fine-mesh flow-field (e) [42] and graphene foam flow field (f) [43].

To this day, the bipolar plates account for 20 - 30 % of the costs, 60 - 80 % of the weight and 80 % of volume of a PEMFC stack [44-49]. Key parameters that have to be concerned in the development of improved bipolar plates according to the Department of Energy (U.S. DOE) are the costs, the plate's

weight, the H₂ permeation rate, the corrosion at anode and cathode respectively, the electrical conductivity, the interfacial contact resistance, the flexural strength and the forming elongation [50].

Gas Diffusion Layer

The gas diffusion layer (GDL) is typically made from carbon paper or woven carbon fabrics [51]. The major tasks of this layer are:

- the electronic connection between catalyst layer and flow plate
- a mechanical strengthening of the membrane electrode assembly
- the protection of the catalyst layer from corrosion and erosion from the gas flow
- the enhancement of the gas transport into the catalyst layer, including the transport of water vapour into the catalyst layer and the membrane
- the facilitation of the removal of liquid water which is mainly produced by the catalytic reduction of O₂ at the cathode.

To realize these substantial tasks, the carbon fibers of the GDL are coated or treated with a hydrophobic agent e.g. PTFE. The GDL's side which is facing the catalyst layer is coated with a microporous layer (MPL), typically carbon black or carbon black impregnated with PTFE is used. As mentioned in [52] the exact manner of functioning of the MPL is still being debated. Explanations of the improved performance of PEMFCs comprising a MPL are an increased removal of water from the cathode by increasing the temperature of the electrodes and preventing condensed water to re-enter from the flow-channels and an increased force of water towards the anode side [53-59]. **Figure 8** illustrates the structure of a GDL and shows its location within the PEMFC [52], [60].

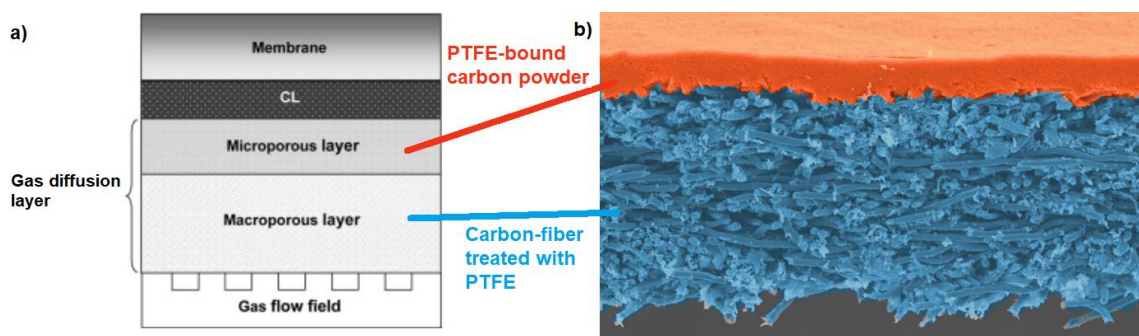


Figure 8: Location of the GDL between flow field and catalyst layer inside the PEMFC (a) [52] and artificially colored SEM image giving the cross section of a GDL highlighting macroporous carbon fiber layer (blue) and microporous carbon black layer (red) [60].

Important parameters for evaluating GDLs are the gas permeability, the hydrophobicity, the pore structure, the porosity and the surface morphology [61].

Electrolyte Membrane

The core part of the fuel cell is the so-called membrane-electrode-assembly (MEA). The MEA comprises of the membrane embedded by the anode catalyst layer on one side and the cathode catalyst layer on the other side. The membrane of PEMFCs is usually a perfluorinated ionomer. Commercially available products are for instance Nafion™, Aquivion®, Fumion®, Aciplex™, 3M™, Flemion™ or Hyflon™. These perfluorosulfonic acid (PFSA) copolymers are mostly synthesized through a free radical polymerization of perfluorinated vinyl ether sulfonyl fluoride (PVESF) with tetrafluoroethylene (TFE) [62]. The two main features of the obtained copolymer are the hydrophobic backbone and the sulfonic acid functional group attached through the side chain. The latter is responsible for the cation conductivity. The structures of important PFSA copolymers are shown in **Figure 9**.

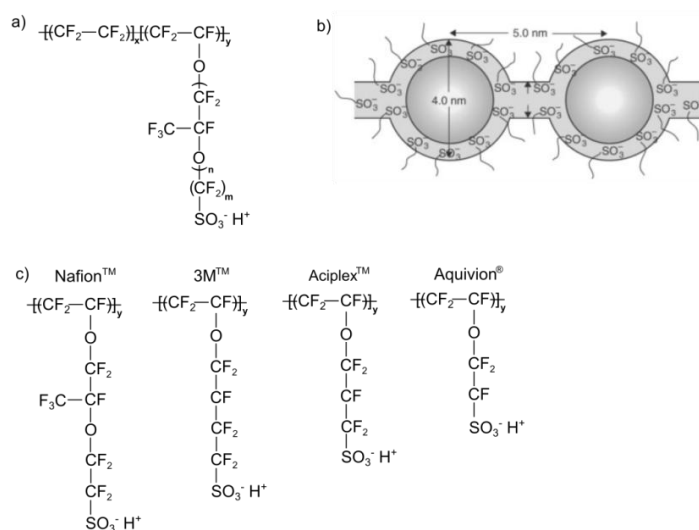


Figure 9: Chemical structure of Nafion™ showing the different possible compositions influenced by the values of the parameters x , y , n and m (a) [63], cluster network model proposed for hydrated PFSA membranes [64] (b) and structure and length of the side chain from different PFSA copolymers [65].

The most relevant parameter considering the PFSA copolymers is the so-called equivalent weight (EW). It is calculated as the weight of dry polymer per mole ion conducting SO_3^- sites. Which means it is determined by the average distance between side chains along the backbone [66] and corresponds to the inverse of the ion exchange capacity (IEC) [67]. Lower EWs usually mean higher proton conductivities but more severe swelling and less mechanical stability through water uptake. Still, the correlation is not straight forward as it was found that Aciplex™ S-1112 (EW: 1050) shows the same proton conductivity as Flemion™ LSH-180 (EW: 1099) of 0.13 S cm^{-1} at 25°C [68]. This behavior was explained by the additional water uptake of Aciplex™ which compensates the increase of ion concentration in comparison to the Flemion™ membrane. Hence, not ion concentration but water mobility is the decisive factor [69]. **Figure 9 b)** further shows the arrangement of the polymer backbone and the polymer side chain into different domains. As illustrated, the TFE backbone of the

PFSA ionomer forms a hydrophobic crystalline region providing thermal and chemical stability. The side chains form hydrophilic channels adsorbing water and enabling the conductivity of protons [70, 71]. To meet the high life time requirements of several thousand hours of operation, state-of-the-art electrolyte membranes further comprise of a mechanical reinforcement layer, mostly PTFE. In particular, thin membranes show low resistance for proton conductivity and advantages considering water management. Contrarily, thinner membranes show less mechanical stability. Mechanical stress on the membrane is occurring for instance during the fabrication of the MEA (exposure to organic solvents), through water uptake during fuel cell operation or during freeze-thaw cycles, occurring during the dynamic operation in vehicles [69]. Reinforced membranes usually show thicknesses of 25 - 35 μm , whereas their mechanical strength is comparable to non-reinforced membranes of 175 μm [69, 72]. Commercially available reinforced membranes often consist of a stabilizing polymer matrix (PTFE or PE) which is filled with a PFSA resin. Examples are the Gore-Select[®], Gore[®] Primera[®], Nafion[™] XL or Flemion[®] RF2. Despite the mechanical stress, electrolyte membranes also need to withstand the influence of chemical attack. In particular, the appearance of reactive oxygen species (ROS) such as hydroxyl or hydroperoxyl radicals play a major role in the degradation of membranes [73]. Cerium-ions or CeO_2 is applied to quench these radicals. A more detailed description on this matter will be given in the part considering the catalyst layer.

Catalyst Layer

Figure 10 shows the schematic of a PEMFC's cathode catalyst layer (CCL) and its interaction with the microporous layer (MPL) and the membrane [74].

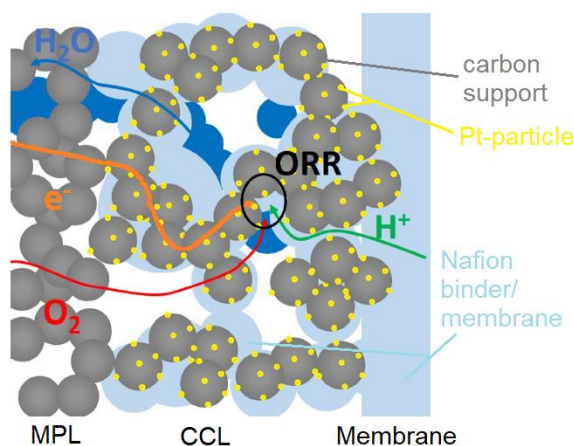


Figure 10: Composition of the cathode catalyst layer (CCL) showing binder, catalyst particles and catalyst support. Transport of reactants and products is illustrated by the interaction of the CCL with the membrane and the microporous layer (MPL) [74].

As it is apparent, the catalyst layer of a fuel cell comprises of several different materials. Those are the catalyst particles, the catalyst support and the binder, each fulfilling a specific task. The **catalytically**

active material is platinum (Pt) nanoparticles (NPs). The Pt-NPs catalyze the reduction of O_2 to water on the cathode side of the PEMFC and the oxidation of H_2 into protons and electrons on the anode. To this date, Pt (Pt-alloy will be discussed later) is the best choice for both the hydrogen oxidation reaction (HOR) and the oxygen reduction reaction (ORR). However, as illustrated in **Figure 11**, Pt is not an ideal catalyst for the ORR. In fact, the ORR on pure Pt shows sluggish reaction kinetics, resulting in severe over-potentials [75].

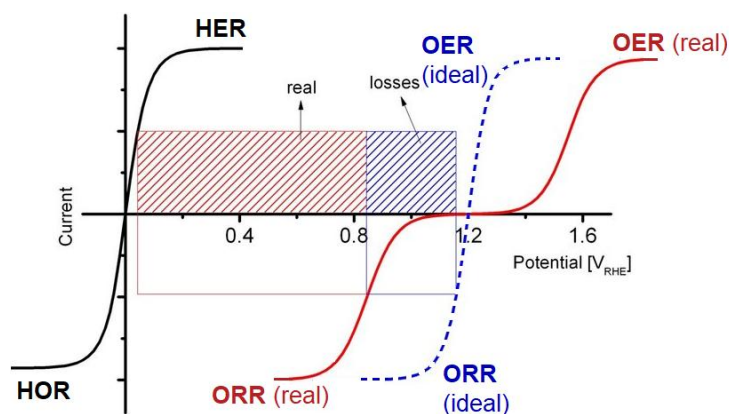


Figure 11: Illustration of the over-potentials for the redox reaction pairs HOR/HER and ORR/OER of Pt [75].

To compensate for this over-potential loss a much greater amount of the precious Pt is required for the ORR in the CCL than for the HOR at the anode. Thus, making the cathode catalyst the major cost driver for PEMFC systems. Since mainly the surface atoms contribute to the activity, the Pt is applied in the form of nanoparticles. The smaller the particles are, the higher is their surface area to volume ratio and the better is the utilization of the precious Pt. However, in situ XAS measurements showed that for Pt clusters with a size of 50 Å and lower, compounds like H, OH, or CO bind very strong [76]. H adsorption is as strong that structure and morphology changes in the particle are induced. Likewise, the ORR is inhibited by the strong adsorption of OH. Furthermore, the increase in curvature of smaller particles increases their surface energy. This leads to a change in thermodynamics of the dissolution of the particles (Gibbs-Thomson Effect), making them significantly less stable than bigger particles [77]. Hence, for real world fuel cell application, a compromise of Pt-NP size considering activity, stability and Pt utilization (costs) is needed, it is typically found in the range of 2-10 nm.

Today's cathode fuel cell catalyst particles usually comprise of a second less precious metal in addition to Pt. These simple bimetallic PtM (M = Fe, Co, Ni, Cu, ...) catalysts show Pt-mass-based activity enhancement of 1.5 - 2.5 compared to pure Pt catalysts [78-81]. Whereas so-called dealloyed bimetallic catalysts show improvements of factor 4 - 8 [82-84]. Dealloyed catalyst particles are obtained after a leaching step where the less precious component is leached out from the surface of the particle. Among others, cobalt has shown to be the most beneficial considering activity, stability and

poisoning behavior. After the leaching and a thermal annealing step of a bimetallic PtCo particle a catalyst possessing a platinum-rich surface and a PtCo alloy core is obtained. Hence, precious Pt from the core of the particle is substituted with cobalt leading to a better platinum utilization. Furthermore, it has been found that the ORR kinetics on dealloyed bimetallic catalysts benefit from a downshift of the Pt *d-band* center relative to the Fermi level [81, 85-87]. The *d-band* width can be described by strain, ligand and particle size effects [88, 89]. The interatomic distance of Pt atoms in Pt-rich shells of dealloyed catalysts was found to be smaller than in pure Pt, which revealed the presence of a compressive lattice strain [90]. The binding energies of smaller adsorbates like H, O, CO or OH is weakened [89]. Hence, the rate determining step of the ORR on Pt-surfaces, which is the removal of OH_{ads} is facilitated, making the catalyst more active.

To prevent particle agglomeration, the Pt NPs are dispersed on (or into the pores) of a **carbon support**. Typical carbon supports are Vulcan® XC 72R, Ketjenblack® EC-300J or Black Pearls® 2000. Furthermore, the presence of the carbon support strongly influences the transport characteristics of the catalyst layer. Carbon blacks have an intrinsically low packing density and high porosity with a void volume of about 60 % leading to facilitated gas-transport characteristics [91, 92]. In general, one can distinguish between two types of carbon supports; high surface area carbon (HSAC or HSC) and medium surface area carbon (MSAC or MSC) supports. HSAC supports possess a greater amount of micropores. This allows for a better Pt dispersion and an easier synthesis of Pt-alloy NPs catalyst like PtNi, PtCo or PtCu. As shown in **Figure 12 a)** the catalyst particles are embedded into the micropores of the HSAC support [93]. Whereas for MSAC the Pt particles are more likely deposited on the outside of the carbon support.

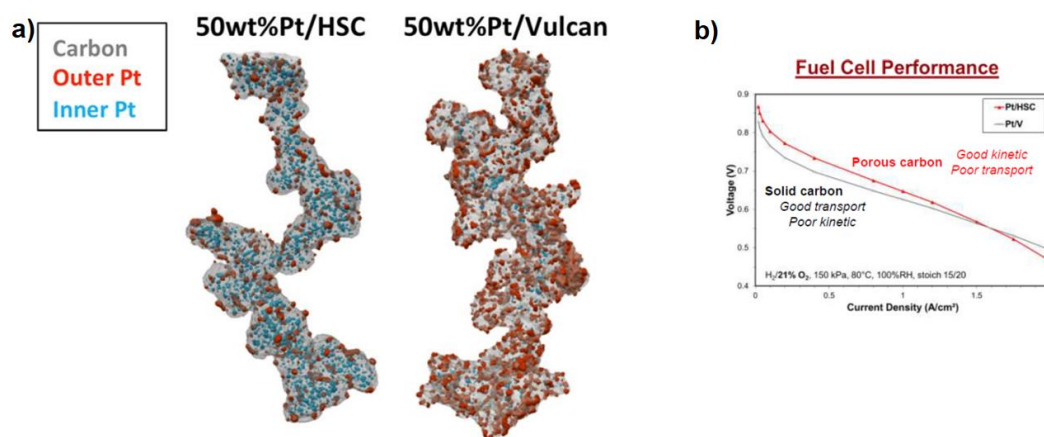


Figure 12: 3D Visualizations (segmented tomograms) of Pt particle deposited on or in different carbon supports (HSC vs Vulcan) [93] (a) and impact of the carbon support on the fuel cell performance [94] (b).

As illustrated in **Figure 12 b)** this strongly affects both, the transport and the kinetic activity of the catalyst [94]. MSAC supported catalysts show particularly good mass transport characteristics due to

enhanced oxygen and proton accessibility of the Pt particles. Whereas HSAC supported catalysts show 3 - 4 times increased performances in the kinetic region. This might be explained by the fact that the particles embedded in carbon pores are better shielded from ionomer adsorption. In case of carbon corrosion, which mainly occurs during high voltage events like fuel starvation and start-ups or shut-downs, the MSAC support shows a better resistance due to a higher degree of graphitization. Contrarily, for the case of Pt dissolution, the HSAC based catalysts show a better stability. This is caused by a so-called non-intrinsic effect, which is an effect not caused by the properties of the Pt itself. Local oversaturation of Pt^{x+} ions inside the nanopores leads to re-deposition of Pt (confinement effect) [95]. Recently developed carbon supports by-pass the issue of low-mass transport properties of HSAC supports by introducing precisely engineered pore sizes and depths, see **Figure 13** [96].

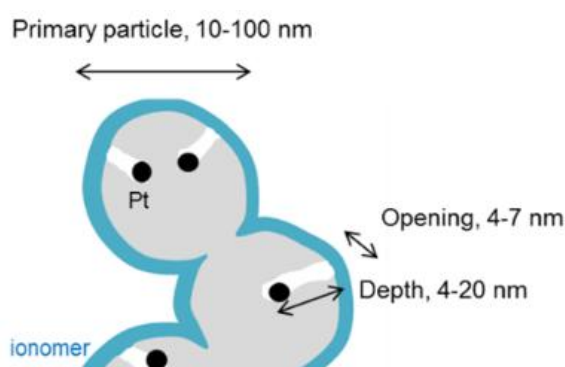


Figure 13: Controlled pore size and depth allows for good O_2 and H^+ mass transport properties, whereas at the same time the catalytically active Pt-surface is protected from ionomer adsorption [96].

The catalyst layers of a fuel cell further comprise of the so-called **binder polymer**. The binder is usually made from the same ionomer as the membrane electrolyte i.e., NafionTM, Aquivion[®], Fumion[®], etc. The tasks of the binder are to facilitate the proton transport inside the catalyst layer, give mechanical stability and to enhance the water transport. The same parameters as for the membrane also apply for the binder. These are the equivalent weight and the side chain length of the polymer. Further, the overall weight content of the binder inside the catalyst layer, which is either given in weight percentage or as the ratio between binder and carbon support. Typically, values between 30 to 40 wt% of binder are applied inside the catalyst layers. A precise adjustment of the mentioned parameters of the binder is crucial to achieve a good fuel cell performance. For instance, catalyst layers with high binder contents show good proton conductivities, whereas at the same time mass transport resistance is increasing with higher binder content. This behavior is illustrated in **Figure 14** [97].

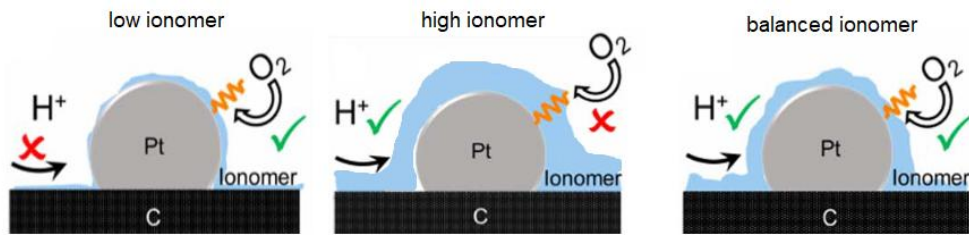


Figure 14: Influence of the ionomer content inside the catalyst layer; low ionomer contents show low mass transport resistances and low proton conductivities, high ionomer contents show high mass transport resistances and high proton conductivities, a balanced ionomer content is needed to fit both needs [97].

Likewise, the length of the side chain influences the mass transport behavior, especially in combination with HSAC supported catalysts. Long side chains tend to reach far into the micropores of the catalyst support blocking the channels to the catalyst particles for the oxygen molecules. Several strategies have been applied to enhance the mass transport characteristics of the catalyst layer. For instance, stiffening of the ionomer backbone through chemical modification with aryl-groups increased the oxygen permeability, this is illustrated in **Figure 15** [22].

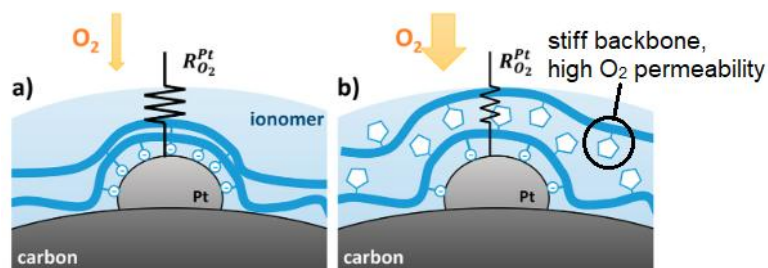


Figure 15: Catalyst particles covered with conventional ionomer (a) and a backbone modified ionomer possessing a higher O_2 permeability (b) [22].

Furthermore, ionomer distribution plays an important role for the fuel cell performance [97, 98]. As shown in **Figure 16** nitrogen functionalization of the carbon support strongly improves the distribution of the ionomer [97].

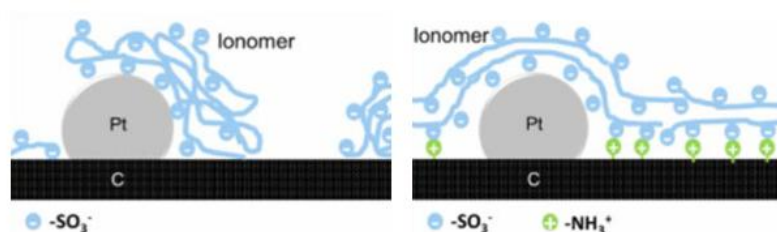


Figure 16: The Coulomb interactions between ionomer and nitrogen functional groups of the support lead to uniformly dispersed ionomer inside the catalyst layer [97].

Additional components that are required in the catalyst layer, especially for long-time durability of the fuel cell are for instance radical scavengers or oxygen evolution catalysts (OER). Radical scavengers are mainly applied in the form of CeO_2 particles to prevent the degradation of the PFSA ionomer (binder and membrane)[73, 99, 100]. Radical oxygen species (ROS) namely hydroxyl and hydroperoxyl radicals are the main driving force of chemical degradation of the MEA. **Figure 17** shows the mechanism of CeO_2 reacting with these radicals [101]. Thereby, cerium strongly benefits from its ability of facilely switching the oxidation states +3 and +4 back and forth.

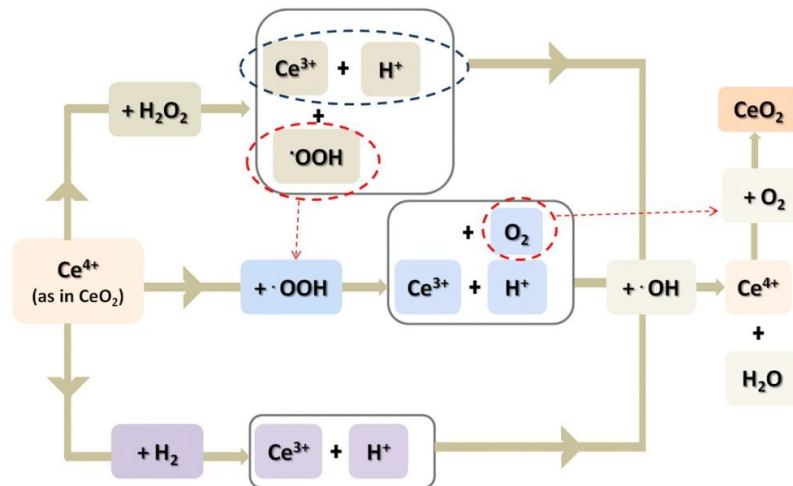


Figure 17: Reaction pathways of Ce(IV)O_2 quenching radical oxygen species [101].

OER catalyst like IrO_2 might be applied for both the anode and the cathode catalyst layer. In both cases the OER catalyst protects the carbon support from undergoing carbon oxidation reaction (COR). COR occurs during high voltage events. In such event, the OER catalyst protects the carbon support by favoring the OER over the COR. For the anode the high voltage events are caused by fuel-starvation [102]. At the cathode start-up and shut-down leads to high potentials [103].

3.2 Current Cost Status and Goals for the Automotive Fuel Cell Industry

In the course of this chapter a brief statement on some of the most important (recent) developments and the current status of PEMFC systems will be made. The view will be focused on criteria considering costs, performance and durability for the application of the PEMFC as propulsion technique for vehicles. Future goals and targets will be discussed with respect to (cathode) catalyst development.

PEMFC System Cost Development

The overall cost of a PEMFC system compose of the cost for the fuel cell stack and the cost for the balance of the plant (BOP) [104]. Inside the fuel cell stack the electrochemical reaction happens. The BOP is needed to ensure that the stack runs properly. It should be mentioned that in general fuel cell system cost reduction can be achieved by several different strategies. For instance, by simplification of individual parts or by complete elimination of parts. Still, in the recent years increasing the power density of the stack lead to the largest reduction in cost. This is because an increased power density allows for a smaller stack size. Therefore, the cost of all stack components (membrane, GDL, flow-field, etc.) decrease proportionally.

Figure 18 shows the significant progress that has been made since 2006 in reducing the overall fuel cell system cost [19]. The numbers are extrapolated assuming either an annual production rate of 100,000 systems or 500,000 systems per year. The latter is based on the assumption of a successful implementation of PEMFC systems in passenger cars. A reduction of 67 % from 140 \$ KW_{net}^{-1} in 2006 to 45 \$ KW_{net}^{-1} in 2018 has been achieved. Still, the target costs of 30 \$ KW_{net}^{-1} set by the U.S. Department of Energy (U.S. DOE) remains a big challenge [19].

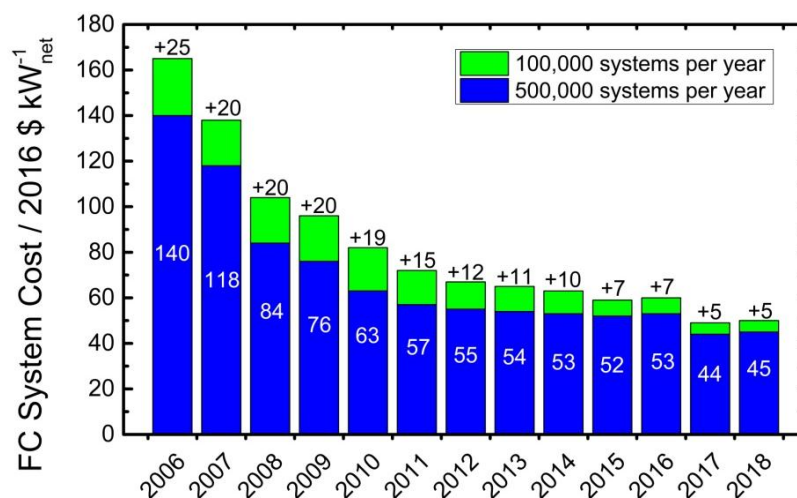


Figure 18: Development of the cost for a 80 kW_{net} PEMFC system since 2006 [19].

Important steps that lead to this significant reduction in cost have been realized for instance by Toyota Motor Corporation for their passenger car Toyota Mirai [105]. Cost reduction was achieved by a new 3-D flow field design which allows for better water removal and lower gas transport resistance. Furthermore, previously used gold coated stainless steel separators were replaced with carbon coated titanium ones. Most decisively, the ORR activity increased by factor 1.8 in comparison to previous systems (prototype model of 2008). By implementation of a PtCo catalyst supported on not hollow carbon but on solid core type support, the Pt utilization was increased significantly. **Table 3** gives an overview of estimated key data considering the fuel cell stack of the Toyota Mirai [106].

Table 3: Key data of the PEMFC stack of the Toyota Mirai Model [106].

Stack Power Net/Gross	91 kW/114 kW
Cell Voltage	0.67 V
Cells per Stack	370
Power Density	1,295 mW cm ⁻²
Stack Pressure (estimated)	2.5 atm
Total Pt loading	0.3 mg cm ⁻² or ~35 g _{Pt} per vehicle

Figure 19 shows the fuel cell performance of a Pt-alloy catalyst in comparison to Pt/C [94]. Higher performance is reached for PtCo in comparison to Pt, even at a lower total Pt-loading. Still, the Toyota Mirai has an estimated fuel cell system cost of 233 \$ kW_{net}⁻¹ at a production rate of 1,000 systems per year [106]. As listed in **Table 3**, these high costs are mainly due to the great amount of Pt which is needed, 35 g_{Pt} per vehicle.

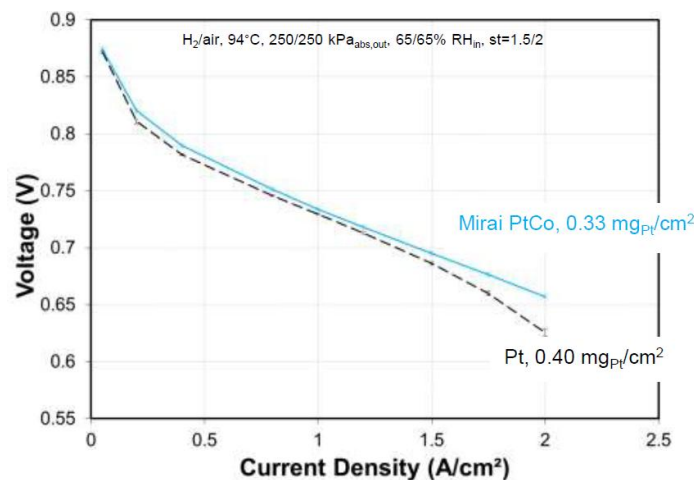


Figure 19: FC performance difference of a PtCo catalyst and a Pt catalyst. Even with lower total Pt loading the PtCo catalyst shows higher current densities [94].

Current Status and Ultimate Goals

Following this very brief summary of some of the important development in cost reduction made during the recent years, **Table 4** summarizes the current status and ultimate targets of cost and durability for PEMFC systems published by the U.S. DOE [19, 20].

Table 4: Current status and ultimate technology targets considering cost and durability of PEMFC systems for the application in LDVs and MDVs [19, 20].

Category	Light Duty Vehicle (LDV)	Medium Duty Vehicle (MDV)
System Size / kW_{net}	80	160
Cost Status / $\$ \text{KW}_{\text{net}}^{-1}$	46.16	92
Cost Target / $\$ \text{KW}_{\text{net}}^{-1}$	30	60
Durability Status / hours	5,000 - 8,000	-
Durability Target / hours	8,000	30,000
Contribution of Catalysts to Costs / %	43	53

Depending on the type of application, the numbers are given for light duty vehicles (LDVs) and medium duty vehicles (MDVs). LDVs include vehicles with a power up to 80 kW, which is typically needed for passenger cars. A power of 160 kW is needed for MDVs such as vans, buses and smaller trucks. Whereas for LDVs the durability goals of 5,000 to 8,000 hours of operation can widely be met with today's technology, it is difficult to identify clear numbers for the MDV case. This work focusses on LDVs. The durability target for MDVs however is significantly higher, up to 30,000 hours of operation are needed. Still, for both LDVs and MDVs the cost of the PEMFC system need to decrease to about two third of the currently reported numbers. Hence, a major challenge that keeps PEMFC developers occupied is the reduction of stack costs. As further listed in **Table 4**, the main single contributor to the costs of a PEMFC are the catalysts.

Table 5 gives an overview of important parameters of the state-of-the-art LDV PEMFC system published by the U.S. DOE in 2018 [20]. The Pt-demand is currently reduced to ~ 10 g per vehicle.

Table 5: Key data of the state-of-the-art PEMFC stack published by U.S. DOE in 2018 [20].

Stack Power Net/Gross	80 kW/87.1 kW
Cell Voltage	0.663 V
Cells per Stack	377
Power Density	1,165 mW cm ⁻²
Stack Pressure (estimated)	2.5 atm
Total Pt loading	0.125 mg cm ⁻² or ~10 g _{Pt} per vehicle
System Cost (500,000 systems per year)	46.16 \$ kW _{net} ⁻¹
Membrane	14 μm Nafion, 850 EW on ePTFE

Point of Weakness: The Cathode Catalyst Layer

As mentioned before, there are several strategies to decrease the fuel cell stack costs, but power density is the most favorable one. This is because the cost of all stack components decreases proportionally as power density increases. The question arises, what are the reasons for low fuel cell power densities? **Figure 20 a)** shows the voltage losses occurring for U.S. DOE's 2018 state-of-the-art membrane electrode assembly operating at 2 A cm⁻² and 3 A cm⁻² [21]. As it is apparent, ORR kinetics are the biggest contributor to voltage loss followed by the Ohmic resistance losses (proton transport resistance and electronic resistance) and the local O₂-transport losses [104]. Both ORR kinetics and local O₂-transport are associated with the cathode of the fuel cell, meaning the cathode catalyst itself and the cathode catalyst layer.

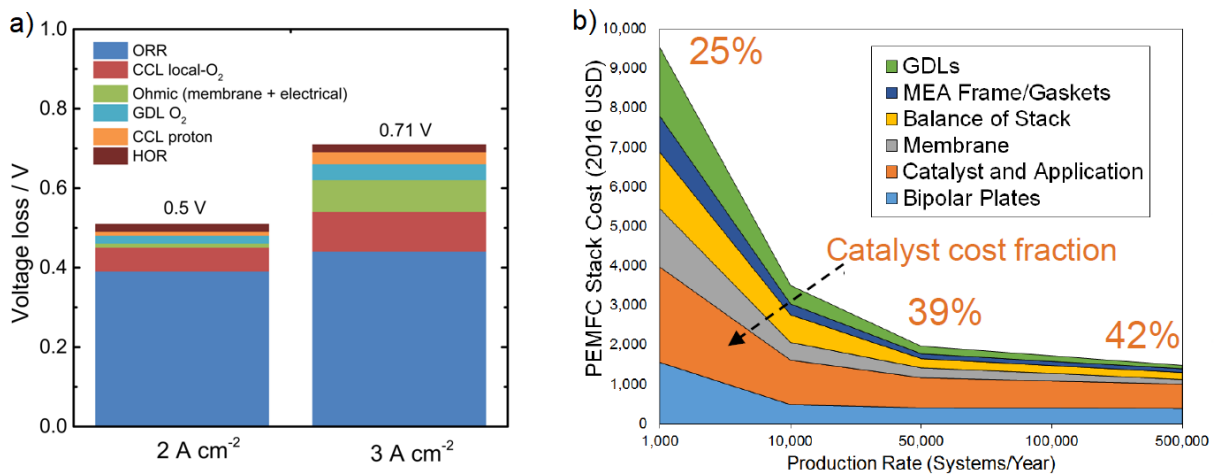


Figure 20: Voltage loss of U.S. DOE's 2018 PEMFC system operating at 2 A cm⁻² or 3 A cm⁻² (a) and state-of-the-art PEMFC stack costs in relation to the yearly production rate (b) [19, 21].

Not only is the cathode catalyst responsible for the most severe voltage losses, leading to high costs due to low power densities on a "passive" way, but it also contributes significantly on an active/direct way to the fuel cell costs. **Figure 20 b)** shows the cost of the U.S. DOE's 2018 PEMFC stack broken down by the individual components with respect to the annual production rate [19]. As it appears, the main position of PEMFC stack cost comes from the catalysts, contributing with over 40 % at a production rate of 500,000 systems per year. The notation "catalyst and application" from **Figure 20 b)** refers to both cathode and anode catalyst, still the cathode catalyst is the decisive factor ($0.1 \text{ mg}_{\text{Pt}} \text{ cm}^{-2}$ for cathode versus $0.025 \text{ mg}_{\text{Pt}} \text{ cm}^{-2}$ for anode). Whereas other components become significantly cheaper at high production rates the relative cost contribution of the catalysts to the stack costs increases with increasing production rate. This is because of the production rate-independent high material costs of Pt.

To have a closer look at the costs of the cathode catalyst, **Table 6** lists the costs of the individual production steps of the state-of-the-art (U.S. DOE 2018) d-PtCo/HSC-f cathode catalyst with respect to the annual production rate [20]. The precursor materials, mainly Pt, contribute significantly to the cost. At a high production rate of 500,000 systems per year the cost of the cathode catalyst for one 80 kW_{net} PEMFC system (one LDV) are 481.55 \$. Whereas 466.64 \$ or 97 % come from the precursor materials alone, mainly Pt.

Table 6: Precursor and individual synthesis steps cost of the U.S. DOE's 2018 state-of-the-art cathode catalyst, d-PtCo/HSC-f with respect to the annual production rate of a 80 kW_{net} system [20].

Step # \$/system	1,000 sys/year	10,000 sys/year	50,000 sys/year	100,000 sys/year	500,000 sys/year
#1 Pt/HSC Precursor	\$722.75	\$647.74	507.92	487.54	466.64
#2 Pt/HSC Filtration	\$15.7	\$6.29	\$1.38	\$0.78	\$0.31
#3 Pt/HSC Wash	\$6.03	\$2.76	\$0.65	\$0.47	\$0.32
#4 Catalyst PtCo/HSC Precursor	\$14.99	\$8.58	\$3.49	\$2.45	\$1.20
#5 Precursor Filtration	\$18.35	\$9.18	\$2.08	\$1.06	\$0.21
#6 Precursor Wash	\$6.87	\$2.51	\$0.49	\$0.27	\$0.08
#7 Precursor Drying	\$47.39	\$17.02	\$3.24	\$1.71	\$0.42
#8 Precursor Crushing	\$24.83	\$8.88	\$1.90	\$0.98	\$0.21
#9 Precursor Annealing	\$131.08	\$47.50	\$9.38	\$5.18	\$3.73
#10 Catalyst Dealloying	\$62.82	\$34.99	\$8.63	\$4.94	\$1.74

#11 Catalyst Filtration	\$17.90	\$8.76	\$1.97	\$1.00	\$0.20
#12 Catalyst Wash	\$6.87	\$2.51	\$0.49	\$0.27	\$0.08
#13 Catalyst Dry	\$47.99	\$17.91	\$3.71	\$2.19	\$1.32
#14 Catalyst Crushing	\$25.04	\$9.42	\$2.23	\$1.30	\$0.28
#15 Quality Control	\$6.67	\$9.49	\$5.42	\$5.32	\$4.59
#16 Packaging	\$11.22	\$4.14	\$1.00	\$0.59	\$0.23
Sum \$/system	\$1,116.52	\$837.68	\$553.98	\$516.05	\$481.55

In addition to the high costs of Pt, its availability on the world market is critical. **Figure 21** gives the mining production of Pt per country [23]. Approximately, 72 % of the worldwide mined Pt in 2019 came from South Africa. Furthermore, over 92 % of Pt-supply came from the top three mining countries South Africa, Russia and Zimbabwe. Hence, Pt-based catalysts make the fuel cell industry in the US or Europe highly depended on a small number of countries of origin.

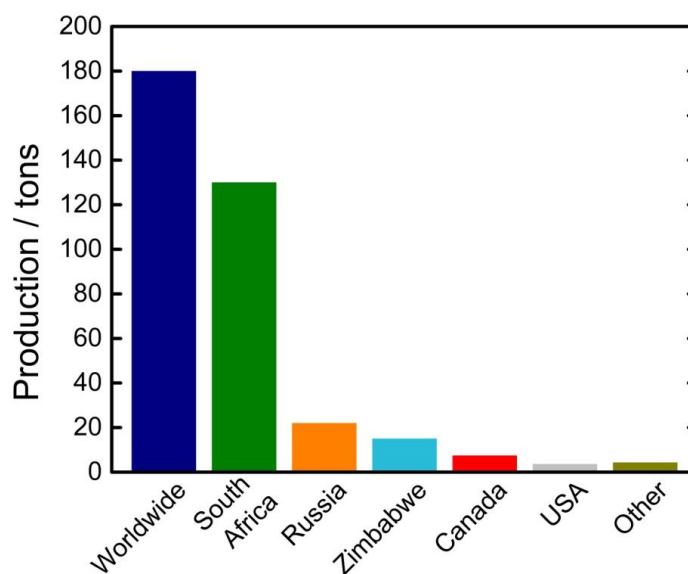


Figure 21: Mined platinum in tons by the year 2019 with respect to country and worldwide [23].

This dependency comes along with potential of geopolitical risks. The possible outcome of geopolitical tension and such one-sided relations considering raw materials can be seen for palladium. After the geopolitical tension related to the Ukraine conflict, Russia the world leading palladium miner adjusted its production rates to account for other economic sanctions [107-109]. In combination with other factors, the price for one fine ounce of palladium rose from 797 \$ in 2014 to 1909 \$ in 2019 [110].

Both, Pt and Co are listed on the so-called list of critical raw materials released by the EU in 2014 and updated in 2017 [111]. It is also an explicit goal of the more recent European Green Deal to reach an economy "[...] where economic growth is decoupled from resource use." [13].

A study conducted by the Roland Berger GmbH in 2013 pointed out another problem related to Pt-use in fuel cells [112]. Two possible scenarios were considered, the outcome is illustrated in **Figure 22**. In Bernhart et al. it is stated:

"**Scenario A** reflects [...]: global production of 300,000 fuel cell vehicles from 2020 onward with a platinum load of about 16 g/vehicle ($0.15 \text{ mg}_{\text{Pt}} \text{ cm}^{-2}$, 300 cm^2 per MEA and 350 MEAs per stack). Assuming that the annual global production of light vehicles exceeds 100 million units by 2020, this scenario allocates less than 0.3% of the market to fuel cell vehicles, a rather conservative estimate. However, even in this scenario, the demand for platinum would increase by 2% compared to 2012 levels [...]. **Scenario B** assumes that fuel cell vehicles will become a fully cost-competitive alternative and therefore forecasts global annual production of 5 million fuel cells [...] accounting for about 5% of the global market. What's more, each vehicle will require only 10 g of platinum per vehicle instead of 16 g as in Scenario A. As a result, platinum demand would rise 21% from 2012 levels. Considering the current state of the platinum industry, it seems unlikely that this demand will be met at today's price levels." [112]

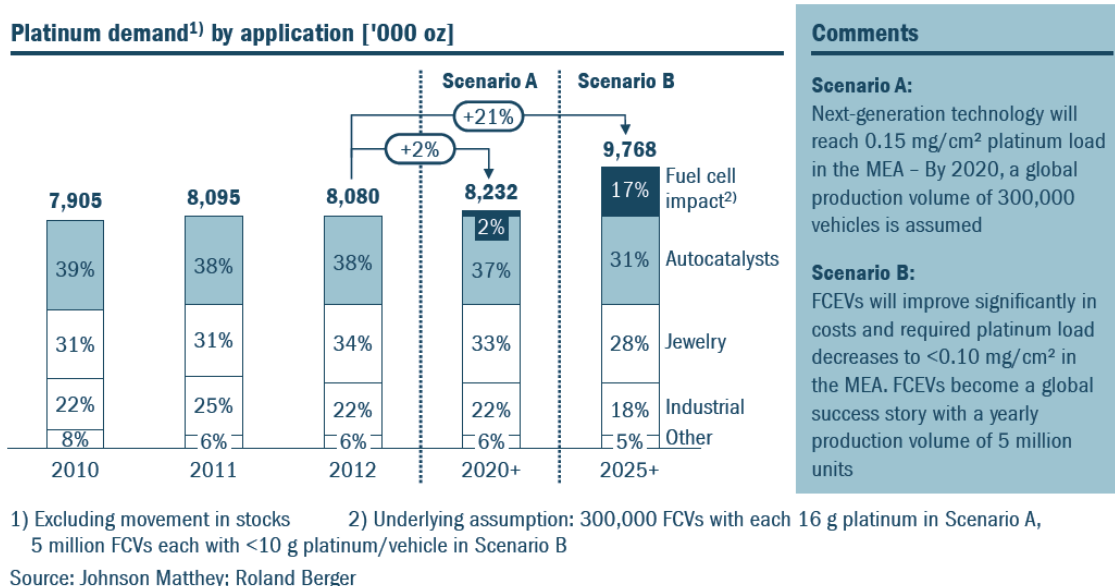


Figure 22: Impact of fuel cell vehicles on platinum demand, study performed 2013 by Roland Berger [112].

The Pt loading of $\sim 10 \text{ g}$ per vehicle can already be achieved with today's (2020) technology. Still, the work from Bernhart et al. clearly shows that in order to become a worldwide success in the automotive industry, fuel cells need to perform with even less precious metal. A more recent study from 2016 by

Kongkanand and Mathias (General Motors) concluded that "*Considering both the cost to consumer and the supply–demand relation in the precious metal market, a stretch target of $0.0625 \text{ g}_{\text{PGM}} \text{ kW}_{\text{gross}}^{-1}$ ($\sim 6 \text{ g}_{\text{PGM}} \text{ per vehicle}$) appears appropriate.*"[22].

To briefly **summarize** this chapter: Fuel cell technique made significant improvements over the last decades. Pt demand of PEMFC systems design for the application in LDVs ($80 \text{ kW}_{\text{net}}$) declined to $\sim 10 \text{ g}$ per vehicle. Costs have been reduced to $46.16 \text{ \$ kW}_{\text{net}}^{-1}$. Despite these promising outcome major challenges remain. In order to become a worldwide success, Pt demands of $\sim 6 \text{ g}$ per vehicle and cost of $30 \text{ \$ kW}_{\text{net}}^{-1}$ have to be reached. The cathode catalyst of PEMFC remains the point of weakness and there are five major reasons why:

- (1) Major voltage losses occur because of sluggish ORR kinetics and local O_2 -transport resistance, this leads to low power densities and drives proportionally the cost of all stack components.
- (2) Cathode catalysts rely on Pt which accounts for 43 % of the stack costs at a production rate of 500,000 systems per year.
- (3) A scale-up of the production rate would minimize the costs of all stack components except those of the precious raw material Pt.
- (4) Pt is a critical raw-material, 92 % of the yearly output is mined in just three countries.
- (5) If implemented worldwide on a million-production rate scale, current Pt demand ($\sim 10 \text{ g}$ per vehicle) will put pressure on the world market and lift the price of the rare metal further.

4 Non-Precious Metal-Based ORR Catalysts

In the previous chapter, five challenges related to the current state-of-the-art Pt-based cathode catalysts have been presented. There are two technical approaches to cope with the dependence on Pt:

(1) Lowering the Pt-demand by **increasing the activity or Pt-utilization** with respect to the currently best performing catalyst (d-PtCo-HSAC-f, see Table 5).

(2) **Complete elimination of the precious metals** (cathode-side) by implementing catalyst that rely on non-precious metals.

Solutions dealing with approach (1) include, shape-controlled nanoparticles, nano-structured thin films or highly ordered dealloyed Pt-based catalysts including vapour deposited catalysts and Pt monolayer catalysts [96, 113-118]. Solutions for approach (2) consider nitrogen doped carbon materials in conjunction with transition metals (mainly Fe and Co) or metal oxides of the 4th and 5th main group of the periodic table (e.g. zirconium, tantalum, titanium or niobium) [25, 119-124]. Promising results have also been achieved by combination of non-precious metal-based catalysts and low amounts of Pt [125-127]. Still, all these strategies come with certain downsides. Mostly, they fail at long-term stability or scale-up possibilities. It is beyond the scope of this work to discuss pros and cons of all the mentioned strategies in detail.

This thesis deals with the synthesis of a precious metal free catalyst. It is based on a transition metal and nitrogen doped carbon. These materials have an enormous potential considering the reduction of stack costs and avoid the problems related to the critical raw-material Pt. In general, this class of catalysts comprise of a highly porous carbonized framework which is doped with one or several heteroatoms (N, S, O) and one or several transition metals (Fe, Co, Ni, Mn, V, Cr, Cu) [128-136]. While the combination of N and Fe or Co showed the best results so far [25, 128, 134, 137-141]. These catalysts are referred to as non-precious metal catalysts (NPMC) or depending on the metal heteroatom combination as iron-nitrogen-carbon (Fe-N-C), cobalt-nitrogen-carbon (Co-N-C), iron-cobalt-nitrogen-carbon (FeCo-N-C) or generally as metal-nitrogen-carbon (Me-N-C) catalysts. With respect to the structure of the active site the notation FeN₄-catalyst or FeN_xC_y catalyst is also common.

4.1 Non-Precious Metal Based Catalysts: Enormous Potential of Cost Reduction

In principle, Me-N-C catalysts have the ability to replace Pt, with a cheap and earth-abundant transition metal such as Fe. This chapter shows the potential of this precious metal free technology considering fuel cell stack costs, independently from the remaining technological challenges. In particular, significant progress related to NPMC has been achieved by researchers from the Los Alamos

National Laboratory (LANL). Here a polyaniline based synthesis approach has been developed [122, 140]. For this catalyst design for manufacturing and assembly (DFMA) cost analysis by Strategic Analysis Inc. was performed [142]. This cost analysis provides a first insight. Since no details of the analysis were published, the following numbers should be considered as a rough guidance rather than a confirmed benchmark.

Table 7 gives the cathode catalyst costs for an 80 kW_{net} fuel cell system at different annual production rates. The state-of-the-art Pt-based catalyst, d-PtCo-HSAC-f is compared to the Fe-N-C catalyst from the LANL, PANI-C-Fe. The costs for the Fe-N-C catalyst are significantly lower than those of the Pt-based catalyst. At a production rate of 500,000 systems per year d-PtCo-HSAC-f is almost 15 times more expensive than PANI-C-Fe.

Table 7: Cathode catalyst costs per 80 kW_{net} system in dependence of the production rate for U.S. DOE's 2018 Pt-based catalyst d-PtCo-HSAC-f and NPM based catalyst from Pajarito Powders PANI-C-Fe [20, 142].

Production rate	1,000 sys/year	10,000 sys/year	100,000 sys/year	500,000 sys/year
d-PtCo-HSAC-f	\$1,116.52	\$837.68	\$516.05	\$481.55
PANI-C-Fe	\$57.4	\$39.8	\$34.3	\$32.4

However, the sole comparison of the catalyst costs gives an incomplete picture. The complete costs always need to consider the cost of the fuel cell stack. As mentioned in chapter 3.2, power density plays a crucial role for the fuel cell stack costs because it correlates with the size of the stack. Fe-N-C catalysts already achieve power densities similar to Pt/C under H₂/O₂ [25, 143]. However, their low volumetric activity requires for high catalyst loadings, leading to severe mass transport losses under H₂/air. Hence, the power densities of Me-N-C catalysts are still lower than that of Pt/C and even lower than that of bimetallic PtCo/C catalysts under H₂/air conditions. Considering today's Me-N-C catalyst performances, two fuel cell stacks would be required to reach a performance of 80 kW_{net}. For the Pt-based materials one stack is sufficient, due to the higher power densities.

Figure 23 shows the effect of the MEA power density of the PANI-C-Fe catalyst based MEA on the stack costs [142].

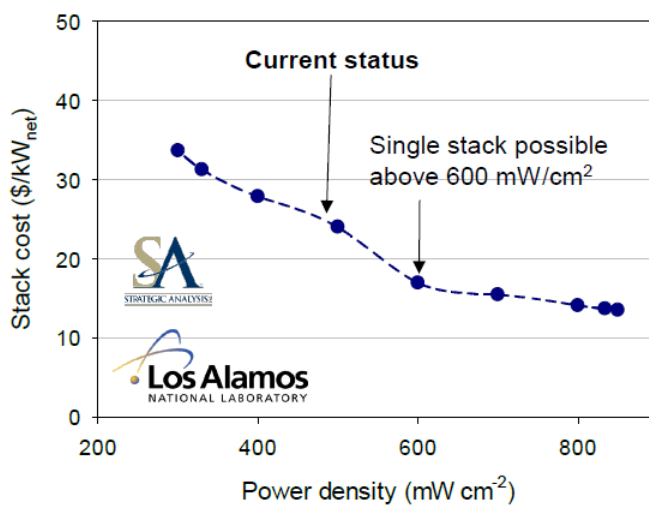


Figure 23: Effect of MEA power density of the PANI-C-Fe catalyst based MEA (LANL) on the fuel cell stack costs [142].

Apparently, for 600 mW cm⁻² a significant drop in stack costs appears. From this power density onwards, only one stack is required to reach 80 kW_{net}. The DFMA cost analysis concludes that the PANI-C-Fe catalyst shows major catalyst cost and per-stack cost advantages over Pt-based catalysts. Still, the power densities of NPMC needs to improve "in order for catalyst costs to make a significant impact on the stack costs [142]".

The perspective on this remaining challenge for Me-N-C catalyst is however quite promising. Precise balancing of parameters has shown to enhance power densities of Me-N-C based MEAs significantly. Those parameters consider the catalyst layer and MEA fabrication, for instance CCL hydrophobicity or thickness, contact pressure, ionomer EW, ionomer type or ionomer content [144, 145]. A power density of 570 mW cm⁻² under H₂/air was achieved by Banham et al. after optimization of the ionomer content in the CCL [145].

4.2 Instability of Me-N-C Catalysts

The major drawback of Me-N-C catalysts is their instability under fuel cell conditions. Within the first 100 hours of potentiostatic fuel cell operation the current density of Me-N-C based MEAs usually declines by 40 - 80 % [25, 146]. Whereas mostly a two-phase degradation process is observed. Within in the first phase (0 - 24 h) a sharp performance loss of up to 50 % of the initial value occurs. The second phase is characterized by a slower sometimes linear decrease in performance. To this day, the underlying mechanism of this performance decay of Me-N-C catalysts is not fully understood. Four main degradation mechanism have been proposed [147-151]. Those are:

-
- (1) the flooding of micropores with water
 - (2) active-site protonation and anion adsorption
 - (3) demetallation of active-sites and spectator phases
 - (4) carbon oxidation induced by water or $\text{H}_2\text{O}_2/\text{ROS}$.

Whereas the main issue of Me-N-C degradation is still being debated, it is likely that a combination of the mentioned degradation paths applies.

In 2016 Zhang et al. suggested that **micropore flooding** might be responsible for the initial current decay of Me-N-C catalysts [147]. It was stated that oxidation of the carbon support leads to an increased hydrophilicity and that consequently water is blocking the micropores of the catalyst where the most active sites are hosted. Contrary, in-situ fuel cell measurements monitoring the change in double layer capacity following cyclic voltammetry conducted by Choi et al. revealed that most of the catalyst is already wetted at beginning of life (B.o.L.) [148]. Further, the performance behavior observed by Choi et al. showed that primarily the kinetic region and not the mass transport region of the polarization curve is affected. Hence, micropore flooding seems not to be the major reason for the performance decay of Me-N-C catalysts.

Protonation of the nitrogen atom of the Me-N_4 **active site** was proposed by Liu et al. [152]. Comparing the stability of two catalysts, one containing pyridinic-N and graphitic-N the other containing graphitic-N only lead to this hypothesis. The higher stability of the graphitic-N catalyst was explained because it cannot be protonated, whereas pyridinic-N can be protonated due to its electron lone pair. Banham et al. argued that this hypothesis is false because of the different activities of the catalysts during acidic RDE testing [150]. Herranz et al. proposed that following the **N-protonation** of a neighboring N-atom of the MeN_4 site **anion adsorption** lowers the TOF of the active-center [151]. This deactivation process is still under debate [146, 147].

Demetallation or leaching of metal from Me-N-C catalysts has been under investigations since decades [150, 153]. Especially because of the thermodynamic instability of the respective transition metals. **Figure 24** shows the Pourbaix diagram of iron [154].

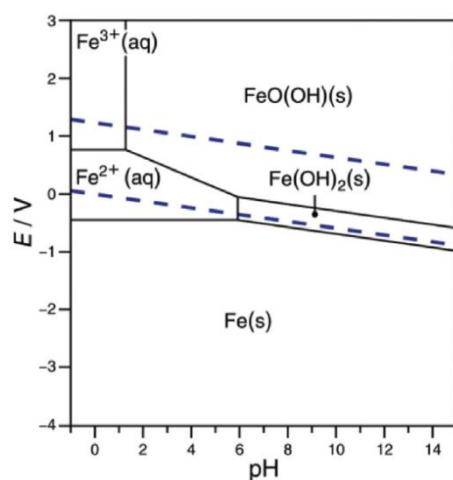


Figure 24: Pourbaix diagram of iron, showing the thermodynamic instability of iron under PEMFC conditions [154].

Baranton et al. investigated non-pyrolyzed iron phthalocyanine (FePc) via in-situ infrared reflectance spectroscopy and found that the iron inside the macrocycle is substituted by two protons, giving H_2Pc a significantly less ORR active complex [155]. The substitution occurred under O_2 but not under Ar. It was concluded that the oxidation of Fe^{2+} to Fe^{3+} in the presence of O_2 leads to a smaller ion radius, making it less stable inside the macrocycle [155, 156]. For the case of pyrolyzed Me-N-C catalysts, Choi et al. applied inductively coupled plasma mass spectrometry (ICP-MS) and differential mass spectrometry (DEMS). It was found that iron side phases (formed as by-product during the pyrolysis process, not active for ORR) such as iron carbides or iron nanoparticles are prone to dissolution whereas MeN_4 moieties seemed stable (Ar, 0 - 1.0 V vs RHE, 0.1 M $HClO_4$) [33, 157]. Recently, Chenitz et al. proposed that the initial sharp current decay of Me-N-C catalysts is due to the fast mass (water, protons and O_2) flux through the micropores where most of the MeN_4 active sites are hosted [158]. The fast water flux in the pores flushes out the iron ions according to the Le Chatelier principle. The stable thermodynamic equilibrium of MeN_4/M^{2+} is therefore not valid in micropores.

Independent from the mechanism, the destructive impact of leaching Me^{X+} cations from the MeN_4 active site is immense. The performance suffers two-fold. First, active sites are being destroyed and second, the leached Me^{X+} cations cause further damage to the MEA. Li et al. showed that operating a fuel cell with an air stream containing 5 ppm Fe^{3+} leads to complete fuel cell failure due to membrane pinhole formation after 191 h [159]. **Figure 25** shows the impact of soaking a fuel cell membrane with ppm amounts of Fe^{2+} cations on the measured polarization curve [160].

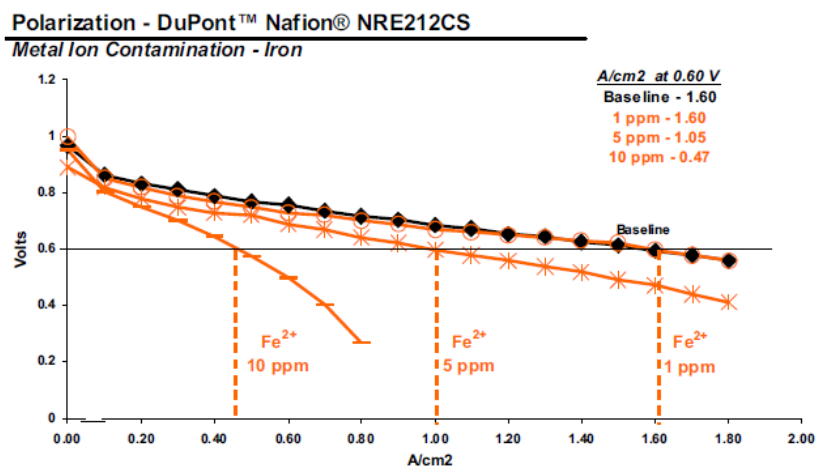


Figure 25: The impact of soaking a Nafion™ membrane in Fe²⁺ containing solution: Severe performance loss in the polarization curve [160].

Me^{X+} cations bind much stronger to the sulfonate-group of the ionomer than protons leading to irreversible loss in proton conductivity. Further, Fe²⁺ ions damage the MEA through reacting with H₂O₂ via Fenton reaction. This will be described in the following section considering carbon oxidation.

The standard thermodynamic potential of **carbon oxidation** by water is 207 mV (vs. RHE). However, carbon oxidation is usually detected at severe over-potentials of several hundred mV. Even though Me-N-C catalysts often show disordered carbon phases which in general are oxidized at lower potentials, Choi et al. detected no CO₂ formation during DEMS experiments for their Me-N-C catalyst at potentials lower than 900 mV (Ar, 0.1 M HClO₄) [157]. Furthermore, the sharp current decay within the first hours of operation occurs mostly potential independent and thus cannot be explained by simple water induced carbon oxidation alone [158]. However, the oxidation of the carbon surface most likely occurs at lower potentials, introducing oxygen containing surface groups like -COOH [27, 161]. According to Choi et al. those surface groups lower the TOF of nearer active sites by withdrawing electron density from the Me center [162]. Today's most widely accepted degradation mechanism of Me-N-C catalysts is related to the ORR by-product, H₂O₂ respectively the radical oxygen species (ROS) formed during the decomposition of H₂O₂ [104, 146, 150, 162, 163]. Those radical species are formed as a product of the so-called Fenton reaction between H₂O₂ and leached Fe²⁺ ions. The formed hydroxyl radical is highly oxidative and can react with several components of the MEA. Carbon corrosion, active site destruction and Nafion™ degradation are the severe processes leading to the performance loss of the MEA. The ROS induced degradation mechanism is also in line with the pH dependence of Me-N-C catalyst degradation [162]. Further, Banham et al. explained the positive correlation of catalyst loading and stability by the ROS induced degradation mechanism [145]. Despite the previously mentioned results by Choi et al., carbon corrosion for another Me-N-C catalyst was detected for potentials as low as 300 mV [164]. At these potentials carbon corrosion induced by water is very unlikely to occur whereas the formation of H₂O₂ and thus ROS induced degradation is possible.

The stability of Me-N-C catalysts is also strongly influenced by its synthesis method. For instance, the C, N-precursors, the pyrolysis parameters (temperature, time, reactive gas or inert gas) or the type of transition metal have a great impact on the stability. Metal organic framework (MOF) derived catalysts or NH_3 treated catalysts show excellent activities, while they have shown to be very unstable [25]. Contrary, PANI based approaches showed stability of up to several hundred hours when operating at lower potentials [140, 165]. The chosen C, N-precursors have shown to strongly effect the structure and morphology of the catalysts. Especially a correlation between micropores and instability of Me-N-C was recognized [147]. Increased pyrolysis temperature showed higher graphitization degrees and thus making the catalyst more resistant against carbon corrosion. Likewise, lower nitrogen content and less MeN_4 active sites were found in highly graphitized catalysts, thus leading to an unfavorable activity-stability trade-off. The influence of the type of transition metal was recently highlighted by Li et al. [166]. Mn-based MeN_4 catalyst showed increased stability compared to their Fe-based counterpart. This was attributed to that fact that Mn-ions are less active for the Fenton reaction.

4.3 Structure and Active Site of Me-N-C Catalysts

In this section, details on the structure of Me-N-C catalyst with respect to the active site are provided. Since the major goal of this work is not fundamental structure analysis, this chapter will only deal with the most important information and will not contain the whole variety of concepts that has been brought up within the scientific community over the last decades. The focus will be on understanding the impact of the different sites hosted in Me-N-C catalysts with respect on catalyst performance (activity and stability).

The structure of the active site of Me-N-C catalysts has intensively been studied by numerous researchers over quite a long period of time. In the 1980, three major models have been proposed dealing with the question "what is the ORR active site after pyrolysis of MeN_4 chelates?". Van Veen proposed that the chelate site stays largely intact (to 500 - 600 °C) and that a ligand modification is occurring during the heat treatment [167, 168]. Yeager assumed that the macrocycle is destroyed and that metal and later metal oxides are formed. Following the exposure with electrolyte the metal is dissolved and adsorbs or coordinates to C-N_x sites forming some sort of $\text{C-N}_x\text{-Me}$ active site [169, 170]. Wiesener suggested that the metal of the chelate promotes its composition and that CN_x sites, formed during the heat treatment are the active sites [171, 172]. A comprehensive review on these models was given by Dodelet in 2013 [173]. It is concluded that indeed all of the three proposed active sites are present inside the catalyst, but their ORR activity and relative population are different.

Today, following intense characterization studies it is mostly accepted that molecular MeN_4 centers embedded in a graphitized or an amorphous carbon phase are mainly responsible for the ORR activity in acidic medium. A model of this structure is illustrated in **Figure 26** [174]. The intense characterizations leading to today's understanding of the active site included methods like X-ray photoelectron spectroscopy (XPS) [175-178], time-of-flight secondary-ion mass spectrometry (ToF-SIMS) [179], Mössbauer spectroscopy [180, 181] or high-angle annular dark-field scanning transmission electron microscopy (HAADF-STEM) [182, 183].

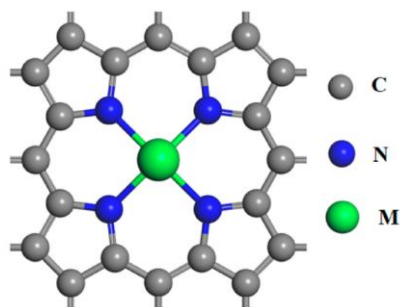


Figure 26: Ball-stick-model of the active site of an Me-N-C catalyst, showing the geometric structure of an MeN_4 center embedded in carbon [174].

However, several questions considering possible further ligands of the MeN_4 site or the role of promoter sites such as nitrogen functionalities and their part in the reduction mechanism remain. There are two major reasons that make the structural analysis of Me-N-C catalysts a challenging field and with respect to Pt-based catalysts significantly more complex:

- (1) Heterogeneous composition induced by the pyrolysis step.
- (2) The need of advanced spectroscopic techniques due to the molecular size of the formed species.

For the structural understanding of Me-N-C catalysts it is particularly important to know that these materials are usually obtained after a pyrolysis step of one or several different C-, N- and metal-containing precursors. The process of heating these chemical compounds under inert conditions results in a reducing chemical environment and the possibility of numerous different reaction products. In sharp contrast to wet-chemical synthesis the control or the pushing of the reaction process towards a specific product during a pyrolysis process is much more challenging. Hence, usually a heterogeneously structured carbon material is obtained possessing a variety of different defects or functionalities. With respect to the active site the most important ones are: (1) metal-free CN_x functionalities or sites (2) Me-carbides and (3) molecular MeN_xC_y moieties including MeN_4 sites.

CN_x sites and Me-carbides have shown to catalyze the acidic ORR following the $2e^-$ pathway resulting H_2O_2 as intermediate [184, 185]. Having in mind that H_2O_2 respectively its decomposition products

(ROS) are involved in the degradation of Me-N-C based MEAs, CN_x sites and Me-carbides are considered as undesired by-products or side phases. In particular, this applies for the Me-carbides. Inductively coupled plasma mass spectrometry (ICP-MS) experiments have shown that those leach out during the operation of the fuel cell releasing Me^{X+} cations [33]. As described in the previous section "Instability of Me-N-C Catalysts" this leads to severe MEA damage. The presence of Me-carbides and other inorganic metal by-products is therefore a major problem considering stability of Me-N-C catalysts. Those phases are often shielded from a highly graphitized carbon layer making them survive the acid leaching step. **Figure 27** shows the TEM picture of such an iron particle which is surrounded by a protective carbon layer.

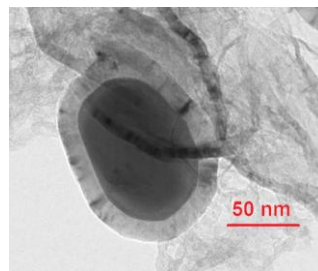


Figure 27: Iron nanoparticle surrounded by a highly graphitized carbon layer which protects the iron from dissolution during acid treatments but not from electrochemical leaching during PEMFC operation.

5 Literature Review on Synthesis of Non-Precious Metal Based ORR Catalysts

Historical Background

Metal phthalocyanines (Me-Pc) have long been known to catalyze different oxidation reactions. In 1939 Cook reported catalytic activity of H_2O_2 decomposition for iron phthalocyanine deposited on charcoal in (75 %) pyridine solutions [186]. Paquot reported catalytic activity of Me-PC for the oxidation of various organic compounds such as, long-chain fatty acids, toluene, ethylbenzene or pinene [187-189]. However, in 1964 Jasinski was first to report the use of Me-Pc for the reduction of oxygen in alkaline media [190]. Following, ORR activities of various additional N_4 - macrocyclic metal complexes were reported also for the acidic media [137, 191-193]. Among these early findings, Jahnke et al. summarized important conclusions in 1976 [191]. These include the enhancement of ORR activity when N_4 - macrocyclic metal complexes are impregnated on a carbon support and the improvement of activity and stability after applying a heat treatment. In 1973 by Savy et al. used molecular orbital theory was used to correlate the activity of different Me-Pc to the filling of the respective metal's d-band levels [194]. An activity trend for the ORR according to $\text{Fe-Pc} > \text{Co-Pc} > \text{Ni-Pc} > \text{Cu-Pc}$ was reported. However, to this point the capabilities of improving the characteristics of the macrocycle-based catalysts by alternating synthesis or similar parameters were quite limited. For instance, as found later in 2004 by Bogdanoff et al. the ORR activity of carbon impregnated with Co-tetra methoxyphenyl porphyrin (TMPP) is governed by its surface area, meaning it is limited at a certain maximum loading of Co-TMPP [195]. Further, the complicated structure of N_4 -macrocyclic metal complexes makes them expensive precursors, even though they don't contain precious metals.

A breakthrough considering these challenges was achieved by Gupta et al., when it was revealed that expensive transition metal complexes can be avoided by applying a heat treatment under inert atmosphere on much more cost-efficient carbon, nitrogen and transition metal precursors. In 1986 Gupta et al. showed that the heat treatment of polypyrrole mixed with Co- or Fe-salts gives catalysts with similar ORR activity of heat treated transition metal complexes [196]. Published in 1989, Gupta et al. further showed that a mixture of carbon black, polyacrylonitrile (PAN) and transition metal salt (FeAc or CoAc) gave similar results [153]. It was proposed that the nitrile nitrogen of the PAN is converted to pyridinic nitrogen during the heat treatment, thus providing a binding site for the transition metal. The active site is believed to be similar to that of heat treated N_4 -macrocyclic metal complexes, meaning of Me- N_4 type.

Concept of Me-N-C Synthesis

Based on the findings from Gupta et al. an enormous amount of different synthesis routes has been developed by scientist worldwide applying a big variety of different C, N and metal precursors. By doing so the underlying principle is mostly based on the same procedure comprising the steps of:

- (I) **Preparation of a precursor mixture** containing at least the elements C, N (others but less important: S, O, F, B, P) and one or several transition metals, mostly Fe or Co (others but less important: Ni, Mn, V, Cr, Cu).
- (II) **Heat treatment** of the precursor mixture at temperatures of about 600 - 1100 °C under either inert gas atmosphere (N₂ or Ar) or reactive gas atmosphere (CO₂, NH₃, N₂/H₂, CH₃CN). Goal: form active sites and carbon structure (catalyst morphology).
- (III) **Acid leaching** (HCl, H₂SO₄ or HNO₃) to remove excessive inorganic metal by-product phases, such as carbides or nanoparticles [33, 120]. Washing with water, filtration and drying.
- (IV) **2nd heat treatment** to (a) either just heal collateral damages induced by the acid leaching (such as surface oxidation, N-protonation and possibly anion-binding) under inert gas atmosphere or to (b) further tune the activity under reactive gas atmosphere [197].

Even though the great majority of reported preparations rely on steps (I) to (IV), there are some synthesis approaches that comprise of further steps such as a second acid leaching and a third heat treatment [166, 198]. Likewise, there are procedures that just comprise of step (I) and (II) [199, 200]. Besides, the precursor mixture can contain further additives that allow for a more distinct control over morphology or active-site formation, for instance silica-based hard templates, Zn-based metal organic frameworks (MOFs) or sulphur. Often Me-N-C catalysts are denoted or classified by their preparation approach. Since the synthesis of Me-N-C catalysts is usually quite complex and includes several components and steps, the classification is often adapted from the most decisive feature of the procedure or the precursors mixture. Hence, quite a number of denotations exists. Most prevalent are, MOF-based, carbon support-based, hard or soft template-based, sacrificial support-based, dual-nitrogen precursors containing-based, N-containing polymer-based, reactive polymer-based, NH₃-treated or metal-chelate-based synthesis approaches. However, these classifications are not strict, actually for the majority of methods several denotations overlap. As an example, there are MOF-based synthesis that apply a NH₃ treatment or an additional N-containing chelate molecule. Therefore, this overview here will be divided by the different precursor molecules according to the three major components of a Me-N-C catalyst, namely the transition metal precursor, the nitrogen precursor and the carbon precursor.

The Type of Transition Metal

Whereas for the case of acidic ORR the vast majority of non-precious metal based catalysts is relying on nitrogen as the heteroatom functionality, the transition metal is more likely to be altered [201]. For instance, Fe, Co, Mn, Ni, Cu, Cr are just some metals that have been investigated [128-136]. Still, the most commonly applied transition metals are Fe and Co. This is because Fe- or Co-based Me-N-C catalysts showed the best performances for the acidic ORR [25, 128, 134, 137-141]. There are several publications investigating the impact of the transition metal for these catalysts. Following, the most important findings will be summarized. As already mentioned, in 1973 Savy et al. ascribed the varying ORR activities of different Me-Pc to the filling of their d-band levels [194]. An activity trend for the ORR according to Fe-Pc > Co-Pc > Ni-Pc > Cu-Pc was reported. In 2007, Shi and Zhang applied density functional theory (DFT) methods on different Me-Pcs and Me-Porphyrins (Me-Ps) [202]. It was reported that the ORR activity is a function of the ionization potential and the dioxygen-binding ability of the Me-complex. Further, these two characteristics are determined by the type of central atom, additional ligands of the MeN₄ and further substitutes of the Pc or P complex. Electron-donating substituents were found to increase the dioxygen-binding ability of Co-Pc. It was calculated that for Me-P macrocycles the highest activity is achieved with Co as the central atom whereas for Me-Pc complexes Fe derivatives gave the best results. Osmieri et al. synthesized Me-N-C catalysts from different Me-Pc (Me = Fe, Co, Cu,) precursors and a mesoporous silica SBA-15 support [203]. Detailed electrochemical characterization of these catalysts with a RRDE revealed the respective reaction orders of oxygen and proton transfer, Tafel slopes, apparent activation energies, selectivity and the reduction kinetics of adsorbed oxygen with respect to the transition metal. These experiments showed the strong influence of the transition metal on the ORR. It was concluded that the ORR activity which follows an "asymmetric volcano plot" is related to the redox potential of the MeN₄ complex. This concept is illustrated in **Figure 28**. The "asymmetric volcano plot" is based on the idea of a potential dependent ORR active site coverage followed by blocking effects and was proposed by several researchers before [204-206].

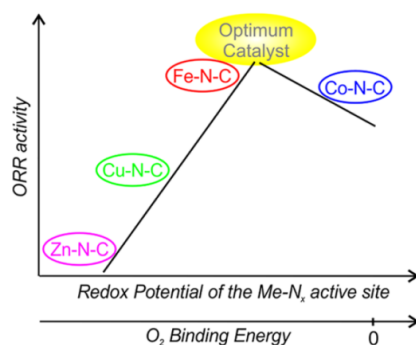


Figure 28: Asymmetric volcano plot relating ORR activity to the redox potential of the MeN₄ complex and the O₂ binding energy, the type of transition metal Me takes great action in governing these parameters [203].

Considering the ORR selectivity, Jaouen and Dodelet prepared Me-N-C catalysts from pyrolysing carbon black and different Me(Ac)₂ first under Ar and subsequently under NH₃ [207]. In acidic media RRDE characterization revealed the strong influence the transition metal has on the selectivity. A trend of higher selectivity for the ORR was found according to: Fe > Co > Cu > Cr > Ni > Mn. Likewise, a strong influence on the activity for H₂O₂ reduction was shown. The results are depicted in **Figure 29**. Peng et al. investigated polyaniline-melanine (PANI-Mela) based catalysts prepared from different transition metal-chlorides [131]. Again, the transition metal was found to have a strong influence on the ORR. A trend for the onset of the ORR of Fe > Co > Cu > Mn > Ni was reported. Further the BET surface area, the total nitrogen content and the type of the formed nitrogen species (graphitic, pyrrolic or pyridinic N) were depending on the used transition metal. The Fe-based PANI-Mela catalyst showed the highest BET surface area and the highest relative content of pyridinic N species of the compared catalysts.

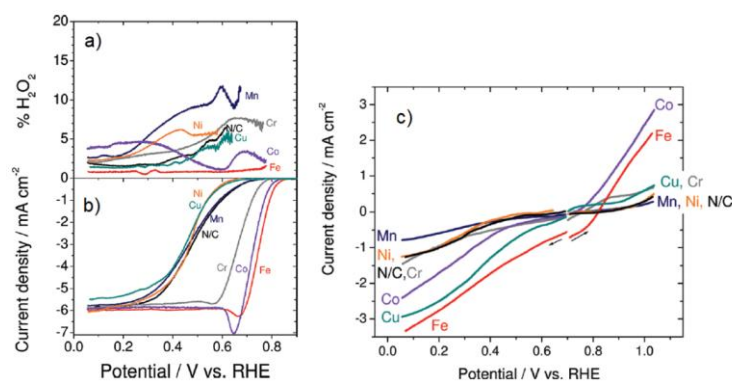


Figure 29: a) H₂O₂ formation and b) ORR activity of different Me-N-C catalysts in O₂ saturated H₂SO₄ solution (pH = 1, 1500 rpm, 0.96 mg cm⁻² catalyst disc loading) and c) H₂O₂ oxidoreduction in 9 mM H₂O₂ (pH = 1, N₂ saturated, 1500 rpm, 0.4 mg cm⁻²) [207].

Still, some recently reported syntheses were able to show that also Mn-based catalysts can indeed reach high performances [31, 166]. Li et al. obtained an atomically dispersed manganese catalyst after the heat treatment of a Mn-doped-ZIF8 precursor [166]. After performing the "standard" synthesis steps according to steps (I) - (IV) as mentioned before, a significant activity enhancement was achieved after the catalyst was subjected to a third heat treatment containing additional MnCl₂ and a nitrogen source (dipicolylamine, cyanamide, phenathroline or melamine). After the third heating step the Mn-N-C catalyst showed higher ORR activity than the respective Co-based version and only slightly less activity than the Fe-based one. Mn and also Co-based Me-N-C catalysts are especially of interest because they are less active for H₂O₂ decomposition via the Fenton reaction pathway. Fenton reaction is likely to play a major role in MEA degradation [208]. Higgins et al. and Li et al. showed better stability of Mn-N-C catalyst during RRDE experiments in comparison to Fe-N-C of the same kind [31, 166]. Further, catalysts prepared from two different transition metals source have shown to perform

better than single metal-based ones. For instance, Sahraie et al. prepared a C-PANI-based catalyst from a mixture of MnCl_2 and FeCl_3 [198]. The Fe-Mn catalyst showed similar ORR activity in acidic media as the Fe-based one, whereas the bimetallic catalyst revealed less loss in half-wave potential after cycling in the RRDE. In 2011, Wu et al. showed higher PEMFC performance for their bimetallic PANI-FeCo-C catalyst compared to PANI-Fe-C and PANI-Co-C [140]. A stability of ~ 700 hours was achieved for the bimetallic catalyst under low-voltage fuel cell operation (0.4 V, 2.8 bar H_2/air). A synergetic effect was also reported for the combination of Fe and Mo, by Lin et al. [209]. It is proposed that the Mo prevents the Fe from aggregation and enhances the graphitization of the carbon support during the heat treatment.

The Amount of the Transition Metal inside the Precursor Mixture

Another decisive factor in the synthesis of Me-N-C catalysts is the amount of transition metal that is added to the precursor mixture. For instance too high amounts of transition metal lead to excessive formation of site phases, such as carbides at the same time the nitrogen retention is lowered [210]. Even so some reports mention that there is a defined range of metal content for the precursor's mixture in the synthesis of Me-N-C catalysts that leads to an optimum in activity, it is important to include that this optimum range is strongly depending on the type of preparation used and can indeed vary strongly. A short overview of the optimum metal content for different synthesis approaches is included in the review from Bezerra et al. [130]. For instance, optimum nominal Fe content of 0.5 wt % have been reported for carbon-black- $\text{Fe}(\text{Ac})_2\text{-NH}_3$ treated catalysts or a $\text{Fe}(\text{Ac})_2$ -perylene-tetracarboxylic-dianhydride (PTCDA) based catalyst [180, 211, 212]. Lefèvre and Dodelet showed that for the same PTCDA supported catalyst approach the optimum Fe content is either 2 wt % if Fe-TMPPCl is used or 0.2 wt % if $\text{Fe}(\text{Ac})_2$ is used as the Fe-precursor [213]. In this case higher Fe contents than the reported optimum lead to the formation of inactive clusters. Similar results of an optimum transition metal content of 2 - 3 wt % were reported for a carbon black-urea-formaldehyde-cobalt-iron-ethylenediamine mixture [152]. Contrary, for polymer-based approaches, for instance those based on PANI or polypyrrole (PPy) optimum metal contents of up to 10 wt % were reported [122, 214]. Here, the transition metal content has a big impact on active site formation but also on the morphology and structure of the catalyst. Wu et al. mentioned that the need of the greater amounts of Fe-salt which was found for their PANI-based precursor mixture (optimum 3 - 10 wt %) compared to other NH_3 -treated catalysts (optimum 0.5 - 2 wt %) is associated with the catalytic decomposition of the polymer in the presence of the Fe-salt [122]. This decomposition needs to take place in order to generate the new carbon structure of the catalyst. The catalytic effect of transition metal salts on the formation of graphitized carbon structures during pyrolysis of organic precursors, especially for Fe-salts is well documented [215-219]. Ganesan et al. prepared catalyst from a mixture of Ketjenblack 600D, $\text{Fe}(\text{Ac})_2$

and melamine [220]. The heat treatment was performed at 800 °C in a sealed quartz ampoule, thus decomposition of precursor generated autogenic pressure. The Fe²⁺ content of the precursor mixture was varied between 0.9 and 4.6 wt %. The highest ORR performance was found for 1.2 wt % of nominal Fe²⁺. More considerably, by performing elemental combustion analysis and X-ray photoelectron spectroscopy (XPS) it was found that iron negatively influences the nitrogen retention of the catalysts, this is illustrated in **Figure 30**. Thermogravimetric analysis (TGA) found a similar connection of iron content and carbon gasification.

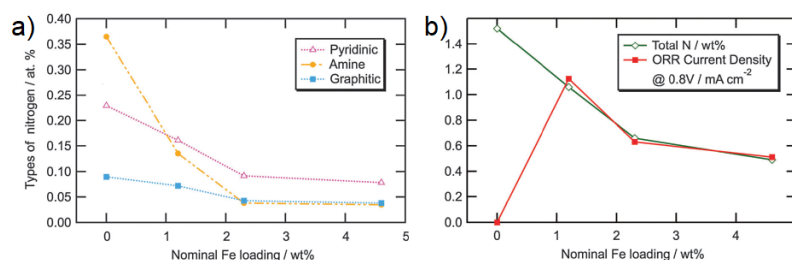


Figure 30: Change of nitrogen composition a), total nitrogen content and ORR current density b) with respect to the nominal Fe loading of the precursor mixture of a carbon black, melamine, Fe(Ac)₂ catalyst system [220].

As concluded by Wu et al., following a certain value where the iron supply becomes sufficient, other factors appear to be limiting the formation of active sites [122]. This conclusion is supported by the work of Osmieri et al., where it was found that further addition of Fe-salt to an already once pyrolyzed catalyst, meaning before the second heat treatment did not enhance the ORR activity any further [221].

The Type of Transition Metal Salt / Counterion

Another important factor that influences the activity of Me-N-C catalysts is the type of salt or the counterion of the applied transition metal. Quite a huge number of Fe-salts have been investigated, among others these include Fe(OH)₂, FeCl₂, FeCl₃, Fe(Ac)₂, FeSO₄, Fe(CN)₆, Fe(NO₃)₃, Fe(C₂O₄), Fe(SCN)₃ or Ferrocene [119, 133, 134, 222-229]. Bogdanoff et al. showed that catalysts based on CoTMPP impregnated on carbon black show significant higher ORR activity when an additional metal oxalate salt is present [195]. The metal oxalate acts as foaming agent enhancing the BET surface area of the catalyst and thus exposing more active sites [195, 230]. Shu et al. reported that Fe(SCN)₃ is the best choice for preparing catalysts based on p-phenylenediamine (p-BDA), because of the better dispersion and stabilization of the Fe³⁺-ions compared to FeCl₃ or Fe(NO₃)₃ [228].

To conclude, the transition metal salts play a decisive role for the synthesis of Me-N-C catalysts. The overall ORR activity and stability is strongly influenced by (I) the type of metal, (II) the amount, (III) the type of ligand or counter ion and (IV) possible synergetic effects of bimetallic mixtures.

The Nitrogen Precursor

A huge variety of different N-precursors can be applied for the synthesis of Me-N-C catalysts. The primary goal of the N-precursor is to form N-functionalities in the carbon matrix that provide binding sites for the transition metal. As already found in 1997 by Lalande et al. catalysts which are prepared without a nitrogen source are not active towards acidic ORR [231]. In most of the cases the N-precursor is fulfilling several tasks for instance it can stabilize the metal-ions and prevent excess formation of inorganic metal phases. Further, some N-precursors have a big influence on the morphology of the catalyst. Due to partly decomposition during the heat treatment, they initiate or enhance pore formation or other specific structures. Likewise, several approaches exist that simultaneously provide the carbon and the nitrogen source or that contain more than one nitrogen or carbon source. Here an overview of the most important N-precursors is provided together with some examples of the specific role and mentioned tasks.

N₄-macrocyclic complexes

N₄-macrocyclic complexes have been studied since the early findings of Jasinski in 1964 [190]. These molecules have the advantage that they already contain the N₄-moieties of the MeN₄ active site. Therefore, they provide excellent stabilization through chelating the transition metal ion. The structure of the Me-porphyrin and the Me-phthalocyanine is given in **Figure 31** [232].

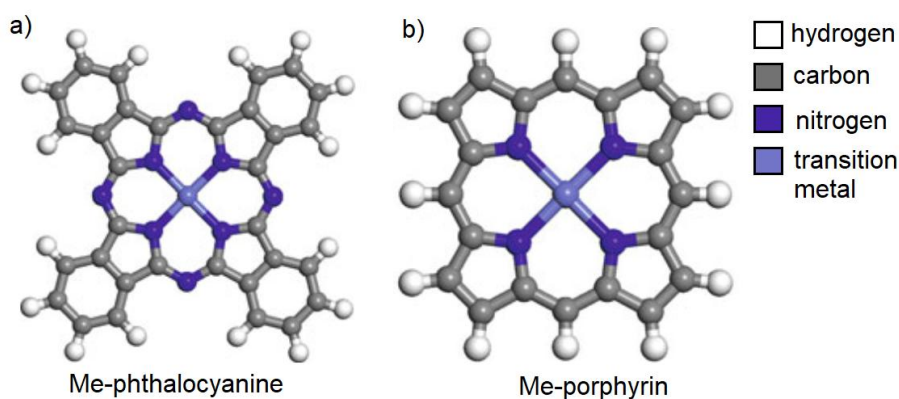


Figure 31: Ball-and-stick model illustrating the chemical structure of Me-phthalocyanine a) and Me-porphyrin b), the hydrogen atoms can be replaced by different substitutes [232].

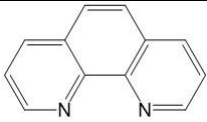
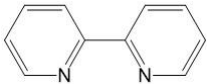
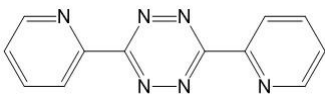
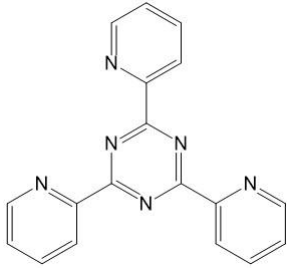
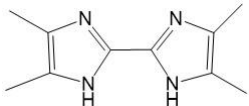
Depending on the pyrolysis temperature, this leads to catalyst with a high fraction of molecular dispersed active sites and very low fractions of inorganic by-products [233, 234]. Problems related to the use of N₄-macrocyclic complexes include comparatively high costs due to their complex structure, the need of an additional support or structuring agent such as carbon blacks or MOFs and in general a limited potential of enhancing or optimizing of active site density. This is why following the findings of

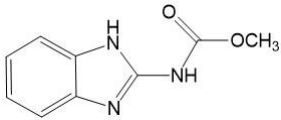
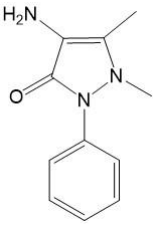
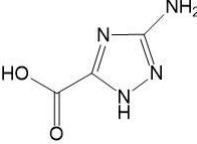
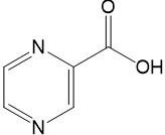
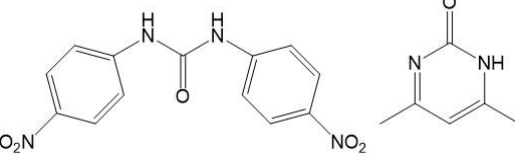
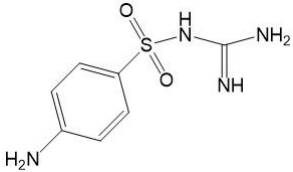
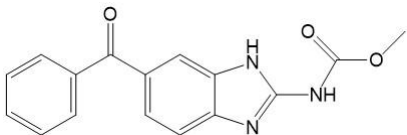
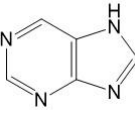
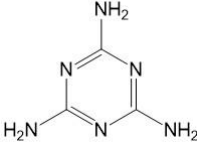
Gupta et al. N_4 -macrocyclic-based synthesis approaches have been of less interest. Some comprehensive reviews on N_4 -macrocyclic based catalysts are given in literature [191, 232, 235-237]. Even though the focus has shifted, recent publications show that new approaches in relation to macrocyclic precursors are still possible [238-241]. For instance, Zion et al. prepared an aerogel structured porphyrin catalyst from $FeCl_2$, 5,10,15,20-(tetra-4-aminophenyl)porphyrin (TAPP) and terephthalaldehyde as crosslinker [241]. After drying this polycondensation product with supercritical CO_2 and heat treating it at 600 °C, a catalyst is obtained with a very high number of active sites, $9.7 \cdot 10^{20}$ sites g^{-1} .

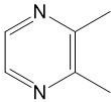
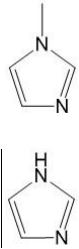
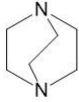
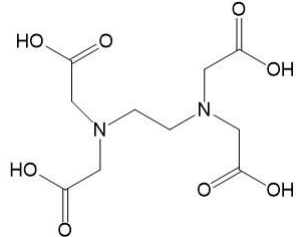
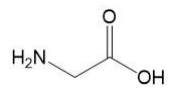
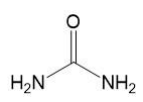
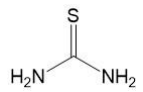
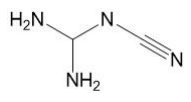
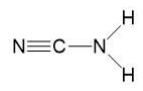
Small Organic Molecules

The most numerous appearing N-precursors in the synthesis of Me-N-C catalysts are **small organic molecules**. These can either be chelating molecules or non-chelating molecules. **Table 8** gives an overview of reported synthesis methods comprising small organic molecules as N-precursor and their chemical structure. It should be mentioned that publications considering this topic are so large in number that the overview here will only focus on the most important ones.

Table 8: Small organic molecules which have been applied as N-precursors to synthesize Me-N-C catalysts (monomers of polymer-based precursors are not included).

Name	Chemical Structure	General Information	Source
1,10-Phenanthroline (Phen)		chelating	[25, 121, 138, 242-251]
2,2'-bipyridine (BP)		chelating	[252-257]
3,6-di-2-pyridyl-1,2,4,5-tetrazine (DPTZ)		chelating	[248]
2,4,6-tri(2-pyridyl)-s-triazine (TPTZ)		chelating	[248, 258-262]
2,20-bis(4,5-dimethylimidazole) (bis-Me-Im)		chelating	[248]

Carbendazim (CBDZ)		chelating	[263-266]
4-aminoantipyrine (AAPyr)		chelating	[267-272]
3-amino-1,2,4-triazole-5-carboxylic acid (ATZC)		chelating	[248]
2-pyrazinecarboxylic acid (Pyr-COOH)		chelating	[248]
Nicarbazin (NCB)		-	[264, 273]
Sulfaguanidin (SGB)		-	[273]
Mebendazol (MBZ)		-	[273]
Purine (Pur)			[254, 274]
Melamine (Mel)			[220, 254, 275-277]
Nitroaniline (NA)			[278, 279]

Pyrazine			[254, 280]
N-methylimidazole (N-Me-Im) or imidazole (Im)		Most widely used as precursor for ZIF synthesis	[166, 199, 281-285]
1,4-diazabicyclo [2.2.2]octane (DABCO)		Precursor for MOF synthesis	[286, 287]
Ethylenediaminetetraacetic acid (EDTA)		strong-chelating	[257, 288-292]
Ethylenediamine (EDA)		chelating, also used as polymer	[293-298]
Glycine (Gly)		chelating	[299]
Urea		decomposes easily, pore former	[257, 275, 300, 301]
Thiourea		decomposes easily, pore former, sulfur-source	[275, 302, 303]
Dicyandiamide (DCDA)		decomposes easily, pore former, forms tubes	[251, 277, 304]
Cyanamide (CA)		decomposes easily, pore former, forms tubes	[166, 305-307]

N-precursors based on small organic molecules are mostly very cheap precursors. Hence, they can be applied in greater concentrations inside the precursor mixture if beneficial. Their relative nitrogen content is high, which means that a high amount of CN_x functionalities and binding sites for the transition metal can be created, this is often an advantage for ORR activity. There is a huge number of different molecules available differing in nitrogen content or containing other promoting functional groups such as sulfur functional groups. Sulfur and sulfur functionalities were found to suppress iron carbide formation and contribute to porosity [308, 309]. These features can easily be adjusted for best ORR performance by choosing from the vast number of available molecules or by combining several. Most of the smaller molecules partly decompose during the heat treatment. On one hand this can be beneficial because pore formation is promoted, on the other hand the transition metal is less likely to be stabilized and more inorganic side phases are produced. Again, the combination of precursors, one acting as stabilizer the other as pore promoter, can be beneficial. Hence, the vast majority of these N-precursors need to be combined with additional components in order to obtain the hierarchical 3-dimensional catalyst structure. Only if both, a high active site density and a hierarchical pore structure are accomplished simultaneously, a good performing catalyst is obtained. Following, some of the most important synthesis approach which comprise small organic N-precursors will be discussed.

N-chelating molecules

1,10-phenanthroline (phen) has widely been used as N-precursor, see **Table 8**. In comparison to the N_4 -macrocyclic complexes phen is a cheap precursor, whereas at the same time it provides excellent stabilization of the Me^{x+} ion through chelating effects. However, if phen is applied as the N-precursor it needs further assistance from structure guiding agents in order to achieve the desired hierarchical catalyst structure. In particular, phen in combination with MOFs as structuring guide has proven to yield highly active catalysts, with and without NH_3 heat treatment [25, 138, 184, 244, 249]. Highly porous carbon blacks have widely been used as a support material for phen based catalysts [121, 242, 246, 247]. A self-made adenine-based support which was pyrolyzed under hypersaline conditions was applied by Tong et al. [243, 310]. Osmieri et al. prepared $FeCl_3$ -phen catalysts from different carbon supports; carbon black, multi-walled carbon nanotubes and two self-made silica-hard-templated sucrose-based supports [245]. It was found that the structure of the support governs the ORR activity of the catalyst. Specific surface area, pore size distribution and occurring weight loss during the synthesis were identified as important parameters. Schardt et al. showed that a $FeCl_3$ -phen-sulfur mixture can also form the desired hierarchical pore structure when decomposing materials such as dicyandiamide (DCDA) or oxalic acid (OA) are added as pore forming agents [251]. A correlation between ORR onset potential and BET surface area was obtained. Other heterocyclic N-precursors that show similar behavior to phen are 2,2'-bipyridine (BP), 3,6-di-2-pyridyl-1,2,4,5-tetrazine (DPTZ),

2,4,6-tri(2-pyridyl)-s-triazine (TPTZ), 2,20-bis(4,5-dimethylimidazole) (bis-Me-Im), carbendazim (CBDZ), 3-amino-1,2,4-triazole-5-carboxylic acid (ATZC), 2-pyrazinecarboxylic acid (Pyr-COOH) or 4-aminoantipyrine (AAPyr), see **Table 8**.

A method that has been applied in combination with a variety of different N-precursors is the so-called **sacrificial support method (SSM)** which was developed by researchers of the University of New Mexico [311]. Here a silica hard-template is wet impregnated or dry-ball milled with the N-precursors and the transition metal source, after pyrolysis the silica template is removed by HF treatment. A scheme of the procedure is shown in **Figure 32** [270].

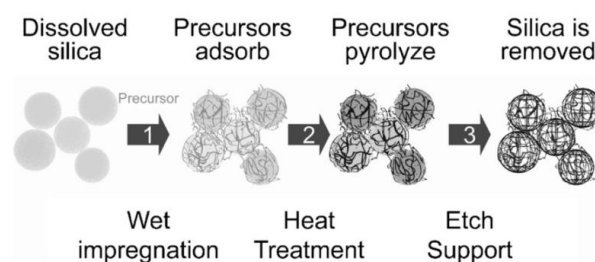


Figure 32: Synthesis steps of the silica-based sacrificial synthesis method (SSM) [270].

The resulting hierarchical pore structure is easily controlled by the type of silica (size and porosity). N-precursors that have been applied according to this method are 4-aminoantipyrine (AAPyr), carbendazim (CBDZ), nicarbazin (NCB), sulfaguanidin (SGB), mebendazol (MBZ), 2-aminobenzimidazole, pol(ethyleneimine) or tetra methoxyphenyl porphyrin [263, 264, 266, 267, 269-273, 298, 312-314]. In 2016 Serov et al. showed that this approach is suited for a scale-up to a batch size of 200 g, the resulting catalyst was stable under PEMFC operation for over 100 hours (0.65 V, 1.25 atm_{air} and 90 % humidity) [268].

Another commonly used N-precursor is imidazole (Im) or its derivate N-methylimidazole (N-Me-Im). Imidazoles are used as precursor for the hydro- or solvothermal synthesis of **zeolitic-imidazolate frameworks (ZIFs)**. ZIFs have shown to be superior precursors for the synthesis of Me-N-C catalysts. A highly porous and hierarchical structure is provided in combination with N-functionalities which act as binding site for the transition metal ions. Ma et al. were first to report a heat treated cobalt-Im framework as catalyst for the ORR, the principle of this ZIF approach is illustrated in **Figure 33** [315, 316].

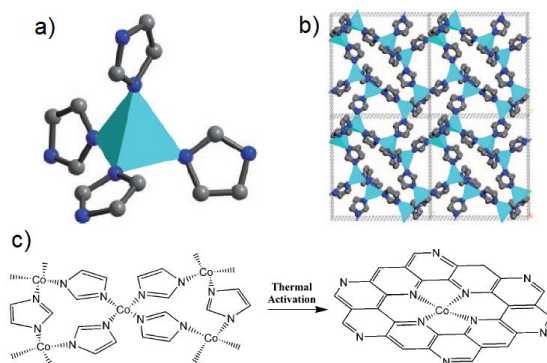


Figure 33: Local coordination environment of the transition metal inside the ZIF (a), hierarchical structure of the ZIF (b) and proposed formation of active sites by Ma et al. (c) [315].

Significant attention was drawn to the ZIF-based Me-N-C catalyst approach since in 2011 Proietti et al. reported a maximum power density of 0.9 W cm^{-2} for their ZIF8-phen-Fe(Ac)₂ catalyst which was treated with NH₃ [25]. Shui et al. emphasized the relation of macro and micropores with the performance of ZIF-based catalyst systems for PEMFC operation [138]. By applying an electrospun fiber catalyst network a slightly higher power density with respect to Proietti was obtained. In 2015, You et al. found that the transition metal, cobalt can directly be added during the ZIF preparation [317]. A bimetallic ZIF structure was obtained from a mixture of Co(NO₃)₃, Zn(NO₃)₂ and N-Me-Im. A highly active catalyst is obtained after one heat treatment in Ar, no acid leaching or other post treatments (as NH₃ treatment) were needed. This approach has been adapted by other researchers for Fe-Zn and Mn-Zn based catalysts [166, 199, 318]. By controlling the ratio of methanol to Zn²⁺, Zhang et al. prepared FeZn-ZIF crystals of varying size (20 - 1000 nm) [284]. It was found that the ORR performance of the subsequently heat-treated catalysts is strongly depending on the crystal size. An optimum ORR activity was found for 50 nm sized FeZn-ZIF crystals. The ZIF-based synthesis approaches usually require high pyrolysis temperatures of >1000 °C to completely remove the Zn. However, high temperatures also increase the formation of inorganic metal products at the cost of molecular active sites [319]. Recently, Al-Zoubi prepared a Cadmium (Cd) based metal organic framework (MOF) from 1,4-diazabicyclo[2.2.2]octane (DABCO) and terephthalic acid (TPA) together with an iron salt [287]. The Fe,Cd-DABCO-TPA MOF precursor showed reasonable ORR activity after a heat treatment at 750 °C in NH₃. Some more comprehensive reviews on ZIF-based catalyst system were recently published [320-324]. It is emphasized that so far, the most active Fe-N-C catalysts were all prepared using ZIF precursors.

Small organic N-precursors that do not contain an aromatic ring are for instance urea, thiourea, CA or DCDA, see **Table 8**. These molecules have several features and thus can fulfill multiple tasks in addition to being just a N-source in the synthesis of Me-N-C catalysts. For instance, DCDA has been shown to partly decompose into gaseous products during the heat treatment. As mentioned before, Schardt et al. used DCDA as pore forming agent in combination with phen, Fe(Ac)₂ and sulfur [251].

Gupta et al. added DCDA to an acid treated carbon black, aniline, FeCl₃, ammonium persulfate polymerization mixture [277]. It was found that the addition of DCDA improved the catalysts performance due to an optimized porosity, an increased BET surface area and the formation of thicker amorphous carbon layers which contained more pyridinic N in comparison to the same mixture without DCDA. Very similar conclusions were drawn by Zhang et al. on the influence of urea addition to a carbon support-free synthesis of approach comprising an aniline, FeCl₃, ammonium persulfate polymerization mixture [300]. Li et al. obtained an ORR catalyst after pyrolysing a MnZn-N-Me-Im(ZIF) precursor [166]. It was found that a subsequent second heat treatment with additional Mn-salt and different N-precursors (CA, phen, mel or dipicolylamine) increased the ORR performance significantly. Among the tested N-precursors CA showed the highest performance enhancement. Chung and Zelenay showed that the pyrolysis of CA in the presence of transition metals such as Fe, Co and Ni yields N-doped carbon nano and microtubes (20 - 1000 nm diameter) [325]. In combination with acid treated carbon black this finding was used to develop a nanotube/nanoparticle comprising catalyst for the acidic as well as for alkaline ORR [305, 307]. The formation of the nanotube structure from CA was also reported for a high-pressure synthesis approach based on mixture of CA, durene and ferrocene by Zhing et al. [306].

Reactive Gas Atmosphere

The introduction of surface **N-functionalities** can also be achieved **through reactive gas atmosphere** which is applied during the heat treatment. In 1997 Lalande et al. used acetonitrile vapor carried by Ar-gas [231]. It was shown that ferrocene impregnated on carbon black yields a material which is mostly inactive for the acidic ORR after a heat treatment in Ar. However, the same precursor mixture could be activated for ORR by performing the heat treatment in acetonitrile/Ar. The authors concluded that both Fe and N are needed to generate the active sites, further it was shown that the N-functionalities can be introduced through the gas feed during the heat treatment. Côté et al. compared different N-precursors in combination with Fe(OH)₂ adsorbed on carbon black. The authors concluded that acetonitrile/Ar and NH₃ gas have a similar effect on the resulting catalyst and rated both as equivalent N-precursors. Contrary, following this result, the same group found that for a Fe(Ac)₂ + perylenetetracarboxylic dianhydride (PTCDA) precursor mixture the NH₃ treatment significantly altered the microporous structure of the catalyst through etching, whereas the treatment with acetonitrile/Ar did not [212]. Following, primarily, NH₃ or NH₃/Ar mixtures have been applied. The NH₃ treatment can be conducted during the first-, the second or both heat-treatments [326]. Its effects can be optimized through adjusting or monitoring the NH₃ concentration in the gas-feed, the ramping and holding times, the absolute temperature, the occurring weight loss, the microporosity of the carbon or additional pore-fillers inside the precursor mixture (presence of amorphous carbon).

Indeed, high ORR performances were achieved for the combination of a support material (carbon black or MOF), an iron salt precursor and a pore-filling N-precursor containing mixture after performing the second heat treatment in NH₃ [25, 121]. Considering the influence of NH₃ concentration in the NH₃/Ar gas feed, Meng et al. prepared several catalysts from a carbon black FeTMPPCl impregnated precursor mixture [26]. The catalysts were heat treated for ten different concentrations of NH₃, ranging from 0 % to 100 %, for 10 min at 950 °C. In dependence on the NH₃ concentration the activity and the stability under PEMFC operation followed an opposing trend, whereas the activity increased but the stability decreased. For low NH₃ concentrations a jump in activity and a decreased stability was found. Only slight difference was found for concentrations ranging from 20 to 80 % of NH₃. Another increase in activity and another decrease in stability was found for high concentrations of 80 - 100 % NH₃. This correlation is shown in **Figure 34**.

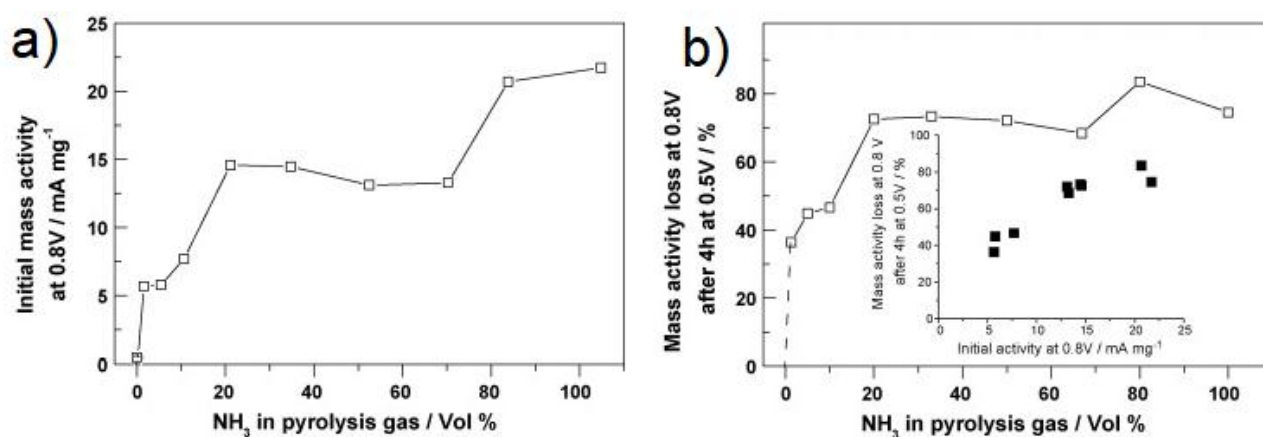


Figure 34: Correlating PEMFC activity (a) and stability (b) of NH₃ treated carbon black FeTMPPCl catalysts with the NH₃ concentration of the gas feed. Activity is increased at the costs of stability [26].

The heat treatment with NH₃ has shown to proceed along with a weight loss of the material [225, 326]. This weight loss is depending on the pyrolysis temperature and time and can be correlated with the micropore content and ORR activity. For a low surface area carbon impregnated with an iron salt the optimum ORR performance is reached after 30 - 35 % of weight loss [151, 180, 326, 327]. An etching reaction is responsible for the weight loss according to [328]:



This etching proceeds much faster for amorphous than for graphitized carbon. Hence, catalysts which contain greater amounts of amorphous phases showed the most significant ORR improvements after the NH₃ treatment [328, 329]. Those are either low-surface area carbons or high-surface area carbons where pores were filled with amorphous phases which emerged from pore fillers such as phen [121,

330, 331]. Due to the etching reaction the specific surface area as well as the microporosity of the catalyst material is increased after a treatment with NH_3 . Both are considered to be a factor for the increased activity. Microporosity has also been discussed to be responsible for the decreased stability of NH_3 treated catalysts. However, the origin of the greater instability is still not 100 % clear. A combination of several factors namely lower hydrophobicity, higher surface nitrogen content and the higher microporosity is most likely responsible for the instability of NH_3 treated catalysts. Some researchers found that the surface nitrogen content of the catalyst is enhanced [212, 332] after the etching process with NH_3 whereas others reported the opposite [333, 334]. For instance, Jaouen et al. found that a treatment time of only 5 min at 900 °C in NH_3 of a carbon black (low-surface area) $\text{Fe}(\text{Ac})_2$ mixture is sufficient to generate high nitrogen surface contents of 2 at% [326]. However, the overall activity of this short treated catalyst remained low in comparison to longer treated catalysts. Thus, it has been stated that the higher surface nitrogen content which is observed for some NH_3 treated catalysts cannot solely be responsible for the increased activity. The findings that led to this conclusion were summarized by Jaouen et al. in 2011 [330]. Kramm et al. prepared catalysts from a $\text{FeTMPPCl-Fe}(\text{Ox})$ -sulphur mixture with a second heat treatment under Ar or NH_3 . Mössbauer spectroscopy revealed that the relative active site (FeN_4) content was similar for all prepared catalysts [335]. However, the turn-over-frequency (TOF) of the NH_3 treated catalyst was 3.5 times higher in comparison to the Ar treated one. Hence, the improved activity after a NH_3 treatment is not caused by the formation of new active sites. Kramm et al. also showed that instable iron-nitride is formed during the NH_3 treatment. Mössbauer spectroscopy and X-ray absorption near-edge spectroscopy (XANES) performed by Zitolo et al. confirmed these findings [244]. NH_3 and Ar treated catalysts contain identical active sites, however the physico-chemical properties of the support enhance the TOF after a NH_3 treatment [336]. Still, when considering the application of Me-N-C catalysts in PEMFCs the induced instability makes a NH_3 treatment rather impracticable.

Polymer-Based Precursors

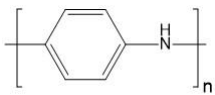
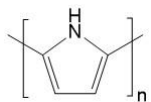
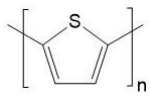
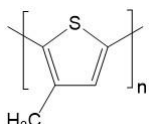
For this synthesis approach the necessary C and N atoms are provided by a polymer. A benefit from using polymers is that they provide the N functionalities and the carbon back bone all in one. In general, the morphology of the resulting catalyst is highly depending on the starting polymer. This enables, at least to a certain degree, control and optimization of the catalysts morphology via adjusting the polymer's structure or polymerization conditions. Still, a wide variety of additional supports and structuring agents can be combined with polymer precursors for fine tuning the catalyst's structure and its ORR performance. Further, the polymer precursor usually plays an important role by stabilizing the transition metal ions through N-functional groups. Here, the polymer precursors are divided in two groups:

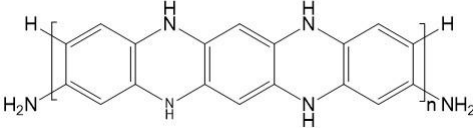
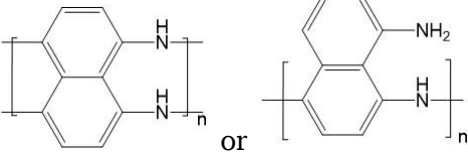
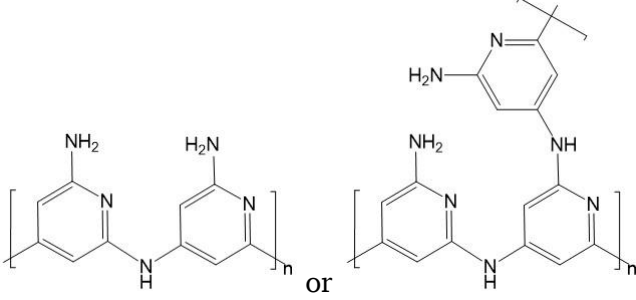
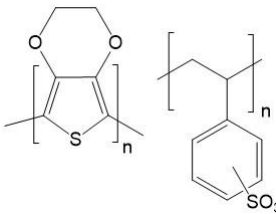
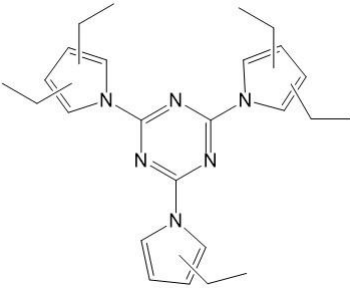
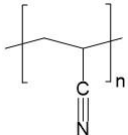
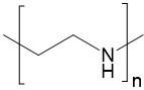
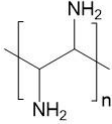
(1) conducting polymers,

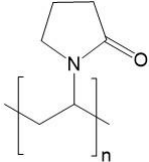
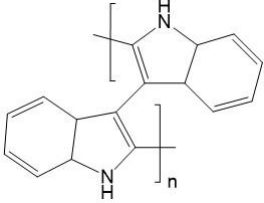
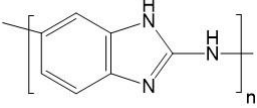
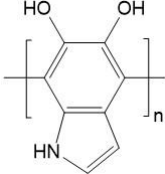
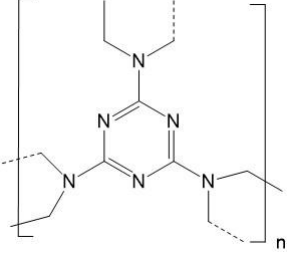
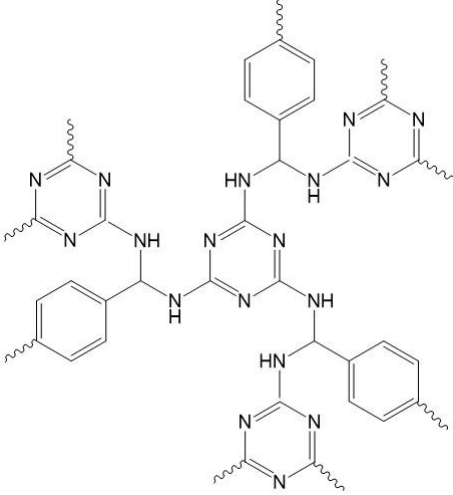
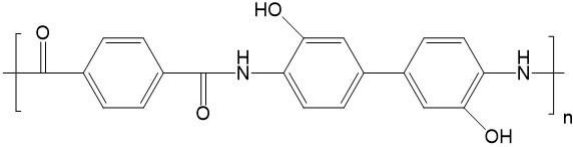
(2) N-containing polymers that are non-conducting.

Among the conducting polymers polyaniline (PANI) and polypyrrole (PPy) have been investigated most intensively (for references see **Table 9**). Other conducting polymers include polythiophene (PTh), poly-*m*-phenylenediamine (PmPDA), poly-(1,5-diaminonaphthalene), poly-diaminopyridine (PDAP), poly-(3,4-ethylenedioxythiophene) polystyrene sulfonate (PEDOT:PSS) and poly-(2,4,6-tripyrrol-1,3,5-triazine) (PTPT) (for references see **Table 9**). The most important N-containing polymers that are non-conducting are polyacrylnitril (PAN), poly-ethylenimine (PEI) and different polymer resins such as melamin- or urea-formaldehyde resins. Others include poly-ethylenediamine (PEDA), polyvinylpyrrolidone (PVP), polyindole (PI), poly-2-aminobenzimidazole (P-2-ABI), poly-dopamine (PDA) and different polyamides, polyimides and polyazoles. An overview of these different polymer precursor, which were used for the synthesis of Me-N-C catalysts is given in **Table 9**. Following a description of the most important synthesis routes and related findings considering the synthesis of Me-N-C catalysts based on polymers will be given.

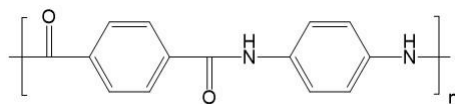
Table 9: Overview of conducting or non-conducting polymers that have been used as precursors for the synthesis of Me-N-C catalysts.

Name	Chemical Structure	General Information	Source
Polyaniline (PANI)		Conducting	[27, 122, 140, 198, 300, 333, 337-348]
Polypyrrole (PPy)		Conducting	[27-29, 196, 200, 221, 349-356]
Polythiophene (PTh)		Conducting	[357-359]
Poly-3-methylthiophene (P3MTh)		Conducting	[360]

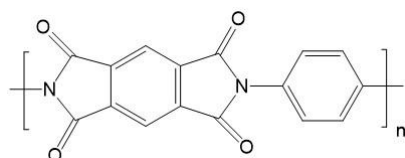
Poly- <i>m</i> -phenylenediamine (PmPDA)		Conducting, ortho and para have also been used	[227, 361-364]
Poly-(1,5-diaminonaphthalene)		Conducting	[365]
Poly-diaminopyridine (PDAP)		Conducting, networked of linking of polymer chains	[366, 367]
Poly-(3,4-ethylenedioxythiophene) polystyrene sulfonate (PEDOT:PSS)		Conducting	[368-371]
Poly-(2,4,6-tripyrrol-1,3,5-triazine) (PTPT)		Conducting	[372, 373]
Poly-acrylnitril (PAN)			[138, 143, 153, 359, 374-380]
Poly-ethylenimine (PEI)			[298, 381, 382]
Poly-ethylendiamine (PEDA)			[383, 384]

Polyvinylpyrrolidone (PVP)		[30, 221, 385-387]
Polyindole (PI)		[388]
Poly-2-aminobenzimidazole (P-2-ABI)		Exact structure not mentioned [389]
Poly-dopamine (PDA)		Exact structure under discussion [391, 392] [390]
Melamine formaldehyde resin (MFR)		Also reported for other formaldehydes [275, 393, 394]
Melamine therephtalaldehyde		[395]
Poly-(3,3'-dihydroxybenzidine-terephtalamide) (DBTA)		Polyhydroxy amide [396]

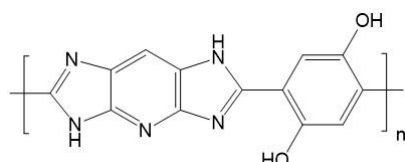
Poly-(phenyldiamine-terephthalamide) (PPTA)



Polyamide [397]

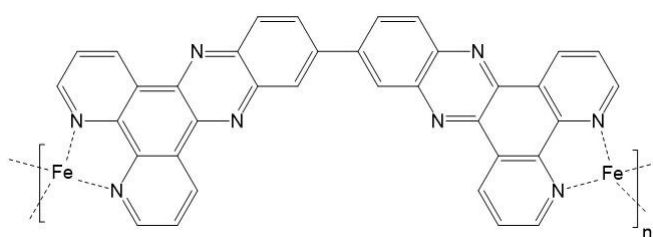


Polyimide [397, 398]



Polyazole [397]

Fe-bi-dipyrido[3,2-a:2',3'-c]phenazine (Fe-biddpz)



Coordination Polymer [209, 399]

A high performing catalyst based on conductive polymers, preferentially **polyaniline (PANI)** was developed at the Los Alamos National Laboratory (LANL) [140]. According to this procedure, an acid treated carbon support, is mixed with a water-based polymerization mixture comprising of aniline, ammonium peroxydisulfate (APS) and the transition metal source. Following the polymerization process, the mixture is vacuum dried, heat treated in inert gas atmosphere, acid leached in H_2SO_4 and again heat treated. A schematic overview of this procedure yielding the catalyst particles with carbon shells containing N-functionalities and the transition metal is given in **Figure 35** [140].

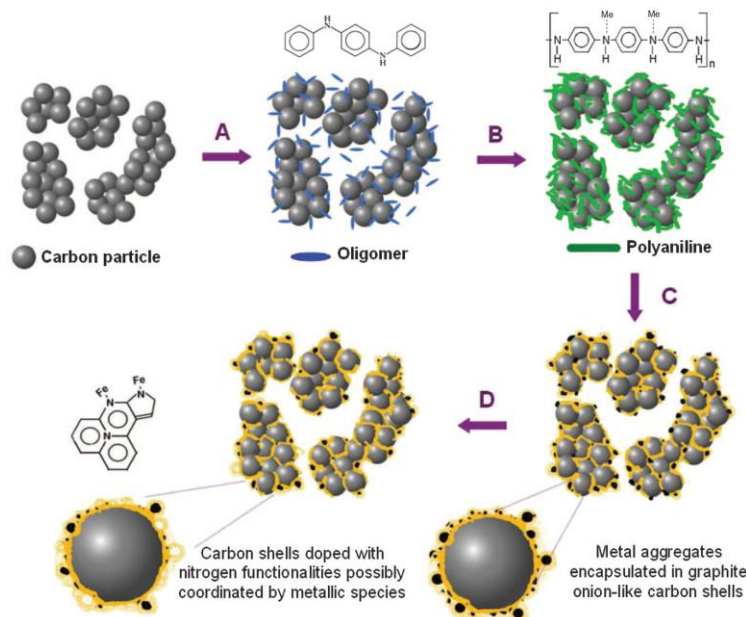


Figure 35: Schematic overview of the synthesis process of a PANI-Me-C catalysts, comprising the steps of mixing the oxidized carbon support with the monomer solution and polymerization agents (A + B), heat-treatment and acid leaching (C+D) [140].

An Fe plus Co based catalyst prepared according to this method showed stable fuel cell performance under low voltage conditions (0.4 V) for ~700 hours [140]. Manganese has also been successfully incorporated via this procedure [31]. Higgins et al. showed that the Mn-based version of the catalyst showed slightly lower activity than the Fe-based one, whereas the durability during RRDE tests was significantly higher. After performing 5,000 stress cycles the Mn-PANI-KJ catalyst showed a loss in half-wave-potential of 20 mV. Contrary the Fe-PANI-KJ catalyst lost 80 mV under the same conditions. Considering the polymerization conditions Ding et al. found that when aniline is polymerized at low proton concentrations a dense product is obtained. Indicating that PANI with high cross-linking is formed (polymerization conducted through FeCl_3 , no APS) [400]. Contrary, high proton concentrations lead to less cross-linking and a nanofibrous morphology of the PANI. Likewise, the addition of decomposable metal salts prohibited the cross-linking. It was shown that the prohibition of the cross-linking is preferable to obtain high activities for fuel cell operation under H_2 -air. Johnston et al. reported that for the mentioned LANL synthesis procedure the catalysts activity correlates with its micropore surface area [401]. It was found that the absolute temperature during the heat treatment has a strong influence on this matter [122, 401]. An optimum synthesis temperature of 900 °C was reported, whereas the performance was limited by an excess loss in surface area at higher temperatures and by insufficient graphitization at lower temperatures [122]. This PANI-based synthesis method is also compatible with different supports, such as carbon black, multi-walled carbon nanotubes or low surface area TiO_2 [27, 402]. A small overview of the influence of different synthesis parameters such as the different synthesis steps, the type or amount of the transition metal and the absolute temperature during the heat treatment with respect to this PANI approach is given by Wu et

al. [122]. However, a drawback of the mentioned approach is that great amount of inorganic side phases is presented in the catalyst [122] [140]. Recently, Yin et al. replaced the aniline monomers with monomer molecules that possess an additional N-functional group, the structure of the resulting polymers is shown in **Figure 36** [346]. All catalysts prepared from these polymers showed higher ORR activity than the PANI based one. As revealed by XPS measurements, the additional functional groups lead to higher N-content and an increased number of N-Fe bonds inside the catalyst.

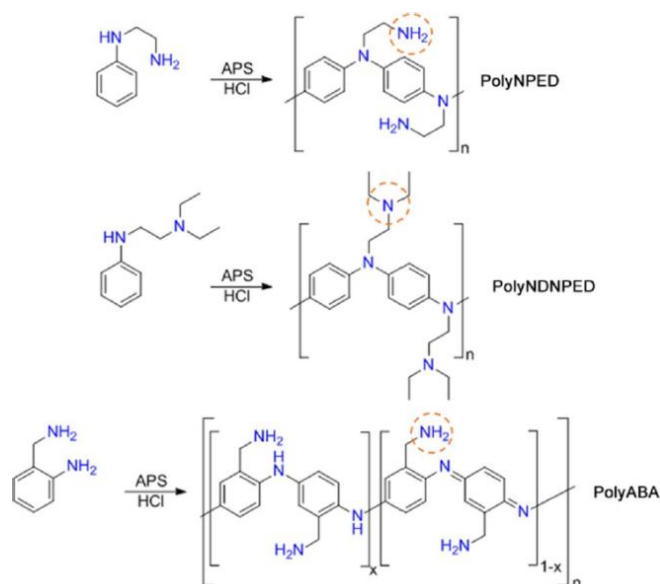


Figure 36: Polymerization of aniline related monomers but with an additional N-functional group, the new side chains of the polymers are in red circles and have a high affinity to Fe-ions [346].

Another reported strategy of increasing the ORR performance of PANI-based Me-N-C catalysts is through addition of small organic N-containing molecules. For instance, Peng et al. prepared a catalyst from a mixture of aniline, FeCl_3 , APS and melamine [339]. This catalyst showed significant higher ORR activity than the same catalyst prepared without melamine addition. Very similar results were obtained by Zhang et al. by adding urea as secondary N-source. As reported by Gupta et al. and Leonard et al., further important characteristics that are influenced by adding secondary N-sources to a PANI based synthesis are the surface area, the porosity and the degree of graphitization of the resulting catalyst [277, 337]. Other molecules that have been used in this manner are for instance DCDA and nicarbazin [277, 337].

Polypyrrole (PPy) is another very widely used polymer precursor for the synthesis of Me-N-C catalysts. Catalysts derived from PPy show similarities to those from PANI [27]. As reported for PANI, PPy based synthesis approaches usually need additional N-precursors, supports or templates in order to achieve the desired hierarchical catalyst morphology and high fuel cell performances. A quite unique method was reported in 2006 by Bashyam and Zelenay, here a non-pyrolyzed catalyst was obtained from

carbon black, polypyrrole and reduced $\text{Co}(\text{NO}_3)_2$ [200]. This catalyst showed decent ORR activity but more remarkable stability under low voltage operation for 100 hours. For the heat treated PPy catalysts a variety of different strategies have been published which deal with achieving a hierarchical catalyst structure. For instance, just like PANI, PPy has been polymerized onto carbon black as support [27-29]. Different silica hard templates have been used such as mesoporous SBA-15 or silica gel particles [221, 349]. Recently, Ferrero et al. prepared Fe-N doped carbon capsules from silica particles with a hollow core and a mesoporous shell (SCMS) [354]. Therefore, the SCMS were impregnated with FeCl_3 and exposed to pyrrole vapor after a heat treatment at $850\text{ }^\circ\text{C}$ under N_2 the silica template was removed with HF. This procedure and the resulting catalyst particles are illustrated below.

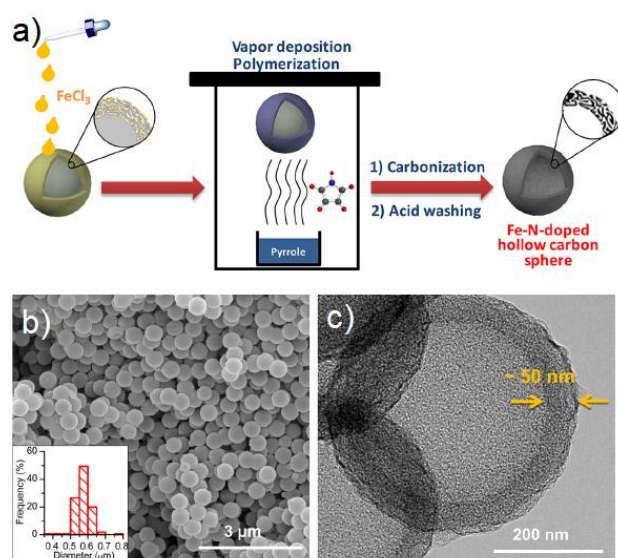


Figure 37: Schematic preparation of hollow PPy spheres from mesoporous SCMS, FeCl_3 and pyrrole vapor (a), final catalyst after pyrolysis SEM image (b) and HR-TEM image revealing uniform particle size and shape (c) [354].

However, the silica hard template-based approaches rely on dangerous HF or hot alkaline liquid for removing the template. To overcome this issue, Meng et al. prepared Fe_3O_4 microspheres by a solvothermal reaction from FeCl_3 and sodium acetate in glycol [352]. These Fe_3O_4 microspheres were added to a polymerization mixture containing pyrrole. Following the heat treatment Fe-N doped mesoporous carbon microspheres are obtained without any dangerous HF or alkaline leaching step. However, the ORR activity of this catalyst was not reported for acidic but only alkaline conditions. Niu et al. used NaCl crystals as easy dissolvable template to generate honeycomb-like porous catalyst structure [353]. Therefore, NaCl crystals were wet impregnated (ethanol) with pyrrole and PVP. FeCl_3 solution was added and the polymerization was performed at $120\text{ }^\circ\text{C}$ for only 3 min to avoid NaCl crystal dissolution. Following, the NaCl is easily dissolved in water and the catalyst is obtained after the usual heat treatment step under inert gas. The schematic overview of this procedure and the morphology of the resulting catalyst is shown in **Figure 38**. Likewise, ORR activity of this catalyst was only reported for alkaline ORR.

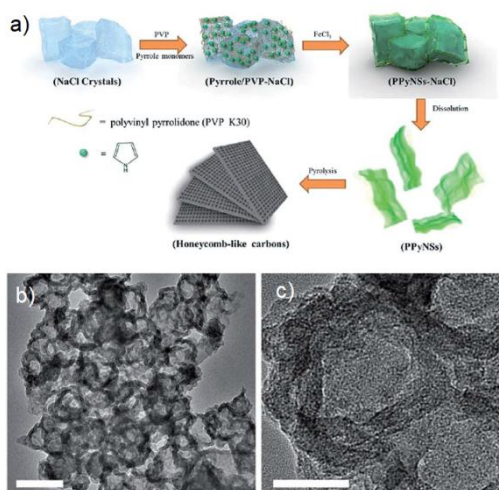


Figure 38: Schematic synthesis route applying NaCl crystals as readily dissolvable hard-template for the synthesis of a PPy-based Fe-N-C catalyst (a) and TEM pictures of the material after pyrolysis showing a disordered honeycomb-like structure [353].

As mentioned, the presented methods that use NaCl crystals or via solvothermal method obtained Fe₃O₄ microspheres do not require the use of dangerous chemicals such as HF to remove the hard template. However, solvothermal methods and also crystal containing solutions need precise reaction control, meaning parameters such as concentrations, temperature and pressure. This can become challenging when the batch is being scale-up. In 2010 Yuan et al. reported that the activity of a carbon black and PPy based Co-N-C catalyst can be enhanced through doping the PPy with *p*-toluenesulfonic acid (TsOH) [350]. TsOH was simply added to the polymerization mixture containing acid treated BlackPearls®2000, pyrrole and APS. The enhanced ORR activity of Co-PPy-TsOH/C in comparison to C-PPy/C was attributed to an enhanced N-content. Similar results were reported by Feng et al. when doping PPy with sodium dodecylbenzene sulfonate (DBSNa), sodium *p*-toluenesulfonic acid (TsONa) and sodium benzenesulfonate (BSNa) [403]. Even so the doping is an easy and highly scalable method, the catalyst did show comparatively low activities. Yuan et al. reported a maximum power density of 204 mW cm⁻² under H₂-O₂ PEMFC operation.

Contrary, a very high power density of over 1 W cm⁻² was achieved by Wang et al., by applying a conductive polymer supported on carbon black [363]. Therefore, Ketjenblack® EC-300J was first grafted with sulfophenyl groups through a diazonium salt reaction with aminobenzenesulfonic acid. The functionalized carbon was then brought into a polymerization mixture of *m*-phenylenediamine, APS and FeCl₃. Following the polymerization, Fe(SCN)₃ was added by wet impregnation with FeCl₃ and KSCN. The catalyst was obtained after performing the first heat treatment, the acid leaching and the second heat treatment. It was proposed that the catalyst benefits from the interaction of the sulfophenyl group grafted carbon support with the poly-*m*-phenylenediamine as well as from the addition of Fe(SCN)₃ as the iron source [362, 363].

Considering the non-conducting polymers polyacrylonitrile (PAN) has been used widely. Chokai et al. prepared a PAN based catalyst by first stabilizing the PAN at 230 °C under air [143]. Subsequently, FeCl₂ was added through wet impregnation with tetrahydrofuran (THF). Activation of the FeCl₂ impregnated stabilized PAN was conducted at 800 °C in Ar for one hour and at 1000 °C in NH₃ for one hour. This catalyst showed stable fuel cell performance over the course of 400 min operating at high potential of 0.8 V in H₂-air. The synthesis route, the PEMFC polarization curves and the stability test is illustrated in Figure 39.

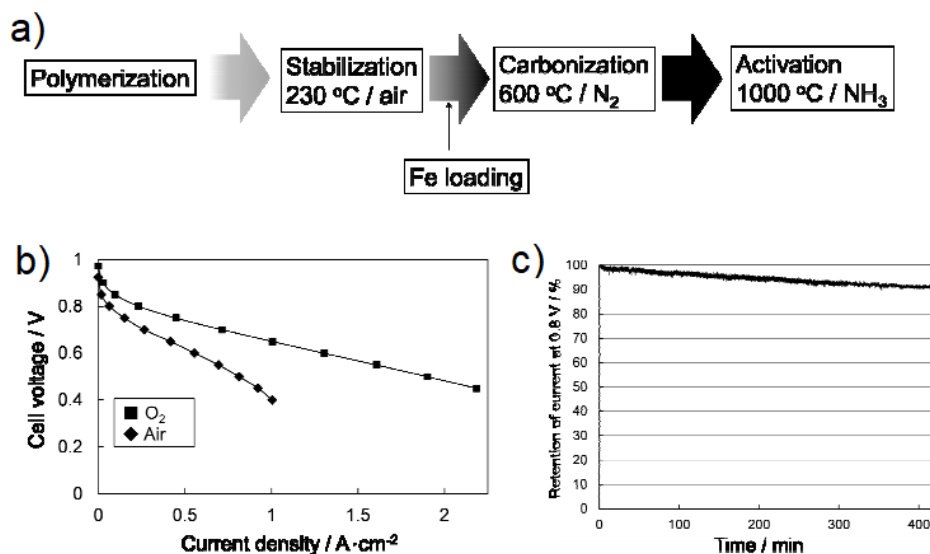


Figure 39: Diagram of the synthesis of a stabilized PAN based ORR catalyst (a), PEMFC polarization curve under O₂ and air (b) and retention of initial current density at 0.8 V (c), PEMFC experiment conditions: cathode loading 3.3 mg cm⁻², anode loading 0.2 mg_{Pt} cm⁻², H₂ and air 0.2 MPa, cell temperature 80 °C and Nafion® NR211 membrane [143].

PAN has also widely been used for the preparation of electrospun catalysts [359, 374, 375, 379, 404]. By electrospinning, the PAN precursor can be fabricated into fibers of several 100 nm size. From these fibers highly porous electrodes can be obtained, thus allowing for excellent mass transport properties inside the catalyst layer. Wu et al. prepared such a catalyst by electrospinning PAN, Fe(Ac)₂ in DMF [379]. The fibers were stabilized in air at 250 °C for 3 hours. Following the catalyst was obtained after performing a heat treatment, acid leaching and a second heat treatment. An Fe-S/N doped electrospun catalyst was reported by Guo et al. [359]. First, a wet impregnated mixture of PAN, melamine and FeCl₃ was fabricated into fibers by electrospinning. Sulphur was added in the form of thiophene, which was coated on top of the fibers by photopolymerization. The final catalyst was obtained after stabilization in air and a heat treatment under inert gas at 700 - 1000 °C. In general, the mass transport properties of electrospun catalysts are excellent due to the macroporous fiber network. However, the micropore content is usually quite low because a highly graphitized material is formed. Shui et al. developed a synthesis approach based on electrospinning where both macro and micropores are present in the final catalyst [138]. The precursor mixture that was electrospun contained PAN, poly

methyl methacrylate, ball-milled ZIF-8 and 1,10-phenanthroline iron(II) perchlorate. The electrospun fibers were first heat treated in Ar and NH₃, acid leached and heat treated again in NH₃. A remarkably high peak power density of $\sim 0.9 \text{ W cm}^{-2}$ (PEMFC, H₂-O₂, 2 bar, cathode 3 mg cm⁻², 80 °C, N211) was reported.

Other non-conducting polymers are reported in **Table 9**. For instance, Li et al. reported a straightforward method where a poly-ethylenediamine coated carbon black doped with Co and Fe transition salts is used. The precursors ethylenediamine, Co(NO₃)₂, FeSO₄ and carbon black are simply refluxed at 85 °C for 4 h [384]. The mixture is dried and the standard two heat treatments with intermediate acid leaching are performed. During RRDE experiments an onset potential for the ORR of 0.88 V and 0.92 V was measured for acidic respectively alkaline conditions. Najam et al. prepared a poly-diamine-pyridine-based catalyst containing no additional transition metal source but a phosphor source, namely phytic acid [366]. This P,N co-doped catalyst showed superior stability against small poisoning molecules such as SO_x, NO_x and PO_x.

The Carbon Precursor

The carbon phase of Me-N-C catalysts fulfils several tasks. Most importantly, it hosts the MeN₄ active sites. Therefore, a correlation between microporosity or disorder in the carbon support with ORR activity is often found [326]. Further, the carbon phase provides electrical conductivity. Considering this matter highly graphitized phases become beneficial. Since carbon is the main element of which Me-N-C catalysts comprise of, the carbon structure is also defining the mass transport properties of the catalyst layer. Carbons which are capable of forming hierarchical macroporous networks are necessary for high fuel cell performances.

Several studies on the influence of the carbon support on a carbon black, iron salt mixture heat treated in NH₃ have been published [211, 225, 405-408]. It has been found that the higher the surface nitrogen content of the final catalyst the higher its ORR activity. The final surface nitrogen content correlates with a mass loss during the NH₃ treatment and the disordered phase of the initial carbon black. Meaning pristine carbon blacks containing high amount of disordered carbon phases showed the best ORR activities. According to Charretre et al. the amount of disordered carbon phase can be monitored from the width at half maximum of the D peak in the Raman spectrum [407, 408]. Further, it has been reported that the catalytic activity increases with a decreasing particle size of the carbon black. Rietveld analysis of the XRD spectra of the pristine carbon blacks further showed a positive correlation of ORR activity and the size of the graphitic crystallites inside the carbon particle, giving hint to a FeN₂₊₂/C bridging structure of the active side for these catalysts.

Likewise, when concerning stability, the carbon support has a big impact. In general, it is reported that carbons with low microporosity and high degree of graphitization are favorable [27, 405, 409]. Wu et al. polymerized PANI in the presence of different carbon supports and an iron source [27, 409]. Following the standard procedure of two heat treatments and an intermediate acid leaching the catalyst based on multi-walled carbon nanotubes (PANI-Fe-MWCNTs) showed 500 hours of stable fuel cell performance. A comparison of ORR activity, selectivity and stability of the MWCNTs supported catalyst with catalyst prepared according to the same method but with varying carbon blacks is given in Figure 40.

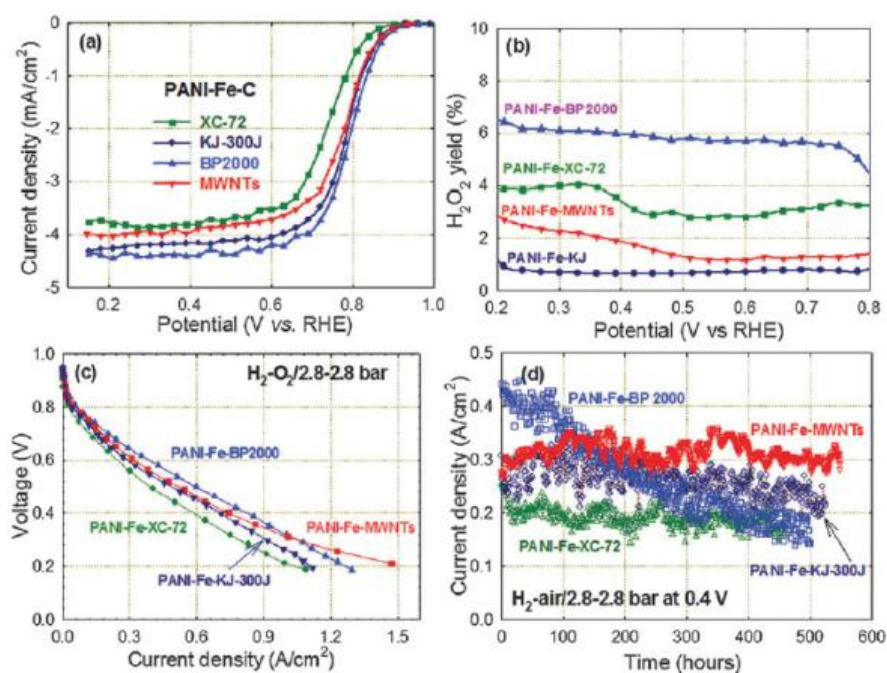


Figure 40: PANI-Fe-C catalysts prepared with different carbon supports, comparison of RRDE activity (a), RRDE selectivity (b), fuel cell activity (c) and fuel cell stability (d) [409].

Wu et al. attributed the enhanced stability of their PANI-Fe-MWCNT catalyst not only to the higher corrosion resistance of the graphitized carbon of the MWCNTs but also to an increased mass transfer which goes along with a better water removal. Enhanced mass transport properties were also reported by Larouche et al., here a ZIF-8, phen and Fe(Ac)₂ based catalyst was mixed with different amounts of carbon fibers [410]. It was found that for both H₂-air and H₂-O₂ fuel cell conditions the performance at 0.6 V was enhanced about 35 % due to a better mass transport. For fibers with a diameter of 150 nm an optimum content of 26 wt% carbon fibers in the precursor mixture was reported.

Byon et al. reported a synthesis method based on reduced graphene oxide (rGO) [411]. FeN_xC_y-moieties were introduced by pyrolysis rGO in the presence of a Fe-salt and graphitic carbon nitride (g-C₃N₄). During RDE tests this Fe-N-rGO catalyst showed 8 times higher ORR mass activity at 0.75 V in comparison to catalysts prepared with carbon black and oxidized carbon black.

Another important discovery about the behavior of different carbon phases was made by Chung et al. [412]. It was reported that carbon, which originates from the pyrolysis of an organic nitrogen precursors (ONPs), has significant different properties considering ORR activity and stability than a carbon phases originating from a carbon black support. Chung et al. prepared two catalysts where pyrrole was polymerized with APS in the presence of an oxidized carbon black and $\text{Co}(\text{NO}_3)_2$. The first catalyst was synthesized in this manner that the carbon support was added after the polymerization of the pyrrole (sequence A). For the second one the carbon support was added before the polymerization started (sequence B). Hence for the catalyst prepared according to sequence A two different carbon phases are exposed at the catalyst's surface, namely carbon black support and carbon originated from PPy. Whereas for the catalyst according to sequence B only carbon originated from PPy is present at the surface. It was found that the carbon from PPy shows less ORR activity but much higher stability during fuel cell testing. This behavior is illustrated in **Figure 41**.

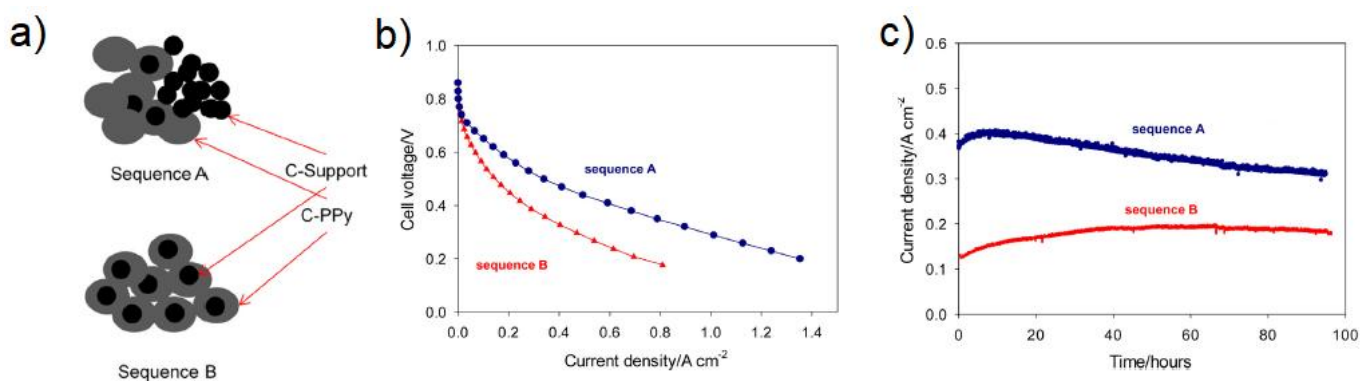


Figure 41: Co-PPy-C catalysts prepared following two different sequences resulting in different surface exposed carbon phases (a) and the respective fuel cell polarization curve and stability tests [412].

6 Experimental Part

In this chapter all experimental details are specified. An overview of the numerous catalysts which were prepared in this work is provided in **Table 10** and a summary of the performed fuel cell tests with cathode catalyst loadings is shown in **Table 11**.

Functionalization of MWCNTs

As described by Kübler et al., "4-Aminopyridine (98%, Alfa Aesar), 5-amino-1H-indazole (98%, Alfa Aesar) and sodium nitrite (98%, Carl Roth) were used for the functionalization step. In 20 ml of deionized water 0.765 g of 5-amino-1H-indazole were dissolved together with 0.5 g of sodium nitrite. The solution temperature was adjusted and kept at 0°C through an ice bath cooling over the whole reaction time. 15 ml of conc. HCl was added slowly. Afterwards, a cooled dispersion of 50 mg cleaned Nanocyll™ 7000 in 50 ml deionized water was added. The solution was kept at 0°C for 20 hours. The final product was obtained after filtering, washing with acetone and water mixture (1:1) until the filtrate was colorless and dried at 80°C in air. A resulting yield around 55 mg was obtained." [413].

Synthesis of CNT-based catalysts

As described by Kübler et al., "For the synthesis of the FeNC catalysts, Fe(Ac)₂ anhydr. (min 29.5% Fe, Alfa Aesar) and 1,10-Phenanthroline (99%, Alfa Aesar) and sulphur (99,5%, Carl Roth) were used. Therefore, 200 mg of MWCNTs (or 200 mg of functionalized MWCNTs) were mixed with 95 mg Fe(Ac)₂, 255 mg 1,10-Phenanthroline and 3 mg of sulphur in a mortar. The mixture was then dispersed in 5 ml EtOH for 20 minutes and subsequently dried at 80°C in air. The dried powder was grinded again in the mortar and transferred into quartz glass boats which were placed in a quartz glass tube of a furnace (CarboLite® HZS/12/900). Afterwards, the sample was heated with 300°C h⁻¹ under N₂, first up to 300 °C then 500 °C where the temperature was hold for 30 minutes, each. The final temperature was 800°C, where the material was dwelled for 60 minutes. The acid leaching step was performed after the oven was cooled down to a temperature below 80 °C in 200 ml 2 M HCl for 2 hours while sonicating and bubbling N₂ through the mixture. The catalyst was filtered, washed with H₂O and dried. The powder then underwent a second heat treatment to heal the effects of the acid leaching by heating it under N₂ atmosphere to 700 °C for 60 min, again applying a heating rate of 300 °C h⁻¹. For the preparation of FeNCind-mix 190 mg of MWCNTs mixed with 10 mg of 5-amino-1H-indazole was used." [413].

Synthesis of Polypyrrole and Doped Polypyrroles

First, 3.6 ml of pyrrole (98 %, Alfa Aesar) monomer was dispersed in 500 ml of water. For the synthesis of doped polypyrroles 2.475 mmol of doping agent (methyl orange, Chromotrope© 2R,

Napthalenedisulfonic acid, aminobenzoic acid, sulfanilic acid or toluenesulfonic acid) was added additionally. To this monomer mixture 8.1 g of FeCl₃ dissolved in 500 ml of a water was added slowly. The reaction mixture was kept at 0 °C for about 24 hours and then filtered. For the samples denoted as C-GPPy, C-PPy_{40x} and C-GPPy_{MixMO}, 40 additional washing steps were applied. C-PPy_{5x} was washed 5 times. One washing step is defined as dispersing the sample in 500 ml of a 1:1 mixture of water and acetone for 30 min followed by filtration. No further washing step were applied for all other samples. The samples were dried at 75 °C under air. Some preparations of polypyrrole were assisted by Janik Scharf, Pascal Theis and Niels Kubitzka as part of their research assistant job or student related lab work. For the validation of the reproducibility of the preparation, Vladislav Gridin prepared polypyrrole for the catalyst VGC21, which is discussed in the appendix.

Synthesis of Polypyrrole-Based Catalysts

Typically, 300 mg of doped or undoped polypyrrole precursor were mortared together with the transition metal source in a hand mortar. The specific type and amount of transition metal for each catalyst is given in **Table 10**. For the preparation of C-GPPy_{MixMO}, 270 mg of undoped polypyrrole plus 30 mg of methyl orange were used. The resulting powder was collected and dispersed in 25 ml of a 1:1 mixture of ethanol and water for 20 min. After evaporation of the solvents (air, 70 °C), the powders were mortared again and transferred into a heating furnace (CarboLite® HZS/12/900). For the best performing catalyst, which is presented in chapter 8.8, the precursors were not wet impregnated but mixed using a ball mill (Retsch MM 400, stainless steel, 10 min, 30 Hz). The precursor was then heated under N₂ atmosphere with a heating rate of 300 °C h⁻¹. If not stated otherwise in **Table 10**, the final temperature of 800 °C was held for 1 hour. After cooling to room temperature, the samples were transferred into 2 M HCl. About 200 ml of 2 M HCl or 150 ml of 2 M HCl and 50 ml isopropanol was used. The acid leaching was performed by sonicating the sample for 1 hour or 2 - 2.5 hours at 50 °C and N₂ bubbling. The samples were kept at room temperature overnight in acid without sonication. Finally, the catalyst was filtered and washed with water. A second heat treatment was performed for some of the samples. Therefore, the powder was transferred again into the heating furnace. The second heat treatment was performed under N₂ gas. More details about heating rate and final temperature are given in **Table 10**. Some preparations of the polypyrrole-based catalysts were assisted by Janik Scharf, Pascal Theis and Niels Kubitzka as part of their research assistant job or student related lab work. For the validation of the reproducibility of the preparation, Vladislav Gridin prepared the catalyst VGC21, which is discussed in the appendix.

Table 10: Overview of all catalysts which were investigated within this thesis.

Catalyst and Chapter	Type	Precursor 1	Precursors 2	First Heat Treatment	Acid Leaching	Second Heat Treatment	Internal denotation
FeNC Chapter 7 Table 12	CNT	Nanocyll7000™	Phen, Fe(Ac) ₂ , S	300 °C h ⁻¹ to 300 °C 30 min; 300 °C h ⁻¹ to 500 °C 30 min; 300 °C h ⁻¹ to 800 °C 60 min	200 ml 2 M HCl for 2 hours	300 °C h ⁻¹ to 700 °C 60 min	MK94
FeNC _{ind-mix} Chapter 7 Table 12	CNT	Nanocyll7000™	Phen, Fe(Ac) ₂ , S, amino-indazole	300 °C h ⁻¹ to 300 °C 30 min; 300 °C h ⁻¹ to 500 °C 30 min; 300 °C h ⁻¹ to 800 °C 60 min	200 ml 2 M HCl for 2 hours	300 °C h ⁻¹ to 700 °C 60 min	MK110
FeNC _{pyr} Chapter 7 Table 12	CNT-Pyridine	Nanocyll7000™ functionalized with pyridine	Phen, Fe(Ac) ₂ , S,	300 °C h ⁻¹ to 300 °C 30 min; 300 °C h ⁻¹ to 500 °C 30 min; 300 °C h ⁻¹ to 800 °C 60 min	200 ml 2 M HCl for 2 hours	300 °C h ⁻¹ to 700 °C 60 min	MK93
FeNC _{ind} Chapter 7 Table 12	CNT-Indazole	Nanocyll7000™ functionalized with indazole	Phen, Fe(Ac) ₂ , S,	300 °C h ⁻¹ to 300 °C 30 min; 300 °C h ⁻¹ to 500 °C 30 min; 300 °C h ⁻¹ to 800 °C 60 min	200 ml 2 M HCl for 2 hours	300 °C h ⁻¹ to 700 °C 60 min	MK77
C-GPPy Chapter 8.2 Table 13	Polypyrrole washed 40x	polypyrrole 300 mg	FeCl ₃ 300 mg, Fe(NO ₃) ₃ x 9 H ₂ O 375 mg	300 °C h ⁻¹ to 800 °C 60 min	200 ml 2 M HCl for 1 hours	-	MK212
C-GPPy _{MnO} Chapter 8.2 Table 13	Polypyrrole washed 40x	polypyrrole 270 mg, methyl orange 30 mg	FeCl ₃ 300 mg, Fe(NO ₃) ₃ x 9 H ₂ O 375 mg	300 °C h ⁻¹ to 800 °C 60 min	200 ml 2 M HCl for 1 hours	-	MK234
C-PPy _{40x} Chapter 8.2 Table 13	Polypyrrole-methyl orange washed 40x	polypyrrole 300 mg	FeCl ₃ 300 mg, Fe(NO ₃) ₃ x 9 H ₂ O 375 mg	300 °C h ⁻¹ to 800 °C 60 min	200 ml 2 M HCl for 1 hours	-	PPN43
C-PPy _{5x} Chapter 8.2 Table 13	Polypyrrole-methyl orange washed 5x	polypyrrole 300 mg	FeCl ₃ 300 mg, Fe(NO ₃) ₃ x 9 H ₂ O 375 mg	300 °C h ⁻¹ to 800 °C 60 min	200 ml 2 M HCl for 1 hours	-	PPN41
C-PPy _{0x} Chapter 8.2 Table 13	Polypyrrole-methyl orange	polypyrrole 300 mg	FeCl ₃ 300 mg, Fe(NO ₃) ₃ x 9 H ₂ O 375 mg	300 °C h ⁻¹ to 800 °C 60 min	200 ml 2 M HCl for 1 hours	-	PPN38
C-2ht-PPy _{0x+} Chapter 8.2 Table 13	Polypyrrole-methyl orange	polypyrrole 300 mg	FeCl ₃ 300 mg, Fe(NO ₃) ₃ x 9 H ₂ O 375 mg	300 °C h ⁻¹ to 800 °C 60 min	200 ml 2 M HCl for 2 hours	450 °C h ⁻¹ to 800 °C 45 min	MK200
C-PPy _{Fe(Ox)} Chapter 8.3 Table 16	Polypyrrole-methyl orange washed 40x	polypyrrole 350 mg	Fe(C ₂ O ₄) x 2 H ₂ O 387 mg	300 °C h ⁻¹ to 800 °C 60 min	230 ml 2 M HCl for 2 hours	-	PPN68
C-PPy _{Fe(Ac)2} Chapter 8.3 Table 16	Polypyrrole-methyl orange washed 40x	polypyrrole 350 mg	Fe(CH ₃ COO) ₂ 374 mg	300 °C h ⁻¹ to 800 °C 60 min	230 ml 2 M HCl for 2 hours	-	PPN67
C-PPy _{Fe(NO3)3} Chapter 8.3 Table 16	Polypyrrole-methyl orange washed 40x	polypyrrole 350 mg	Fe(NO ₃) ₃ x 9 H ₂ O 871 mg	300 °C h ⁻¹ to 800 °C 60 min	230 ml 2 M HCl for 2 hours	-	PPN63
C-PPy _{FeCl3} Chapter 8.3 Table 16	Polypyrrole-methyl orange washed 40x	polypyrrole 350 mg	FeCl ₃ 350 mg	300 °C h ⁻¹ to 800 °C 60 min	230 ml 2 M HCl for 2 hours	-	PPN65
C-PPy _{FeCl2} Chapter 8.3 Table 16	Polypyrrole-methyl orange washed 40x	polypyrrole 350 mg	FeCl ₂ x 6 H ₂ O 506 mg	300 °C h ⁻¹ to 800 °C 60 min	230 ml 2 M HCl for 2 hours	-	PPN64
C-PPy _{FeCl3/Fe(NO3)3} Chapter 8.3 Table 16	Polypyrrole-methyl orange washed 40x	polypyrrole 350 mg	FeCl ₃ 233 mg, Fe(NO ₃) ₃ x 9 H ₂ O 292 mg	300 °C h ⁻¹ to 800 °C 60 min	230 ml 2 M HCl for 2 hours	-	PPN66
C-2ht-PPy _{FeCl3} Chapter 8.3 Table 17	Polypyrrole-methyl orange	polypyrrole 350 mg	FeCl ₃ 350 mg	300 °C h ⁻¹ to 800 °C 60 min	230 ml 2 M HCl for 2 hours	450 °C h ⁻¹ to 800 °C 45 min	PPN70
C-2ht-PPy _{FeCl3/Fe(NO3)3} Chapter 8.3 Table 17	Polypyrrole-methyl orange	polypyrrole 350 mg	FeCl ₃ 233 mg, Fe(NO ₃) ₃ x 9 H ₂ O 292 mg	300 °C h ⁻¹ to 800 °C 60 min	230 ml 2 M HCl for 2 hours	450 °C h ⁻¹ to 800 °C 45 min	PPN71/ PPN66b
C-2ht-PPy _{FeCl2} Chapter 8.3 Table 17	Polypyrrole-methyl orange	polypyrrole 350 mg	FeCl ₂ x 6 H ₂ O 506 mg	300 °C h ⁻¹ to 800 °C 60 min	230 ml 2 M HCl for 2 hours	450 °C h ⁻¹ to 800 °C 45 min	PPN64_2
C-2ht-PPy _{+FeCl2} Chapter 8.3 Table 17	Polypyrrole-methyl orange	polypyrrole 350 mg	FeCl ₂ x 6 H ₂ O 700 mg	300 °C h ⁻¹ to 800 °C 60 min	230 ml 2 M HCl for 2 hours	450 °C h ⁻¹ to 800 °C 45 min	PPN74
C-2ht-PPy _{++FeCl2} Chapter 8.3 Table 17	Polypyrrole-methyl orange	polypyrrole 350 mg	FeCl ₂ x 6 H ₂ O 850 mg	300 °C h ⁻¹ to 800 °C 60 min	230 ml 2 M HCl for 2 hours	450 °C h ⁻¹ to 800 °C 45 min	PPN73
C-2ht-PPy _{+FeCl3/+Fe(NO3)3} Chapter 8.3 Table 17	Polypyrrole-methyl orange	polypyrrole 350 mg	FeCl ₃ 350 mg, Fe(NO ₃) ₃ x 9 H ₂ O 437 mg	300 °C h ⁻¹ to 800 °C 60 min	230 ml 2 M HCl for 2 hours	450 °C h ⁻¹ to 800 °C 45 min	MK200
C-PPy _{FeCl3} 2 Chapter 8.4 Table 19	Polypyrrole-methyl orange washed 40x	polypyrrole 350 mg	FeCl ₃ 350 mg	300 °C h ⁻¹ to 800 °C 60 min	230 ml 2 M HCl for 2 hours	-	PPN60
C-PPy _{KMnO4} Chapter 8.4 Table 19	Polypyrrole-methyl orange washed 40x	polypyrrole 350 mg	KMnO ₄ 341 mg	300 °C h ⁻¹ to 800 °C 60 min	230 ml 2 M HCl for 2 hours	-	PPN61
C-PPy _{Mn(Ac)2} Chapter 8.4 Table 19	Polypyrrole-methyl orange washed 40x	polypyrrole 350 mg	Mn(CH ₃ COO) ₂ 372 mg	300 °C h ⁻¹ to 800 °C 60 min	230 ml 2 M HCl for 2 hours	-	PPN62
C-PPy _{FeCl3/Mn(Ac)2} Chapter 8.4	Polypyrrole-methyl orange washed 40x	polypyrrole 350 mg	FeCl ₃ 350 mg, Mn(CH ₃ COO) ₂	300 °C h ⁻¹ to 800 °C 60 min	230 ml 2 M HCl for 2 hours	-	PPN59

Table 19			372 mg				
C-PPy_{FeCl₃/KMnO₄} Chapter 8.4 Table 19	Polypyrrole-methyl orange washed 40x	polypyrrole 350 mg	FeCl ₃ 350 mg KMnO ₄ 341 mg	300 °C h ⁻¹ to 800 °C 60 min	230 ml 2 M HCl for 2 hours	-	PPN58
C-2ht-PPy_{FeCl₃/KMnO₄} Chapter 8.4 Table 19	Polypyrrole-methyl orange	polypyrrole 350 mg	FeCl ₃ 350 mg KMnO ₄ 341 mg	300 °C h ⁻¹ to 800 °C 60 min	230 ml 2 M HCl for 2 hours	300 °C h ⁻¹ to 800 °C 45 min	MK204
C-PPy_{FeCl₃-KMnO₄} Chapter 8.4 Table 19	Polypyrrole-methyl orange	polypyrrole 350 mg	FeCl ₃ 590 mg KMnO ₄ 176 mg	300 °C h ⁻¹ to 800 °C 60 min	230 ml 2 M HCl for 2 hours	-	MK207_1
C-2ht-PPy_{FeCl₃-KMnO₄} Chapter 8.5 Table 20	Polypyrrole-methyl orange	polypyrrole 350 mg	FeCl ₃ 590 mg KMnO ₄ 176 mg	300 °C h ⁻¹ to 800 °C 60 min	230 ml 2 M HCl for 2 hours	300 °C h ⁻¹ to 800 °C 45 min	MK207_2
C-2htm-PPy_{FeCl₃-KMnO₄} Chapter 8.5 Table 20	Polypyrrole-methyl orange	polypyrrole 350 mg	FeCl ₃ 590 mg KMnO ₄ 176 mg	300 °C h ⁻¹ to 800 °C 60 min	230 ml 2 M HCl for 2 hours	800 °C h ⁻¹ to 800 °C 15 min	MK207_3
C-2hts-PPy_{FeCl₃-KMnO₄} Chapter 8.5 Table 20	Polypyrrole-methyl orange	polypyrrole 350 mg	FeCl ₃ 590 mg KMnO ₄ 176 mg	300 °C h ⁻¹ to 800 °C 60 min	230 ml 2 M HCl for 2 hours	1000 °C h ⁻¹ to 800 °C 1 min	MK216
C-2htm-PPy_{FeCl₃-KMnO₄_1000} Chapter 8.5 Table 21	Polypyrrole-methyl orange	polypyrrole 350 mg	FeCl ₃ 590 mg KMnO ₄ 176 mg	300 °C h ⁻¹ to 1000 °C 60 min	230 ml 2 M HCl for 2 hours	800 °C h ⁻¹ to 800 °C 15 min	MK240
C-PPy-1000 Chapter 8.6 Table 22	Polypyrrole-methyl orange	polypyrrole 350 mg	FeCl ₃ 590 mg KMnO ₄ 176 mg	300 °C h ⁻¹ to 1000 °C 60 min	230 ml 2 M HCl for 2 hours	800 °C h ⁻¹ to 800 °C 15 min	MK240
C-PPy-1000-IsoAL Chapter 8.6 Table 22	Polypyrrole-methyl orange	polypyrrole 350 mg	FeCl ₃ 590 mg KMnO ₄ 176 mg	300 °C h ⁻¹ to 1000 °C 60 min	175 ml 2 M HCl, 60 ml isopropanol for 2 hours	800 °C h ⁻¹ to 800 °C 15 min	MK248
C-PPy-MO Chapter 8.7 Table 23	Polypyrrole-methyl orange	polypyrrole 350 mg	FeCl ₃ 590 mg KMnO ₄ 176 mg	300 °C h ⁻¹ to 1000 °C 60 min	175 ml 2 M HCl, 60 ml isopropanol for 2 hours	800 °C h ⁻¹ to 800 °C 15 min	MK248/JS3
C-PPy-SA Chapter 8.7 Table 23	Polypyrrole-sulfanilic acid	polypyrrole 350 mg	FeCl ₃ 590 mg KMnO ₄ 176 mg	300 °C h ⁻¹ to 1000 °C 60 min	175 ml 2 M HCl, 60 ml isopropanol for 2 hours	800 °C h ⁻¹ to 800 °C 15 min	MK257/NK4
C-PPy-TSA Chapter 8.7 Table 23	Polypyrrole-toluene sulfonic acid	polypyrrole 350 mg	FeCl ₃ 590 mg KMnO ₄ 176 mg	300 °C h ⁻¹ to 1000 °C 60 min	175 ml 2 M HCl, 60 ml isopropanol for 2 hours	800 °C h ⁻¹ to 800 °C 15 min	NK5
C-PPy-ABA Chapter 8.7 Table 23	Polypyrrole-amino benzoic acid	polypyrrole 350 mg	FeCl ₃ 590 mg KMnO ₄ 176 mg	300°C/h to 1000°C 60 min	175 ml 2 M HCl, 60 ml isopropanol for 2 hours	800 °C h ⁻¹ to 800 °C 15 min	MK258
C-PPy-NDSA Chapter 8.7 Table 23	Polypyrrole-napthalene disulfonic acid	polypyrrole 350 mg	FeCl ₃ 590 mg KMnO ₄ 176 mg	300 °C h ⁻¹ to 1000 °C 60 min	175 ml 2 M HCl, 60 ml isopropanol for 2 hours	800 °C h ⁻¹ to 800 °C 15 min	NK8
C-PPy-CT2R Chapter 8.7 Table 23	Polypyrrole-Chromotrop2R®	polypyrrole 350 mg	FeCl ₃ 590 mg KMnO ₄ 176 mg	300 °C h ⁻¹ to 1000 °C 60 min	175 ml 2 M HCl, 60 ml isopropanol for 2 hours	800 °C h ⁻¹ to 800 °C 15 min	MK259
Cat A Chapter 8.8	Polypyrrole-methyl orange	polypyrrole 350 mg	FeCl ₃ 350 mg, Fe(NO ₃) ₃ x 9 H ₂ O 437 mg	300 °C h ⁻¹ to 800 °C 60 min	230 ml 2 M HCl for 2 hours	450 °C h ⁻¹ to 800 °C 45 min	MK200
Cat B Chapter 8.8	Polypyrrole-methyl orange	polypyrrole 350 mg	FeCl ₃ 590 mg KMnO ₄ 176 mg	300 °C h ⁻¹ to 800 °C 60 min	230 ml 2 M HCl for 2 hours	300 °C h ⁻¹ to 800 °C 45 min	MK207_2
Cat C Chapter 8.8	Polypyrrole-methyl orange	polypyrrole 350 mg	FeCl ₃ 590 mg KMnO ₄ 176 mg	300 °C h ⁻¹ to 1000 °C 60 min	230 ml 2 M HCl for 2 hours	800 °C h ⁻¹ to 800 °C 15 min	MK240
Cat D Chapter 8.8	Polypyrrole-methyl orange	polypyrrole 350 mg	FeCl ₃ 590 mg KMnO ₄ 176 mg	300 °C h ⁻¹ to 1000 °C 60 min	175 ml 2 M HCl, 60 ml isopropanol for 2 hours	800 °C h ⁻¹ to 800 °C 15 min	MK248 / JS3
Cat E Chapter 8.8	Polypyrrole-sulfanilic acid	polypyrrole 350 mg	FeCl ₃ 590 mg KMnO ₄ 176 mg	300 °C h ⁻¹ to 1000 °C 60 min	175 ml 2 M HCl, 60 ml isopropanol for 2 hours	800 °C h ⁻¹ to 800 °C 15 min	NK3 precursors were ball milled

Transmission Electron Microscopy (TEM)

The TEM pictures were recorded with a FEI-Philips CM20 device. The acceleration was set to 120 kV. A LaB₆ electrode was used. Samples were prepared by dispersing them in ethanol and pipetting about 2 - 5 μ l onto a conventional copper TEM grid with carbon film, S147-4 PlanoTM.

Brunauer-Emmett-Teller (BET) Surface Area

N₂ adsorption and desorption isotherms were recorded to determine the specific surface area of the catalysts (Device: Autosorb-3B, Quantochrome, Boynton Beach, FL, USA). The software to analyze the obtained data was provided by Quantochrome. Degassing the samples (~40 mg) was carried out at 200 °C under vacuum for about 18 hours. The BET measurements were mostly conducted by Stephen Paul and David Wallace.

Raman Spectroscopy

The catalyst samples for Raman measurements were prepared by pipetting 5 μ l of the respective inks onto a silica wafer and were left to dry at room temperature. Raman spectra were obtained at room temperature with an alpha 300R confocal Raman microscope from WiTec (Ulm, Germany) with a grid of 600 lines mm⁻¹ using an excitation laser (532.2 nm) with a laser power of 1 mW. The range of the measured spectra spreads from 0 to 4000 cm⁻¹. The spectra were recorded by performing 10 scans, each with integration time of 10 s. For each catalyst sample, spectra were recorded at three different locations and normalized with respect to the G band maximum intensity. The mean intensity of these spectra was taken and used for the fitting. The bands can be assigned as G band (1580 cm⁻¹), D band (1360 cm⁻¹), D2 band (1615 cm⁻¹), D3 band (1500 cm⁻¹) and D4 band (1200 cm⁻¹). Raman spectroscopy was conducted by David Wallace and Lingmei Ni. Data fitting was performed by David Wallace.

⁵⁷Fe-Mössbauer Spectroscopy (MS)

As described by Kübler et al. "*Mössbauer spectra were recorded in constant acceleration mode with a ⁵⁷Co/Rh source at room temperature. All samples were measured without isotopic enrichment, typically 80 – 100 mg were used and measured about 3-4 days. The measurements were performed in transmission mode within a velocity range of ± 10 mm s⁻¹, calibration of the velocity axis was made with respect to α -Fe. The spectra resolution is given by the 1024 multichannel analyzer, resulting in 512 points and the chosen velocity, leading to a step size of 0.08 mm s⁻¹. The program Recoil was used for fitting the spectra.*" [413]. The Mössbauer spectra within this work were recorded and fitted by Lingmei Ni and Stephan Wagner.

Differential Electrochemical Mass Spectrometry (DEMS)

As described by Kübler et al. "*A differential electrochemical mass spectrometry (DEMS) setup comprises of an electrochemical half-cell which is connected to a mass spectrometer (MS). The custom made cell and the rest of the setup is described in detail elsewhere [414]. In short, the investigated catalyst material is spray*

coated on a gas diffusion layer (see experimental part fuel cell) which serves as working electrode. The applied catalyst loading was 1.4 mg cm^{-2} for $\text{FeNC}_{\text{ind-mix}}$, 2.3 mg cm^{-2} for CB-FeNC and 2.2 mg cm^{-2} for the Pt/C catalyst (60 wt% Pt, Tanaka), with PTFE contents in the ink of 35 wt%. The working electrode is covered by a Nafion™ Membrane (N117 Quintech GmbH), a 4 M H_2SO_4 reservoir on top connects a reference HydroFlex® (Gaskatel GmbH) and Pt-wire as counter electrode. N_2 gas is supplied below the working electrode with a flow rate of 50 ml min^{-1} . The mass spectrometer is set to monitor the signal of $m/z = 44$, which refers to CO_2 . The used potentiostat was a Reference 600 from Gamry Instruments and the mass spectrometer Prisma™ was purchased from Pfeiffer Vacuum GmbH. Linear sweep voltammetry was performed from 0.05 to 1.4 V with a scan rate of 10 mV s^{-1} at 23 °C and 60 °C, respectively." [413]. The DEMS experiments were conducted at the Fraunhofer Institute for Chemical Technology (ICT) at the faculty of Applied Electrochemistry (AE) by the author of this work.

Rotating Ring Disc Electrode (RRDE) Measurements

As described by Kübler et al. "RRDE measurements were performed using a MSR rotator, an OD PEEK shaft (AFE6MB, Pine Research) and a glassy carbon disk platinum ring disc electrode (AFE6R2GCPT, Pine Research) as working electrode. In order to avoid Pt impurities a glassy carbon rod was used as counter electrode. A standard Ag/AgCl (C3 Prozess und Analysetechnik GmbH) was used as the reference electrode. All potentials in this work are given versus the reversible hydrogen electrode (RHE), measured with a Hydroflex® (Gaskatel GmbH). The used potentiostat was a Parstat3000A (AMETEK). VersaStudio software (Princeton Applied Research) was used to record the experiments. CV and RRDE measurements were made in 0.1 M H_2SO_4 at room temperature. For the ink, 5 mg of catalyst is dispersed in $142 \mu\text{l H}_2\text{O}$, $83 \mu\text{l}$ isopropanol and $25 \mu\text{l}$ Nafion™ solution (Quintech GmbH, PFSA 5 wt%) for 45 minutes (ice-cooled Emmi®-H120, EMAG AG ultrasonic bath, 50 Watt). The catalyst loading on the working electrode was set to 0.8 mg cm^{-2} . Ten voltammetric cycles under N_2 saturated electrolyte were performed from 1.2 V to 0 V with a scan rate of 100 mV s^{-1} followed by two cycles with 10 mV s^{-1} in the same potential range. The ORR activity was investigated by performing cyclic voltammetry in the mentioned potential window with a sweep rate of 10 mV s^{-1} and applying different rotation rates for each cycle (0, 200, 400, 900, 1500 rpm). Simultaneously the ring current was traced at a constant potential of 1.2 V. The hydrogen peroxide amount and electrode transfer number n_e were determined from the ring and disc currents according to:

$$n = \frac{4I_d}{I_d + I_r/N} \quad (4)$$

$$\%H_2O_2 = \frac{2I_r/N}{I_d + I_r/N} \quad (5)$$

Where N is the collection efficiency of the ring 0.38, I_r is the measured ring current and I_d is the measured disc current." [413]. The catalyst loading of all CNT based catalysts was 0.8 mg cm^{-2} and 0.5 mg cm^{-2} for all other samples in this work. All RRDE experiments in this work were conducted twice. The error bars are included in the displayed figures.

RRDE Durability Measurements for CNT Catalysts

As described by Kübler et al. "Durability measurements were carried out in N_2 saturated electrolyte. The same potential window was applied, and 10,000 cycles with a scan rate of 500 mV s^{-1} were performed. Each durability cycle needs therefore 2.4 seconds and in total the 10,000 cycles require 6.6 hours. Activity and selectivity, as well as cyclic voltammetry were measured at the beginning of test (B.o.T.) and End of Life (E.o.T.)." [413].

Electrode and Membrane Electrode Assembly (MEA) Preparation

For the anode ink, 80 mg of Pt/C Elyst Pt20 0390 (Umicore NV/SA) was dispersed in 0.8 ml H_2O , 0.8 ml Nafion™ (PFSA 5 wt%) and 1.6 ml isopropanol. The CNT based cathode was prepared from an ink formulation according to; 42.5 mg catalyst powder dispersed in 1 ml isopropanol, 0.5 ml Nafion™ (PFSA 5 wt%) and 0.13 ml H_2O . The polypyrrole catalysts were worked up by dispersing 80 mg catalyst powder in 0.97 ml Nafion™ (PFSA 5 wt%), 1.05 ml isopropanol and 0.185 ml H_2O . All inks were dispersed for one hour in an ultrasonic bath. Following, the inks were sprayed on a gas diffusion layer (GDL, Freudenberg SE H23C9 purchased from Quintech GmbH) and hand-cut to obtain an area of 4.84 cm^2 . The specific loading of each electrode was obtained after weighing the dry GDL before and after spraying. MEAs were obtained after hot-pressing the electrodes together with a Nafion N212 membrane (Quintech GmbH) at 125°C for 2 minutes and pressure of 2 kN. The spraying process was assisted by Janik Scharf, Pascal Theis and Niels Kubitza as part of their research assistant job or student related lab work. For the validation of the reproducibility of the preparation, Vladislav Gridin prepared the MEA of the VGC21 catalyst, which is discussed in the appendix.

Fuel Cell Testing

The fuel cell tests were performed with a Model 840e from Scribner Associates. As typical for Fe-N-C catalysts no break-in procedure was performed. The temperature of the humidifiers was set to 80°C . In

order to avoid condensation, the cell temperature was set to 81 °C, thus humidification was 96 %. The tests were conducted with 1 bar gauge back pressure. Considering the vapor pressure, the absolute pressure was therefore 1.5 bar. All gas flows were set to 0.2 L min⁻¹. The measurement protocol started by recording the open circuit potential for 180 seconds. Following, the polarization curve was measured by increasing the current from 0 A stepwise with a rate of 0.03 A every 10 seconds. Fuel cell resistance was corrected for the measurements in H₂-O₂, which was performed by the automated tool provided from the test station. The stability tests were conducted after measuring the polarization curve. A constant potential was applied for a certain amount of time and the current output was recorded. The specific potentials and specific holding times are all given in the figure caption of the respective graphs.

For the fuel cell tests 40 - 50 % of the samples were randomly selected for a second measurement. For these samples error bars are included in the figures. Some measurements were very accurate, so that the error bars are not visible. Because the fuel cell measurements are very time consuming, not all of them were conducted twice. For evaluation of the reproducibility of the overall synthesis process the reader is referred to chapter 12. Since the electrode preparation was performed by hand (airbrush spraying method), the catalyst loadings differ slightly from another. **Table 11** summarizes which samples were measured twice and gives the respective catalyst loadings.

Table 11: Overview of fuel cell measurements and catalyst loadings.

Catalyst	Loading 1 / mg cm ⁻²	Loading 2 / mg cm ⁻²	Figure
FeNC	1.7	-	Figure 51, Figure 52
FeNC _{pyr}	1.7	-	Figure 51, Figure 52
FeNC _{ind}	1.7	-	Figure 51, Figure 52
C-GPPy	3.1	3.1	Figure 62
C-PPy _{40x}	2.5	-	Figure 62
C-PPy _{5x}	2.6	2.6	Figure 62
C-PPy _{0x}	2.2	-	Figure 62
C-2ht-PPy _{0x+}	3.3	-	Figure 62
C-2ht-PPy _{FeCl3}	3.3	-	Figure 67
C-2ht-PPy _{FeCl3/Fe(NO3)3}	3.4	-	Figure 67
C-2ht-PPy _{FeCl2}	3.3	-	Figure 67, Figure 68
C-2ht-PPy _{+FeCl2}	3.2	3.2	Figure 68
C-2ht-PPy _{++FeCl2}	3.4	3.4	Figure 68
C-2ht-PPy _{+FeCl3/+Fe(NO3)3}	3.3	-	Figure 68
C-PPy _{FeCl3_2}	2.8	2.8	Figure 73, Figure 74
C-PPy _{KMnO4}	3.2	3.2	Figure 73, Figure 74
C-PPy _{FeCl3/Mn(Ac)2}	3.4	3.4	Figure 73, Figure 74
C-PPy _{FeCl3/KMnO4}	2.7	2.7	Figure 73, Figure 74
C-2ht-PPy _{FeCl3/KMnO4}	3.2	3.2	Figure 75, Figure 76
C-PPy _{+FeCl3/-KMnO4}	3.7	-	Figure 78, Figure 79

C-2ht-PPy _{+FeCl3/-KMnO4}	3.3	3.6	Figure 75, Figure 76, Figure 78, Figure 79
C-2htm-PPy _{+FeCl3/-KMnO4}	3.6	3.6	Figure 78, Figure 79, Figure 83, Figure 84, Figure 85, Figure 86
C-2hts-PPy _{+FeCl3/-KMnO4}	3.3	3.3	Figure 78, Figure 79, Figure 83, Figure 84
C-2htm-PPy _{+FeCl3/-KMnO4-1000}	3.4	3.4	Figure 83, Figure 84, Figure 85, Figure 86
C-PPy-1000	3.4	3.4	Figure 83, Figure 84, Figure 85, Figure 86, Figure 90, Figure 91, Figure S5
C-PPy-1000-IsoAL	3.5	3.2	Figure 90, Figure 91
C-PPy-MO	3.5	-	Figure 96
C-PPy-SA	3.5	2.7	Figure 96, Figure 97
C-PPy-TSA	3.7	-	Figure 96
C-PPy-ABA	2.7	-	Figure 97
C-PPy-NDSA	3.5	-	Figure 96
C-PPy-CT2R	2.7	-	Figure 97
Cat A	3.3	-	Figure 98, Figure 99
Cat B	3.3	-	Figure 98, Figure 99
Cat C	3.4	-	Figure 98, Figure 99
Cat D	3.2	-	Figure 98, Figure 99
Cat E	3.9	-	Figure 98, Figure 99
VGC21	3.4	-	Figure S5

6.1 Remark on the ⁵⁷Fe-Mössbauer Analysis in this Work

This thesis was part of a broader project in which Fe-N-C catalysts were studied very comprehensively. The two major fundamental topics of that project were:

- (I) Improved understanding of the structural composition and the reaction mechanistic of Fe-N-C catalysts.
- (II) Improved understanding of synthesis parameters on performance characteristics and the development of a new synthesis strategy for a Fe-N-C catalyst.

This thesis addresses the (II) major topic of the broader project. Hence, a detailed discussion of the structural composition with respect to ⁵⁷Fe-Mössbauer spectroscopy is not included within the scope of this work. The results of the spectroscopic experiments will be discussed in a condensed fashion, in that way that still important findings with respect the synthesis are given. Hence, this work focuses on the synthesis parameters and performance. Details on fundamental topic (I) are provided within the work of Lingmei Ni. The ⁵⁷Fe-Mössbauer spectroscopy experiments and data analysis of this work were conducted by Stephan Wagner and Lingmei Ni.

7 Results and Discussion on Surface Functionalized Multi-Walled Carbon Nanotubes as Non-Precious Metal Oxygen Reduction Catalysts

This chapter deals with a synthesis approach based on carbon nanotubes as backbone of a Fe-N-C catalyst. First, the main concept of this approach and how the FeN_xC_y moieties were attached to the carbon nanotube is explained. Important physical characterization methods, such as TEM, BET and Mössbauer spectroscopy are performed. This helps to understand the structure and composition of the material. Further, the catalysts are electrochemically evaluated using RRDE, DEMS and PEMFC testing. High ORR performance during RRDE tests was achieved. However, the results could not be transferred to the fuel cell level. Subsequently, the findings of this first approach helped revising the synthesis method and contributed to the improved second approach which is presented from chapter 8 onwards. The results of this chapter were published here [413].

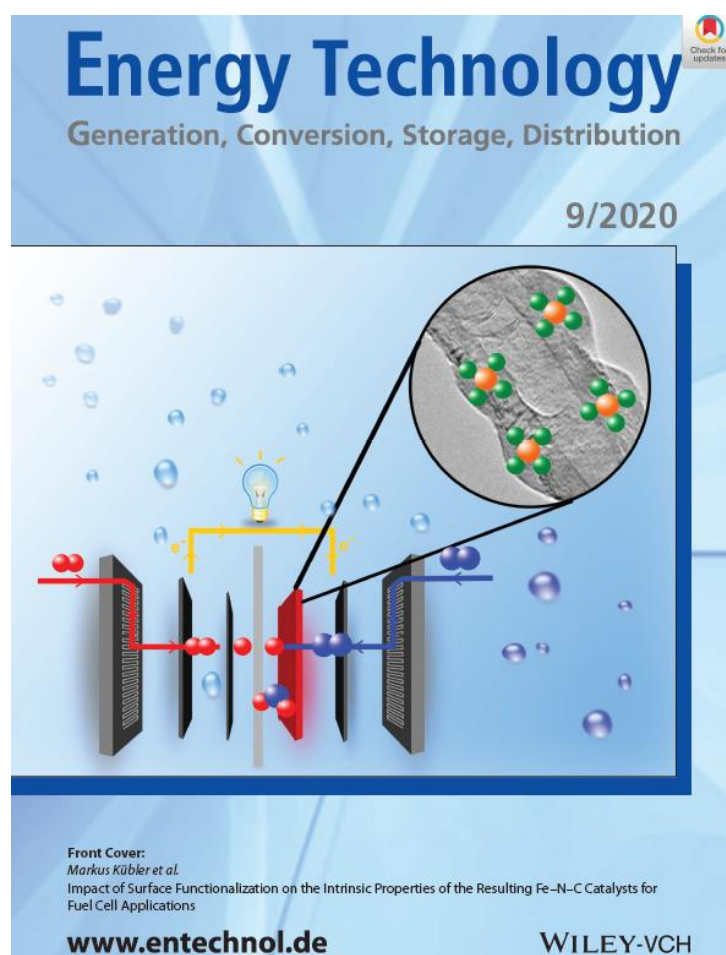


Figure 42: Cover image of Energy Technology featuring the results of chapter 7 on surface functionalized multi-walled carbon nanotubes as non-precious metal oxygen reduction catalysts [413].

7.1 Background and Motivation on MWCNT Based ORR Catalysts

Multi-walled carbon nanotubes (MWCNTs) are implemented as the carbon backbone of a Fe-phen based Fe-N-C catalyst. Due to their high degree of graphitization and specific structure, carbon nanotubes evidence a better chemical stability in comparison to commonly applied carbon blacks. This specific structure, which is described as several coaxially arranged graphene sheets rolled into a cylinder, is given in **Figure 43**. The main idea is that the resulting catalysts show improved corrosion resistance due to a minimized fraction of amorphous carbon.

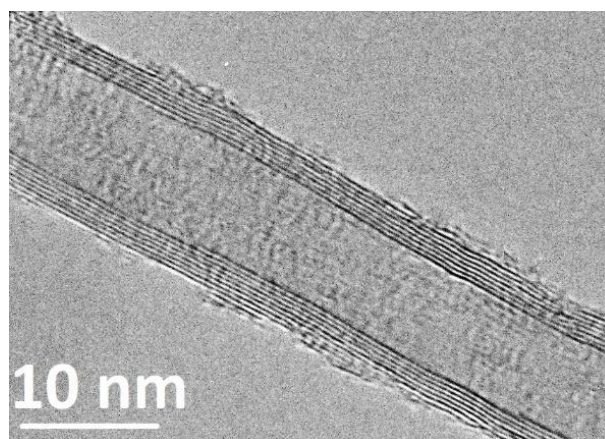


Figure 43: TEM picture of a MWCNT consisting of several coaxially arranged graphene sheets rolled into a cylinder.

For platinum-based ORR catalysts the benefit of using MWCNTs as carbon support has already been demonstrated. Wang et al. revealed that in comparison to Vulcan® XC-72, MWCNTs form less surface oxide species under potentiostatic conditions (60 °C, 0.5 M H₂SO₄ and 0.9 V vs. RHE) [415]. Likewise, about 30 % lower corrosion induced current was measured. Hasche et al. performed stability tests on Pt/C and Pt/MWCNTs [416]. A smaller mass activity loss, as well as less decrease in electrochemical active surface area (ECSA) was reported for Pt/MWCNT.

Considering Me-N-C catalysts, Gao et al. reported an activation energy barrier of about 15 eV for the acidic ORR on a FeN₄/MWCNT system [417]. The activation energy was obtained by performing first-principles spin-polarized local density approximation (LDA) and generalized gradient approximation (GGA) calculations. Some experimental approaches have been reported with the aim of combining FeN_xC_y moieties with a MWCNT structure. For instance, Chung et al. obtained a mixture of nanotubes and nanoparticles comprising iron, nitrogen and carbon after carbonization of iron acetate in the present of cyanamide [305]. The resulting material demonstrated excellent ORR activity ($E_{1/2} = 0.87$ V) as well as better stability than commercial 20 wt % Pt/C (E-TEK) in alkaline media. Hijazi et al., as well as Jia et al. attached Co- respectively Fe-porphyrin on MWCNTs through surface adsorption followed by dimerization of the porphyrin's triple bonds after Hay-coupling reaction [418, 419].

7.2 Synthesis Method and Prepared MWCNT Catalysts

In this chapter, surface functionalized MWCNTs in combination with Fe-phen are used. The surface functionalization of the MWCNTs enables a direct connection between the MWCNTs and the Fe-phen complex. The particular synthesis steps are shown in **Figure 44**. First, an amino compound which is either amino-pyridine or amino-indazole is attached covalently onto the surface of the MWCNTs. This functionalization is achieved through a diazoniumsalt reaction [420]. Next, Fe(Ac)₂, phen and sulphur are added. The sulphur is added in order to suppress the formation of excess amounts of insoluble inorganic iron species during the heat treatment process. **Figure 44** shows the assumed interaction between the functionalized MWCNTs and the Fe-phen complex. It is assumed that FeN_xC_y-like structures are directly attached on top of a MWCNT substructure after carbonization.

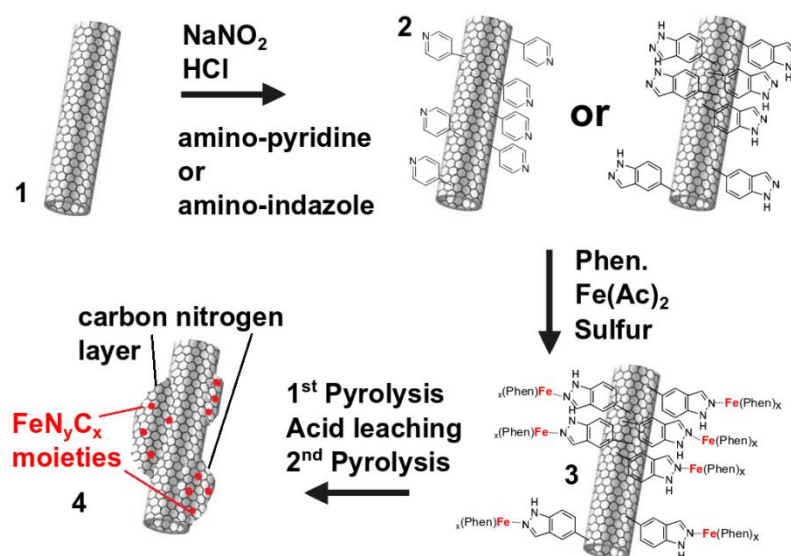


Figure 44: Schematic presentation of the different synthesis steps and assumed coordination of Fe-phen.

Overall, four different catalyst are prepared, an overview is shown in **Table 12**. To examine the impact of the surface functionalization, the samples labeled as FeNC, FeNC_{pyr} and FeNC_{ind} are prepared. The denotation FeNC_{pyr} and FeNC_{ind} reveres to samples that are synthesized applying the pyridinic respectively the indazolic functionalized MWCNTs. FeNC is prepared as a reference material, where MWCNTs were used without any surface modification. Likewise, FeNC_{ind-mix} serves as a reference material, for which indazole is simply mixed but not chemically attached on the MWCNTs' surface. The used amount of phen, Fe(Ac)₂ and sulphur is the same for all of the prepared samples.

Table 12: Overview of investigated MWCNTs based FeNC catalyst materials.

Sample Name	Type of MWCNTs	MWCNTs / mol e.q.	Fe(Ac) ₂ / mol e.q.	Phenanthroline / mol e.q.	Sulfur / mol e.q.
FeNC	Unmodified	30.5	1.0	2.6	0.2
FeNC _{pyr}	Pyridinic	30.5	1.0	2.6	0.2
FeNC _{ind}	Indazolic	30.5	1.0	2.6	0.2
FeNC _{ind-mix}	Unmodified, mixed with indazole	30.5	1.0	2.6	0.2

7.3 Structural Characterization

Transmission Electron Microscopy

TEM pictures were recorded to validate the structure of the catalysts. The results are given in **Figure 45**.

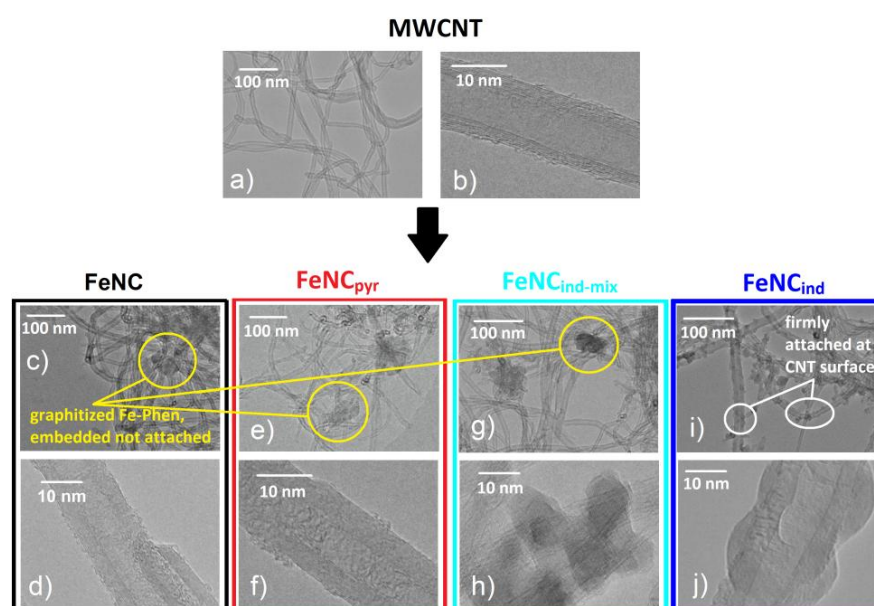


Figure 45: TEM pictures of pristine MWCNTs before (a, b) and after pyrolysis together with Fe(Ac)₂, phenanthroline and sulphur (c-j). Unmodified MWCNTs (c, d), pyridinic functionalized (e, f), unmodified but mixed with amino-indazole (g, h) and indazolic functionalized (i, j).

As shown in **Figure 45 a)** and **b)**, the pristine MWCNTs have a diameter of about 10 nm and comprise of several parallel graphene sheets rolled together into a tube. After the pyrolysis of the MWCNTs in the presence of Fe(Ac)₂, phen and sulphur the MWCNT substructure remains intact for all of the

prepared catalysts (**Figure 45 c-j**)). As it has been shown earlier through thermogravimetric analysis (TGA), the unchanged morphology of the MWCNTs after the heat treatment in N₂ at 800 °C is expected [421, 422]. Further, the TEM pictures show graphitized Fe-phen particles/remains. These particles are found besides or in between the MWCNT network without a direct attachment or linkage to the MWCNTs. This observation is made for the catalyst prepared from the unmodified MWCNTs (**Figure 45 c, d**)), the one synthesized from pyridinic MWCNTs (**Figure 45 e, f**) as well as for the one obtained from unmodified MWCNTs and added amino-indazole (**Figure 45 g, h**)). The pictures recorded at higher magnification (**Figure 45 d, f** and **h**)) clearly show that the surface of the MWCNTs is clean of any pyrolysis residues and that the Fe-phen remains are only embedded between the MWCNT framework. For FeNC this result is reasonable, since the unmodified MWCNTs do not contain any additional surface functionalization which would provoke an interaction between Fe-phen and the MWCNT surface. The same explanation applies for FeNC_{ind-mix}. In contrast, FeNC_{pyr} is prepared from MWCNTs which were functionalized with pyridinic groups. These could in general interact with the iron cations through the electron lone pair of the nitrogen atom. However, this interaction does either not occur, or it is not decisive enough to result in the desired outcome. On the contrary, for the catalyst prepared from indazole functionalized MWCNTs, FeNC_{ind}, the TEM pictures show that the pyrolyzed Fe-phen is directly attached onto the outside of the MWCNT walls (**Figure 45 i, j**)). This layer is only appearing in sections and is of varying thickness. Still, a distinct difference between FeNC_{ind} and the other three samples is identifiable. Hence, it is stated that through prior surface modification of MWCNTs with indazole molecules it was possible to attach carbonized Fe-phen, meaning FeN_xC_y moieties on top of a MWCNT backbone.

BET Results

The multi-walled carbon nanotubes, Nanocyl7000TM were commercially purchased from Nanocyl SA. Due to possible metal impurities of the Nanocyl7000TM, an acid leaching step was performed before any further synthesis steps. Subsequently, the acid treated MWCNTs underwent a heat treatment at 800 °C under N₂ atmosphere to remove excessive oxygen containing surface groups and to heal possible defects caused by the acid leaching step. The specific BET surface areas of the different materials were determined through N₂ sorption experiments. The results are shown in **Figure 46**.

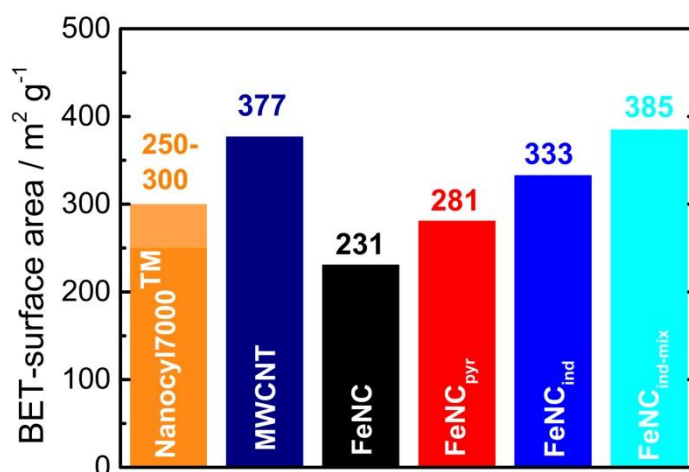


Figure 46: Overview of the N₂ sorption experiments and resulting BET surface areas for MWCNT-based catalysts.

After the acid leaching and annealing step, the clean MWCNTs show a specific surface area of 377 m² g⁻¹. This value is slightly higher than the reported value of 250 - 300 m² g⁻¹ for the as received MWCNTs from the manufacturer [423]. After the synthesis steps involving Fe-phen, the specific surface area of most of the materials is lower. For FeNC and FeNC_{pyr} a value of 231 m² g⁻¹ respectively 281 m² g⁻¹ are measured. FeNC_{ind} has a specific surface area of 333 m² g⁻¹. The lower BET surface area of the catalysts in comparison to the acid washed and annealed MWCNTs is due to the contribution of the carbonized Fe-phen. Schardt et al. stated a specific surface area of 295 m² g⁻¹ after carbonization of Fe-phen with sulphur [251]. Still, this value was measured for a sample applying just one heat treatment. Considering that a second heat treatment in general lowers the BET surface through partial pore and structure collapsing [122] the lower values for the catalysts prepared in this study (between 231 – 333 m² g⁻¹) are reasonable. The catalysts which were prepared from the MWCNTs that underwent a prior surface modification show slightly higher BET values than FeNC. In accordance with the TEM images this is caused by slightly smaller and better dispersed Fe-phen phases. However, considering the high specific surface area of FeNC_{ind-mix} (385 m² g⁻¹), it is also likely that pyridine and indazole, respectively their amino compounds, provoke pore formation. This is in accordance with previous findings where other amino group containing molecules like dicyandiamide have shown to enhance the specific BET surface area by decomposing into gaseous products [251, 277].

⁵⁷Fe-Mössbauer Spectroscopy Results

⁵⁷Fe-Mössbauer spectroscopy gives important insights on the structural composition of the catalysts with respect to iron. The results are displayed in **Figure 47**. Whereas **Figure 47 a) - c)** show the Mössbauer spectra and **Figure 47 d)** gives the isomer shift and the quadrupole splitting of the detected doublet species.

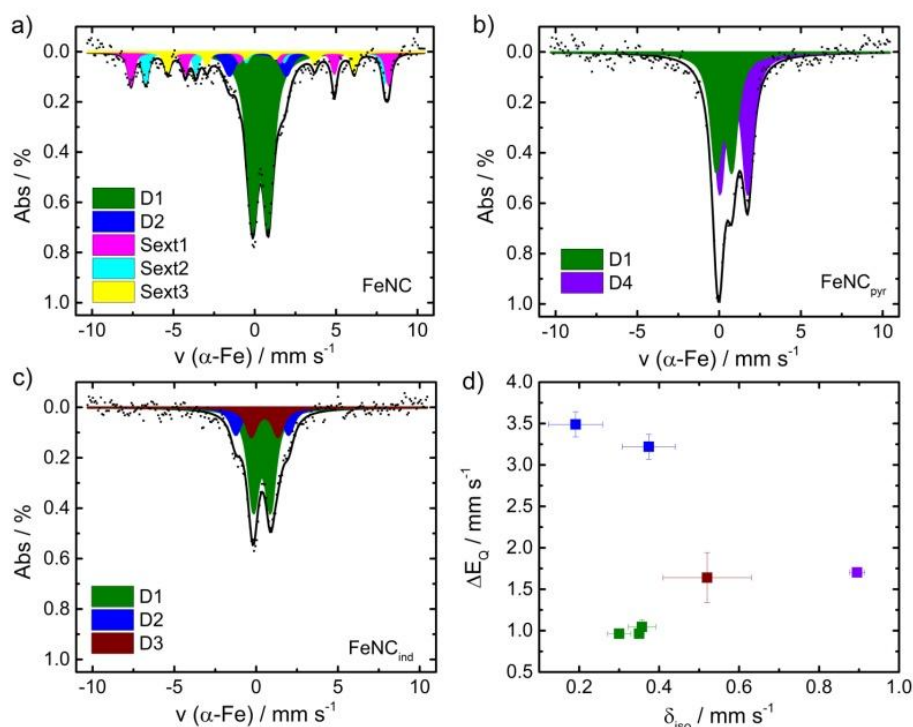


Figure 47: Mössbauer spectra of the catalysts FeNC (a), FeNC_{pyr} (b) and FeNC_{ind} (c) and quadrupole splitting versus isomer shift (d).

The spectra of the three catalysts are dominated by a doublet labeled as D1. In general, this doublet species is identified as FeN₄ site of different oxidation and spin states [424]. However, since the experiments were performed at room temperature, D1 could also be attributed to iron or iron oxide nano clusters [425]. Starting with FeNC_{ind}, three doublets are measured. D2 shows a high quadrupole splitting of 3.49 mm s⁻¹. This could be assigned to a intermediate spin species such as FeN₄ plus weak axial ligands [424]. The D3 is related to an intermediate spin state FeN₄ species. Only two doublets are found for FeNC_{pyr}, labelled as D1 and D4. Where D4 is probably a fivefold coordinated iron with nitrogen or oxygen in high spin state [424]. Interestingly, besides D1 and D2, three sextets are found for FeNC. Those can be assigned to Fe₃O₄ and α -FeOOH. Inorganic iron species were found to be less active and less stable under fuel cell operations. Hence, they are undesired by-products [33]. From these results it is expected that FeNC shows less activity and stability than the other two catalysts, FeNC_{pyr} and FeNC_{ind}.

7.4 Electrochemical Experiments

Rotating Ring Disc Electrode Measurements

The electrocatalytic ORR performance in acidic electrolyte of the prepared catalysts was analyzed by rotating ring disc electrode (RRDE) measurements. The results are displayed in **Figure 48 a)**. The H_2O_2 yield is given in **Figure 48 b)**.

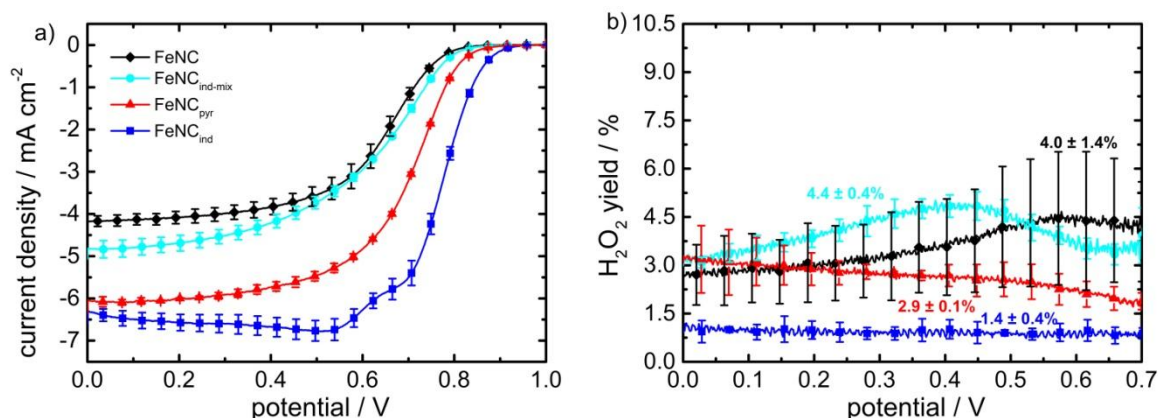


Figure 48: ORR polarization curves (A) and respective H_2O_2 yield (B) for the different MWCNT catalysts recorded with a sweep rate of 10 mV s^{-1} in O_2 saturated $0.1 \text{ M H}_2\text{SO}_4$, a rotation rate of 1500 rpm and a loading of 0.8 mg cm^{-2} .

The ORR activity is increasing according to: $\text{FeNC} < \text{FeNC}_{\text{ind-mix}} < \text{FeNC}_{\text{pyr}} < \text{FeNC}_{\text{ind}}$. The shift in onset potential from the least active material, FeNC (800 mV) to the most active one, FeNC_{ind} (900 mV) is 100 mV . Similar onset potentials were found for other highly active Fe-Phen based catalysts [251, 426]. **Figure 48 a)** shows that the functionalization of the MWCNTs also has a positive impact on the diffusion limited current density. For FeNC_{ind}, the diffusion limited current density is above the theoretical limit ($> 6 \text{ mA cm}^{-2}$). This can be explained by the high electrode loading of 0.8 mg cm^{-2} in combination with the porosity of the material. The real electrode surface area is regularly higher than the one obtained from the simple geometrical area of the disc. Regarding the ORR selectivity, the same trend as for ORR activity is observable. FeNC shows an average H_2O_2 yield of 5.4% , both functionalized MWCNTs exhibit lower values; 2.8% for FeNC_{pyr} and 1.0% for FeNC_{ind}. It is important to mention that the very low H_2O_2 yields which are reported here, are also influenced by the catalyst loading on the RRDE disc [427]. Considering these results, it is concluded, that surface functionalization of the MWCNTs with N-containing groups before the pyrolysis with Fe-phen is leading to an increased ORR activity and selectivity during RRDE experiments.

In addition to the activity tests, experiments on stability under N_2 were performed. **Figure 49** shows the initial ORR sweep versus the respective sweep after performing $10,000$ cycles between 0 and 1.2 V .

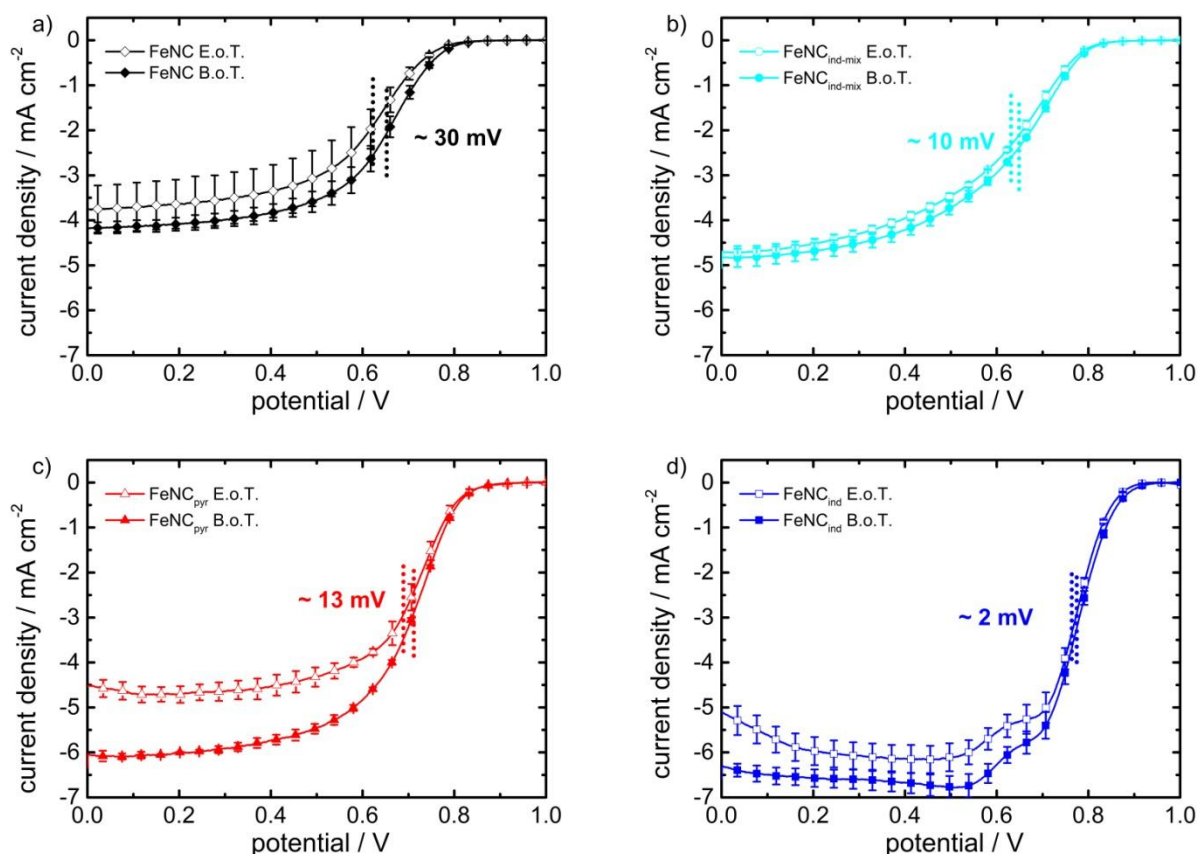


Figure 49: Initial ORR sweep (solid) and after performing 10,000 scans ranging from 0 to 1.2 V in N_2 saturated 0.1 M H_2SO_4 with a sweep rate of 500 mV s^{-1} (hollow) for the different MWCNT catalysts (a-d).

Since it was shown that the exposure of FeNC based catalysts to H_2O_2 in acidic media leads to a significant decrease in ORR activity, the stability tests here were performed under N_2 [162]. Hence, the obtained results are not influenced by the different H_2O_2 production rates of the catalysts. A more appropriate statement on the influence of the role of the MWCNT substructure can be made. By comparing the four catalysts, a similar but not the same trend as for the ORR activity is observed. As indicated by the shift in half-wave potential the stability increases from FeNC ($\sim 30 \text{ mV}$) < FeNC_{pyr} ($\sim 13 \text{ mV}$) < FeNC_{ind-mix} ($\sim 10 \text{ mV}$) < FeNC_{ind} ($\sim 2 \text{ mV}$). Again, these results are in good accordance with the results of Mössbauer spectroscopic experiments. FeNC contains additional inorganic Fe-species, these tend to dissolve more easily than FeN_xC_y-moieties. This effect was shown by an operando spectroscopic analysis of different catalysts under RRDE and fuel cell conditions [33]. When comparing the pyridinic to the indazolic derived catalyst, **from Figure 49 c) and d)** it appears that the catalyst with a direct linkage of the MWCNT substructure to the FeN_xC_y-moieties, FeNC_{ind} has a lower shift in half-wave potential after cycling. As mentioned before, the stability tests were performed under N_2 so no effect of different H_2O_2 production rates influences the stability of the materials. From these results

it is concluded that the direct linkage of the FeN_xC_y -moieties to the MWCNT framework leads to a more stable catalyst compared to the same material without that direct linkage.

Differential Electrochemical Mass-Spectroscopic Investigations

To gain further insight on the stability of FeNC_{ind} differential electrochemical mass spectroscopy (DEMS) measurements were performed. These experiments were conducted by the author of this theses at the facility of the Fraunhofer ICT in Pfinztal. The applied half-cell setup uses a catalyst spray-coated gas diffusion layer in combination with a membrane and allows to measure under gaseous flow conditions. Hence, the obtained results come close to the real application conditions of a fuel cell. All details about the DEMS setup are given elsewhere [414]. For the DEMS experiments FeNC_{ind} was compared with Pt/C and a carbon-black porphyrin-based (CB-FeNC) catalyst. Hence, the carbon corrosion behavior of the novel structure (attached FeNC moieties to MWCNT substructure) are compared with a standard Pt/C and a usual FeNC ORR catalyst (not MWCNT based). Linear sweep voltammetry was performed from 0 to 1.4 V under N_2 at 23 °C and 60 °C. Besides the electrochemical data the mass spectrometer of the DEMS setup simultaneously records the ion current of CO_2 ($m/z = 44$), the results are given in **Figure 50**.

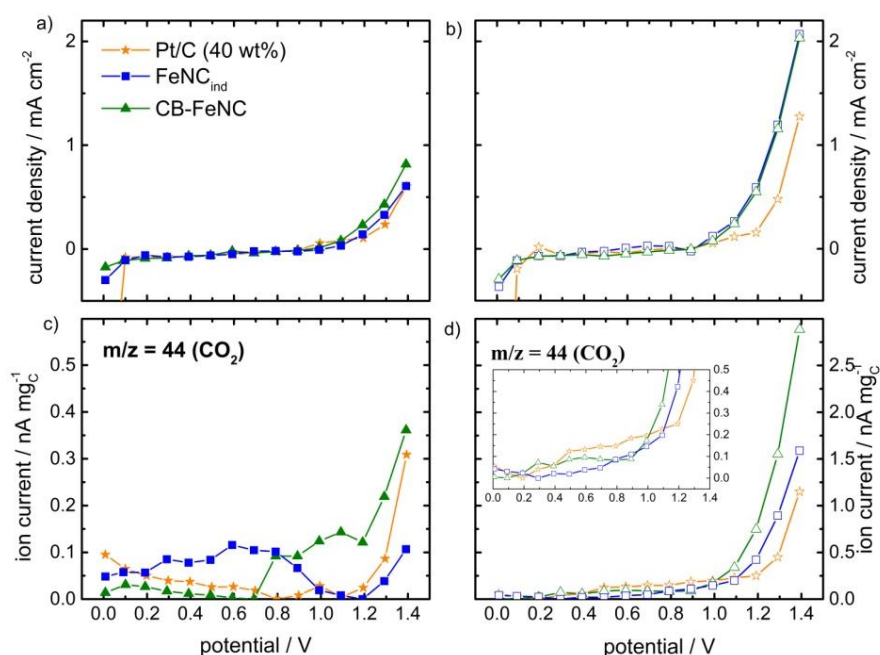


Figure 50: DEMS experiments showing LSV scans under N_2 saturated atmosphere at 23 °C (left) and 60 °C (right), electrochemical output (upper) and ion current $m/z = 44$ detected with the mass spectrometer (lower).

The upper graphs show the electrochemical data and the lower graphs display the ion currents. Looking at the LSV, the typical electrochemical response for Pt/C and both Fe-N-C catalysts is obtained. Whereas it is important to mention that the specific redox peaks are less pronounced for the measurements performed with the half-cell DEMS setup as they are for the RDE/RRDE. This

phenomenon was also observed by Jurzinsky et al. [428]. The phenomenon is explained due to different transport behavior and surface conductivity of the differing interfaces of catalyst/NafionTM (DEMS) to Catalyst/H₂SO₄ (RDE/RRDE) [429, 430]. For both Fe-N-C catalysts an almost feature-less curve arises from 0 to 1.0 V. At higher potentials an oxidative current is measured, which is ascribed to carbon oxidation. This oxidative current is more pronounced for the measurements performed at 60 °C. A similar feature-less electrochemical response for the medium potential range is obtained for the Pt/C catalyst. On the opposite, for low potentials the Pt/C catalysts shows the typical hydrogen adsorption/desorption and hydrogen evolution behavior. This is indicated by the reductive current. For the experiments performed at 60 °C the Pt-based material is characterized by an overall lower oxidative current response for the high potential range compared to both of the Fe-N-C catalysts. The simultaneously recorded ion currents of CO₂ show that the oxidative current starting at around 1.1 V for the 23 °C measurement is related to carbon corrosion/ CO₂ formation, which begins at slightly higher potentials, for 23 °C at around 1.2 V. The same applies for the experiments performed at 60 °C. Even so, at 60 °C all currents (electrochemical and ion currents) are more pronounced and evolve at lower potentials (electrochemical current about 1.0 V ion current about 1.1 V). The small potential delay of about 50 - 100 mV between electrochemical oxidation current and ion current is due to the fact that the electrochemical current also includes surface oxidation processes which take place before the complete oxidation of carbon to CO₂. The latter is then detected in the mass spectrometer. When comparing the CO₂ formation of the three catalyst at 23 °C it appears that CB-FeNC produces slightly more CO₂, but the difference is not distinctively. On the contrary, for the experiments at 60 °C not only the overall electrochemical oxidative currents but also the overall ion currents are significantly enhanced. Further, there is a slight onset shift of the oxidative currents to lower potentials. Both effects are ascribed to the temperature dependence of the carbon corrosion process and emphasize the importance of performing measurements at elevated temperatures (PEMFC usually runs at 80 °C). Considering the ion currents, the intensity of the carbon corrosion follows the trend CB-FeNC > FeNC_{ind} > Pt/C. For a potential of 1.4 V, the $m/z = 44$ ion current for CB-FeNC shows about 1.8 times the value of FeNC_{ind} and about 2.4 times that of the Pt/C. It is concluded that a Fe-N-C catalyst based on carbon black and a Fe-porphyrin is significantly less stable against carbon corrosion. For FeNC_{ind} ion current at 1.4 V reaches about 1.6 nA mg_C⁻¹. For Pt/C it is about 1.2 nA mg_C⁻¹. However, for lower potentials (0.8 to 1.0 V) Pt/C shows the highest CO₂ formation of all three catalysts. This might be explained due to the findings about the catalytic effect of Pt on the carbon oxidation reaction [431-433]. In total, DEMS experiments reveal that at higher potentials and elevated temperatures Fe-N-C catalysts in general show less carbon oxidation resistance than the commercial Pt/C catalyst. Still, the combination of pyrolyzed Fe-phen on top of a MWCNT substructure shows almost half the CO₂ formation compared to the carbon black Fe-porphyrin-based one.

PEMFC Tests

The activity of the catalysts was also analyzed by performing PEMFC single cell tests. The polarization curves in H₂-O₂ of FeNC, FeNC_{pyr} and FeNC_{ind} are shown in **Figure 51**.

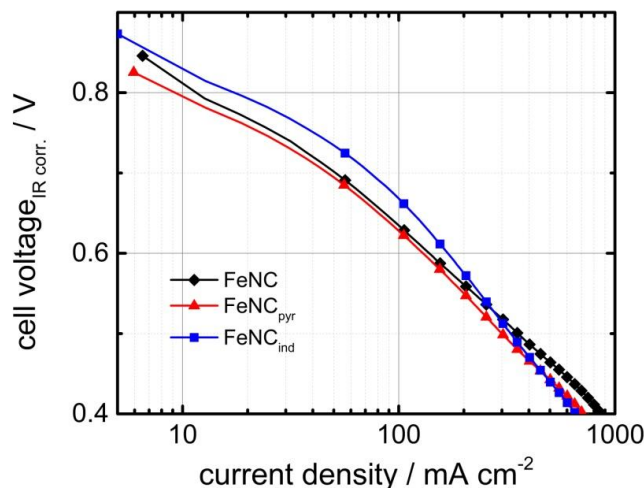


Figure 51: Outcome of the PEMFC tests showing the cell voltage versus current density for the MWCNTs-based catalysts (experiment conditions: H₂-O₂, cathode loading 1.7 mg cm⁻², N212 membrane, 1 bar gauge back pressure, 0.2 L min⁻¹ oxidant and fuel flow, 81 °C, 96 % humidity).

The activity trend, which was first obtained during RRDE tests is not confirmed here. The performance at 600 mV is 123 mA cm⁻² for FeNC_{pyr}, 130 mA cm⁻² for FeNC and 161 mA cm⁻² for FeNC_{ind}. The overall performance of the materials is closer to each other than it was during RRDE experiments. A possible explanation for this behavior is that the NafionTM content of the investigated catalysts in this work has been fixed to 35 wt%. However, it has been shown that the optimum NafionTM content can vary strongly depending on the respective catalyst material [182, 434]. Sahraie et al. reported a similar discrepancy between RRDE and FC testing for their Ketjenblack-Pani-Fe based catalyst [198]. The authors stated that an optimization of the ink recipe (NafionTM to catalyst ratio) might improve FC performance. Still, the fuel cell performance of the catalysts of this work is low compared to other phen based catalysts [121, 262]. Since the work up of the MWCNT based catalysts into firm catalysts layer is quite challenging the loading of the cathode was limited to 1.7 mg cm⁻².

Figure 52 shows the results of a short stability test of the MWCNT based catalysts under potentiostatic fuel cell conditions. After the initial polarization curve a constant potential of 600 mV was applied while the current output was monitored.

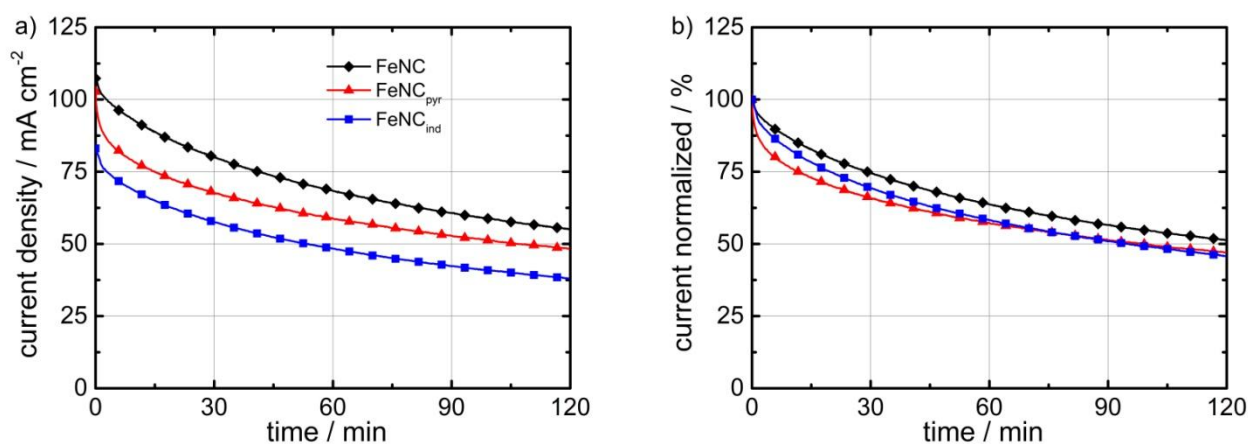


Figure 52: Short PEMFC stability test of MWCNTs based Fe-N-C catalysts performed at a constant potential of 600 mV, showing the measured absolute current density a) and the remaining current density in percent b) (experiment conditions: H₂-O₂, cathode loading 1.7 mg cm⁻², N212 membrane, 1 bar gauge back pressure, 0.2 L min⁻¹ oxidant and fuel flow, 81 °C, 96 % humidity).

FeNC shows the highest current output and FeNC_{ind} the lowest. Even so the difference is not significant, these results are still surprising. Especially having in mind, the large performance difference of FeNC in comparison to FeNC_{ind} during RRDE testing. Furthermore, for all three catalysts the current decay over the course of the 2-hour stability test is about 50 %, **Figure 52 b**). Current decay values of 40 – 80 % are normally reported within the first 100 hours of PEMFC operation applying non-precious metal-based ORR catalysts [25, 435]. Whereas the main degradation occurs within the first 24 hours. Hence, for the developed synthesis method of applying functionalized MWCNTs and Fe-phen neither the high ORR performance during RRDE testing nor the good stability against carbon corrosion found during DEMS measurements could be transferred to the fuel cell testing level. Possible reasons are the not optimized ratio of NafionTM content to catalyst loading and the low catalyst loading of 1.7 mg cm⁻². The latter seems to be limited by the fact that the nanotube morphology hinders the fabrication of stable catalyst layers with higher loadings.

7.5 Summary and Conclusions on MWCNTs Based Fe-N-C Catalyst

A synthesis method was presented that is capable of attaching carbonized Fe-phen onto MWCNTs. This was achieved when the MWCNTs underwent a surface functionalization with indazole. The direct linkage of the active site containing Fe-phen pyrolysis product and MWCNTs-indazole was verified by TEM.

For the MWCNT-indazole based catalyst, ^{57}Fe Mössbauer-spectroscopy showed that the Fe sites were solely of molecular-type. 36.8 % of the containing Fe atoms were assigned to a ferrous FeN_4 site in low-spin state, which are responsible for the catalytic ORR activity. The remaining Fe atoms were ascribed to a porphyrin-type iron site and a p450 heme-like structure. No inorganic Fe phases were detected.

RRDE experiments showed a significant higher ORR activity and selectivity for the FeNC_{ind} catalyst where the active sites are directly attached to the MWCNT backbone in comparison to the rest of the samples where this linkage is not present. Likewise, 10,000 durability cycles under N_2 reveal a shift in half-wave potential of about only 2 mV for FeNC_{ind} . Furthermore, DEMS experiments have shown that the new nanotube-based catalyst is less prone to carbon corrosion than a simple carbon black (CB) based Fe-N-C catalyst. At 60 °C and 1.4 V the measured CO_2 ($m/z = 44$) ion current is 1.6 $\text{nA mg}_\text{C}^{-1}$ for FeNC_{ind} , 2.9 $\text{nA mg}_\text{C}^{-1}$ for CB-FeNC and 1.2 $\text{nA mg}_\text{C}^{-1}$ for Pt/C.

Despite these very promising results, it was not possible to transfer this outcome to the fuel cell testing level. Very low PEMFC activity, as well as a sharp current decay of about 50 % of the initial current was measured within a short 2-hour stability test ($\text{H}_2\text{-O}_2$).

Several reasons explain this outcome. The most crucial one being the difficult processing of a carbon nanotube-based catalyst powder into a homogenous ink and into a firm catalyst layer. Due to the general low volumetric activity of non-precious metal-based ORR catalyst, very high catalyst loadings of 4.0 mg cm^{-2} are normally needed in order to achieve a good PEMFC performance. However, this goes along with a strong increase of catalyst layer thickness. Pushing cathode layer thickness to 100 μm (Pt/C usually 10 μm). For the MWCNT-based catalysts, it was not possible to prepare cathode layers with loadings greater than 1.7 mg cm^{-2} . At higher loadings the firm layer became inhomogeneous and rich in cracks. Close to the commonly used 4.0 mg cm^{-2} some catalyst material flaked off. During PEMFC stability tests of a different Fe-N-C catalyst Banham et al. found that a cathode loading of 4.0 mg cm^{-2} results in a loss about 10 % of its initial activity whereas for a loading of 1.0 mg cm^{-2} 55 % of the activity decays within 100 hours (constant potential 500 mV, $\text{H}_2\text{-air}$) [145]. Hence, both fuel cell activity and stability are strongly affected by the catalyst loading.

Through optimization of the ink composition, the overall Nafion™ content, the catalyst layer fabrication process or the CNTs diameter and length, an optimized fuel cell performance might be achieved.

Still, there is another major drawback of the presented synthesis method which ultimately lead to the decision of no further pursuing optimization towards fuel cell performance. The overall synthesis process of the catalyst comprises of various different steps and time consuming, the major ones are:

- (1) Fabrication/purchasing of the MWCNTs.
- (2) Cleaning of the MWCNTs (acid leaching + annealing).
- (3) Functionalization with indazole and cleaning.
- (4) Preparation of precursor mixture/ mixing of MWCNT-ind with Fe-phen and sulphur.
- (5) Actual catalyst synthesis: first pyrolysis step, acid leaching and washing and second pyrolysis step.

From a cost perspective, a commercial feasible fuel cell catalyst should not only minimize the consumption of precious raw materials such as platinum, but its overall fabrication process should also be simple. No cost reduction compared to Pt/C is achieved by implementing a non-precious metal-based ORR catalyst which is obtained by a much more complex and impractical (scale-up) synthesis.

Hence, the following chapters deal with a different synthesis approach that by-passes the drawbacks of the MWCNT based one. For this approach, polypyrrole is used as a simple precursor. The fabrication steps (1) - (3) are reduced to just one step. Further a successful transfer from RRDE testing to the fuel cell level is achieved.

8 Results and Discussion on the Synthesis of Polypyrrole Based Me-N-C Catalyst

The following chapter covers the results and discussions about the polypyrrole based Me-N-C catalyst synthesis. This chapter is considered the main part of this thesis.

First, the major idea behind the synthesis is explained. It is emphasized why the synthesis was chosen and why it is worth further optimization and scientific investigations. The presented approach applies polypyrrole containing methyl orange as a C, N precursor. In this context, the influence of methyl orange during the synthesis is investigated first. The following two sections consider the optimization of the type and the amount of the used metal precursor. The influence of different Fe and Mn precursors salts is looked into detail. Further, the temperature of both, the first and the second heat treatment step is optimized. A new approach which significantly enhances the effectiveness of the acid leaching step is presented. Finally, by making use of the earlier findings about the influence of methyl orange, additional doping agents are implemented of which sulfanilic acid further improves the catalysts fuel cell performance. At the very end, a summary of the most relevant developments is made by comparing the PEMFC activity and stability of the best catalyst of each chapter. A table containing information about H₂-air PEMFC performance and stability is provided, including the data of the final catalyst of this work and the best published catalyst from literature. Also, a comparative discussion on the feasibility of the overall synthesis process of the new polypyrrole catalyst of this work and the two most advanced commercial non-precious metal-based catalysts is provided.

8.1 The Concept and the Preparation Process

The new synthesis approach is based on polypyrrole, a conducting C, N containing polymer. The goal is to keep the overall synthesis process as simple as possible, whereas at the same time a high performing catalyst should be obtained. The main feature of the synthesis in this work is the replacement of commonly used C, N precursor polypyrrole by methyl orange templated polypyrrole nanotubes. **Figure 53 a)** shows the one-pot synthesis of polypyrrole. Where an aqueous solution of pyrrole monomer is polymerized oxidatively with FeCl_3 as catalyst. By adding methyl orange to this solution, polypyrrole nanotubes are formed, see **Figure 53 b)**. This simple reaction has been described in detail earlier [436-440].

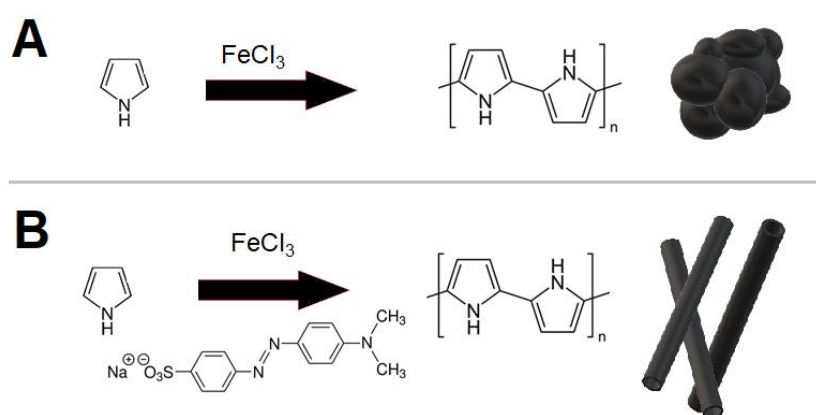


Figure 53: Oxidative polymerization of pyrrole monomer to polypyrrole in the presence of FeCl_3 (A) and FeCl_3 + methyl orange (B).

For the final catalyst precursor mixture, the obtained polypyrrole precursors are mixed with additional amounts of FeCl_3 . Following, the usual steps of Fe-N-C catalyst synthesis are applied: first heat treatment, acid leaching and second heat treatment. The final Fe-N-C catalyst powder is obtained. The process is given in **Figure 54**.

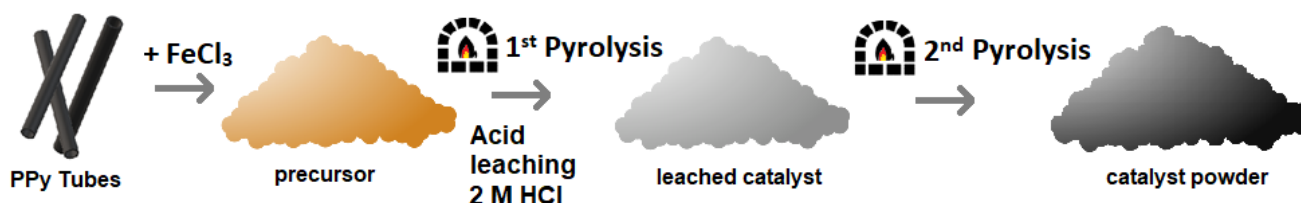


Figure 54: Schematic synthesis process of polypyrrole (PPy) nanotube based ORR catalyst.

Figure 55 shows the reductive scan of the polypyrrole Fe-N-C and polypyrrole-methyl orange nanotube Fe-N-C catalyst in O_2 saturated electrolyte.

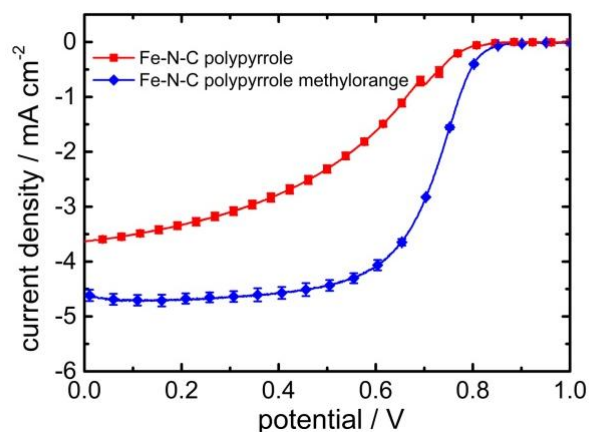


Figure 55: Acidic RDE polarization curve of a polypyrrole Fe-N-C catalyst and a polypyrrole nanotube Fe-N-C catalyst in O₂ saturated electrolyte (experiment conditions: 10 mV s⁻¹, 1500 rpm, 0.5 mg_{Catalyst} cm⁻²).

The curves clearly show that the catalyst synthesized from polypyrrole-methyl orange nanotubes has a higher ORR activity than the same Fe-N-C catalyst which was obtained from common polypyrrole.

In short, this approach becomes very promising because it:

- I) uses few and simple precursors materials (pyrrole, methyl orange and FeCl₃);
- II) consists of few synthesis steps (polypyrrole synthesis, mixing with Fe-precursor, common oven and acid leaching steps);
- III) shows high ORR activity during first RDE tests.

Further, from a scientific perspective the reason behind the significant ORR enhancement of polypyrrole + methyl orange in comparison to common polypyrrole is unknown and could lead to a deeper understanding of polymer-based Fe-N-C catalyst synthesis.

However, it is important to keep in mind that during the first synthesis approach (MWCNTs), a successful work-up of the catalyst powder into a firm catalyst layer of higher loading was not possible due to the nanotube morphology of the catalyst. The nanotubes obtained from polypyrrole have a diameter of 60 - 120 nm, which is much bigger than the Nanocyl7000TM (~ 10 nm) which were used before. This makes the polypyrrole-methyl orange nanotubes much more convenient for fabricating fuel cell catalyst layers. Loadings of ca. 3.3 mg cm⁻² were easily achieved (twice as high as for Nanocyl7000TM MWCNTs). Still, even with the much bigger polypyrrole nanotubes catalyst layer preparation with loadings of 4.0 mg cm⁻² stayed challenging. After gaining a refined understanding which role the methyl orange plays in the catalyst synthesis, a catalyst is prepared with sulfanilic acid instead of methyl orange. The latter shows the same high ORR activity but does not have the feature of a nanotube morphology. Which means that high loadings of 4.0 mg cm⁻² were feasible.

8.2 On the Influence of Methyl Orange During the Synthesis of Polypyrrole-Based Fe-N-C Catalysts

So far it has been shown that the pyrolysis of non-precious metal salts in combination with a methyl orange templated polypyrrole precursors yields ORR catalysts featuring a very high activity. However, the same catalysts derived from just mere polypyrrole shows much lower activity. Hence, the question arises, what is the reason between this striking different behavior. Evidently, the only difference in the synthesis process is the presence of methyl orange during the polymerization of pyrrole. Consequently, this chapter provides insights on how the presence of methyl orange influences the synthesis of the catalyst.

8.2.1 Prepared Catalysts for Investigating the Influence of Methyl Orange

In line with the following chapters, this one will start with a short overview of which catalysts were synthesized and what was the purpose of comparing them. **Table 13** gives the overview of six different catalysts that were prepared.

Table 13: Overview of investigated catalyst materials comparing common PPy to nanotube PPy and investigating the influence of methyl orange.

Sample Name	Polypyrrole Type	Polypyrrole / mg	FeCl ₃ anhydr. / mg	Fe(NO ₃) ₃ x9 H ₂ O / mg	Additional Information
C-GPPy	Globular (common)	300	300	375	40 washing steps
C-GPPy _{MixMO}	Globular (common)	270	300	375	40 washing steps, + 30 mg methyl orange
C-PPy _{40x}	Nanotube	300	300	375	40 washing steps
C-PPy _{5x}	Nanotube	300	300	375	5 washing steps
C-PPy _{0x}	Nanotube	300	300	375	0 washing steps
C-2ht-PPy _{0x+}	Nanotube	300	300	375	Longer acid leaching and 2 heat treatment N ₂ , same as C-2ht-PPy _{+FeCl₃/+Fe(NO₃)₃} (see chapter 8.3.1)

All catalysts are prepared with the same amount of FeCl₃/Fe(NO₃)₃ iron precursor mixture and subjected to the same first heat treatment and acid leaching step. This specific iron precursor mixture yields catalysts that show high ORR activities. The influence of different iron precursors is dealt with in

chapter 8.3. The material denoted as C-GPPy is prepared from "globular" polypyrrole (GPPy). It serves as a reference material. Likewise, C-GPPy_{mixMO} is prepared as a reference catalyst. This catalyst is obtained from globular polypyrrole. Methyl orange is just physically added after the actual polymerization step but before the pyrolysis. Several catalysts are synthesized based on methyl orange templated polypyrrole nanotubes. Trchova et al. showed that methyl orange is likely to be found in trace amounts as dopant inside the polypyrrole network, even after thoroughly washing the polypyrrole nanotubes [441]. The influence of this is investigated by comparing a catalyst that was synthesized from polypyrrole-methyl orange nanotubes that have not been washed after polymerization, C-PPy_{0x}, to a catalyst that has been washed five times according to the procedure given in the experimental part, C-PPy_{5x} and to a catalyst that has been washed thoroughly, 40 times, C-PPy_{40x}. Hence, it is expected that these three catalysts differ in the amount of methyl orange which is still present after the polymerization. The last catalyst, denoted as C-2ht-PPy_{0x+}, is prepared from unwashed polypyrrole-methyl orange nanotubes with a longer acid leaching step (two hours instead of one hour) and underwent a second heat treatment.

Some remarks on the sample notation in this work:

- (1) "GPPy" stands for globular polypyrrole (normal polypyrrole).
- (2) "PPy" stands for polypyrrole that has been synthesized in the presence of methyl orange.
- (3) "C" stands as prefix for a catalyst that has been heat treated and acid leached once.
- (4) "C-2ht" stands for catalyst, which was heat treated, acid leached and heat treated again.
- (5) "C-PPy" following from (2) and (3) stands for a catalyst which was heat treated, acid leached and is based on methyl orange templated polypyrrole.
- (5) "C-GPPy" following from (1) and (3) stands for a catalyst which was heat treated, acid leached and is based on globular polypyrrole.
- (6) "C-PPy_{xyy}" stands for a catalyst which was heat treated, acid leached and is based on methyl orange templated polypyrrole. "xyy" is related to specific information about the catalyst. For instance, the number of washing steps ("40x" or "5x" or "0x"), the type of transition metal precursor ("FeCl₃" or "KMnO₄"), an elongated acid leaching step ("+") or others.

8.2.2 Structural Characterizations

Transmission Electron Microscopy

The morphology of the synthesized materials is investigated by recording TEM photographs. The images of the pristine polypyrrole precursors are given in **Figure 56 a)** and **Figure 56 b)**. The polypyrrole tubes have diameters ranging from 60 nm to several hundred nm. This is in accordance with previously reported values [438, 440]. The morphology of the "common" polypyrrole, is ascribed as aggregation of globular shaped particles [439].

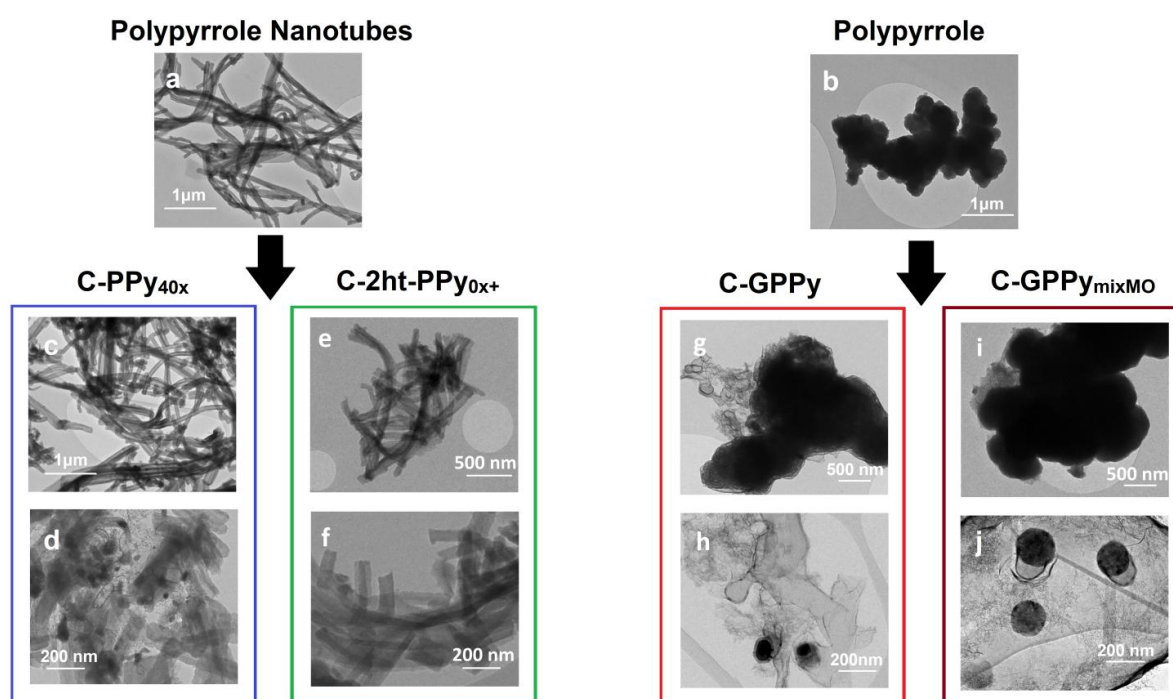


Figure 56: TEM photographs of the two polypyrrole C-N precursors possessing either no specific morphology (b) or showing a nanotube morphology (a), the respective catalyst resulting after pyrolysis are given below (c-j).

After pyrolysis of the globular polypyrrole in combination with the iron salt mixture the morphology is slightly changed (**Figure 56 g) + h)**). Sections of highly graphitized material ascribed to stacked graphene layers were formed around carbon-encapsulated iron particles (see **Figure 56 h)**). It has been shown by temperature dependent X-ray diffraction analysis, that the pyrolysis of a carbon precursor in the presence of iron salts leads to magnetically separable mesoporous graphitic carbon [216]. Whereas in the absence of iron salt, nonporous amorphous carbon was obtained. Iron acts as a catalyst for the graphitization process. For the catalysts prepared from polypyrrole-methyl orange nanotubes this change in morphology is not as distinct as it is for C-GPPy. **Figure 56 c)** and **d)** show the TEM images of C-PPy_{40x}. Similar results are obtained for C-PPy_{5x} and C-PPy₀, related TEM images are given in the appendix (**Figure S6**). For all polypyrrole-methyl orange catalysts the nanotube structure remains

intact after the heat treatment. Small sections of globular-like structured material with embedded iron particles and high degree of graphitization are visible too, but to a smaller extent than for the globular polypyrrole-based catalyst. For C-2ht-PPy_{0x+}, which is shown in **Figure 56 e)** and **f)**, no carbon encapsulated iron particles are found. It is assumed this is due to the longer acid leaching step (extended from 1 hour to 2 hours) and the larger amount of methyl orange residuals that lead to less side phase formation (see Mössbauer part **Figure 58**).

Since sulphur containing precursor mixtures suppress the formation of non-leachable inorganic species, the question arises whether the lower amount of iron particles found for the nanotube catalysts is due to presence of sulphur (from methyl orange residuals) [210, 442]. To gain a deeper understanding of this, the sample C-GPPy_{MixMO} was prepared from a dispersion of globular polypyrrole, iron salts and methyl orange. The TEM photographs are shown in **Figure 56 i)** and **j)**. For C-GPPy_{MixMO} inorganic iron sites are still present relativizing the positive impact of sulphur on this pyrolysis process.

BET-Results

To determine the specific BET surface area of the catalyst, N₂ sorption experiments were conducted. The results are summarized in **Figure 57**.

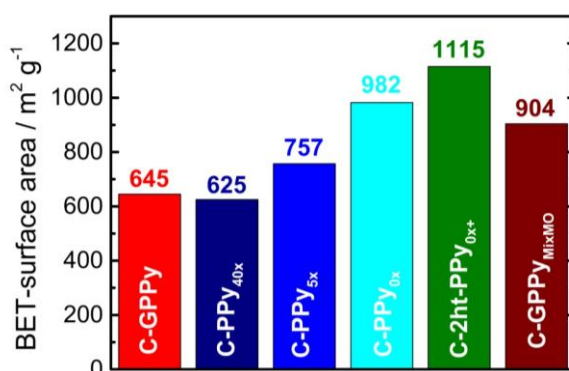


Figure 57: Bar-graphs are presenting the results of the N₂ sorption experiments for catalysts prepared from different polypyrrole precursors.

C-GPPy exhibits a specific surface area of 645 m² g⁻¹. Very similar results for globular polypyrrole-based Fe-N-C catalysts were obtained by Tran et al. who found values ranging from 355 up to 726 m² g⁻¹ depending on the temperature of the pyrolysis process and other synthesis parameters [351]. The surface area of C-PPy_{40x} (40 washing steps, 625 m² g⁻¹) does not differ significantly from C-GPPy. On the contrary, the catalysts derived from polypyrrole nanotubes that still contain methyl orange residues, C-PPy_{5x} and C-PPy_{0x} show a higher BET surface area. C-PPy_{5x} underwent only 5 washing steps and therefore contains more methyl orange than C-PPy_{40x}. The surface area of C-PPy_{5x} is 757 m² g⁻¹. For C-PPy_{0x}, that is prepared from nanotubes without any washing step the N₂-sorption experiments reveal a value of 982 m² g⁻¹. Likewise, C-2ht-PPy_{0x+} that is prepared from unwashed

nanotubes and with twice the time for the acid leaching, the BET surface area of $1115 \text{ m}^2 \text{ g}^{-1}$ is the highest recorded from all the investigated materials. From these experiments, it is stated that the presence of methyl orange is enhancing the overall BET surface area. This statement is also confirmed by the high surface area found for C-PPy_{mixMO}, which is $904 \text{ m}^2 \text{ g}^{-1}$. When comparing C-GPPy to C-PPy_{mixMO} it appears that the surface area enhances about 40 % by solely dispersing methyl orange additionally into the precursor mixture. The decomposition of functional groups present in methyl orange into gaseous products might contribute to a higher BET surface area. Previous work showed that molecules containing functional groups like amino- or cyano-groups decompose and enhance the specific BET surface area significantly [251, 277]. Methyl orange contains an azo-group, a sulfonic acid-group and a tertiary amine. A precise statement on which of the mentioned functional group is responsible is not within the scope of this thesis.

⁵⁷Fe-Mössbauer Spectroscopy

Information on the different iron phases which are present in the catalysts are gained by performing ⁵⁷Fe-Mössbauer spectroscopy. The outcome of these measurements is displayed in **Figure 58**.

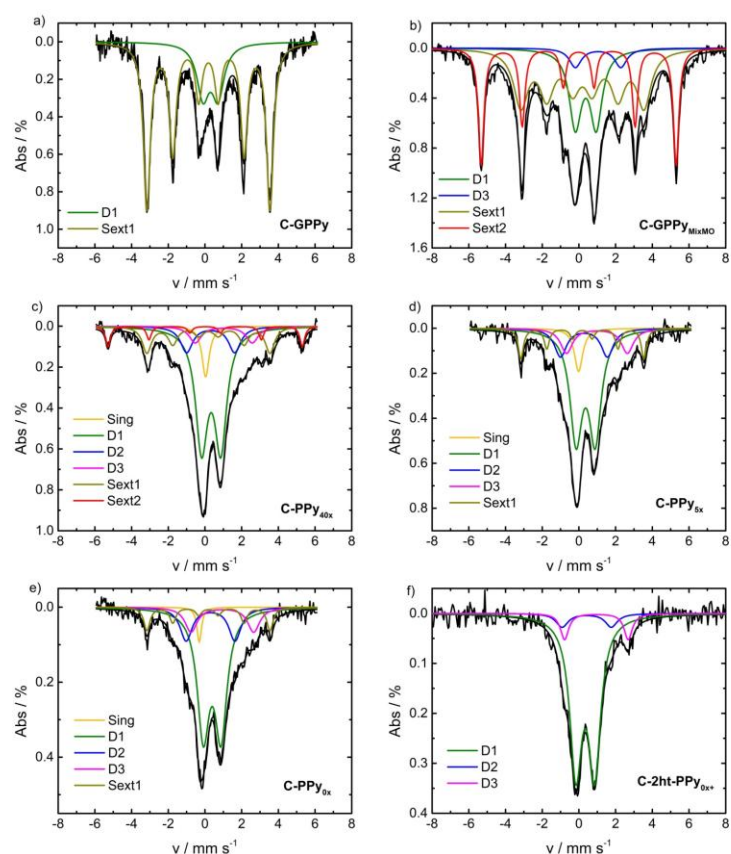


Figure 58: Mössbauer spectra of catalysts prepared from different PPY precursors and from different polypyrrole methyl orange nanotubes.

The isomer shifts, quadrupole splittings and the associated iron species of the obtained signals are summarized in **Table 14**.

Table 14: Mössbauer parameters and iron species assignment.

	C-GPPy		C-GPPy _{MixMO}		C-PPy _{40x}		C-PPy _{5x}		C-PPy _{0x}		C-2ht-PPy _{0x+}	
	population / %		population / %		population / %		population / %		population / %		population / %	
	$\delta_{iso}/$ mm s ⁻¹	$\Delta E_q /$ mm s ⁻¹	$\delta_{iso}/$ mm s ⁻¹	$\Delta E_q /$ mm s ⁻¹	$\delta_{iso}/$ mm s ⁻¹	$\Delta E_q /$ mm s ⁻¹	$\delta_{iso}/$ mm s ⁻¹	$\Delta E_q /$ mm s ⁻¹	$\delta_{iso}/$ mm s ⁻¹	$\Delta E_q /$ mm s ⁻¹	$\delta_{iso}/$ mm s ⁻¹	$\Delta E_q /$ mm s ⁻¹
D1 L ₂ FeN ₄ (2+, S = 0), LFeN ₄ or (3+, S = 5/2), cluster	21.8		21.0		50.9		53.4		58.0		82.9	
	0.30	0.82	0.38	1.14	0.34	1.05	0.37	1.04	0.39	0.97	0.35	1.03
D2 FeN ₄ (2+, S = 1)	-	-	-	-	11.3		14.1		15.9		7.4	
	-	-	-	-	0.31	2.62	0.27	2.55	0.31	2.66	0.43	2.68
D3 FeN ₄ (2+, S = 2)	-	-	5.3		7.2		12.4		11.8		9.6	
	-	-	1.05	2.48	1.03	3.10	0.98	3.32	0.95	3.41	0.95	3.47
Sing	-	-	-	-	6.6		7.3		3.1		-	
	-	-	-	-	0.04		-0.02		-0.31		-	-
Sext1	78.2		44.4		17.2		12.8		11.2		-	
	H = 20.8 T		H = 20.8 T		H = 20.8 T		H = 20.8 T		H = 20.8 T		-	-
Sext2	-	-	29.3		6.8		-		-		-	
	-	-	H = 33.0 T		H = 32.8 T		-	-	-	-	-	-

Inorganic iron, i.e. iron carbide (sext1) is the main iron phase found for the catalyst prepared from globular polypyrrole, C-GPPy and C-GPPy_{MixMO}. In comparison to that, a significant different iron composition is obtained for the polypyrrole methyl orange nanotube-based catalysts, C-PPy_{40x}, C-PPy_{5x}, C-PPy_{0x} and C-2ht-PPy_{0x+}. Doublet species (D1 - D3), which are associated with different FeN₄ centers are the main species present in the polypyrrole methyl orange nanotubes catalysts. From these results one can conclude that methyl orange suppresses the formation of undesired inorganic iron if it is added during the polymerization process. As evident from the data of C-PPy_{40x}, C-PPy_{5x} and C-PPy_{0x} washing of the polypyrrole-methyl orange does have a minor effect on the iron side composition. Still, slightly less inorganic side-phases are formed when the polypyrrole is not washed. The purest iron composition is found for C-2ht-PPy_{0x+}. It is assumed that the longer acid leaching time is responsible for the removal of all sextet species. Note, that the experiments were performed at room temperature, meaning that the doublet species could also be attributed to iron or iron oxide nano clusters, as reported by Wagner et al. [425].

Raman-Spectroscopy

To validate the carbonization process of the polypyrrole precursors Raman spectroscopy was conducted. **Figure 59 a)** and **c)** show the Raman spectra of polypyrrole and polypyrrole nanotubes after pyrolysis at different temperatures. For this experiment thoroughly washed polypyrrole and polypyrrole tubes were used to avoid the influence of possible effects of FeCl_3 or remaining excess methyl orange.

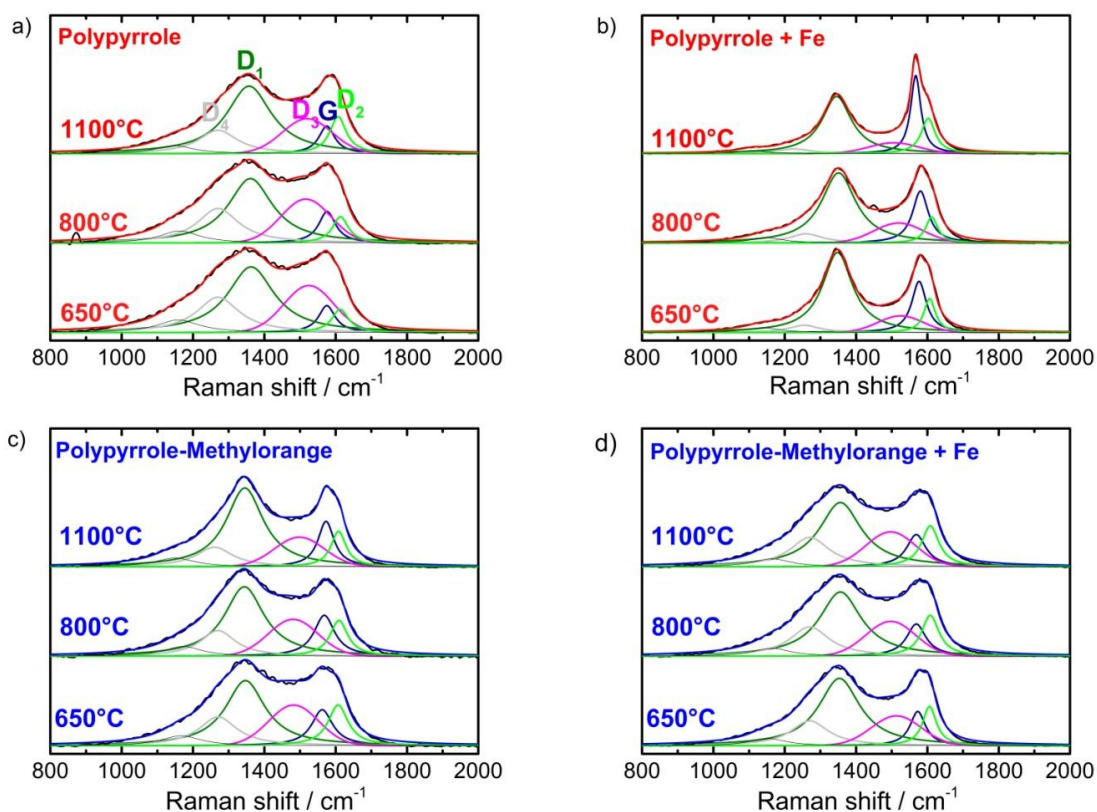


Figure 59: Raman spectra obtained after pyrolysis at different temperatures for polypyrrole (a), polypyrrole-methyl orange nanotubes (b), polypyrrole and Fe-precursor mixture (c) and polypyrrole-methyl orange nanotubes and Fe-precursor mixture (d).

The spectra show main features of broad D- and G-bands ranging from around 1330 cm^{-1} to 1600 cm^{-1} . These broad features are generally ascribed to amorphous sp^2 -carbons, as found for instance in soot [443, 444]. Similar predominant features were obtained for FeTMPPCl based Fe-N-C catalysts by Kramm et al. and for a polyaniline-Ketjenblack based catalyst by Wu et al. [32, 122]. With increasing pyrolysis temperature, the graphitization of both polypyrrole types proceeds almost unnoticeably as indicated by the very slight lowering of the D_3 -band ($1480\text{--}1510\text{ cm}^{-1}$) intensities in relation with the increasing prominence of the D_1 - ($1330\text{--}1350\text{ cm}^{-1}$), D_2 - ($1480\text{--}1510\text{ cm}^{-1}$) and G-band ($1560\text{--}1570\text{ cm}^{-1}$) [445]. Whereas for the polypyrrole-methyl orange nanotubes this transformation might be slightly more pronounced. Particularly for the higher pyrolysis temperatures of $1100\text{ }^\circ\text{C}$. Still, the overall changes of the Raman spectra without the addition of any iron precursors are of minor extent.

Figure 59 b) and **d)** give the Raman spectra of unwashed polypyrrole and polypyrrole-methyl orange nanotubes in the presence of $\text{FeCl}_3/\text{Fe}(\text{NO}_3)_3$, again for the different pyrolysis temperatures. Which means the same precursors mixtures as for the preparation of the catalysts were used. In comparison to the sample which was pyrolyzed in absence of any iron, **Figure 59 a)**, a significant increase in the G-band feature as well as a lowering of the D_3 -band is found for the mixture of normal polypyrrole and the iron salts, **Figure 59 b)**. This finding is expected because in the presence of iron salts highly graphitized sections of iron carbide are formed, especially at elevated temperatures [216, 319, 424, 446]. Contrary, no significant changes in the Raman spectra are obtained after heat treating the polypyrrole-methyl orange nanotube precursor. Neither in the absence nor in the presence of iron salts, even at high temperatures of 1100 °C.

In short, the reported Raman spectra support the previous findings of TEM and ^{57}Fe -Mössbauer spectroscopy experiments. Fe-salts catalyze the graphitization of polypyrrole by forming inorganic iron compounds. This appears to happen at even mild temperatures of 650 °C. Contrary, if polypyrrole-methyl orange nanotubes are exposed to a heat treatment in the presence of iron salts no higher degree of graphitization is found. This means that the formation of undesired inorganic iron phases is suppressed. Even at significantly elevated temperatures of 1100 °C, the main carbon phase of polypyrrole-methyl orange nanotubes remains amorphous.

8.2.3 Electrochemical Experiments

RRDE Performance of Fe-N-C Catalysts Prepared from Different Polypyrrole Precursors

The electrochemical activity of the prepared catalysts towards acidic ORR is determined via RRDE. The reductive scan in oxygen saturated electrolyte with a rotation rate of 1500 rpm and the respective hydrogen peroxide yield for C-GPPy, C-GPPy_{mixMO} and C-PPy_{40x} are shown in Figure 60.

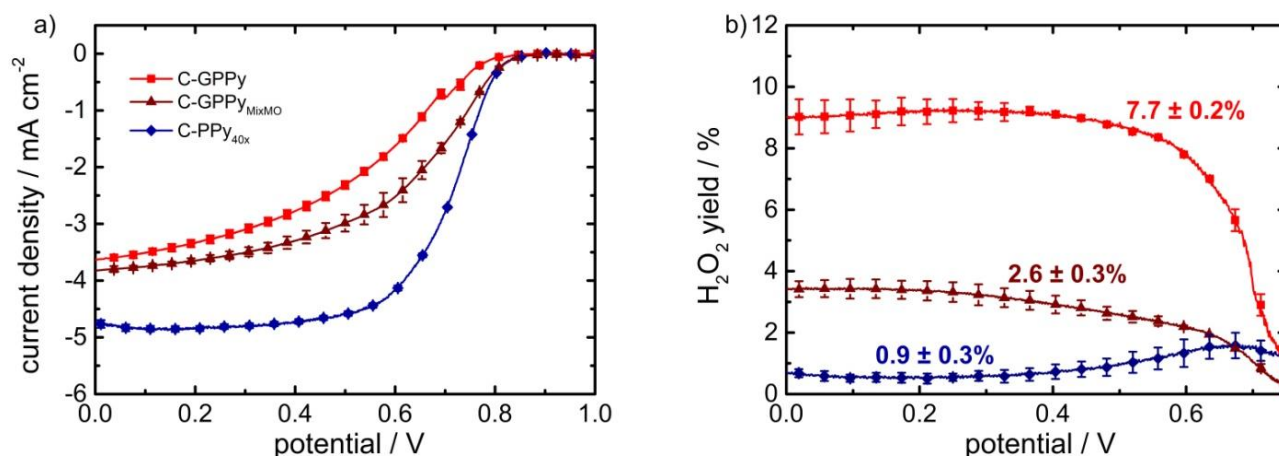


Figure 60: Reductive scans of the polarization curves obtained in 0.1 M H₂SO₄ saturated with O₂, rotation rate of 1500 rpm, 10 mV s⁻¹ and a disc loading of 0.5 mg cm⁻². The disc current density is given in a) and the H₂O₂ yield in b).

The ORR activity of C-GPPy and C-GPPy_{mixMO} is significantly lower compared to that of the catalyst prepared from the nanotube structured C, N precursor, C-PPy_{40x}. In comparison to C-PPy_{40x}, the onset potential of C-GPPy is shifted by a value of about 50 mV towards lower potentials (C-GPPy 790 mV – C-PPy_{40x} 840 mV). For a very similar synthesis approach but with two heat treatments at 800 °C and an intermediate acid leaching step in H₂SO₄ applying globular polypyrrole and FeCl₃, Tran et al. obtained an onset potential in acidic media of 720 mV (0.5 M H₂SO₄, catalyst disc loading of 0.4 mg cm⁻²) [351]. A similar trend of activity for globular and nanotube structured catalysts was found by Morozan et al. in alkaline media [447]. The acid red based templated polypyrrole synthesis resulted in a catalyst with a onset potential shift of 178 mV towards lower potentials than the respective catalyst prepared from globular polypyrrole. In addition to the onset potential, the diffusion limited current of C-GPPy barely reaches a plateau, a maximum value of 3.67 mA cm⁻² is measured. Whereas for C-PPy_{40x} a defined plateau is formed. The value of the diffusion limited current is ~ 4.80 mA cm⁻². As seen for C-GPPy_{mixMO}, additional mixing of methyl orange to the globular polypyrrole precursors slightly enhances the ORR activity. Still, the ORR activity remains much lower than that of C-PPy_{40x}. The hydrogen peroxide formation follows the reverse sequence as the ORR activity, C-GPPy > C-GPPy_{mixMO} > C-PPy_{40x}. It is noticeable that in case of selectivity the difference between C-GPPy (7.5 %) and C-GPPy_{mixMO} (2.4 %) is more significant than the difference found for ORR activity. This behavior is

explained by the presence of a sulphur containing functional group of methyl orange in the precursor mixture of C-GPPy_{mixMO}. Sulphur has been shown to affect the synthesis process of Fe-N-C catalysts in numerous ways. For instance, Kicinsky et al. showed that sulphur addition enhances the micro porosity of the resulting catalyst materials [309]. Furthermore, it was shown experimentally and by thermodynamic calculations that sulphur restrains the formation of iron carbide [210]. Both, a higher BET surface area and the suppression of iron carbide formation have been shown to increase selectivity of the ORR in RRDE experiments [184, 250]. The N₂ sorption and Mössbauer experiments in this work confirm these previous reports. To further understand the influence of methyl orange which remains in the precursor mixture **Figure 61** shows the ORR activity and selectivity for the catalyst prepared from differently washed nanotube precursors.

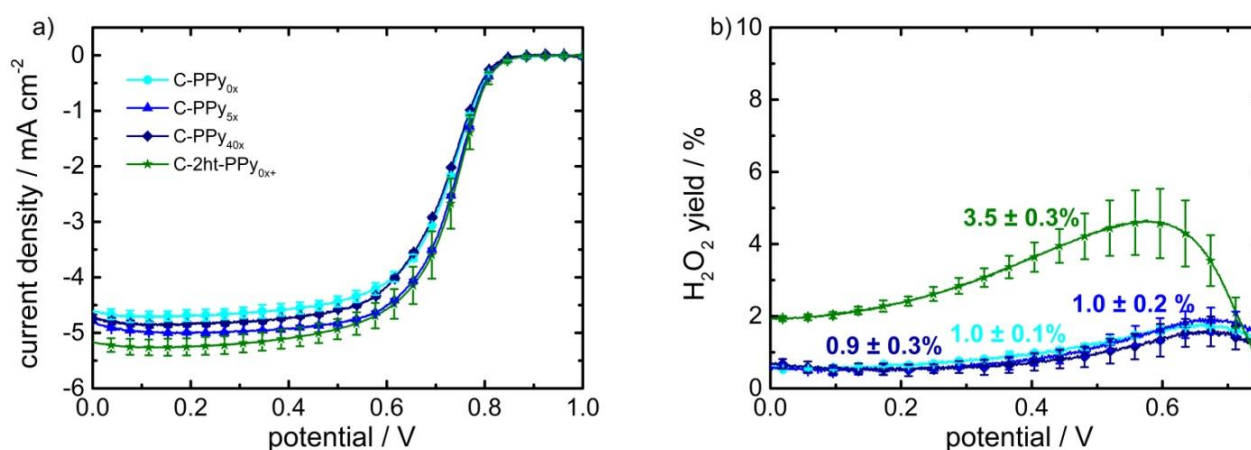


Figure 61: Polarization curves of prepared catalysts in O₂ saturated 0.1 M H₂SO₄ obtained with a rotation rate of 1500 rpm, a sweep rate of 10 mV s⁻¹ and a disc loading of 0.5 mg cm⁻², disc currents density a) and H₂O₂ yield calculated from the measured ring currents b).

From these curves it is concluded that the ORR activity and selectivity during RRDE experiments is not affected noticeably. This outcome is expected as these catalysts do not differ significantly in their composition (Mössbauer experiments) but only slightly in their BET surface area. Applying a longer acid leaching and a second heat treatment on C-PPy_{0x} gives a slightly more active catalyst material, C-2ht-C-PPy_{0x+}. The onset potential of C-2ht-PPy_{0x+} is 850 mV. Applying two heat treatments at 900 °C and an intermediate acid leaching step in H₂SO₄ on a mixture of globular polypyrrole and FeCl₃, Tran et al. obtained an onset potential of 814 mV (0.5 M H₂SO₄, catalyst loading 0.4 mg cm⁻²)[351]. Contrary, the selectivity of C-2ht-C-PPy_{0x+} is the lowest found for all polypyrrole nanotube-based catalyst materials.

PEMFC Tests

To validate the catalysts performance under fuel cell conditions, PEMFC single cell tests were performed. Catalyst stability will be investigated within the later chapters. The polarization curves and power outputs of C-PPy_{40x}, C-PPy_{5x}, C-PPy_{0x}, C-2ht-PPy_{0x+} and C-GPPy in H₂-O₂ are displayed in **Figure 62**. The trends from RRDE are confirmed during PEMFC single cell tests.

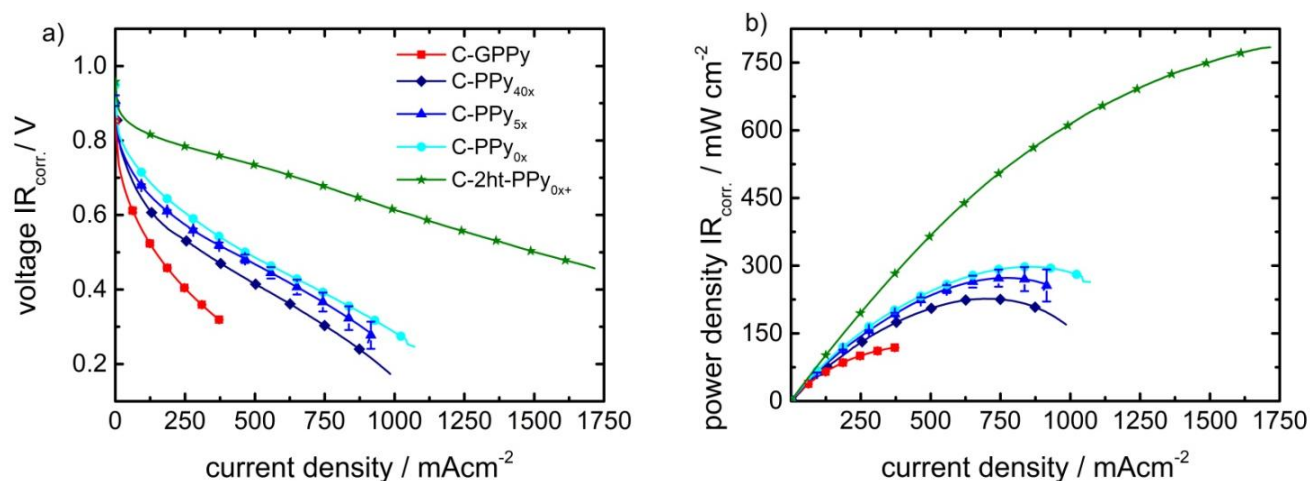


Figure 62: PEMFC polarization curves of different polypyrrole catalysts, voltage against current density (a) and voltage against power density (b). (experiment conditions: H₂-O₂, cathode loading 2.1 - 3.3 mg cm⁻², N212 membrane, 1 bar gauge back pressure, 0.2 L min⁻¹ oxidant and fuel flow, 80 °C, 96 % humidity).

C-PPy_{40x} reaches a maximum power output (227 mW cm⁻²) which is almost twice as high as to that of C-GPPy (115 mW cm⁻²). Further, **Figure 62** shows the results for the washing variation series investigating the influence of methyl orange. Contrary to the results obtained during RRDE experiments, where ORR activity was not significantly different, the PEMFC single cell tests reveal that with increasing amount of remaining methyl orange the cell performance increases simultaneously. What might be explained by the slight increase in BET surface area. **Table 15** summarizes characteristic values of the fuel cell testing, methyl orange content and the BET values.

Table 15: Correlation of relative methyl orange content of the polypyrrole nanotube precursor to the BET surface area of the final catalyst and the maximum power output during PEMFC tests.

Sample Name	Cathode loading / mg cm ⁻²	Washing steps	Relative methyl orange content	BET-surface area / m ² g ⁻¹	Maximum power output / mW cm ⁻²
C-PPy _{40x}	2.5	40 washing steps	Low	625	227
C-PPy _{5x}	2.6	5 washing steps	Medium	757	254
C-PPy _{0x}	2.2	0 washing steps	High	982	297
C-2ht-PPy _{0x+}	3.3	0 washing steps	High	1115	780

The polarization curves of C-PPy_{0x} and C-2ht-PPy_{0x+} are also given in **Figure 62**. The additional synthesis steps further enhance the cell performance (longer acid leaching and second heat treatment). The maximum power output of C-2ht-PPy_{0x+} is about 780 mW cm⁻². It should be mentioned that the cathode catalyst loading of the compared catalysts is not equal. However, they differ in such manner that the trend in activity is not affected. Meaning slightly higher loadings for less active catalysts. The great outperformance of C-2ht-PPy_{0x+} in comparison to the other catalysts is not caused by the higher loading. Details on all cathode loadings of this work are found in **Table 11** (experimental part). The polarization curves of C-2ht-PPy_{0x+} as well as stability under H₂-air are discussed in detail in chapter 9. Likewise, a comparison to other high performing catalysts prepared in this work and the best performing catalysts known from literature is given later.

8.2.4 Brief Summary on the Influence of Methyl Orange

Polypyrrole synthesized in the presence of methyl orange yields a material with a nanotube morphology. Whereas the standard polymerization yields globular-like polypyrrole particles. Catalysts prepared from those two types of polypyrrole show that globular polypyrrole catalysts contain a high amount of inorganic iron particles embedded by highly graphitized carbon layers. Contrary, no iron particles are found for the catalysts prepared from polypyrrole methyl orange nanotubes. By simply mixing methyl orange after the actual polymerization of the polypyrrole, inorganic phase can only slightly be reduced. In other words, methyl orange needs already to be present during the polymerization of pyrrole monomers. It is suggested that methyl orange is strongly implemented into the polymer structure through doping or related effects. Further, N₂-sorption experiments reveal that methyl orange is enhancing the BET surface area of the catalysts. Electrochemical performance tests show a great performance enhancement for the acidic ORR of catalyst synthesized from polypyrrole-methyl orange nanotubes in comparison to common polypyrrole.

8.3 On the Influence of the Fe-Precursor Salt

This chapter will address the influence of the Fe precursor on the synthesis of the polypyrrole-methyl orange nanotubes catalyst. As outline in chapter 5 (page 42) it is one of the most crucial parameters in Fe-N-C catalyst preparation. Within the following chapter several catalysts are prepared, characterized and optimized towards acidic ORR and the application inside PEMFCs. The investigated salts here were chosen because they are commonly used in Fe-N-C catalyst synthesis meaning they are cheap and practical. Further, the salts were chosen so that a statement on the influence the oxidation states (Fe^{2+} vs Fe^{3+}) and type of counterions (chloride vs nitrate etc.) can be made.

8.3.1 Prepared Catalysts and Investigated Fe-Precursors

All catalysts prepared in this chapter have been synthesized based on the polypyrrole-methyl orange approach. In total five different iron salts and one iron salt mixture has been tested. Following the polymerization, the polypyrrole was mixed with the different types of iron salts. These mixtures were carbonized and acid leached. **Table 16** gives an overview of the prepared catalysts and the investigated iron salts. All details are given in the experimental part, chapter 6.

Table 16: Summary of prepared Fe-N-C catalysts based on different iron salt precursors.

Sample Name	Polypyrrole Tube Type	Type of Iron Salt	Polypyrrole Tube / mg	Iron salt / mg	Mass 1 HT / mg
C-PPy _{Fe(Ox)}	washed	$\text{Fe}(\text{C}_2\text{O}_4) \times 2 \text{H}_2\text{O}$	350	387	233
C-PPy _{Fe(Ac)₂}	washed	$\text{Fe}(\text{CH}_3\text{CO}_2)_2$	350	374	263
C-PPy _{Fe(NO₃)₃}	washed	$\text{Fe}(\text{NO}_3)_3 \times 9 \text{H}_2\text{O}$	350	871	74
C-PPy _{FeCl₃}	washed	FeCl_3	350	350	277
C-PPy _{FeCl₂}	washed	$\text{FeCl}_2 \times 6 \text{H}_2\text{O}$	350	506	250
C-PPy _{FeCl₃/Fe(NO₃)₃}	washed	$\text{FeCl}_3 + \text{Fe}(\text{NO}_3)_3 \times 9 \text{H}_2\text{O}$	350	233 + 292	240

Based on RRDE results, a selection of three catalysts were subjected to a second heat treatment and tested in the PEMFC. These are listed in **Table 17**. Further, for the best performing catalysts the amounts of iron salts were varied in order to obtain an optimized fuel cell performance.

Table 17: Overview of catalyst materials that underwent a second heat treatment and further investigations during PEMFC testing.

Sample Name	Polypyrrole Tube Type	Type of Iron Salt	Polypyrrole Tube / mg	Iron salt / mg
C-2ht-PPy _{FeCl₃}	unwashed	FeCl ₃	350	350
C-2ht-PPy _{FeCl₃/Fe(NO₃)₃}	unwashed	FeCl ₃ + Fe(NO ₃) ₃ x 9 H ₂ O	350	233 + 292
C-2ht-PPy _{FeCl₂}	unwashed	FeCl ₂ x 6 H ₂ O	350	506
C-2ht-PPy _{+FeCl₂}	unwashed	FeCl ₂ x 6 H ₂ O	350	700
C-2ht-PPy _{++FeCl₂}	unwashed	FeCl ₂ x 6 H ₂ O	350	850
C-2ht-PPy _{+FeCl₃/+Fe(NO₃)₃}	unwashed	FeCl ₃ + Fe(NO ₃) ₃ x 9 H ₂ O	350	350 + 437

8.3.2 Structural Characterizations

Transmission Electron Microscopy

The TEM pictures of the catalysts, which were prepared with different iron precursors are given **Figure 63**.

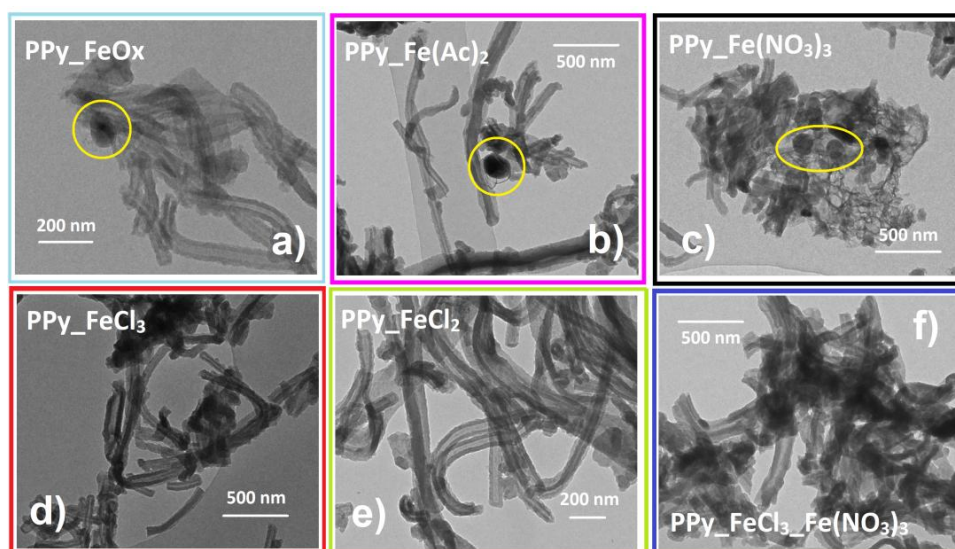


Figure 63: TEM images of polypyrrole-methyl orange nanotubes after pyrolyzation with different iron salts.

The carbonization of nanotubes in the presence of different iron salts yields various structured materials. For C-PPy_{Fe(Ox)}, C-PPy_{Fe(Ac)₂} and C-PPy_{Fe(NO₃)₃} carbon encapsulated iron particles are present (yellow cycles). Contrary, when using FeCl₂, FeCl₃ or the mixture of FeCl₃ and Fe(NO₃)₃ no inorganic species are visible. In addition, when comparing C-PPy_{Fe(NO₃)₃} and C-PPy_{FeCl₃/Fe(NO₃)₃} it appears that the nanotubes structure is altered when greater amounts of C-PPy_{Fe(NO₃)₃} are used. For both samples, the nanotubes are shorter in length and are agglomerated or even melted together in comparison to the rest of the materials. In C-PPy_{Fe(NO₃)₃}, sections of carbonized material were formed that are not resembling the initial nanotube morphology anymore. Contrary, when applying FeCl₂, FeCl₃, Fe(Ac)₂ or Fe(Ox) the morphology of the nanotubes stays largely intact.

BET Results

Figure 64 gives the BET surface areas of the prepared catalysts. The values were obtained by N₂ sorption experiments.

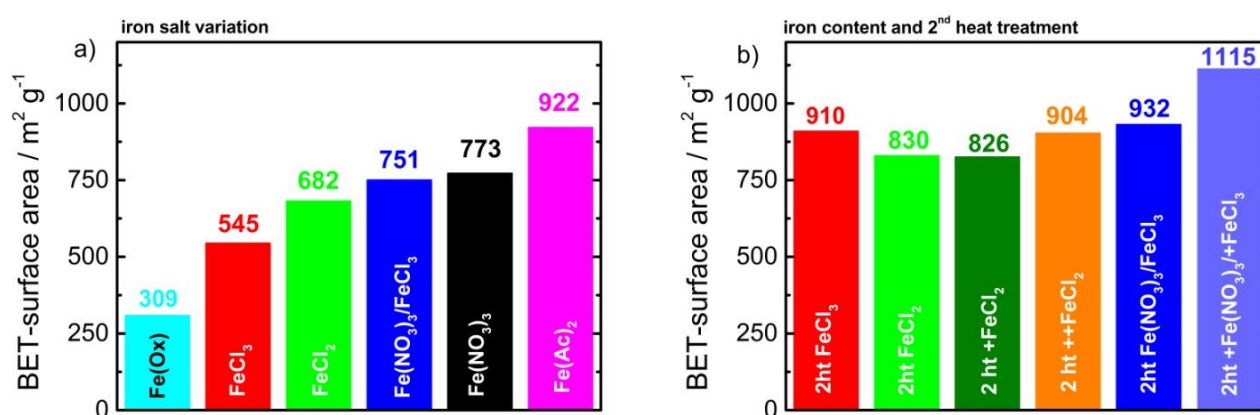


Figure 64: BET surface areas of polypyrrole methyl orange nanotube catalysts prepared from different iron salts (a) and BET surface areas after a second heat treatment and with varying iron salt content (b).

Before the pyrolysis, the surface area of the polypyrrole nanotubes is 81 m² g⁻¹ (not shown in Figure 64). After pyrolysis in the presence of iron salts, the surface area is significantly enhanced. Values of 309 up to 1115 m² g⁻¹ were measured. When comparing the different type of iron salts in Figure 64 a), it appears that the oxygen-containing iron salts (counter ions) result in catalysts with high BET surface areas. Those are C-PPy_{Fe(Ac)₂} and C-PPy_{Fe(NO₃)₃}, the measured BET surface area is 773 and 922 m² g⁻¹. However, PPy_{Fe(Ox)} fails to confirm this trend. For C-PPy_{FeCl₂} and C-PPy_{FeCl₃} values of 682 m² g⁻¹ and 545 m² g⁻¹ are measured. The C-PPy_{FeCl₃/Fe(NO₃)₃} sample has a BET surface area of 751 m² g⁻¹, which is slightly higher than that of C-PPy_{FeCl₃}. Hence, the mixture of FeCl₃ and Fe(NO₃)₃ seems to be a good compromise. It is reaching a relatively high surface area caused by the oxygen containing NO₃-ions, while keeping a pure iron composition. After a second heat treatment the surface area is further

increased, see **Figure 64 b**). For instance, C-PPy_{FeCl₃/Fe(NO₃)₃} shows a surface area of 751 m² g⁻¹ and after the second heat treatment the surface area of C-2ht-PPy_{FeCl₃/Fe(NO₃)₃} is enhanced to 932 m² g⁻¹. This corresponds to an increase of about 20 %. Similar results are obtained for C-PPy_{FeCl₂} and C-PPy_{FeCl₃}. Likewise, Koslowski et al. reported an increased surface area after a second heat treatment for porphyrin-based catalysts [197]. In addition, the BET surface area of C-2ht-PPy_{FeCl₃/Fe(NO₃)₃} is increased by adding greater amounts of FeCl₃ and Fe(NO₃)₃. This catalyst, denoted as C-2ht-PPy_{+FeCl₃/+Fe(NO₃)₃}, exhibits a surface area of 1115 m² g⁻¹. Contrary, when increasing the amount of FeCl₂ no clear trend was obtained, as seen from the values measured for C-2ht-PPy_{+FeCl₂} and C-2ht-PPy_{+FeCl₂}.

Mössbauer Spectroscopy

The iron salt has a strong influence of the formed iron phases inside the catalyst. This becomes apparent from the measured Mössbauer spectra in **Figure 65**.

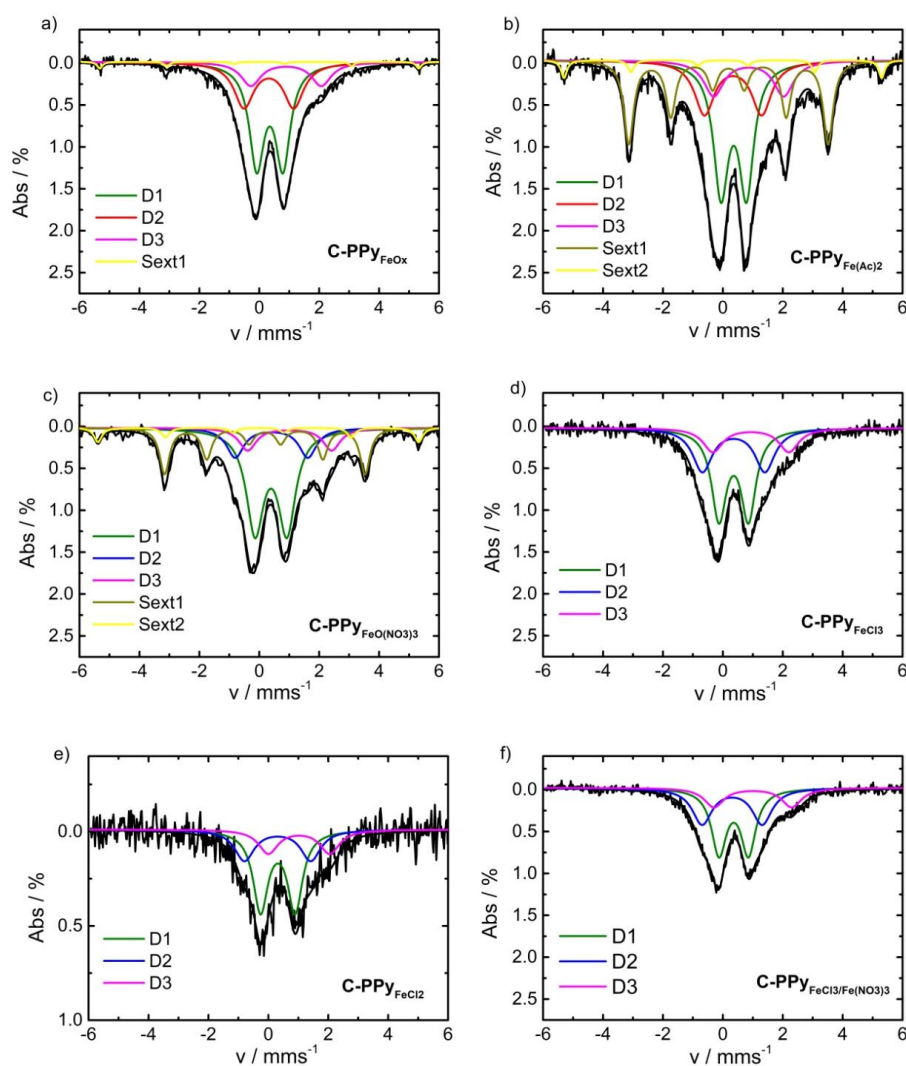


Figure 65: Mössbauer spectra of polypyrrole methyl orange nanotube catalysts prepared with different iron salts.

Table 18 gives the Mössbauer parameters and the assignment of the different iron species for the examined catalysts.

Table 18: Mössbauer parameters and assignment of iron species for the polypyrrole-methyl orange-based catalysts which were prepared with different iron salts.

	C-PPy _{Fe(Ox)}		C-PPy _{Fe(Ac)2}		C-PPy _{Fe(NO3)3}		C-PPy _{FeCl2}		C-PPy _{FeCl3}		C-PPy FeCl3/Fe(NO3)3	
	population / %		population / %		population / %		population / %		population / %		population / %	
	$\delta_{iso} /$ mm s ⁻¹	$\Delta E_q /$ mm s ⁻¹	$\delta_{iso} /$ mm s ⁻¹	$\Delta E_q /$ mm s ⁻¹	$\delta_{iso} /$ mm s ⁻¹	$\Delta E_q /$ mm s ⁻¹	$\delta_{iso} /$ mm s ⁻¹	$\Delta E_q /$ mm s ⁻¹	$\delta_{iso} /$ mm s ⁻¹	$\Delta E_q /$ mm s ⁻¹	$\delta_{iso} /$ mm s ⁻¹	$\Delta E_q /$ mm s ⁻¹
D1 L ₂ FeN ₄ (2+, S = 0), LFeN ₄ (3+, S = 5/2), cluster	51.5		34.8		46.3		52.5		49.8		46.7	
	0.35	0.88	0.36	0.85	0.39	1.07	0.32	1.15	0.36	0.98	0.36	0.98
D2 FeN ₄ (2+, S = 1)	30.2		19.2		13.6		27		32.3		34.7	
	0.32	1.66	0.34	1.91	0.41	2.42	0.31	2.21	0.36	2.01	0.31	2.00
D3 FeN ₄ (2+, S = 2)	16.1		12.8		10.4		21		17.9		18.6	
	0.90	2.35	0.86	2.34	1.01	2.80	1.02	2.05	0.94	2.54	1.00	2.59
Sext1 iron carbide	-	-	29.4		23.9		-	-	-	-	-	-
			H = 20.63 T		H = 20.75 T							
Sext2 α -iron	2.3		3.8		5.9		-	-	-	-	-	-
	H = 33.02 T		H = 32.89 T		H = 33.2 T							

From the prepared catalysts three show major contribution of inorganic iron phases. These are C-PPy_{Fe(Ox)}, C-PPy_{Fe(Ac)2} and C-PPy_{Fe(NO3)3}. The detected inorganic phases can be ascribed to iron carbide and α -iron [424]. Interestingly, the counter ion of these iron salts contains an oxygen atom. In contrast to this, the catalysts prepared from FeCl₂ and FeCl₃ do not show contributions of inorganic phases. The shown doublet species (D1- D3) can be assigned to different FeN₄ centers of different oxidation and spin states as well as different axial ligands [424]. As apparent from the spectra of C-PPy_{FeCl3/Fe(NO3)3}, it is possible to obtain a "sextet-free" catalyst from a mixture of FeCl₃ and Fe(NO₃)₃. From these results one can conclude that the type and also the amount of iron salt plays an important role when it comes to iron composition of the final catalyst.

8.3.3 Electrochemical Experiments

RRDE Experiments of Catalysts Prepared with Different Iron Salts

The linear sweep voltammograms and H₂O₂ yields of the iron salt variation are shown **Figure 66**.

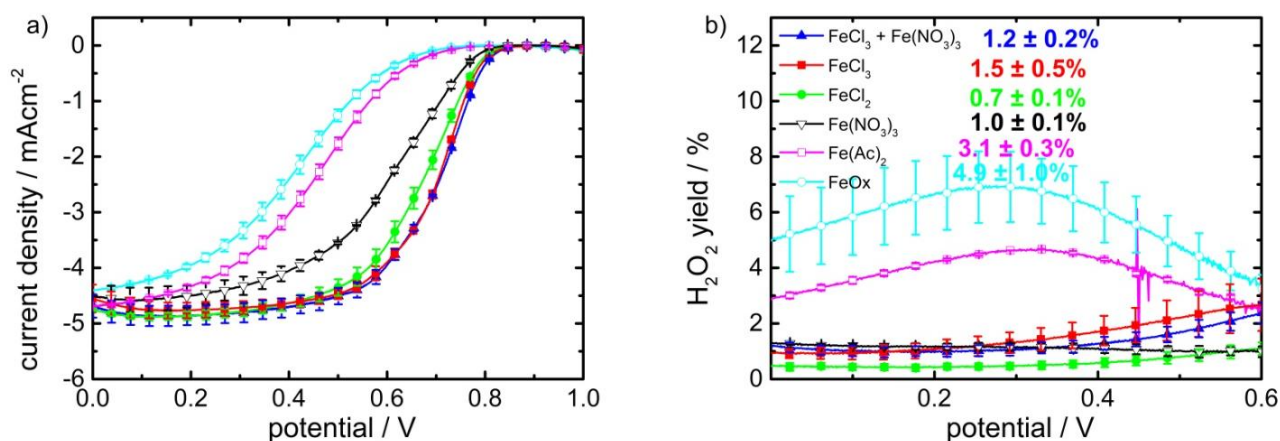


Figure 66: ORR polarization curves a) and respective H₂O₂ yields b) for the catalysts prepared from different iron precursors recorded with a sweep rate of 10 mV s⁻¹ in O₂ saturated 0.1 M H₂SO₄ a rotation rate of 1500 rpm and a disc loading of 0.5 mg cm⁻².

The ORR performance is strongly depending on the type of iron precursor which was used. The observed trend in activity is C-PPy_{Fe(Ox)} < C-PPy_{Fe(Ac)₂} < C-PPy_{Fe(NO₃)₃} < C-PPy_{FeCl₂} < C-PPy_{FeCl₃} < C-PPy_{FeCl₃/Fe(NO₃)₃}. The maximum shift in the onset potential of 145 mV is observed between the catalysts prepared with Fe(Ox) (680 mV) and FeCl₃ + Fe(NO₃)₃ (825 mV). This emphasizes that the type of iron precursor plays a crucial role for ORR activity of Fe-N-C catalysts. In light of that, a systematic validation of different iron precursors is necessary in order to obtain a high ORR performance. Whereas it is important to notice that the appropriate iron salt is also strongly depending on the C, N precursor. For instance, in this study, the catalysts based on polypyrrole and Fe(Ox) have the lowest ORR activity. On contrary, for porphyrin-based catalysts systems, Fe(Ox) is capable to function as a structure forming agent and therefore has proven to be an excellent iron precursor / structuring template [181, 195, 230]. Considering the ORR selectivity in **Figure 66 b)**, a similar trend to the ORR activity is observed. Here, C-PPy_{Fe(Ox)} and C-PPy_{FeCl₂} differ the most. The average H₂O₂ yield decreases from 6.1 % (FeOx) to 0.5 % (FeCl₂). The high H₂O₂ yields, which are measured for C-PPy_{Fe(Ox)} and C-PPy_{Fe(Ac)₂}, are in good accordance with the strong contribution of inorganic iron phases found during Mössbauer experiments. For the acidic ORR, these species have been proven to be less selective than the atomically dispersed Fe-sites [184]. C-PPy_{Fe(NO₃)₃} does not show this correlation between inorganic iron species and higher H₂O₂ yield. This is because ORR selectivities are also influenced by (I) high disc loadings of the RRDE which are typically used when investigating Fe-N-C

catalysts and (II) the BET surface area of the catalysts [427]. In combination both might lead to trapping of H_2O_2 inside the catalyst layer, so less is detected at the RRDE ring. Experiments with lower catalyst loadings could help to estimate the true selectivity.

PEMFC Tests

After screening the activity of the catalysts in the RRDE setup, the most promising catalysts were subjected to a second heat treatment and investigated by PEMFC tests. These are $\text{C-PPy}_{\text{FeCl}_2}$, $\text{C-PPy}_{\text{FeCl}_3}$ and $\text{C-PPy}_{\text{FeCl}_3/\text{Fe}(\text{NO}_3)_3}$. The fuel cell polarization curves measured under $\text{H}_2\text{-O}_2$ are shown in **Figure 67**. The catalysts exhibit good ORR activities under PEMFC testing conditions, the peak power densities range from 350 to over 600 mW cm^{-2} . The current density recorded for an IR corrected cell voltage of 800 mV are 31 mA cm^{-2} ($\text{C-2ht-PPy}_{\text{FeCl}_3}$), 64 mA cm^{-2} ($\text{C-2ht-PPy}_{\text{FeCl}_2}$) and 70 mA cm^{-2} ($\text{C-2ht-PPy}_{\text{FeCl}_3/\text{Fe}(\text{NO}_3)_3}$).

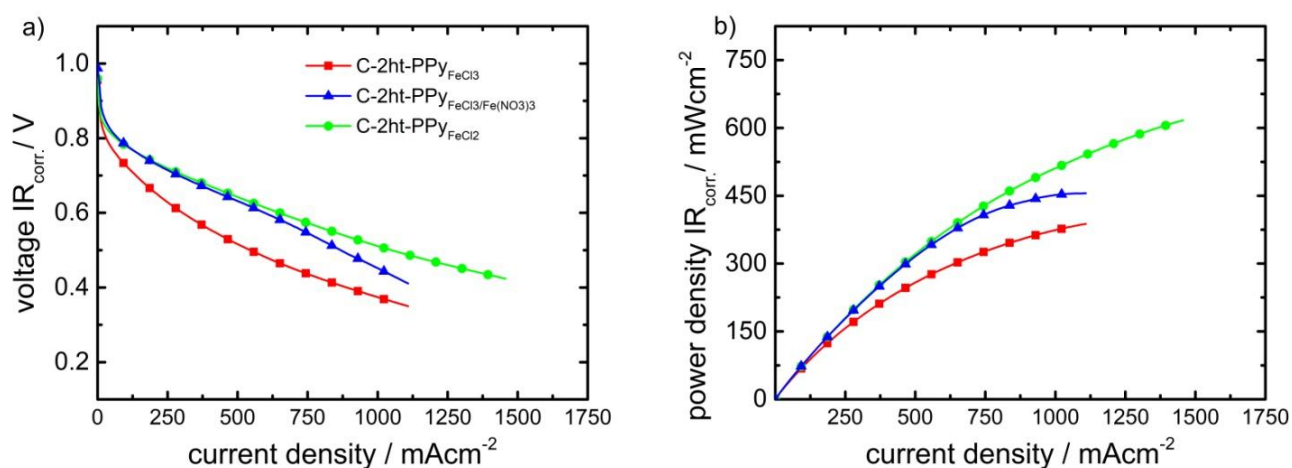


Figure 67: PEMFC polarization curves of polypyrrole-methyl orange catalysts prepared with different iron salts, voltage against current density (a) and voltage against power density (b). (experiment conditions: $\text{H}_2\text{-O}_2$, cathode loading 3.3 - 3.4 mg cm^{-2} , N212 membrane, 1 bar gauge back pressure, 0.2 L min^{-1} oxidant and fuel flow, 80 °C, 96 % humidity).

Since $\text{C-2ht-PPy}_{\text{FeCl}_2}$ and $\text{C-2ht-PPy}_{\text{FeCl}_3/\text{Fe}(\text{NO}_3)_3}$ show the most promising performances, these two materials were selected for further optimization considering the amount of used iron salt. For FeCl_2 , two additional samples were prepared, each containing a higher amount of iron precursor. These samples are denoted as $\text{C-2ht-PPy}_{+\text{FeCl}_2}$ and $\text{C-2ht-PPy}_{++\text{FeCl}_2}$. With reference to $\text{C-2ht-PPy}_{\text{FeCl}_3/\text{Fe}(\text{NO}_3)_3}$ one more catalyst with a higher $\text{Fe}(\text{NO}_3)_3$ and FeCl_3 content in the precursor mixture was prepared. It is denoted as $\text{C-2ht-PPy}_{+\text{FeCl}_3/+ \text{Fe}(\text{NO}_3)_3}$. The polarization curves and power densities of these catalysts are shown in **Figure 68**. When adding more FeCl_2 to the precursor mixture of $\text{C-2ht-PPy}_{\text{FeCl}_2}$ only a slight increase in activity is achieved, as seen for $\text{C-2ht-PPy}_{+\text{FeCl}_2}$. The iron salt amount seems to be already at or very close to an optimum. However, when adding excess amounts of FeCl_2 the activity is again decreasing, this is the case for $\text{C-2ht-PPy}_{++\text{FeCl}_2}$. Contrary, $\text{C-2ht-PPy}_{+\text{FeCl}_3/+ \text{Fe}(\text{NO}_3)_3}$ shows a more

decisive improvement. In comparison to C-2ht_{PPy}FeCl₃/Fe(NO₃)₃ the current density recorded for a IR corrected cell voltage of 800 mV increases from 70 mA cm⁻² to 180 mA cm⁻². Likewise, a peak power density of 780 mW cm⁻² is measured for C-2ht-PPy_{+FeCl₃/+Fe(NO₃)₃}.

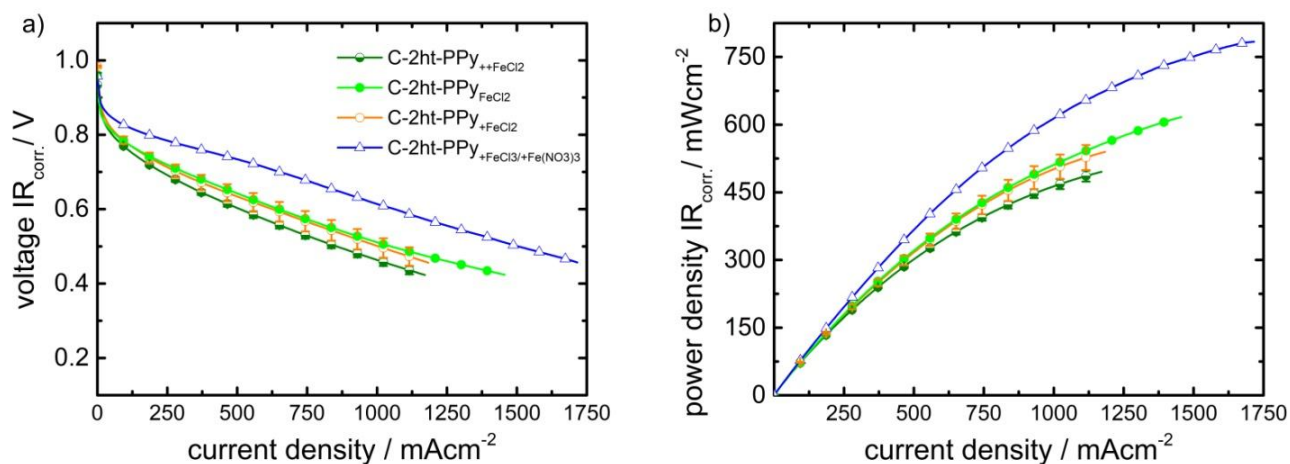


Figure 68: PEMFC polarization curves of polypyrrole-methyl orange catalysts prepared with different iron salts and with altering iron salts amounts after a second heat treatment, voltage against current density (a) and voltage against power density (b). (experiment conditions: H₂-O₂, cathode loading 3.2 - 3.4 mg cm⁻², N212 membrane, 1 bar gauge back pressure, 0.2 L min⁻¹ oxidant and fuel flow, 80 °C, 96 % humidity).

8.3.4 Brief Summary on the Influence of Different Iron Salts

The type and the amount of the iron salt which is used in the synthesis of Fe-N-C catalysts plays a crucial role. The activity can be boosted by choosing optimized parameters. In particular, it was shown that a catalyst prepared with a FeCl₃/Fe(NO₃)₃ mixture benefits from the compromise of a pure active site composition, which is obtained when adding FeCl₃, and the high surface, induced by the pore forming properties of Fe(NO₃)₃. Mössbauer spectroscopy revealed that the amount and more especially the type of iron precursor governs the nature of the formed iron sites as well as the catalyst's BET surface area. Both of these characteristics govern the performance of a non-precious metal-based ORR catalyst to a very high degree. Choosing the right iron salts during the preparation of Fe-N-C catalysts is therefore of exceptional high relevance.

8.4 Optimization of a Mn-Fe-precursor Mixture

The previous chapter revealed that the iron salts, used in the precursor mixture during synthesis of Fe-N-C catalysts, play an important role. However, iron was established as the only type of non-precious metal. In this chapter the influence of different manganese salts as well as the combination of manganese with iron precursor salts is identified. In general, manganese based non-precious metal ORR catalysts are reported to be less active than iron-based ones. However, Higgins et al. showed for an iron, polyaniline and Ketjenblack derived catalyst system a half-wave potential loss about 80 mV after 5,000 durability cycles in RDE experiments [31]. Whereas the same catalyst synthesized with manganese instead of iron revealed a shift of only 20 mV. Likewise, Li et al. demonstrated comparatively good stability for a manganese + ZIF-8 catalyst during a 100-hour test of PEMFC operation [166]. Hence, manganese based non-precious metal catalysts are very promising for improving the stability. This is why manganese was chosen as the second metal for optimization of the developed polypyrrole-methyl orange approach in this work. The main goal is to improve the stability without suffering loss in activity compared to an iron only based catalyst. This chapter will deal in detail with the synthesis and characterization of these manganese catalysts. PEMFC activity tests are presented, as well as short stability tests in H₂-O₂. A more precise look at stability under longer operation time under H₂-air together with a direct comparison of manganese + iron to the solely Fe-based catalyst is given later in chapter 8.8.

8.4.1 Prepared Catalysts and Investigated Iron/Manganese-Precursors

A summary of the prepared catalysts of this chapter is given in **Table 19**. Three catalysts are synthesized from just one metal source; C-PPy_{FeCl₃}(2), C-PPy_{KMnO₄} and C-PPy_{Mn(Ac)₂}. The notation C-PPy_{FeCl₃}(2) implies that this catalyst was prepared identical to the catalysts C-PPy_{FeCl₃} from chapter 8.3. It would be possible to just take the data obtained from C-PPy_{FeCl₃}. Instead, this catalyst was re-prepared for the sake of reproducibility of the synthesis approach. In general, a good reproducibility of the synthesis process was found, more details on this are given in the appendix.

Table 19: Overview of prepared Fe, Mn and Fe + Mn based polypyrrole-methyl orange catalysts.

Sample Name	Type of Metal Salts	Polypyrrole Tube / mg	Iron salt / mg	Manganese Salt / mg
C-PPy_{FeCl₃(2)}	FeCl ₃	350	350	-
C-PPy_{KMnO₄}	KMnO ₄	350	-	341
C-PPy_{Mn(Ac)₂}	Mn(Ac) ₂	350	-	372
C-PPy_{FeCl₃/Mn(Ac)₂}	FeCl ₃ + Mn(Ac) ₂	350	350	372
C-PPy_{FeCl₃/KMnO₄}	FeCl ₃ + KMnO ₄	350	350	341
C-2ht-PPy_{FeCl₃/KMnO₄}	FeCl ₃ + KMnO ₄	350	350	341
C-2ht-PPy_{+FeCl₃-KMnO₄}	FeCl ₃ + KMnO ₄	350	590	176

Further, two catalysts are prepared from a mixture of iron and manganese salts, namely C-PPy_{FeCl₃/Mn(Ac)₂} and C-PPy_{FeCl₃/KMnO₄}. All mentioned catalysts are evaluated after one heat treatment and subsequent acid leaching. Following the preparation, the materials are characterized via TEM and Mössbauer spectroscopy, screened in the RRDE setup as well as during H₂-O₂ PEMFC activity and short two-hour stability tests. The most promising catalyst material C-PPy_{FeCl₃/KMnO₄} underwent a second heat treatment in order to obtain the maximum performance values during PEMFC tests, it is denoted as C-2ht-PPy_{FeCl₃/KMnO₄}. This catalyst was also further optimized for PEMFC performance considering the ratio of FeCl₃ and KMnO₄ and named C-2ht-PPy_{+FeCl₃-KMnO₄}.

8.4.2 Structural Characterizations

Transmission Electron Microscopy

TEM pictures of the prepared catalyst are given below, in **Figure 69**. All catalysts which were synthesized within this chapter are shown, except of C-2ht-PPy_{FeCl₃/KMnO₄}. This is because the morphology usually does not change during a second heat treatment. Hence, the TEM pictures of C-2ht-PPy_{FeCl₃/KMnO₄} resemble those of C-PPy_{FeCl₃/KMnO₄} and are shown in Figure S7 (appendix).

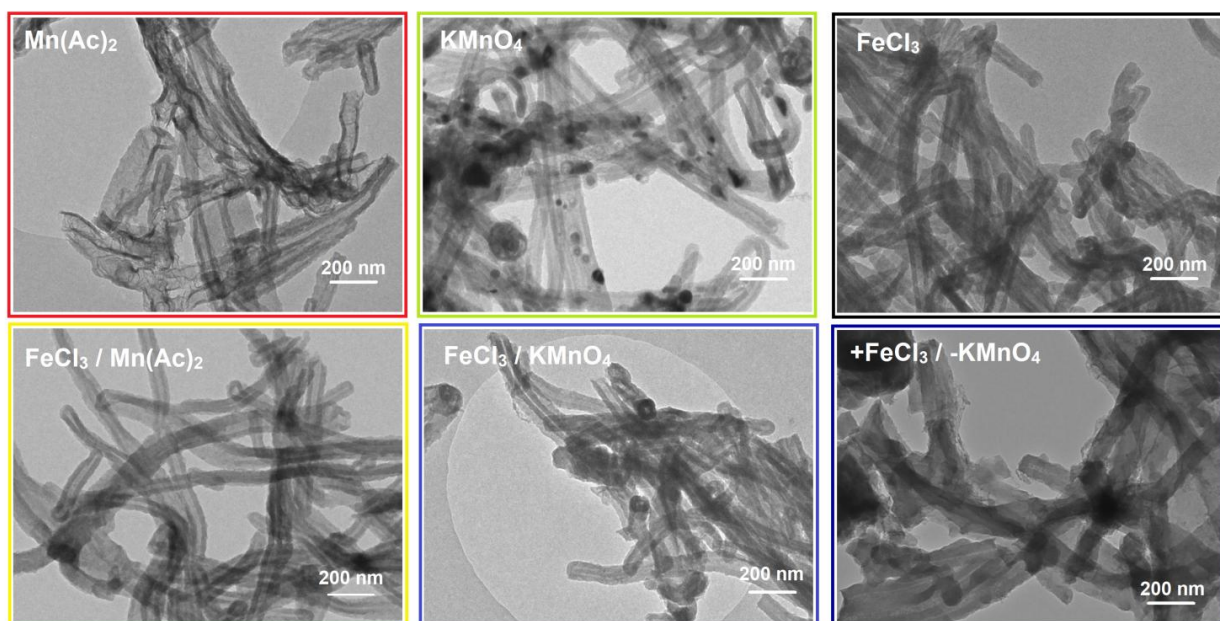


Figure 69: TEM pictures of polypyrrole-methyl orange-based catalysts prepared with different Fe, Mn or Fe + Mn salts. The catalyst in the lower right was prepared with a different amount of transition metal salts.

All catalysts show a similar morphology and carbon structure. Moreover, for all catalysts the nanotube structure remains largely intact after the synthesis procedure. However, it seems that for C-PPy_{Mn(Ac)2} carbon phases of higher graphitization are present next to the amorphous nanotube structure. Metal nanoparticles are only observed in C-PPy_{KMnO4} but not for mixtures of FeCl₃ and KMnO₄.

BET-Results

In line with the catalysts prepared in the previous chapters, the BET surface areas of the Fe/Mn catalysts were determined via N₂ sorption experiments. The bar graph of Figure 70 summarizes the results.

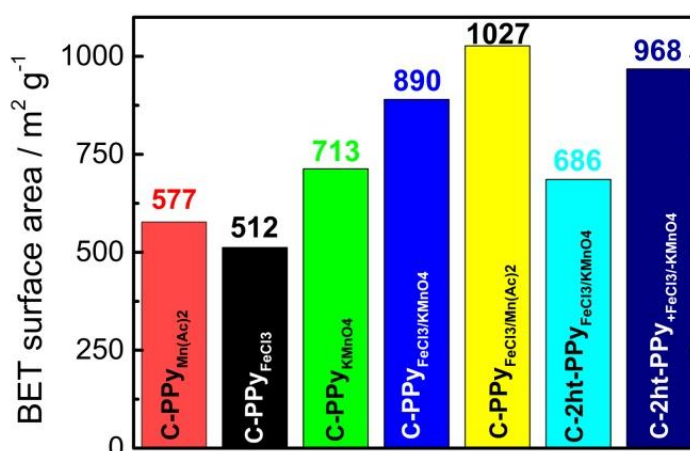


Figure 70: BET surface areas for Fe, Mn and Fe/Mn-based Me-N-C catalysts obtained from N₂ sorption experiments.

The BET surface areas strongly vary with the used type of metal salt. C-PPy_{FeCl₃}(2) exhibits a specific surface area of 512 m² g⁻¹. When using KMnO₄ as the metal source, a very high surface area of 713 m² g⁻¹ was measured. This can be explained by the high oxygen content of the permanganate ion. Oxygen containing groups promote pore formation through "consuming" e.g. near carbon atoms. Those are removed in the form of gaseous carbon oxides, leaving vacancies and pores. This behavior of KMnO₄ is within good accordance to the previous results observed when implementing different iron-salts. Here, acetate (CH₃COO⁻) and nitrate (NO₃²⁻) containing salts gave the highest BET surface areas. For C-PPy_{Mn(Ac)₂} a surface area of 577 m² g⁻¹ is found. Even though this value is higher in comparison to the FeCl₃-based catalyst it is surprisingly low in comparison the Fe(Ac)₂-based one from chapter 8.3. When a combination of Fe and Mn-salts is used, a significant higher BET surface area is obtained in comparison to the precursors pyrolyzed with just one type of metal. 980 m² g⁻¹ is measured for C-PPy_{FeCl₃/KMnO₄} and 1027 m² g⁻¹ for C-PPy_{FeCl₃/Mn(Ac)₂}. This suggests a synergetic effect of the two metal salts when it comes to boosting the surface area of the catalyst. For the catalysts prepared from the combination of FeCl₃ and KMnO₄, the most promising ORR performance was found. Hence, for this catalyst a second heat treatment was performed. Subsequently, the BET surface area is reduced significantly. For C-2ht-PPy_{FeCl₃/KMnO₄} it is 686 m² g⁻¹. For catalysts which solely contain iron, an increase of about 20 % in BET surface area is typically found after the second pyrolysis, see chapter 8.3. As mentioned earlier, Koslowski et al. investigated porphyrin-based catalysts before and after the second heat treatment [197]. It was found that about 15 % of the catalyst material burned-off during the process of the second heat treatment in N₂ (depending on time and overall temperature). Very similar results were found for the polypyrrole-methyl orange catalysts of this work which were prepared solely with iron salts. Contrary, a much more decisive burn-off was measured for C-2ht-PPy_{FeCl₃/KMnO₄}. About 30 % of initial mass was lost during the second heat treatment. This leads to the conclusion that Fe/Mn salt-based catalyst show a significant different behavior considering BET surface area and mass loss during a second heat treatment in N₂ than solely Fe-based ones. Partial pore and structure collapsing of C-2ht-PPy_{FeCl₃/KMnO₄} might explain the strong decrease of the surface area. A decrease in BET surface area was also reported by Wu et al. for a carbon black polyaniline-based catalyst [122]. Fortunately, it was possible to compensate these losses by altering the total amount and ratio of FeCl₃ to KMnO₄. C-2ht-PPy_{+FeCl₃/-KMnO₄} exhibits a surface area of 968 m² g⁻¹.

Mössbauer Spectroscopy

The ⁵⁷Fe-Mössbauer spectra of the catalysts C-PPy_{FeCl₃}(2), C-PPy_{FeCl₃/KMnO₄} and C-PPy_{FeCl₃/Mn(Ac)₂} do not show any contribution of inorganic iron side phases. Since the results are very similar to the spectra of the previously shown catalysts C-PPy_{FeCl₃} and C-PPy_{FeCl₂}, the graphs are given in the appendix, see **Figure S1** and **Table S1**.

8.4.3 Electrochemical Experiments

RRDE Evaluation of Iron, Manganese and Iron + Manganese Based Polypyrrole Catalysts

After gaining detailed insights on the surface area, morphology and the structural composition of the prepared catalysts, the electrochemical performance for the acidic ORR is measured. In order to keep experimental time short, the catalysts C-PPy_{FeCl₃(2)}, C-PPy_{Mn(Ac)₂}, C-PPy_{KMnO₄}, C-PPy_{FeCl₃/KMnO₄} and C-PPy_{FeCl₃/Mn(Ac)₂} were fast-screened in a RRDE setup after one heat treatment and acid leaching. The polarization curves in O₂ saturated 0.1 M H₂SO₄ are shown in **Figure 71 a)**. Simultaneously recorded ring currents allow for calculating the respective H₂O₂ yield. Hence, **Figure 71 b)** gives information about the selectivity of the catalysts.

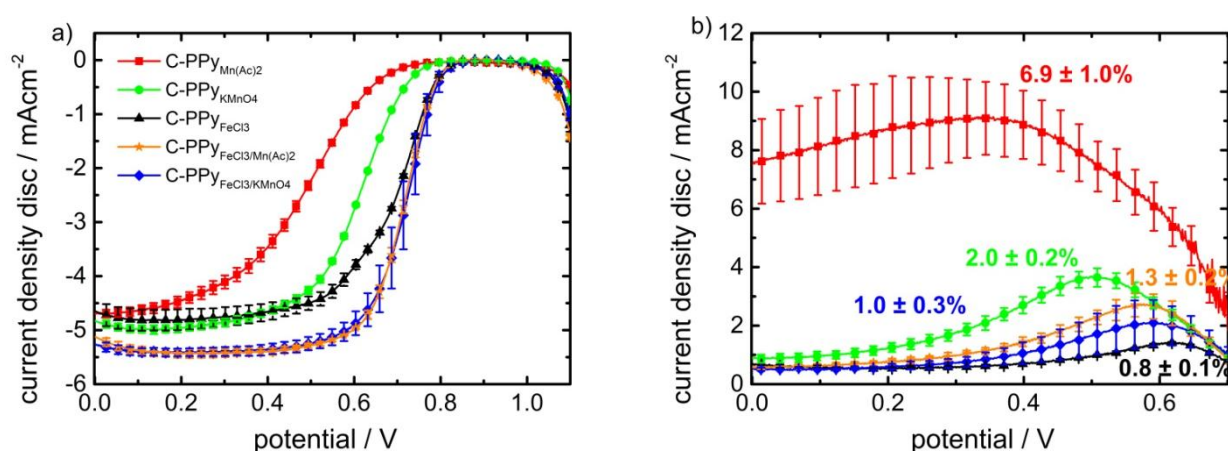


Figure 71: ORR polarization curves (a) and respective H₂O₂ yields (b) for the catalysts prepared from different iron, manganese and iron + manganese precursors recorded with a sweep rate of 10 mV s⁻¹ in O₂ saturated 0.1 M H₂SO₄, a rotation rate of 1500 rpm and a disc loading of 0.5 mg cm⁻².

The lowest ORR activities are found for the two catalysts prepared solely from manganese salt, C-PPy_{Mn(Ac)₂} and C-PPy_{KMnO₄}. This is in accordance with previous findings, where manganese based Me-N-C catalysts have been shown to be slightly less active than their respective iron counterparts [31, 134, 166]. Still, there is a noticeable influence of the type of manganese metal salt which is used. This nicely fits with the previous findings about iron precursors where the same strong influence of the type of iron salt (chloride, acetate, nitrate, ...) on ORR activity was established. As indicated by the respective onset potentials, C-PPy_{KMnO₄} has an enhanced activity in comparison to C-PPy_{Mn(Ac)₂}. The measured ORR onset potentials are 732 mV for C-PPy_{Mn(Ac)₂} and 770 mV for C-PPy_{KMnO₄}. However, a comparison between iron and manganese salt precursors from **Figure 71** is non-conclusive, since different salts were used, FeCl₃ vs. Mn(Ac)₂ vs. KMnO₄. Therefore, **Figure 72** includes the results from chapter 8.3. ORR performances of the catalysts which are prepared both from acetate salts, Fe(Ac)₂ and Mn(Ac)₂ are given. Surprisingly, for the polypyrrole-methyl orange synthesis approach of this work, C-PPy_{Mn(Ac)₂}

shows a slightly enhanced ORR activity in comparison to C-PPy_{Fe(Ac)₂}. Still, the iron-based Me-N-C catalyst shows a much better ORR selectivity, as seen in **Figure 72 b**).

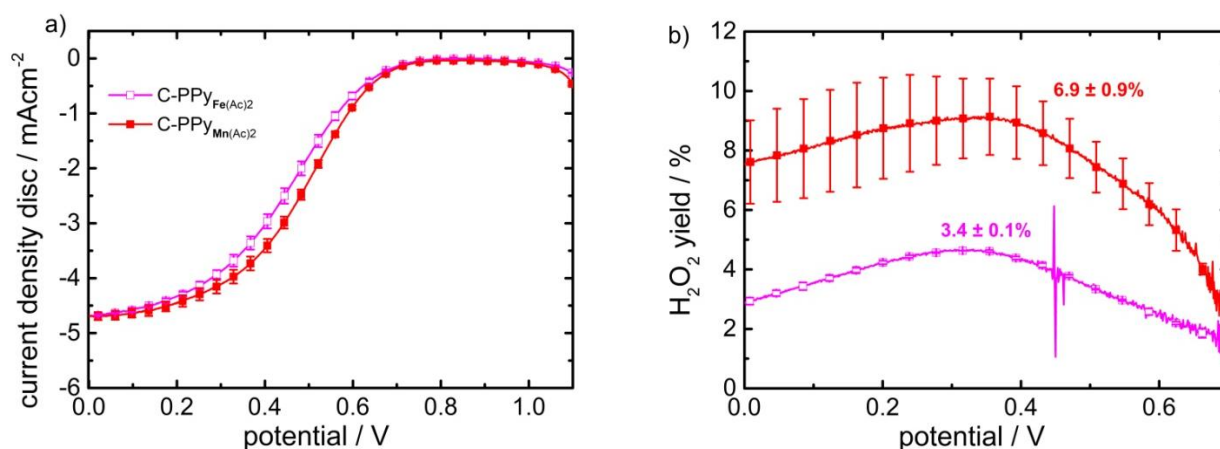


Figure 72: ORR polarization curves (a) and respective H₂O₂ yields (b) for the catalysts prepared from either Fe(Ac)₂ or Mn(Ac)₂ recorded with a sweep rate of 10 mV s⁻¹ in O₂ saturated 0.1 M H₂SO₄, a rotation rate of 1500 rpm and a disc loading of 0.5 mg cm⁻².

Interestingly, when combining the metals manganese and iron an enhancement of ORR activity is achieved, see **Figure 71**. C-PPy_{FeCl₃/Mn(Ac)₂} and C-PPy_{FeCl₃/KMnO₄} show a slightly enhanced onset potential as well as more distinct plateau in the diffusion controlled region of the polarization curve, compared to C-PPy_{FeCl₃}(2). In accordance, Wu et al. found synergistic effects when combining Fe- and Co-precursors for a polyaniline/carbon black based Me-N-C catalyst [140]. Considering the ORR selectivity, C-PPy_{FeCl₃/Mn(Ac)₂} shows a slightly higher H₂O₂ formation rate than the pure iron containing catalyst, C-PPy_{FeCl₃}(2). Still, in comparison to the high values found for the manganese-based material C-PPy_{Mn(Ac)₂} a good ORR selectivity is achieved for C-PPy_{FeCl₃/Mn(Ac)₂}. For the combination of FeCl₃ and KMnO₄ an excellent ORR activity and selectivity is measured during the RRDE experiments. This makes C-PPy_{FeCl₃/KMnO₄} a very promising catalyst material for further investigations during PEMFC tests.

PEMFC Tests

Finally, the most promising catalysts of the Fe, Mn variation series are evaluated considering their performance during PEMFC tests. These are C-PPy_{KMnO₄}, C-PPy_{FeCl₃}(2), C-PPy_{FeCl₃/Mn(Ac)₂} and C-PPy_{FeCl₃/KMnO₄}. The catalysts have been measured after one heat treatment and acid leaching. Polarization curves giving the voltage respectively the power density against the current density are depicted in **Figure 73**. After confirming the superior performance of C-PPy_{FeCl₃/KMnO₄}, this catalyst underwent a second heat treatment and a further optimization step considering the total amount and ratio of FeCl₃ to KMnO₄ salt. This is discussed later in this section. C-PPy_{Mn(Ac)₂} was not measured in the PEMFC setup since very little ORR activity and low selectivity during RRDE tests were found earlier. In order to still gain insights about a pure manganese-based Me-N-C catalyst, C-PPy_{KMnO₄} is measured.

As obtained from **Figure 73**, the ORR activity trend measured during the preceding RRDE experiments is confirmed during the PEMFC tests. C-PPy_{KMnO₄}, which was prepared solely from a manganese precursor shows a very low performance. A shortfall in the kinetic region (high voltages) as well as diffusion limited part (low voltages) of the polarization curve in comparison to the other three catalysts is striking.

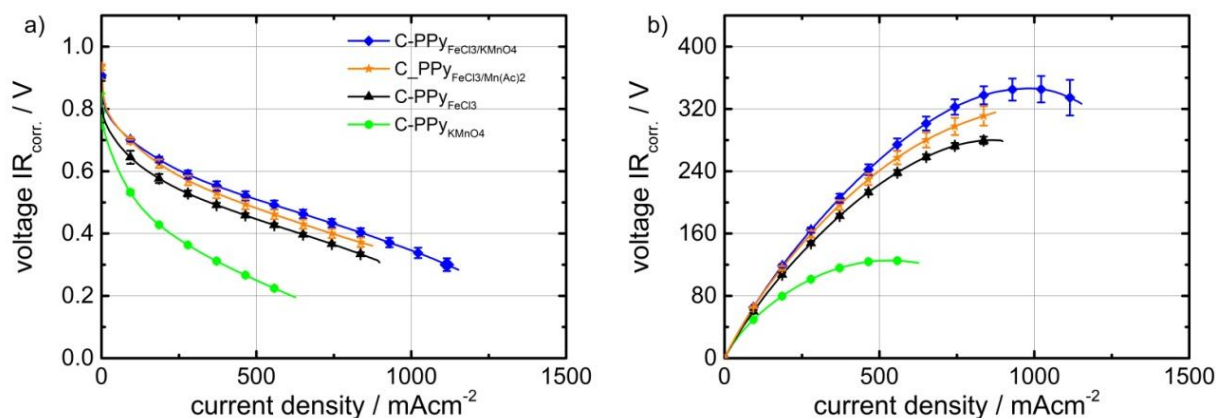


Figure 73: PEMFC polarization curves of different Fe, Mn polypyrrole-methyl orange catalysts, voltage against current density (a) and voltage against power density (b). (experiment conditions: H₂-O₂, cathode loading 2.8 - 3.4 mg cm⁻², N212 membrane, 1 bar gauge back pressure, 0.2 L min⁻¹ oxidant and fuel flow, 80 °C, 96 % humidity).

Contrary, advanced performance is measured for the MEAs prepared with C-PPy_{FeCl₃}(b), C-PPy_{FeCl₃/Mn(Ac)₂} and C-PPy_{FeCl₃/KMnO₄}. Maximum power densities of 285 mW cm⁻², 337 mW cm⁻² and 362 mW cm⁻² are obtained. Hence, a performance enhancement is achieved when combining FeCl₃ with manganese salts like Mn(Ac)₂ or KMnO₄. Whereas the combination of FeCl₃ and KMnO₄ shows the best performance. These results are in line with the outcome of the RRDE experiments.

However, as stated in the introduction part of this chapter, the main purpose of combining an iron and a manganese metal into a bimetallic Me-N-C catalyst was not solely to enhance the activity. More importantly the challenge was to enhance the poor stability of Fe-N-C catalysts. **Figure 74 a)** shows the absolute current values of the different Fe, Mn catalysts at a constant potential of 600 mV over a time period of 120 min. **Figure 74 b)** gives the remaining current, taking the respective current value of 0 min as point of reference (= 100 %).

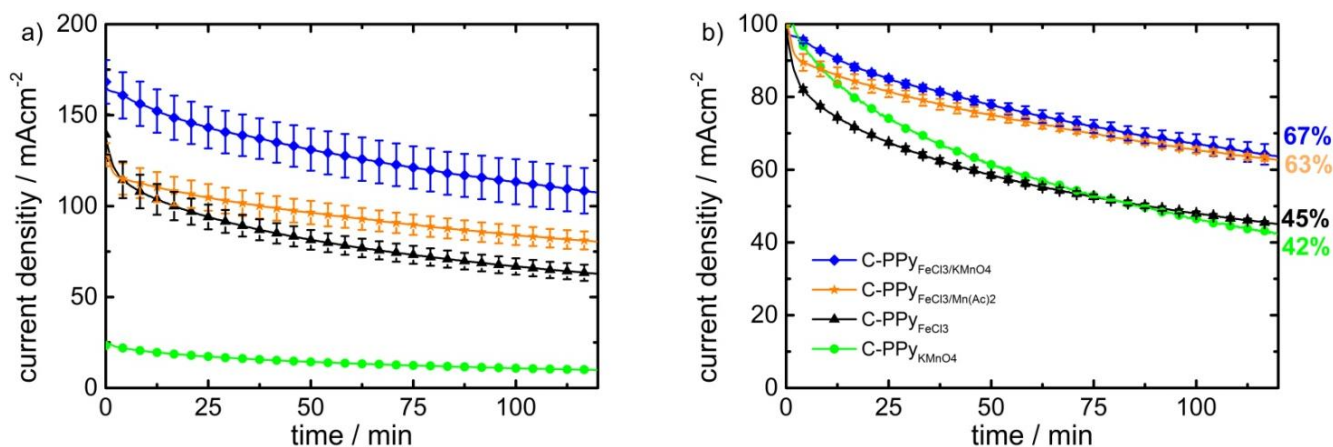


Figure 74: PEMFC stability tests of catalysts that were prepared from Fe, Mn or Fe + Mn salts. The durability tests are performed at a constant potential of 600 mV. (experiment conditions: H₂-O₂, cathode loading 2.8 - 3.4 mg cm⁻², N212 membrane, 1 bar gauge back pressure, 0.2 L min⁻¹ oxidant and fuel flow, 80 °C, 96 % humidity).

The starting performances (at time = 0 min) displayed in **Figure 74 a)** again show that C-PPy_{FeCl3/KMnO4} has the highest current output, C-PPy_{KMnO4} the lowest, whereas the values of C-PPy_{FeCl3(2)} and C-PPy_{FeCl3/Mn(Ac)2} are found in between but closer to those of C-PPy_{FeCl3/KMnO4}. Following the starting point of the measurements, the typical sharp current decay of Me-N-C catalysts is found for all four of these catalysts, as well. Still, from **Figure 74 b)** it appears that all catalysts prepared with manganese salts are more stable than the catalyst prepared just with iron, C-PPy_{FeCl3(2)}. For instance, when comparing C-PPy_{KMnO4} to C-PPy_{FeCl3(2)}, the first 60 min C-PPy_{KMnO4} shows a less distinct current decay. Unfortunately, the current decay of C-PPy_{KMnO4} matches the one of C-PPy_{FeCl3(2)} the following 60 min (time = 60 - 120 min). Hence, after an operation time of 120 min, a current output of about 45 % remains for C-PPy_{KMnO4} as well as for C-PPy_{FeCl3(2)}. A longer experiment time can clarify which of these two catalysts is actually more stable. Nevertheless, a significant higher stability is observed for C-PPy_{FeCl3/Mn(Ac)2} and C-PPy_{FeCl3/KMnO4}. Within the first minutes of operation the sharp current decay is much less pronounced, especially compared to C-PPy_{FeCl3(2)}. Overall, about 65 % of the initial current is retained after 120 min of operation time, a significant improvement compared to both single metal-based catalyst.

Of the catalysts under review in this chapter, C-PPy_{FeCl3/KMnO4} reveals the highest activity as well as the best stability. Therefore, C-PPy_{FeCl3/KMnO4} underwent a second heat treatment, it is labelled as C-2ht-PPy_{FeCl3/KMnO4} afterwards. Further, the total amount and ratio of FeCl₃ to KMnO₄ precursors in C-PPy_{FeCl3/KMnO4} was varied, this catalyst is denoted as C-2ht-PPy_{+FeCl3/-KMnO4}. The polarization curves of these two catalysts are shown in Figure 75. A maximum power density of about 640 mW cm⁻² is reached for C-2ht-PPy_{FeCl3/KMnO4}, a slightly higher value of about 675 mW cm⁻² is obtained for C-2ht-PPy_{+FeCl3/-KMnO4}. Hence, compared to C-PPy_{FeCl3/KMnO4} a great enhancement in fuel cell performance was accomplished with a second heat treatment.

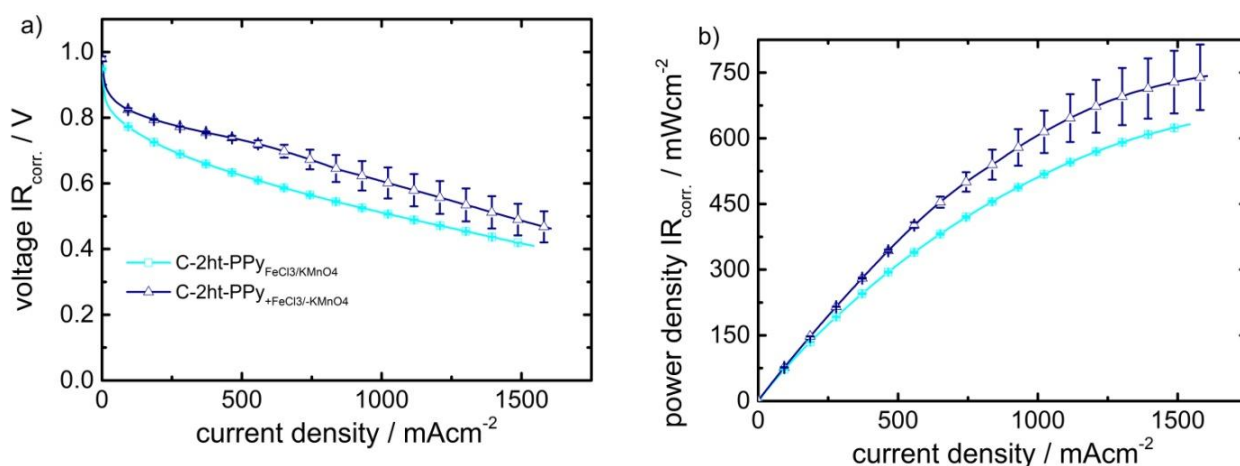


Figure 75: PEMFC polarization curves of different FeCl₃ + KMnO₄ based polypyrrole-methyl orange catalysts after a second heat treatment with altering Fe to Mn-salt ratio and amounts, voltage against current density (a) and voltage against power density (b). (experiment conditions: H₂-O₂, cathode loading 3.2 - 3.3 mg cm⁻², N212 membrane, 1 bar gauge back pressure, 0.2 L min⁻¹ oxidant and fuel flow, 80° C, 96 % humidity).

Figure 76 a) gives again the current density at a constant potential of 600 mV over a time period of 120 min. Figure 76 b) the retained current in %. Considering the performance, the constant potential holds at 600 mV emphasize the improved activity after the optimization of the precursor contents. An initial current density of 308 mA cm⁻² is measured for C-2ht-PPy_{FeCl₃/KMnO₄}. A significant higher value of 525 mA cm⁻² is obtained for C-2ht-PPy_{+FeCl₃/-KMnO₄}. Furthermore, for C-2ht-PPy_{+FeCl₃/-KMnO₄} a great stability over the course of 120 min is found. 74% of the initial current is retained for C-2ht-PPy_{+FeCl₃/-KMnO₄}. Whereas for C-2ht-PPy_{FeCl₃/KMnO₄} 65% of the initial current density is measured at the end of the stability test.

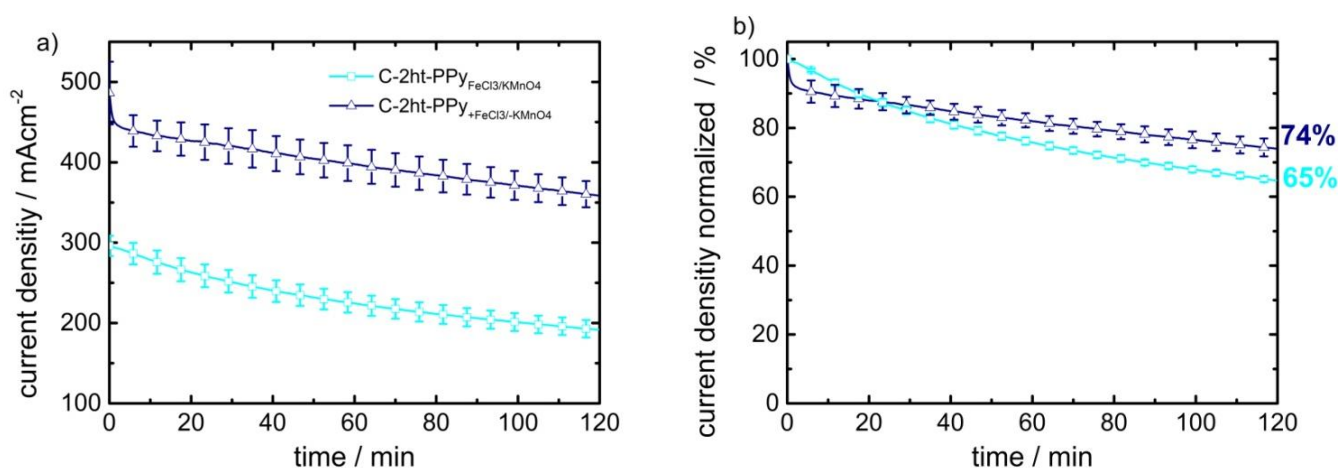


Figure 76: PEMFC stability tests of FeCl₃ + KMnO₄ based polypyrrole-methyl orange catalysts after a second heat treatment with altering Fe to Mn-salt ratio and amounts, performed at a constant potential of 600 mV. (experiment conditions: H₂-O₂, cathode loading 3.2 - 3.3 mg cm⁻², N212 membrane, 1 bar gauge back pressure, 0.2 L min⁻¹ oxidant and fuel flow, 80 °C, 96 % humidity).

8.4.4 Brief Summary on the Influence of Different Fe/Mn Salts

A set of different catalysts containing Fe, Mn and Fe + Mn was prepared from polypyrrole-methyl orange nanotubes and comparatively investigated.

N₂ sorption experiments revealed that catalysts prepared from Mn(Ac)₂ and KMnO₄ yield materials with higher BET surface areas in comparison to a catalyst which is prepared with FeCl₃. Further, the combination of a manganese salt and FeCl₃ gives catalysts with a high surface area.

Electrochemical measurements, reveal a synergetic effect of FeCl₃ with Mn(Ac)₂ and KMnO₄. Both catalysts prepared from Fe + Mn salt mixtures show an improved performance for the ORR in comparison to the catalysts prepared from the respective single metal source. PEMFC short stability tests showed that the combination of Fe + Mn yields catalysts that are less prone for degradation, compared to the respective single metal version.

8.5 Variation of the Temperature during the Synthesis of Polypyrrole-Based Me-N-C Catalysts

The parameters of absolute temperature, pyrolysis time, heating rate and gas-atmosphere play an important role during the heat treatment step of the synthesis of Fe-N-C catalyst. A main difficulty during the pyrolysis is the trade-off between activity and stability. Very briefly; applying longer heat treatments at higher temperatures leads to a more stable carbon phase. At the same time, these pyrolysis parameters lead to a destruction of active sites and push the formation of inorganic iron phases, yielding poorly active catalysts. It is the aim of this chapter to identify the influence of the two most crucial parameters during the pyrolysis steps for the newly developed $\text{FeCl}_3/\text{KMnO}_4$ -based polypyrrole-methyl orange nanotube synthesis. The duration of the second heat treatment and the absolute temperature of the first heat treatment is considered for analysis.

However, a detailed investigation including a wider range of temperatures and parameters is not performed at this stage. Instead, after the first promising findings of this work a master thesis project which was supervised within the scope of this thesis addresses this topic in more detail. The experiments of the master thesis and this work finished simultaneously and are therefore not included here.

8.5.1 Catalysts Prepared with Varying Duration of the Second Heat Treatment

As shown in chapter 8.4, a second heat treatment on $\text{C-PPy}_{\text{FeCl}_3/\text{KMnO}_4}$ significantly lowers the specific BET surface area. A BET surface area of $890 \text{ m}^2 \text{ g}^{-1}$ was measured for $\text{C-PPy}_{\text{FeCl}_3/\text{KMnO}_4}$, whereas only $686 \text{ m}^2 \text{ g}^{-1}$ is obtained after the second heat treatment for $\text{C-2ht-PPy}_{\text{FeCl}_3/\text{KMnO}_4}$. A similar behavior was reported by Wu et al. for a carbon black polyaniline-based catalyst system [122]. Further, in chapter 8.2.1, a strong correlation between BET surface area and PEMFC performance was revealed. Hence, the question arises, can the PEMFC performance of the catalysts be increased, if the collapse of the BET surface area during the second heat treatment is by-passed or minimized?

The parameters of the second heat treatment for $\text{C-2ht-PPy}_{\text{FeCl}_3/\text{KMnO}_4}$ and $\text{C-2ht-PPy}_{+\text{FeCl}_3/-\text{KMnO}_4}$ are; heating rate of $300 \text{ }^\circ\text{C h}^{-1}$, absolute temperature $800 \text{ }^\circ\text{C}$, holding time 45 min. The approach here is to increase the heating rate and lower the holding time of the sample. **Table 20** shows which samples are prepared and what the respective parameters for the second heat treatment are. Since $\text{C-2ht-PPy}_{+\text{FeCl}_3/-\text{KMnO}_4}$ showed the best performance, considering PEMFC activity and stability, this specific mixture of FeCl_3 , KMnO_4 and polypyrrole-methyl orange nanotubes is chosen hereafter. Composition of the precursor mixture, first heat treatment and acid leaching are identical for all samples prepared in this chapter. $\text{C-PPy}_{+\text{FeCl}_3/-\text{KMnO}_4}$ refers to a sample which was synthesized with just

one heat treatment and acid leaching. The notations 2ht, 2htm and 2hts represent the different durations for the second heat treatment (m = medium, s = short), the details are given in **Table 20**.

Table 20: Fe, Mn-Catalysts prepared without a second heat treatment and with a varying total duration time of the second heat treatment.

Sample Name	First Heat Treatment 300 °C h ⁻¹	Second Heat treatment
C-PPy _{+FeCl₃/-KMnO₄}	800 °C hold 1 h	-
C-2ht-PPy _{+FeCl₃/-KMnO₄}	800 °C hold 1 h	300 °C h ⁻¹ to 800 °C hold 45 min
C-2htm-PPy _{+FeCl₃/-KMnO₄}	800 °C hold 1 h	800 °C h ⁻¹ to 800 °C hold 15 min
C-2hts-PPy _{+FeCl₃/-KMnO₄}	800 °C hold 1 h	1000 °C h ⁻¹ to 800 °C hold 1 min

PEMFC Performance and BET Surface Area

Figure 77 summarizes the results of the N₂ sorption experiments for the catalysts prepared with differing durations of the second heat treatment. The highest value of 1485 m² g⁻¹ is found for the catalyst that did not undergo a second heat treatment, C-PPy_{+FeCl₃/-KMnO₄}. This value is remarkably high. Zhang et al. reported a BET surface area of 640 m² g⁻¹ after performing one heat treatment on a ZIF-8-based precursor [448]. Higher values are normally measured after a second heat treatment with NH₃. Proietti et al. reported 964 m² g⁻¹ after 15 min pyrolysis in NH₃ at 950 °C [25]. Likewise, Li et al. boosted the BET surface area of their ZIF-8-based catalyst from 378 m² g⁻¹ to 1360 m² g⁻¹ after a second heat treatment with NH₃ [449]. As already reported earlier in this work, the specific surface area of the FeCl₃/KMnO₄ polypyrrole-methyl orange-based catalysts partly collapses after the second heat treatment. A significant decrease is observed for the sample that underwent the heat treatment for a long duration time. A BET area 968 m² g⁻¹ is measured for C-2ht-PPy_{+FeCl₃/-KMnO₄}. This corresponds to a loss of about 35 % in comparison to the initial sample C-PPy_{+FeCl₃/-KMnO₄}. However, as intended, the loss in surface area is much less pronounced for shorter heat treatment durations. Most importantly C-2hts-PPy_{+FeCl₃/-KMnO₄} exhibits a surface area of 1382 m² g⁻¹, i.e. 93 % of the initial surface area was retained.

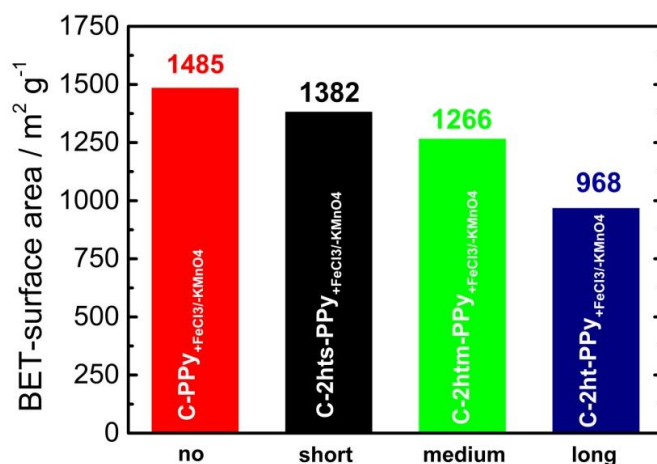


Figure 77: Specific BET surface area obtained from N₂ sorption measurements for catalysts that underwent different second heat treatment duration times and the initial catalyst that was treated once.

Figure 78 gives the measured PEMFC polarization curves, i.e. plots of the voltage and the power density versus the current density. The samples C-2hts-PPy_{+FeCl₃/-KMnO₄} and C-2htm-PPy_{+FeCl₃/-KMnO₄} were measured twice. Hence, the average value of the two measurements is plotted together with the respective error bars. The latter are barely visible due to the strong overlap of the two measurements.

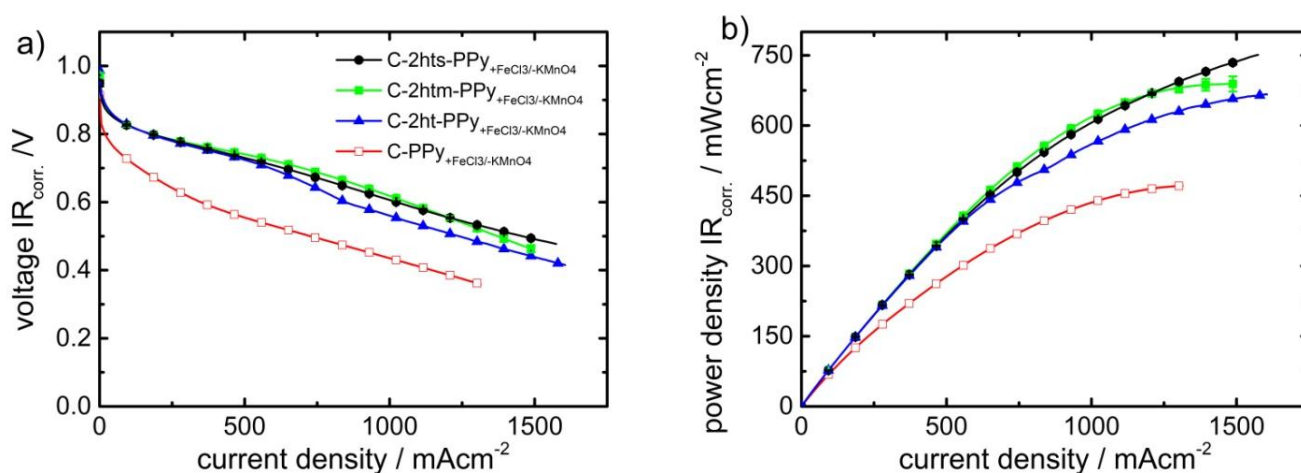


Figure 78: PEMFC performance of catalysts that underwent no second heat treatment or a second heat treatment with a varying duration time. (experiment conditions: H₂O₂, cathode loading 3.3 - 3.7 mg cm⁻², N212 membrane, 1 bar gauge back pressure, 0.2 L min⁻¹ oxidant and fuel flow, 80 °C, 96 % humidity).

The difference between C-PPy_{+FeCl₃/-KMnO₄} and the rest of the curves is much more pronounced than the changes among C-2hts-PPy_{+FeCl₃/-KMnO₄}, C-2htm-PPy_{+FeCl₃/-KMnO₄} and C-2ht-PPy_{+FeCl₃/-KMnO₄}. C-PPy_{+FeCl₃/-KMnO₄} has the lowest performance of all investigated catalysts. In general, after the second heat treatment the activity is enhanced for all catalysts. Reasons for this are the removal of N-protonation and/or anion-binding effects, the removal of surface oxide groups and therefore the increase in hydrophobicity and electron density at the active site [122, 151, 162, 197]. The duration of

the second heat treatment has only a small effect on performance of the catalyst. The overall changes are not distinctive. Still, in accordance with the enhanced BET surface area for shorter heat treatments, the current in the mass transport region profits. The peak power density of the catalyst that underwent the shortest treatment C-2hts-PPy_{+FeCl₃/-KMnO₄} is 742 mW cm⁻². Slightly less peak power density is obtained for a medium duration time C-2htm-PPy_{+FeCl₃/-KMnO₄}, 709 mW cm⁻². 670 mW cm⁻² is measured for the catalysts with the lowest BET surface and the longest duration of the second heat treatment C-2ht-PPy_{+FeCl₃/-KMnO₄}. The BET surface areas of C-2hts-PPy_{+FeCl₃/-KMnO₄} and C-2htm-PPy_{+FeCl₃/-KMnO₄} are both very high and further do not differ significantly from each other. Therefore, the just slight effect on the polarization curves of these two catalysts is reasonable. Still, it can be stated that by lowering the duration time of the second heat treatment the collapsing of the pores is minimized, subsequently improving the mass transport properties during PEMFC operation. Due to the concentration dependence of mass transports phenomena, measurements in H₂-air instead of H₂-O₂ might display a greater difference in the polarization curves of these catalysts.

Figure 79 shows the 120 min durability tests of the catalysts. The experiments were conducted in H₂-O₂ at a constant potential of 600 mV. Whereas **Figure 79 a)** displays the absolute values of the measured current densities and **Figure 79 b)** gives the normalized current in %. As already established from the polarization curves in **Figure 78**, C-PPy_{+FeCl₃/-KMnO₄} shows the lowest performance of all measured catalyst, also during the potential hold. Contrary to the polarization curves, the difference of the measured current densities during the constant potential hold of C-2hts-PPy_{+FeCl₃/-KMnO₄}, C-2htm-PPy_{+FeCl₃/-KMnO₄} and C-2ht-PPy_{+FeCl₃/-KMnO₄} is more pronounced. The highest initial performance of 629 mA cm⁻² is measured for the sample that was treated for the medium duration time, C-2htm-PPy_{+FeCl₃/-KMnO₄}. The sample treated for the shortest time C-2hts-PPy_{+FeCl₃/-KMnO₄} only shows an initial current density of 386 mA cm⁻² and the longest treatment gives 486 mA cm⁻² for C-2ht-PPy_{+FeCl₃/-KMnO₄}. Having in mind the values of the specific BET surface areas, displayed in **Figure 77**, it becomes clear that the performance during constant potential holds is a trade-off between retaining a high surface area (short treatment times) and sufficiently healing the defects induced by the acid leaching (long treatment times).

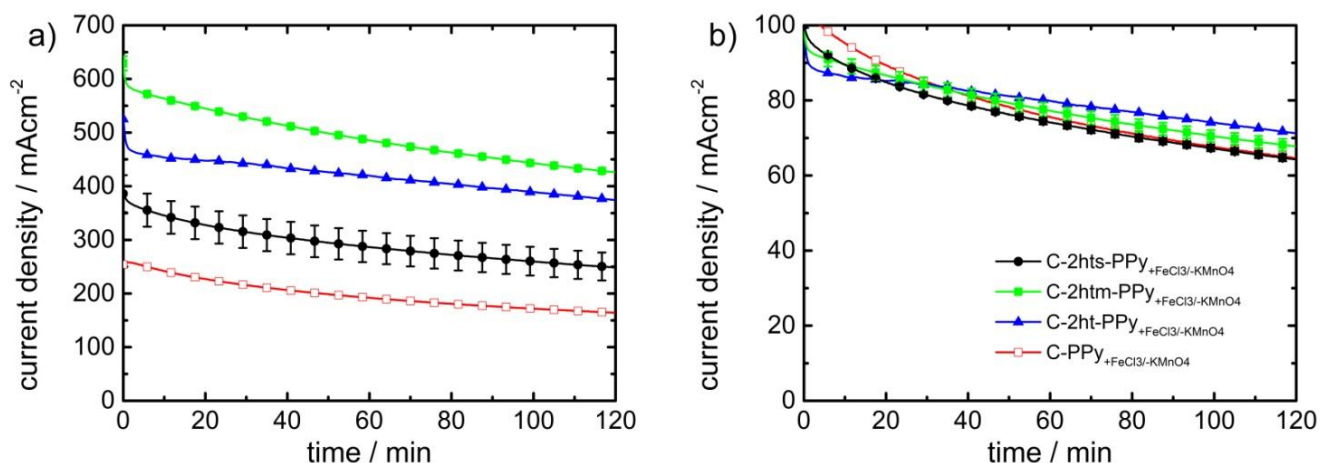


Figure 79: PEMFC stability tests of catalysts that underwent no second heat treatment or a second heat treatment with a varying duration time. The durability tests are performed at a constant potential of 600 mV. (experiment conditions: $\text{H}_2\text{-O}_2$, cathode loading 3.3 - 3.7 mg cm^{-2} , N212 membrane, 1 bar gauge back pressure, 0.2 L min^{-1} oxidant and fuel flow, 80 °C, 96 % humidity).

It is very interesting to notice, that the second heat treatment is not a decisive factor considering the stability of these catalysts. **Figure 79 b)** displays the remaining current density in percentage over the time. Neither without a second heat treatment nor with different duration times of the second heat treatment the stability is changed. However, it is important to keep in mind that the stability tests were performed for an overall time of only 120 minutes. It is known that non-precious metal-based catalysts decay in two different stages. A first very sharp initial decay within the first 24 hours followed by a more slowly linear decay. Hence, to be precise from the results of **Figure 79 b)** it is stated that the initial decay of the catalysts is not influenced by a second heat treatment.

8.5.2 Catalysts Prepared with Varying Temperature of the First Heat-Treatment

Raman spectroscopy (chapter 8.2.2) indicated that the polypyrrole-methyl orange precursor is able to suppress the formation of highly graphitized iron carbide phases. Very briefly, catalysts prepared from normal polypyrrole contain sharp peaks in their Raman spectra. Those are attributed to highly graphitized carbon phases induced together with the formation of inorganic iron by-products (as verified by TEM and Mössbauer spectroscopy). Contrary, if polypyrrole-methyl orange nanotubes are applied, no sharp peaks are found. This behavior was observed even at very high temperatures of 1100 °C. A general problem related to Me-N-C catalyst synthesis is the trade-off between activity and stability. At high temperatures, a highly ordered carbon phase is formed, i.e. more resistance against carbon corrosion and subsequently a more stable catalyst is obtained. However, molecular active sites are being destroyed at high temperatures and inorganic iron phases emerge. For low temperatures, a high amount of molecular active sites is usually linked to conjunction with an amorphous, instable carbon back bone. In summary, either an active but unstable or an inactive but stable catalyst is obtained depending on the pyrolysis temperature.

As it is indicated from the Raman spectra, the polypyrrole-methyl orange nanotube precursor has the potential to overcome this dilemma. So far, all catalysts in this work have been prepared at a temperature of 800 °C. It is the intend of this chapter to prepare a more stable catalyst by increasing the temperature of the first heat treatment. Therefore, two catalysts are prepared, differing in the absolute temperature of the first heat treatment. C-2htm-PPy_{+FeCl₃/-KMnO₄} serves as the respective reference catalyst prepared at 800 °C. Further, C-2htm-PPy_{+FeCl₃/-KMnO₄} is re-prepared in the exact same manner except that the pyrolysis temperature of the first heat treatment was increased to 1000 °C. This catalyst is denoted as C-2htm-PPy_{+FeCl₃/-KMnO₄_1000. The synthesis parameters of all relevant catalysts of this chapter are summarized in **Table 21**.}

Table 21: Fe and Mn-based polypyrrole-methyl orange catalysts prepared at 800 °C and 1000 °C.

Sample Name	Polypyrrole Tubes / mg	FeCl ₃ / mg	KMnO ₄ / mg	First Heat Treatment 300 °C h ⁻¹	Second Heat treatment
C-2htm-PPy _{+FeCl₃/-KMnO₄}	350	590	176	800 °C hold 1 h	800 °C h ⁻¹ to 800 °C hold 15 min
C-2htm-PPy _{+FeCl₃/-KMnO₄_1000}	350	590	176	1000 °C hold 1 h	800 °C h ⁻¹ to 800 °C hold 15 min
C-2hts-PPy _{+FeCl₃/-KMnO₄}	350	590	176	800 °C hold 1 h	1000 °C h ⁻¹ to 800 °C hold 1 min

Table 9 further shows C-2hts-PPy_{+FeCl₃/-KMnO₄}, a catalyst prepared at 800 °C but with a shorter second heat treatment time. As it has been shown in chapter 8.5.1, **Figure 79**, that fuel cell stability of catalysts prepared with fast second heat treatment (2hts) and the medium lasting one (2htm) is not affected. Hence, for establishing a relationship of the temperature during the first heat treatment and the stability of the catalysts a comparison of C-2hts-PPy_{+FeCl₃/-KMnO₄} with C-2htm-PPy_{+FeCl₃/-KMnO₄_1000 is reasonable. The reason behind is the availability of experimental stability data of C-2hts-PPy_{+FeCl₃/-KMnO₄} and C-2htm-PPy_{+FeCl₃/-KMnO₄_1000 with more than 120 minutes. The measurement for C-2htm-PPy_{+FeCl₃/-KMnO₄} could not be performed to that extent due to a shutdown of the laboratories for renovation.}}

Physical Characterization

BET

N₂ sorption experiments were performed to obtain the specific BET surface area of the catalysts, the results are addressed in **Figure 80**. Increasing the pyrolysis temperature from 800 °C to 1000 °C leads

to a catalyst with slightly lower BET surface area. In numbers, a decrease from $1266 \text{ m}^2 \text{ g}^{-1}$ for the $800 \text{ }^\circ\text{C}$ sample to $1178 \text{ m}^2 \text{ g}^{-1}$ for the $1000 \text{ }^\circ\text{C}$ sample is measured. Considering the influence on BET surface area which was found earlier for the second heat treatment in **Figure 77**, the impact of the overall temperature of the first heat treatment is rather low.

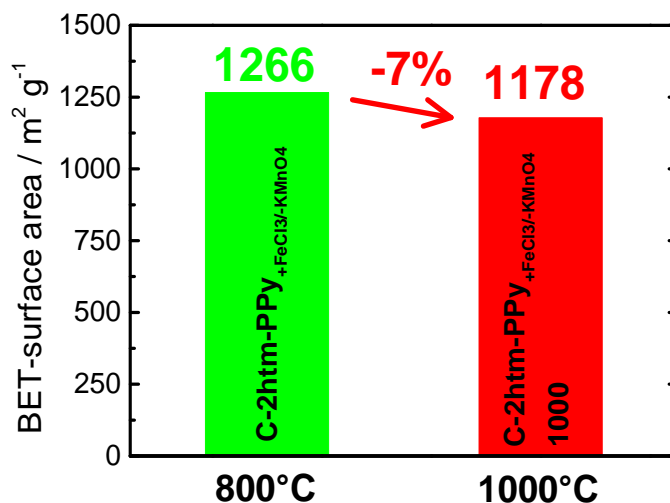


Figure 80: BET surface areas obtained from N_2 sorption measurements for two $\text{FeCl}_3/\text{KMnO}_4$, polypyrrole-methyl orange-based catalysts that differ only in the absolute temperature of their first heat treatment.

TEM

The TEM photographs of the two samples are shown in **Figure 81**. Both samples have a similar carbon morphology which was described earlier. However, the particles of the sample prepared at $1000 \text{ }^\circ\text{C}$ are slightly more agglomerated. More importantly, this catalyst clearly shows inorganic iron particles. It is concluded that by increasing the temperature from $800 \text{ }^\circ\text{C}$ to $1000 \text{ }^\circ\text{C}$ visible amounts of nanoparticles form.

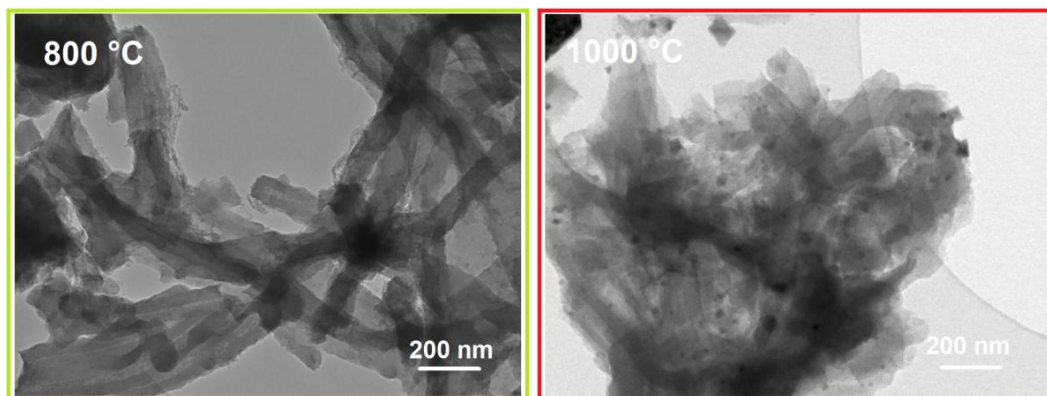


Figure 81: TEM photographs of $\text{FeCl}_3/\text{KMnO}_4$, polypyrrole-methyl orange-based catalysts prepared at $800 \text{ }^\circ\text{C}$ (left) or $1000 \text{ }^\circ\text{C}$ (right).

Mössbauer Spectroscopy

The ^{57}Fe -Mössbauer spectra of the two catalysts are given below in **Figure 82**.

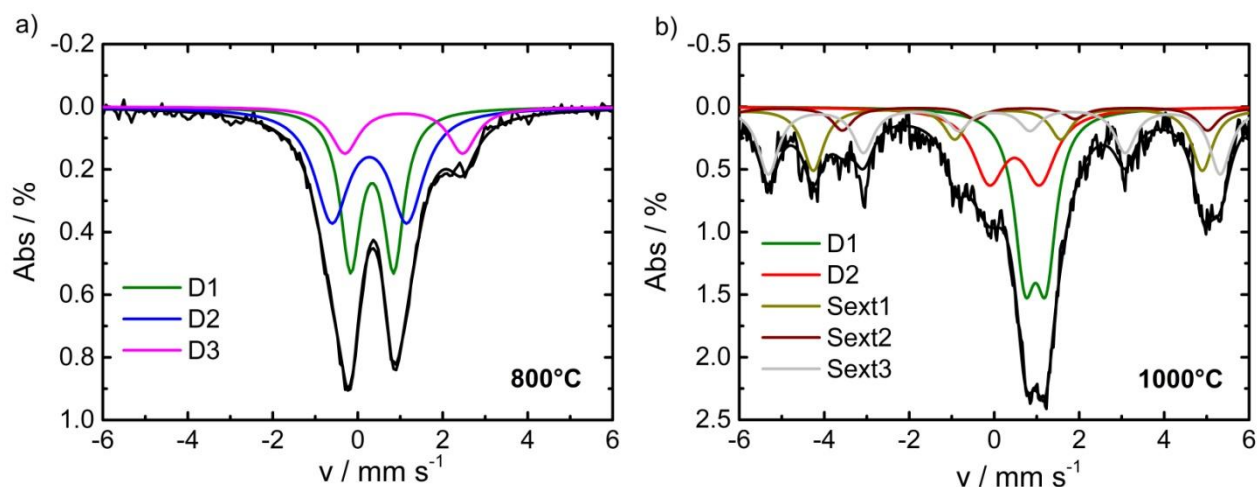


Figure 82: Mössbauer spectra of catalysts which were prepared at different temperatures.

Despite the differences, in both spectra the already mentioned D1 doublet specie appears. It can be ascribed to FeN_4 sites of different oxidation spin states, with different axial ligands or iron / ironoxide nano clusters [424, 450]. For the sample prepared at 1000 °C further inorganic iron species are detected, see **Figure 82 b**). To these oxide phases sext 1, sext 2 but also the D2 species is contributing. The high isomer shift and but small quadrupole splitting of the D2 is assigned to Wüstite like Fe_xO and is rather unusual for Fe-N-C catalysts. A possible explanation for its occurrence might the high temperature in combination with an oxygen source, which is present in the form of KMnO_4 in the precursor mixture. Hence, from a standpoint of iron composition the higher pyrolysis comes with the drawback of excessive side product formation. The detailed Mössbauer parameters of the spectra from **Figure 82** are given in **Table S2**.

Performance and Durability during PEMFC Tests

Figure 83 shows the polarization curves of the three catalysts which were measured in $\text{H}_2\text{-O}_2$ in this chapter. There is no significant difference in the polarization curves of the displayed catalysts. Indeed, it is a very promising result that the sample prepared at 1000 °C, $\text{C-2htm-PPy}_{+\text{FeCl}_3/-\text{KMnO}_4}\text{-1000}$ shows an almost identical performance as the sample prepared at 800 °C, $\text{C-2htm-PPy}_{+\text{FeCl}_3/-\text{KMnO}_4}$. Considering the ^{57}Fe Mössbauer spectra, where a significant higher amount of less active inorganic iron species was found for $\text{C-2htm-PPy}_{+\text{FeCl}_3/-\text{KMnO}_4}\text{-1000}$, this is a surprising result. However, even so ^{57}Fe Mössbauer spectroscopy contains important information on the iron (active-site) composition, there is no

information about how many of the active-sites are actually accessible for the reaction. Therefore, a possible explanation is that the active sites in C-2htm-PPy_{+FeCl3/-KMnO4_1000} are less buried in the bulk of the sample but more present at the surface and hence more accessible for the reaction in comparison to C-2htm-PPy_{+FeCl3/-KMnO4}.

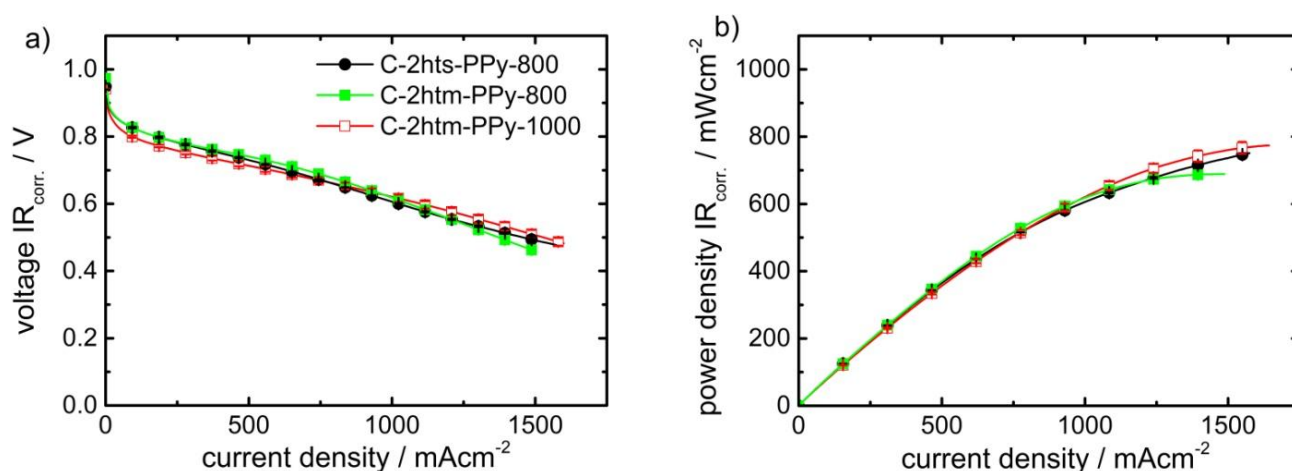


Figure 83: PEMFC polarization curves of catalysts that are prepared at different temperatures during the first heat treatment. (experiment conditions: H₂-O₂, cathode loading 3.4 - 3.6 mg cm⁻², N212 membrane, 1 bar gauge back pressure, 0.2 L min⁻¹ oxidant and fuel flow, 80 °C, 96 % humidity).

The durability of the catalysts in H₂-O₂ at a constant potential 600 mV is displayed in **Figure 84**. Displayed are the two catalysts that were prepared by the exact same protocol despite the change in temperature during the first heat treatment. As mentioned before, due to a lab shutdown C-2htm-PPy_{+FeCl3/-KMnO4} was measured for only 120 minutes. For this reason, C-2hts-PPy_{+FeCl3/-KMnO4} is included in **Figure 84**. C-2hts-PPy_{+FeCl3/-KMnO4} is likewise prepared at 800 °C but with a different duration time for the second heat treatment. As follows from **Figure 84 a)**, the overall current density is affected by changing the duration of the second heat treatment but not its relative change, the relative change is given **Figure 84 b)**. Hence, for discussing the matter of long-term stability C-2hts-PPy_{+FeCl3/-KMnO4} can be used too. The results clearly show that the catalyst prepared at 1000 °C shows a superior stability in comparison to both 800 °C samples. Within the first 120 minutes of constant operation about 85 % of the initial current density is measured for C-2htm-PPy_{+FeCl3/-KMnO4_1000}. For C-2htm-PPy_{+FeCl3/-KMnO4} and C-2hts-PPy_{+FeCl3/-KMnO4} it is 68 % and 65 % respectively. For a longer operation time of 525 min the difference becomes even more decisive, about 59 % remain for the 1000 °C sample whereas only 33 % are retained for the 800 °C one.

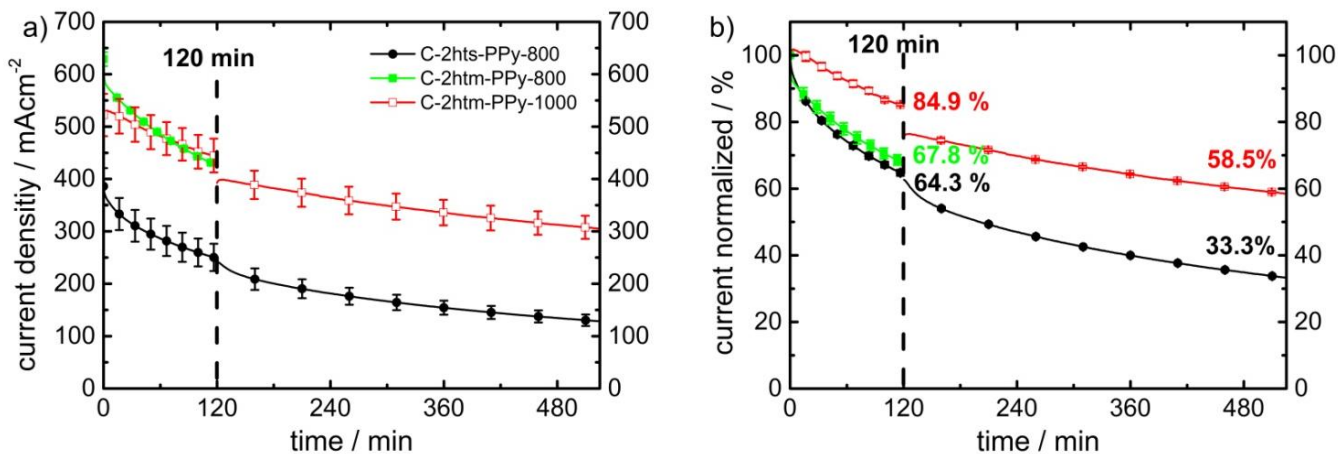


Figure 84: PEMFC stability tests of catalysts that that are prepared at different temperatures during the first heat treatment. The durability tests are performed at a constant potential of 600 mV. (experiment conditions: H₂-O₂, cathode loading 3.4 - 3.6 mg cm⁻², N212 membrane, 1 bar gauge back pressure, 0.2 L min⁻¹ oxidant and fuel flow, 80 °C, 96 % humidity).

As for most common real world fuel cell applications air and not pure O₂ is used as oxidant C-2htm-PPy_{+FeCl₃/-KMnO₄_1000} and C-2htm-PPy_{+FeCl₃/-KMnO₄} were further investigated in H₂-air. The polarization curves are presented in **Figure 85**. Here, contrary to the polarization curves measured in H₂-O₂, the respective curves in H₂-air reveal a performance difference between the two samples. For the sample prepared at 1000 °C a slightly lower current density is measured. This behavior can be explained by the slightly lower BET surface area of C-2htm-PPy_{+FeCl₃/-KMnO₄_1000}. **Figure 86** shows a 60-hour stability test of these two catalysts, likewise under H₂-air at a constant potential of 500 mV. Once again there is a slight difference in behavior when comparing the measurements in H₂-air with those obtained under H₂-O₂ (**Figure 84**). When operating in air, the initial current decay over the first 20 hours of the two catalysts is almost identical. About 63 % of the initial current density is measured after 20 hours of operation time. However, when the constant potential hold is extended further the 1000 °C sample, C-2htm-PPy_{+FeCl₃/-KMnO₄_1000} reveals an enhanced stability. After operating for 60 hours 39 % of the initial current density remains for C-2htm-PPy_{+FeCl₃/-KMnO₄_1000}. Whereas only 20 % are obtained under same conditions for the catalysts prepared at the lower pyrolysis temperature of 800 °C.

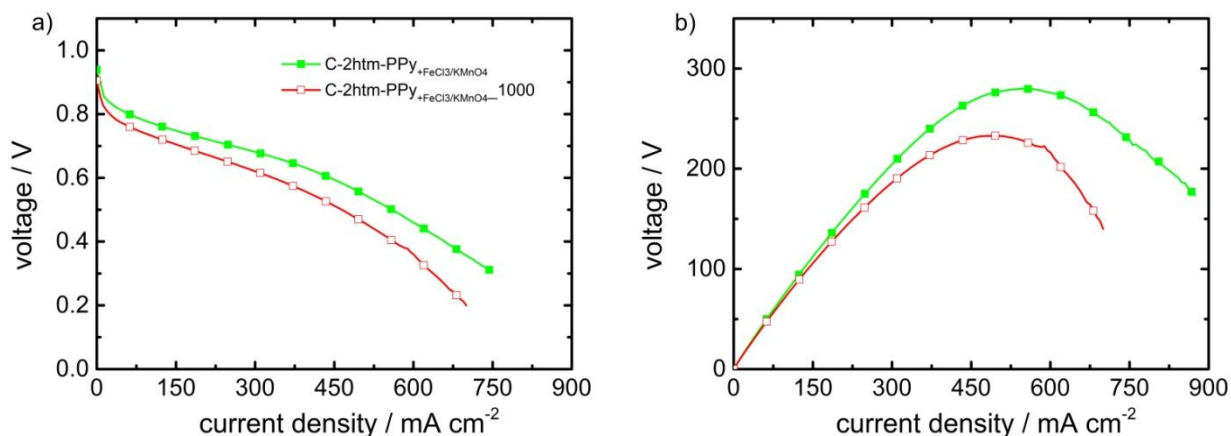


Figure 85: PEMFC polarization curves of catalysts that are prepared at different temperatures during the first heat treatment. (experiment conditions: H₂-air, cathode loading 3.4 - 3.6 mg cm⁻², N212 membrane, 1 bar gauge back pressure, 0.2 L min⁻¹ oxidant and fuel flow, 80 °C, 96 % humidity).

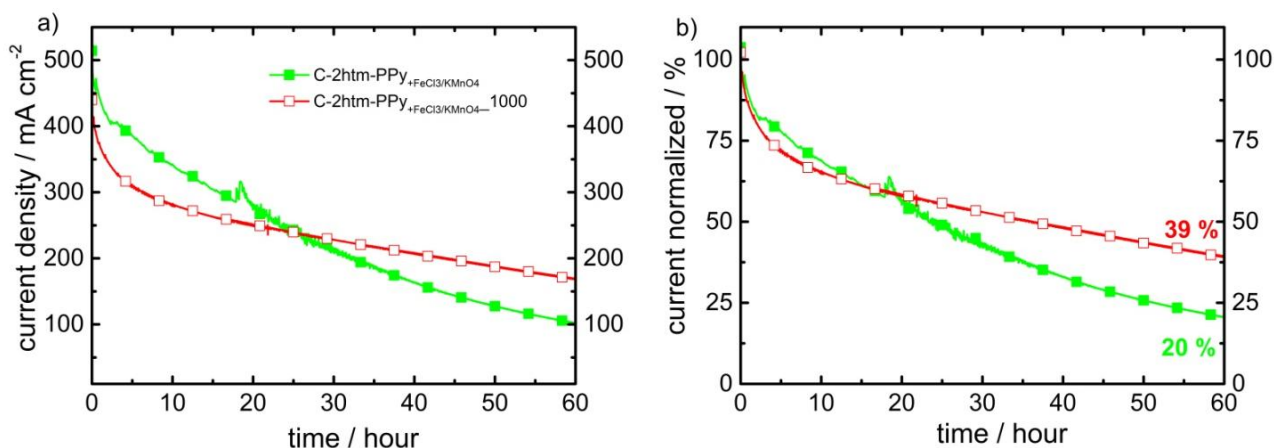


Figure 86: PEMFC stability tests of catalysts that that are prepared at different temperatures during the first heat treatment. The durability tests are performed at a constant potential of 600 mV. (experiment conditions: H₂-air, cathode loading 3.4 - 3.6 mg cm⁻², N212 membrane, 1 bar gauge back pressure, 0.2 L min⁻¹ oxidant and fuel flow, 80 °C, 96 % humidity).

Brief Summary on the Influence of Pyrolysis Temperatures

For the polypyrrole catalysts a second heat treatment significantly enhances the performance. However, during the second heat treatment the BET surface area is partly collapsing. Here, an optimum duration time for the second heat treatment was found which is explained by yielding a good compromise between retaining a high surface area (short treatment times) and sufficiently healing the defects induced by the acid leaching (long treatment times). Further, 2-hour stability tests indicate that there is no influence of the second heat treatment or its duration time on the initial current decay of these catalysts.

When the absolute temperature of the first heat treatment is increased from 800°C to 1000°C the catalyst shows a significant better stability, whereas the activity is only slightly lower.

8.6 Increasing the Acid Leaching of Inorganic Metal Species

In the previous chapter it was revealed that by increasing the temperature of the first heat treatment from 800 °C to 1000 °C a significantly more stable PEMFC operation was achieved. Whereas at the same time the performance in H₂-O₂ was preserved and the performance in H₂-air only declined to a minor extent. However, TEM and ⁵⁷Fe-Mössbauer spectroscopy showed the formation of inorganic Fe by-products at 1000 °C. These inorganic phases are detrimental because they can leach out during fuel cell operation [33]. The Fe²⁺/Fe³⁺-ions bind more strongly to the proton conducting functional sides of Nafion™ than protons do. This results in a lowering of the proton conductivity in the membrane and in the catalyst layer itself. Even worse the Fe²⁺/Fe³⁺-ions can damage the membrane and the catalyst oxidatively through Fenton-like reactions [159, 160].

It is the purpose of this chapter to minimize the formation of these by-product phases while retaining the good stability which was gained through performing the pyrolysis at 1000 °C. The approach aims for improving the acid leaching step. Commonly, the acid leaching is performed in mineral acids like HCl, H₂SO₄ or HNO₃ with varying concentrations of about 0.1 to 5 M. To further enhance the leaching process, the sample might be heated and placed in an ultra-sonic bath. The latter helps to disperse the catalyst powder by breaking-up agglomerates. As a consequence, inorganic Fe phases which are protected by surrounding carbon might survive the acid leaching. The acid leaching of the samples that are reported in previous chapters was performed in 2 M HCl, at 50 °C in an ultra-sonic bath for 2 - 2.5 hours followed by aging this mixture at room temperature over-night. To avoid the formation of acid stable iron oxides or hydroxide the leaching process is performed in N₂ saturated solution [33]. The problem that was identified while applying this procedure is the insufficient dispersion of the catalyst powder. The catalysts might consist of smaller particles but those combine and form bigger agglomerates. The latter are not being broken up completely during the acid leaching step and therefore protect inorganic Fe phases from being removed by the acid.

The idea on how to overcome this issue is to add a certain amount of isopropanol to the aqueous HCl solution. The additional solvent is lowering the surface tension of the water-based acid solution and thereby helps the solvent and the acid molecules to penetrate the agglomerates and pores. In general, all kind of water miscible and low-surface tension solvents can be used for this purpose. Isopropanol was chosen here because of its capacity to form very uniform and fine catalyst dispersions during ink formulation.

Two catalysts were prepared according to the previously developed methods. The best performing catalyst was chosen. Hence, polypyrrole-methyl orange was used in combination with FeCl₃ and KMnO₄ as the precursor mixture. The precursors were heated to 1000 °C. The subsequent acid leaching

was either performed according to the standard protocol in 2 M HCl or with a mixture of 150 ml 2 M HCl and 50 ml isopropanol. A second heat treatment was performed as well. All details on the synthesis are given in **Table 22**.

Table 22: Fe and Mn-based polypyrrole-methyl orange catalysts prepared at 1000 °C with a different acid leaching step.

sample name	polypyrrole Tubes / mg	FeCl ₃ / mg	KMnO ₄ / mg	1 st heat treatment 300 °C/h	2 nd heat treatment	acid leaching
C-PPy-1000	350	590	176	1000 °C hold 1h	800 °C h ⁻¹ to 800 °C hold 15 min	standard
C-PPy-1000-IsoAL	350	590	176	1000 °C hold 1 h	800 °C h ⁻¹ to 800 °C hold 15 min	with isopropanol

Physical Characterization BET, TEM and Mössbauer-Spectroscopy

As before, N₂ sorption experiments are used to evaluate the BET surface area of the catalysts. The results are depicted in **Figure 87**. The surface area of the isopropanol acid leached catalyst is slightly enhanced. This result is expected because iron particles are usually embedded in carbon pores or holes. The removal of these Fe particles leaves the pores exposed to the surface, the overall surface area increases. However, the obtained BET data only indicates a successful removal of more Fe particles for the isopropanol acid leached sample. The be certain, TEM and ⁵⁷Fe-Mössbauer spectroscopy are evaluated.

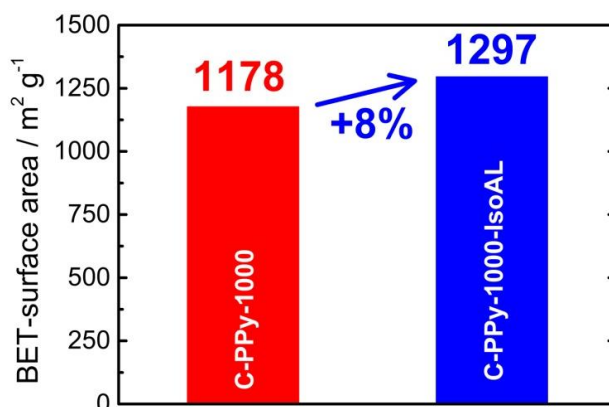


Figure 87: BET surface areas obtained from N₂ sorption measurements for two FeCl₃/KMnO₄, polypyrrole-methyl orange-based catalysts prepared with a normal acid leaching C-PPy-1000 and with an isopropanol acid leaching C-PPy-1000-IsoAL.

The TEM pictures of the two samples are given in **Figure 88**. The upper pictures (red box) contain the results of C-PPy-1000. This catalyst contains plenty of visible inorganic Fe phases, e.g. Fe nanoparticles. Contrary, in the catalyst that was acid leached with additional isopropanol no nanoparticles are found. The TEM results of C-PPy-1000-IsoAL are depicted in the lower part (blue box).

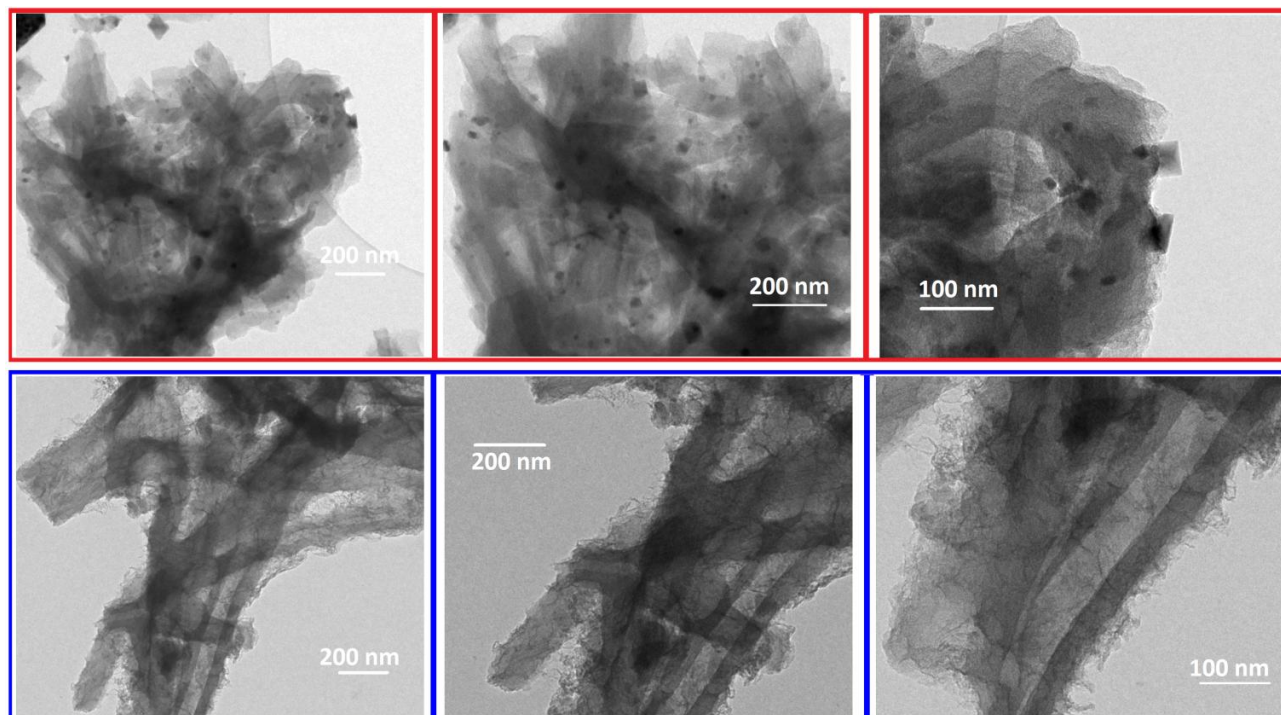


Figure 88: TEM photographs of $\text{FeCl}_3/\text{KMnO}_4$ polypyrrole-methyl orange catalysts that are prepared at 1000 °C but with a different acid leaching, upper (red box) pictures of catalysts that underwent a 2 M HCl acid leaching and lower (blue box) pictures of catalyst that was acid leached with 2 M HCl + isopropanol.

^{57}Fe -Mössbauer spectroscopy is a bulk method and allows for a more certain statement on the presence of any inorganic iron products in comparison to TEM. The obtained ^{57}Fe -Mössbauer spectra of the regular and the isopropanol acid leached sample are given in **Figure 89**. Despite the dominant D1 doublet species, as discussed in chapter 8.5.2, C-PPy-1000 contains inorganic iron and different iron oxide phases. Later are not found in C-PPy-1000-IsoAL. Thus, it is concluded that the isopropanol assisted acid leaching removes or at least increases the removal of inorganic side phases. Furthermore, the overall iron content of the isopropanol acid leached sample, C-PPy-1000-IsoAL is significantly lowered compared to C-PPy-1000, this is illustrated in **Figure 89 c)**. The absorption signal is much lower for both, doublet as well as for sextet species. There are two possible explanations for this observation: (I) The isopropanol assisted acid leaching removes all iron sites in the same manner, meaning active sites as well as inorganic spectator phases. This would be a drawback of the new leaching method and would manifest itself in a significant lower activity of the catalyst. (II) As stated by Wagner et al. [450], the recorded doublets signals in C-PPy-1000 are actually not only composed of

different FeN₄ sites of different oxidation spin states and with different axial ligands but also of iron and iron oxide nano clusters. The isopropanol assisted acid leaching removes the major amount of these nano clusters. Since those are most probably not active for the ORR, hypothesis (II) would manifest itself in a similar activity of C-PPy-1000 and C-PPy-100-IsoAL. Likewise as given by Wagner et al. ⁵⁷Fe-Mössbauer spectroscopy at low temperatures (~5K) in combination with an external magnetic field could resolve the presence of any iron or iron oxide nano clusters [450]. A table with the Mössbauer parameters is given in **Table S2**.

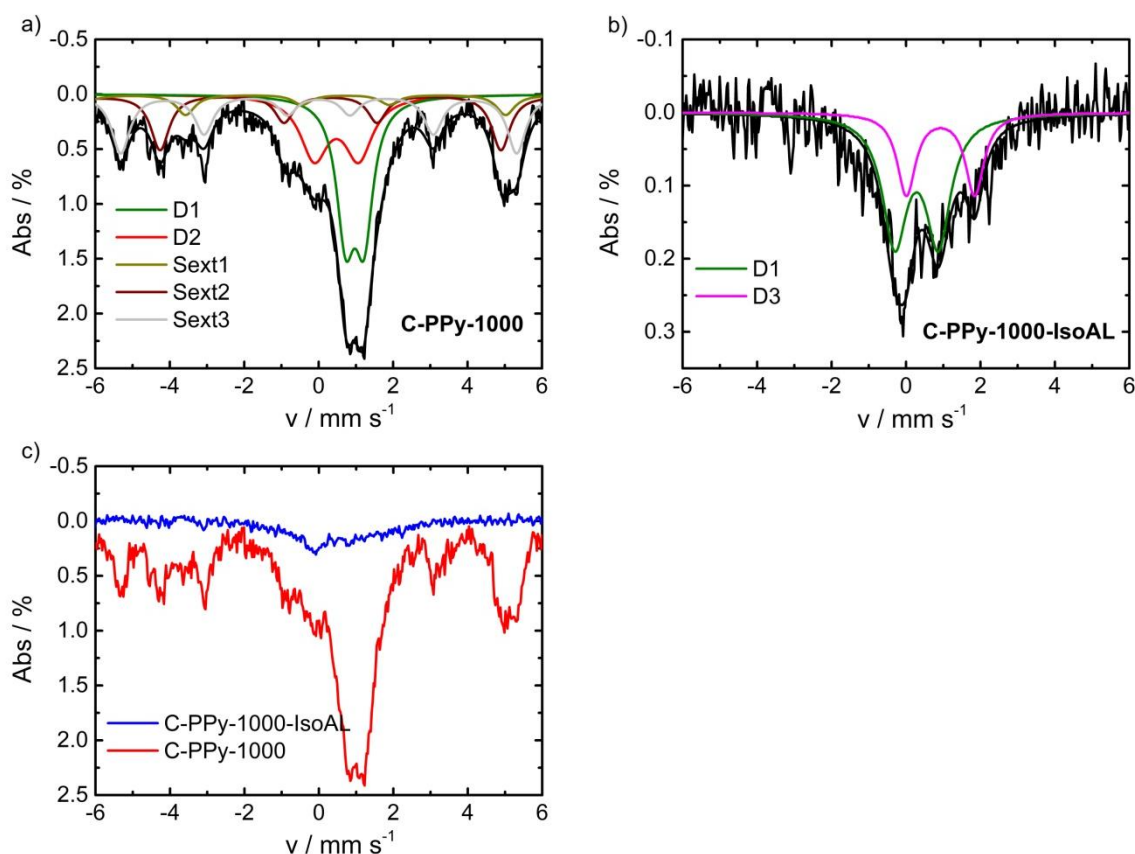


Figure 89: Influence of the acid leaching procedure on the ⁵⁷Fe-Mössbauer spectra of polypyrrole catalysts.

Performance and Durability during PEMFC Tests

The fuel cell performance of the acid leached and isopropanol acid leached catalyst are evaluated in H₂-air. The polarization curves are presented in **Figure 90**. Both samples were measured twice, displayed is the average value as well as the error bars. When conducting the enhanced acid leaching with isopropanol the performance is slightly higher in comparison to the commonly acid leached sample. The polarization curves reveal that the performance enhancement correlates over the whole potential range. Meaning that the mass transport at the lower potential region, as well as the kinetic properties emerging at high potentials are positively affected by the treatment. This is a very promising

result, when considering that at the same time a significant amount of inorganic by-products is removed with this method. Further, from the data of **Figure 90** it is stated that the solvent plus acid treatment does not damage or attack the actual molecular FeN_xC_y active sites. From this standpoint, hypothesis (II) explains the outcome of the ^{57}Fe -Mössbauer spectra.

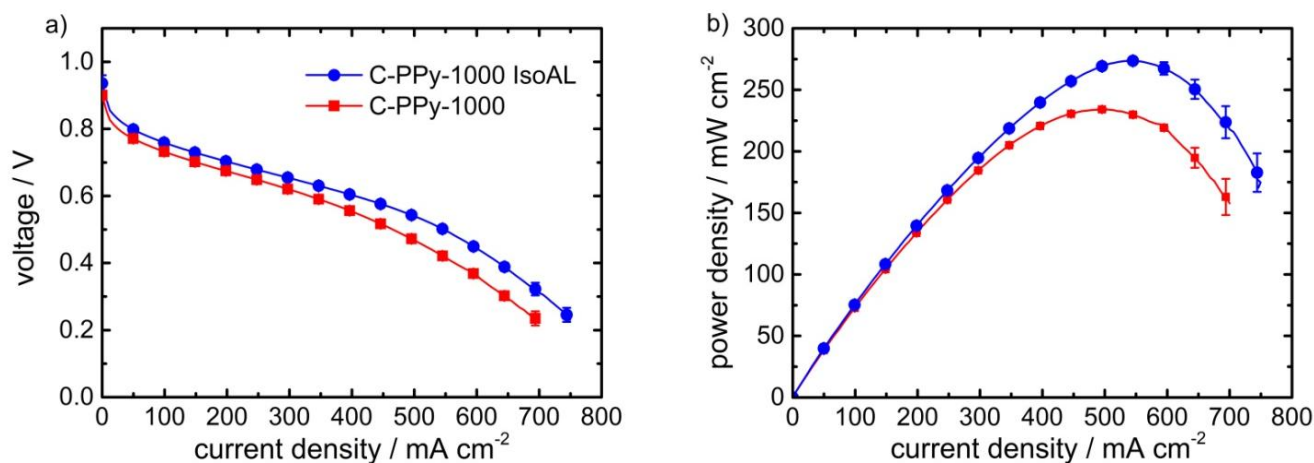


Figure 90: PEMFC polarization curves of catalysts that are prepared at different temperatures during the first heat treatment. (experiment conditions: H_2 -air, cathode loading $3.2 - 3.5 \text{ mg cm}^{-2}$, N212 membrane, 1 bar gauge back pressure, 0.2 Lmin^{-1} oxidant and fuel flow, $80 \text{ }^\circ\text{C}$, 96 % humidity).

Fuel cell stability of C-PPy-1000 and C-PPy-100-IsoAL is depicted in **Figure 91**. The tests were run in H_2 -air at a constant potential of 500 mV. The overall current density values are shown in **Figure 91 a)**. The MEA prepared with C-PPy-1000-IsoAL gives a higher initial value of 523 mA cm^{-2} than the one made with C-PPy-1000, its initial current density is 440 mA cm^{-2} . This result is in line with the data obtained from the polarization curves in **Figure 90**. In terms of stability, both samples show the same initial current decay over the first 10 hours of the experiment. After 10 hours about 65 % of the initial current density is retained for C-PPy-1000 and 66 % is obtained for C-PPy-1000-IsoAL. Following the rapid initial decay of both samples the isopropanol acid leached sample shows a slightly better stability. After 27 hours of testing the isopropanol acid leached sample, C-PPy-1000-IsoAL retains 57 % of its initial current density. Conducting the same experiment for C-PPy-1000 gives a value of 54 %. The corresponding time frame after the rapid initial decay where C-PPy-1000-IsoAL slowly begins to perform more stable than C-PPy-1000 is included separately and in magnification in **Figure 91 b)**. Unfortunately, due to a lab shutdown because of renovation work, the sample C-PPy-1000-IsoAL could not be measured for a longer period. Hence, we can only state that the initial current decay within the first 10 hours is not affected and therefore also not caused by leaching of inorganic Fe by-products like Fe carbides or Fe nanoparticles. The results indicate that the isopropanol acid leached sample exhibits an enhanced stability following the stage of the initial decay. However, the experiment needs to be conducted over a course of at least 50 hours in order to confirm this first quite promising results.

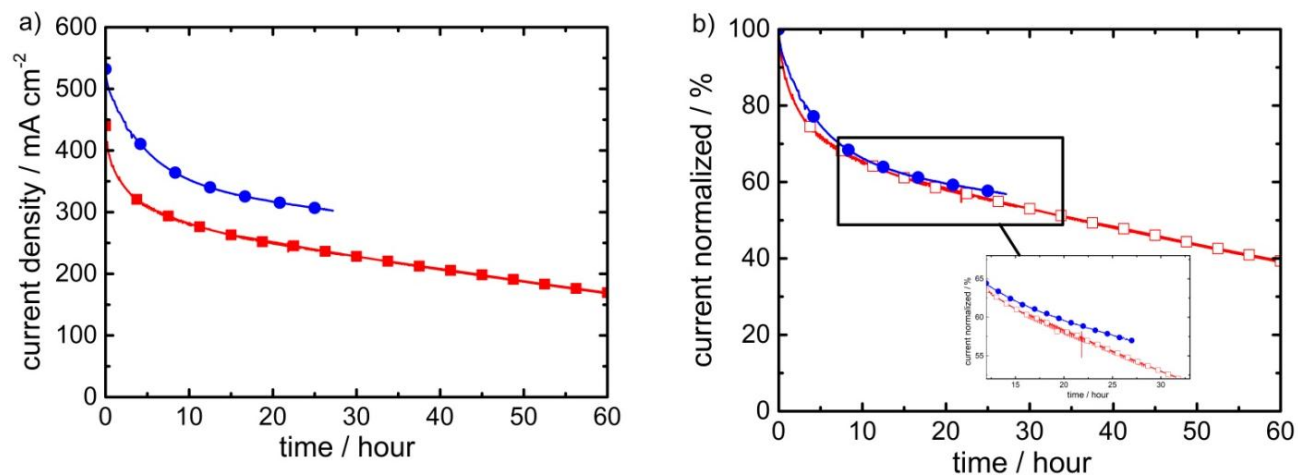


Figure 91: PEMFC stability tests of a $\text{FeCl}_3/\text{KMnO}_4$ polypyrrole-methyl orange catalyst that was prepared with a common 2M HCl acid treatment and of the same catalyst prepared with a 2 M HCl + isopropanol acid treatment. The durability tests are performed at a constant potential of 500 mV. (experiment conditions: H_2 -air, cathode loading 3.2 - 3.5 mg cm^{-2} , N212 membrane, 1 bar gauge back pressure, 0.2 L min^{-1} oxidant and fuel flow, 80 °C, 96 % humidity).

8.7 The Influence of Doping Agents on Polypyrrole based Me-N-C Catalysts

The lab work considering some results within this chapter was assisted by Niels Kubitzka during a research lab internship.

In chapter 8.2, it was shown that methyl orange has a significant influence on the characteristics and performance of polypyrrole based Fe-N-C catalysts. Very briefly, it was found that polypyrrole which is synthesized in the presence of methyl orange is capable of suppressing the formation of iron by-products during the pyrolysis. Instead, the formation of molecular active sites is boosted. The underlying effect behind this is associated with the methyl orange molecules being incorporated into the polymer structure either by doping or similar effects. Beforehand it should be mentioned that the investigations within this chapter were conducted at the very end of this thesis project and the overall experimental work had to come to an end. This means that the depth of characterization and electrochemical experiments within this chapter is limited. Still, some first interesting results on the described phenomena are presented. The idea is to investigate other organic molecules besides methyl orange and their effect on the fuel cell performance of the resulting catalyst. The motivation is to find another doping agent that exceeds the effects of methyl orange. Even more, it is of interest to study which structural part of the methyl orange molecule is responsible for the performance enhancement of the catalysts. Hence, organic molecules are selected in a way that a systematic comparison of functional groups is possible. An overview of the inspected compounds is shown in **Figure 92**.

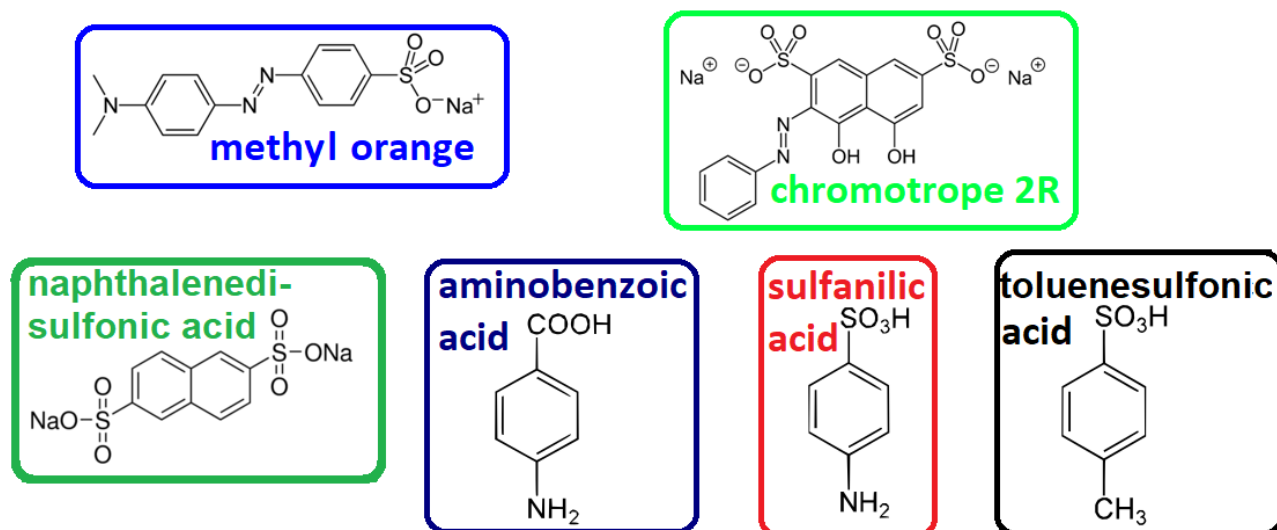


Figure 92: Lewis-structure and name of the as doping agents investigated compounds for the preparation of polypyrrole-based catalysts.

Methyl orange serves as the starting compound. Its characteristic functional groups are the two aromatic benzene rings that are linked by an azo-group (RN=NR'), the sulfonic acid group and the

dimethylamine group. Chromotrope© 2R is chosen to explore if larger aromatic parts influence the characteristics of the catalyst. It comprises of a third benzene ring. Naphthalenedisulfonic acid has no azo-group linkage but a second sulfonic acid group. A very systematic comparison is possible between aminobenzoic acid, sulfanilic acid and toluenesulfonic acid. Investigation of these molecules will give information about the influence of the sulfonic acid group, the carboxylic acid group, the amino group and the methyl group.

For the synthesis of the catalysts one polypyrrole batch was synthesized in the presence of each of the mentioned organic compounds. The doped polypyrrole samples were then impregnated with FeCl_3 and KMnO_4 as described earlier for C-2ht-PPy_{+FeCl₃/-KMnO₄}. The first heat treatment was conducted at 1000 °C, followed by the isopropanol acid leaching. All samples underwent a second heat treatment at 800 °C. These details and the sample denotation are summarized below in **Table 23**.

Table 23: Catalysts prepared from $\text{FeCl}_3/\text{KMnO}_4$ polypyrrole mixtures. The polypyrrole is doped with different organic compounds.

Sample Name	Polypyrrole synthesized in presence of	First heat treatment 300 °C/h	Second heat treatment	Acid Leaching
C-PPy-MO	methyl orange	300 °C h ⁻¹ 1000 °C hold 1 h	800 °C h ⁻¹ to 800 °C hold 15 min	2 M HCl +isopropanol
C-PPy-SA	sulfanilic acid	300 °C h ⁻¹ 1000 °C hold 1 h	800 °C h ⁻¹ to 800 °C hold 15 min	2 M HCl +isopropanol
C-PPy-TSA	toluenesulfonic acid	300 °C h ⁻¹ 1000 °C hold 1 h	800 °C h ⁻¹ to 800 °C hold 15 min	2 M HCl +isopropanol
C-PPy-ABA	aminobenzoic acid	300 °C h ⁻¹ 1000 °C hold 1 h	800 °C h ⁻¹ to 800 °C hold 15 min	2 M HCl +isopropanol
C-PPy-NDSA	naphthalenedisulfonic acid	300 °C h ⁻¹ 1000 °C hold 1 h	800 °C h ⁻¹ to 800 °C hold 15 min	2 M HCl +isopropanol
C-PPy-CT2R	Chromotrop© 2R	300 °C h ⁻¹ 1000 °C hold 1 h	800 °C h ⁻¹ to 800 °C hold 15 min	2 M HCl +isopropanol

Physical Characterization BET, and TEM

Due to the mentioned time limitations of this project and the fact that C-PPy-ABA showed very poor fuel cell performance (see next chapter), C-PPy-ABA was not physically characterized.

All the other samples which were prepared in the course of this chapter are characterized by TEM and BET. The TEM pictures of C-PPy-MO and C-PPy-CT2R are shown in **Figure 93**. The catalyst prepared from polypyrrole-methyl orange shows the typical nanotube morphology as described earlier. The nanotubes are slightly deformed and even appear to be partially melted together after the pyrolysis and acid leaching. C-PPy-CT2R was prepared from polypyrrole-chromotrop©2R. Here a mixture of bigger spherical particles and nano rods is obtained. Interestingly even mixed morphologies (spherical + rod) are created with just one type of dopant.

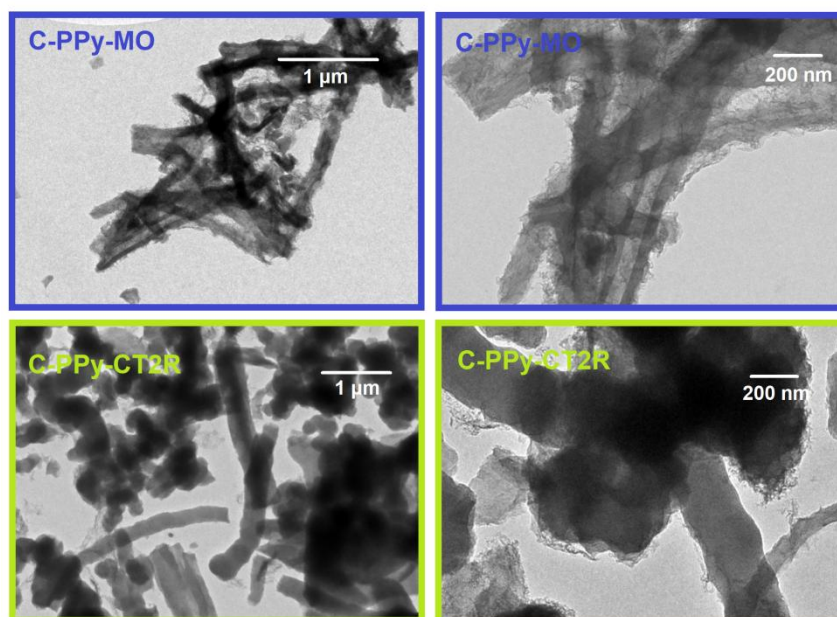


Figure 93: TEM photographs of different polypyrrole based catalysts. Upper pictures show catalyst obtained from polypyrrole-methyl orange, C-PPy-MO and lower pictures gives C-PPy-CT2R a catalyst prepared from polypyrrole-Chromotrop©2R.

Figure 94 gives the TEM photographs of C-PPy-TSA (upper), C-PPy-NDSA (middle) and C-PPy-SA (lower). Neither nanotubes, nor nano rods are found. The morphology of all three catalysts is dominated by a spherical shaped polypyrrole framework. However, there are also some specific differences among these materials. For C-PPy-TSA large and densely packed particles with an estimated size of at least several μm are visible. These particles show sharp and very defined edges. For C-PPy-NDSA, very similar, dense and micrometer-sized particles are obtained. However, as it can be seen at the edges of these particles, the dense spherical polypyrrole backbone is coated with thin layers of disordered graphene sheets. These sheets further contain carbon encapsulated iron nanoparticles. Contrary to the first two spherical samples, C-PPy-SA comprises of much smaller particles. The polypyrrole framework particles of C-PPy-SA show a stronger distribution in their size but are all well below $1 \mu\text{m}$. The morphology of C-PPy-SA resembles the morphology of carbon blacks very much. Later are typically used as support in Pt/C and have demonstrated good mass transport characteristics.

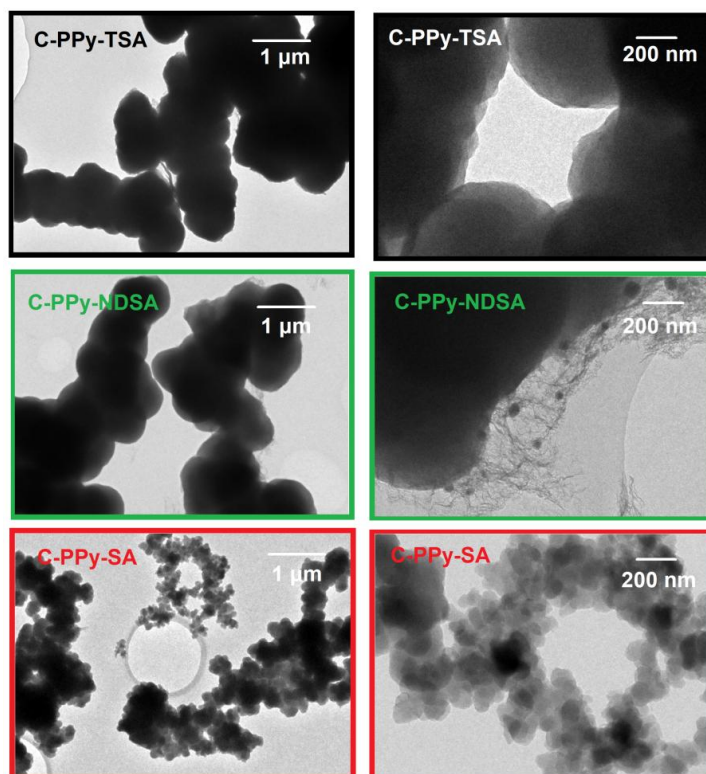


Figure 94: TEM photographs of different polypyrrole based catalysts. Upper pictures show catalyst obtained from polypyrrole-toluenesulfonic acid, C-PPy-TSA, middle pictures show the catalyst synthesized with polypyrrole- naphthalenedisulfonic acid and lower pictures gives C-PPy-SA a catalyst prepared from polypyrrole-sulfanilic acid.

The results of the N_2 sorption measurements are given in **Figure 95**. All the synthesized catalysts exhibit very high BET surface areas ($> 1200 \text{ m}^2 \text{ g}^{-1}$). As mentioned earlier, these results are remarkable high compared to other reported catalysts [448]. Usually high surface areas of $> 1000 \text{ m}^2 \text{ g}^{-1}$ are only obtained after a second heat treatment with NH_3 [25]. However, from all of the prepared catalysts, C-PPy-SA shows an exceptionally high BET surface area of $1503 \text{ m}^2 \text{ g}^{-1}$. This is in good accordance with the TEM photographs which revealed significantly smaller particles sizes for C-PPy-SA then for the other catalysts.

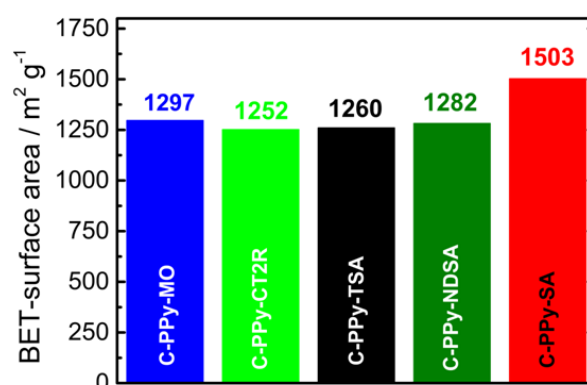


Figure 95: BET surface area obtained from N_2 sorption experiments for catalysts which are synthesized from different polypyrrole + organic molecule precursors.

Activity during PEMFC Tests

The activity of the catalysts was evaluated by performing PEMFC tests under H₂-air. The results are shown in **Figure 96** and **Figure 97**. Whereas **Figure 96** gives the results for C-PPy-TSA, C-PPy-NDSA, C-PPy-MO and C-PPy-SA the catalyst loadings follow the same chronological order and are 3.7 mg cm⁻², 3.5 mg cm⁻², 3.5 mg cm⁻² and 3.5 mg cm⁻². It becomes apparent that all these catalysts show very similar OCV values as well as similar behavior in the kinetic region of the polarization curve (only C-PPy-TSA lacks behind slightly). This indicates, that for all of the used dopants the effect of enhancing the ORR activity in comparison to a catalyst prepared without an additional dopant is true (see **Figure 60** and **Figure 62**). The characteristic functional groups that are common in the used dopants from **Figure 96** (toluenesulfonic acid, naphthalenedisulfonic acid, methyl orange and sulfanilic acid) are at least one phenyl-group and one sulfonic acid group. However, **Figure 96** also reveals some drastic differences in the mass transport region of the polarization curves. Especially C-PPy-TSA suffers from a very low performance at the lower potential region. A maximum power density of only ~175 mW cm⁻² is reached. Contrary, the catalyst which already showed the highest BET surface area as well as favorable particle morphology during TEM, C-PPy-SA reveals great performance during kinetic and mass transport limited region of the polarization curve. A maximum power density of 316 mW cm⁻² is reached.

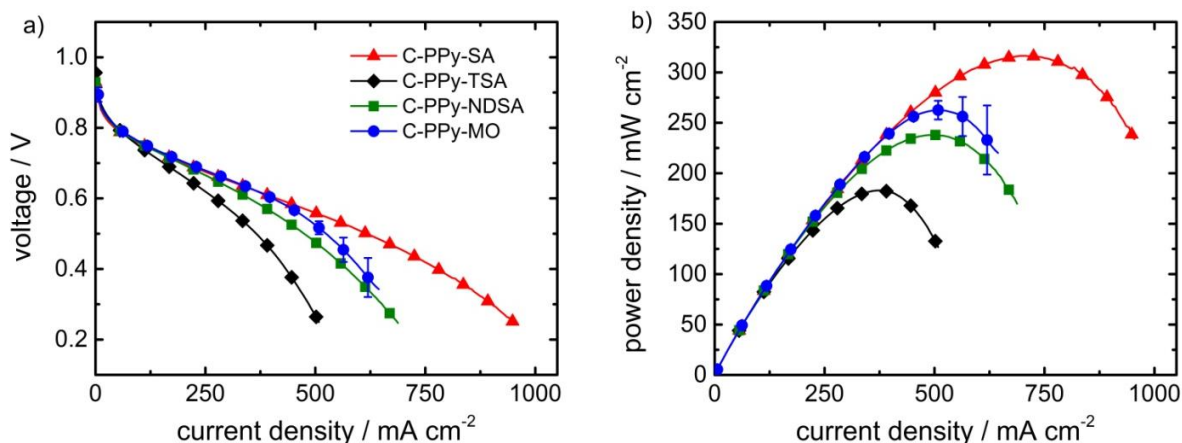


Figure 96: PEMFC polarization curves of catalysts that are prepared from differently doped polypyrrole. (experiment conditions: H₂-air, cathode loading 3.5 - 3.7 mg cm⁻², N212 membrane, 1 bar gauge back pressure, 0.2 L min⁻¹ oxidant and fuel flow, 80 °C, 96 % humidity).

It was not possible to produce stable catalyst layers with loadings of 3.5 mg cm⁻² for C-PPy-ABA and C-PPy-CT2R. Therefore, these two catalysts were evaluated separately with a catalyst loading of 2.7 mg cm⁻². For comparison, a second MEA from C-PPy-SA with a loading of 2.7 mg cm⁻² was prepared and is displayed together with C-PPy-ABA and C-PPy-CT2R in **Figure 97**. As already obtained by the comparison of the other dopants in **Figure 96**, C-PPy-SA also shows the highest performance in relevance to C-PPy-C2TR and C-PPy-ABA. Further, C-PPy-CT2R shows a quite good performance, a

maximum power density of 231 mW cm^{-2} is measured. On the contrary, a very poor activity is measured for C-PPy-ABA. The polarization curve of C-PPy-ABA falls short in terms of the kinetic as well as the mass transport limited region of the polarization curves in comparison the rest of the displayed curves from in **Figure 97**. The measured maximum power density of C-PPy-ABA is 52 mW cm^{-2} . It becomes apparent that the pyrrole which is polymerized in the presence of aminobenzoic acid does not result in a catalyst material with the specific performance enhancement.

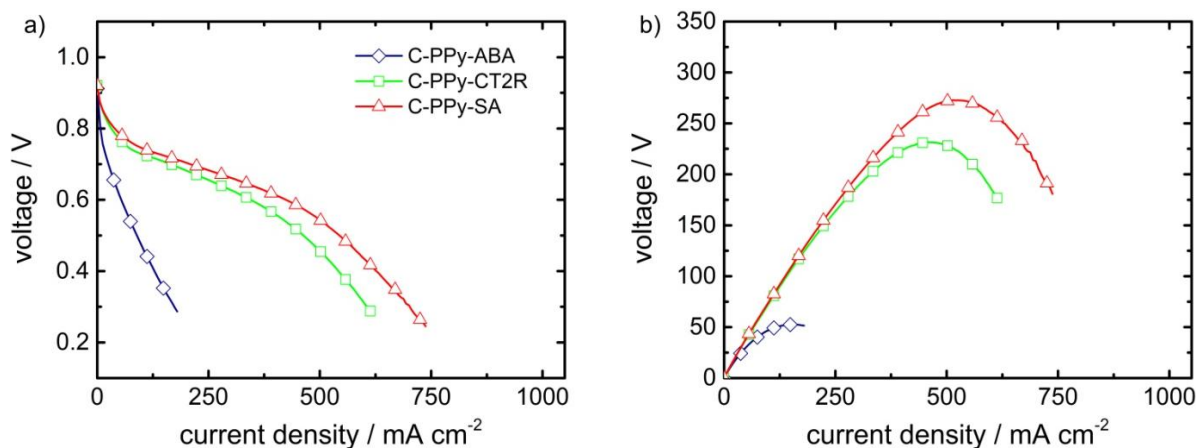


Figure 97: PEMFC polarization curves of catalysts that are prepared from differently doped polypyrrole. (experiment conditions: H₂-air, cathode loading 2.7 mg cm^{-2} , N212 membrane, 1 bar gauge back pressure, 0.2 L min^{-1} oxidant and fuel flow, $80 \text{ }^\circ\text{C}$, 96 % humidity).

From these results it is proposed that at least a phenyl-group and a sulfonic acid group are necessary for achieving the performance enhancement of polypyrrole-dopant-based catalysts in comparison to the normal polypyrrole-based catalyst. As the results further show, despite the general effect of significantly enhancing the ORR activity, the dopants also have a big impact on the morphology of the catalysts. The latter is an important factor because it determines the performance of the catalyst in the mass transport limited region of the polarization curve. The sulfanilic acid doped polypyrrole-based catalyst shows the best performance of the investigated materials. This is because sulfanilic acid is capable of boosting the ORR activity through the "doping effect". Whereas at the same time sulfanilic acid generates polypyrrole particles that show a favourable morphology. High current densities are reached because the catalysts benefit from the "morphology effect".

Due to the mentioned time limitation of this project no stability curves were measured for the catalysts in this chapter. However, for the most important catalyst, C-PPy-SA, these are given and discussed in the following chapter. Further, it should be noted that the catalysts C-PPy-NDSA, C-PPy-TSA and C-PPy-SA have been prepared with an additional washing step. This washing step was performed after the polymerization with 15 ml of EtOH. It has been proven for C-PPy-SA that this washing does not affect the fuel cell performance. Polarization curves for C-PPy-SA with and without EtOH washing step are given in the appendix.

8.8 Summary of Key Findings and Systematic Comparison of the Most Relevant Catalysts

In chapter 2, challenges related to Fe-N-C catalyst synthesis were formulated. During the course of this work these challenges were addressed. It is the aim of this chapter to reflect the outcome of the initially formulated topics. To visualize the process, this chapter also includes fuel cell measurements of all the relevant catalysts under identical testing conditions. This chapter gives the most important results in an abbreviated form, so that the focus is on the fuel cell graphs. A detailed summary and the outlook are provided in chapter 10.

Table 24 gives a summarizing overview of the addressed topics and developed solutions of each chapter using key words.

Table 24: Chapters of this thesis by addressed problem of Fe-N-C catalyst preparation and provided solution.

Key-word/ Chapter + page	Problem Addressed	Solution Approach / Outcome
Simple C, N-Precursor/ Chapter 8.1/8.2, page: 91	Expensive C, N precursors due to complex structure (e.g. ZIF-8 or porphyrins).	Cheap and reliable precursor found: polypyrrole doped with methyl orange.
Iron Precursors/ Chapter 8.3, page: 105	Low activity due to inhomogeneous iron site composition.	Mixture of FeCl ₃ and Fe(NO ₃) ₃ gives high activity and homogenous iron site composition.
Iron-Manganese Precursors/ Chapter 8.4, page: 113	Low activity but higher stability reported for manganese catalysts.	Synergetic effect of iron and manganese boosts activity.
Heat-Treatment and Stability/ Chapter 8.5, page: 123	Low stability caused by amorphous carbon phases.	Heat treatment at 1000 °C improves stability.
Inorganic Side-Phases/ Chapter 8.6, page: 134	Catalysts can contain inorganic iron, even after acid leaching.	Adding isopropanol improves the leaching process.
Doping Agents/ Chapter 8.7, page: 140	Low mass transport due to unfavorable catalyst particle morphology and high catalyst loadings.	Replacing methyl orange with sulfanilic acid as the doping agents improves catalyst particle morphology towards better mass transport in fuel cell.

Simple C, N-Precursor (0)

It was found that the major iron phase formed in polypyrrole based catalysts is iron carbide, which has no relevant ORR activity (acidic media). This problem is depending on the iron salt to polypyrrole ratio and is more severe for a high iron salt content. However, at low ratios an overall insufficient number of active sites are formed so that the catalyst is again non-relevant for any applications. Here, it was found that when polypyrrole is doped with methyl orange the main iron phases are not inorganic iron but atomically dispersed FeN_xC_y centers, even at high iron salt to polypyrrole ratios.

Iron Precursors (Cat A)

It was shown that the amount and type of iron salt which is used during the preparation influences the iron site composition, the BET surface area, the pore distribution and the overall morphology of the final catalyst. For the methyl orange doped polypyrrole approach a mixture of FeCl_3 and $\text{Fe}(\text{NO}_3)_3$ gives the best results among the tested iron precursor mixtures. The catalyst benefits from a pure active site formation, which was obtained when using FeCl_3 and a high surface area induced by the pore forming properties of $\text{Fe}(\text{NO}_3)_3$.

Iron-Manganese Precursors (Cat B)

Synergetic effects for a bimetallic iron and manganese-based variation of the catalysts were found. The most significant performance enhancement was found for a mixture of FeCl_3 and KMnO_4 .

Heat-Treatment and Stability (Cat C)

The absolute temperature during the first heat-treatment strongly impacts the activity as well as the stability of the catalyst. A balanced performance, meaning a good trade-off between activity (usually at lower temperatures) and stability (usually at higher temperature) was found at 1000 °C.

Enhanced Removal of Inorganic-Side Phases (Cat D)

Even so Fe-N-C catalysts undergo an acid leaching step, undesired inorganic-side phase can survive the cleaning procedure because they are often shielded by carbon. Isopropanol was added to the water-based acid solution. This lowered the surface tension and agglomerates were broken-up more efficiently. Significant amounts of iron were removed from the catalyst, whereas the activity remained unchanged.

Morphology and Mass Transport (Cat E)

Several other doping agents than methyl orange have been systematically examined. The results indicate that the structure of the doping molecule must feature a phenyl and a sulfonic acid group. A sulfanilic acid-based catalyst showed the best results. A favorable morphology of the polymer particles with respect to mass transport was identified as the major reason for enhanced fuel cell performance.

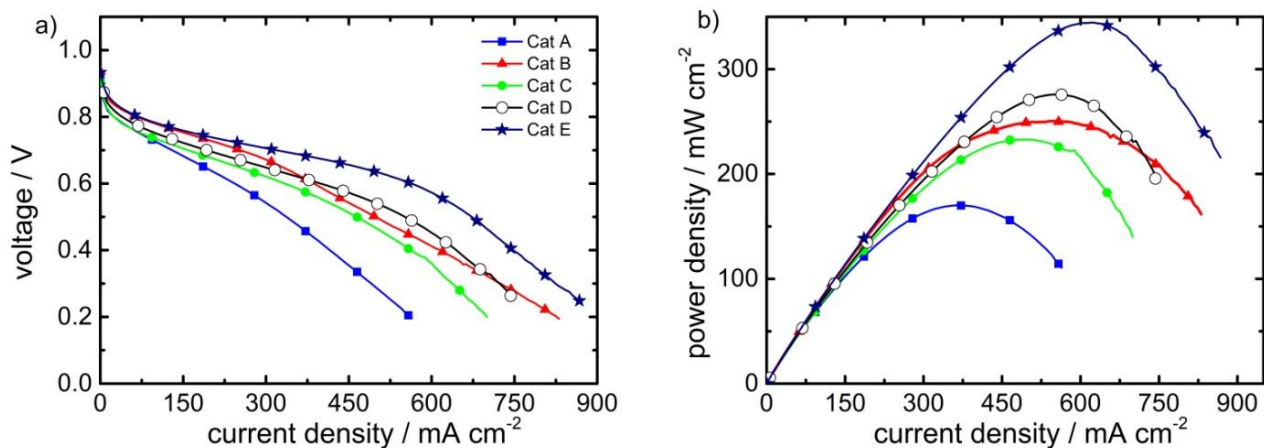


Figure 98: Polarization curve of catalysts A - E, (experiment conditions: H₂-air, cathode loading 3.3 -3.9 mg cm⁻², N212 membrane, 1 bar gauge back pressure, 0.2 L min⁻¹ oxidant and fuel flow, 80 °C, 96 % humidity).

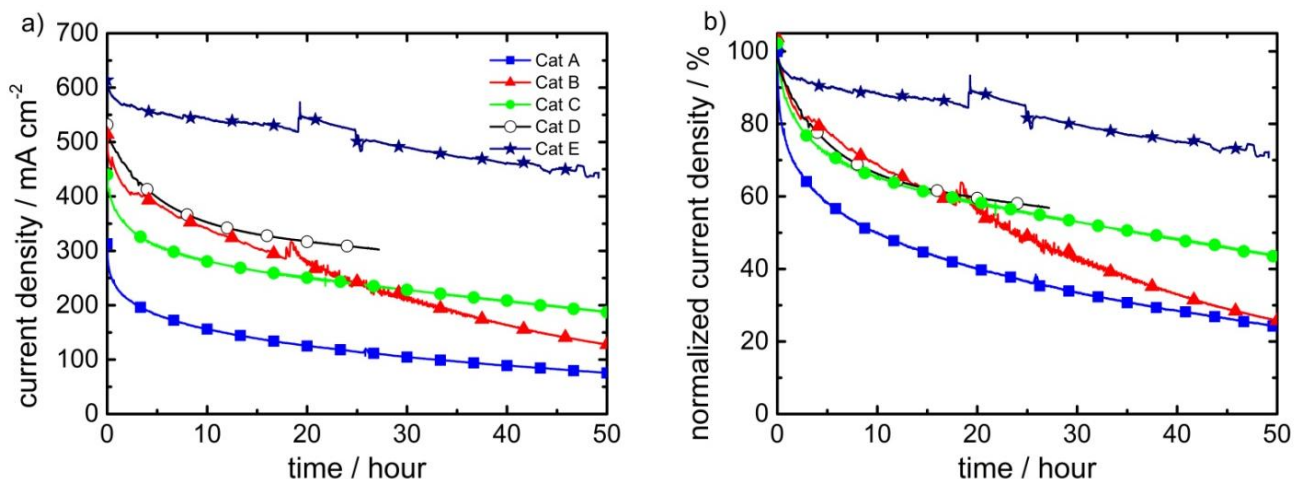


Figure 99: 50-hour Stability test of catalysts A - E. (experiment conditions: H₂-air, cathode loading 3.3 - 3.9 mg cm⁻², N212 membrane, 1 bar gauge back pressure, 0.2 L min⁻¹ oxidant and fuel flow, 80 °C, 96 % humidity, 500 mV constant potential).

Table 25: Key-parameters for the catalysts Cat A - E.

Catalyst	$j_{\text{initial}}(0.8V)$ /mAcm ⁻²	$j_{\text{initial}}(0.5V)$ /mAcm ⁻²	P_{max} /mWcm ⁻²	$U @ P_{\text{max}}$ / V	BET / m ² g ⁻¹	Loading /mg cm ⁻²	remaining j after 50 h CA / %
Cat A	24	345	170	365	1115	3.3	24
Cat B	61	503	250	545	968	3.3	26
Cat C	24	455	232	470	1178	3.4	43
Cat D	37	551	275	557	1297	3.2	56 (27 h)
Cat E	68	670	344	619	1503	3.9	71

9 Comparison to Best-Off Materials

The following chapter compares the developed catalyst to the best-off FeNC, reported in literature. Therefore, fuel cell activity and stability are considered. Further, the practicability of the synthesis process is discussed very briefly.

PEMFC Performance, Activity and Stability

For the comparison of the fuel cell performance, the activity and the stability during PEMFC conditions under H₂-air is used. The best-performing published catalysts are listed in **Table 26**. However, the huge variety of different MEA fabrication procedures and different testing conditions make a reliable comparison of the values difficult.

Table 26: Comparison of the so-far published best performing non-precious metal-based ORR catalyst during PEMFC tests in H₂-air.

Catalyst Name	Activity		Stability	Test Conditions	Ref.
	Current density @0.8 V / mA cm ⁻²	Peak power density / mW cm ⁻²	Current Retention / % (Potential or current, time)		
Cat E	68	344	70 % (0.5 V, 50 h)	cathode loading 3.9 mg cm ⁻² , N212 membrane, 1 bar back pressure, 0.2 L min ⁻¹ oxidant and fuel flow, 80 °C, 96 % humidity	This work
CA#1	120	570	> 90 % (galvanostatic 0.5 A cm ⁻² , 50 h)	cathode loading 4.0 mg cm ⁻² , NR211 membrane, 0.83 bar back pressure, 40 stoich. oxidant and fuel flow, 75 °C, 100 % humidity	[145]
PANI-FeCo-C(1)	105	550	> 90 % (0.4 V, 50 h)	cathode loading 4.0 mg cm ⁻² , 2x N1135 membrane, 1.8 bar back pressure, 0.6 air 0.4 H ₂ Lmin ⁻¹ flow, 80 °C, 100 % humidity	[140]
TPI@Z8(SiO₂)-650-C	105	410	60 % (galvanostatic 0.5 A cm ⁻² , 20 h)	cathode loading 2.7 mg cm ⁻² , N211 membrane, ?? bar back pressure, 0.5 air 0.3 H ₂ Lmin ⁻¹ flow, 80 °C, 100 % humidity - stability 1 bar back pressure, 0.1 L min ⁻¹ flow rates	[451]
Fe/TPPZ/Z8	90	305	-	cathode loading 4.0 mg cm ⁻² , NRE211 membrane, 1.0 bar back pressure, 0.3 L min ⁻¹ oxidant and fuel flow, 80 °C, 100 % humidity	[262]
Fe-N-C-Phen-PANI	80	380	-	cathode loading 4.0 mg cm ⁻² , N211 membrane, 1.38 bar back pressure, 0.5 air 0.3 H ₂ Lmin ⁻¹ flow, 80 °C, 100 % humidity	[452]
1.5Fe-ZIF	75	360	64 % (0.55V, 50h)	cathode loading 4.0 mg cm ⁻² , N211 membrane, 1 bar back pressure, 0.2 Lmin ⁻¹ oxidant and fuel flow, 80 °C, 100 % humidity	[448]
FePhenMOF-ArNH₃	50	400	-	cathode loading 2.0 mg cm ⁻² , N211 membrane, 2 bar back pressure, 0.2 L min ⁻¹ oxidant and fuel flow, 80 °C, 90 % humidity	[449]

FePhen@MOF-ArNH₃	50	380	-	cathode loading 0.3 mg cm ⁻² , N211 membrane, 1.5 bar back pressure, ?? L min ⁻¹ oxidant and fuel flow, 80 °C, 100 % humidity	[453]
Fe-MOF-700/950	28	302	-	cathode loading 4.0 mg cm ⁻² , NRE211 membrane, 1.0 bar back pressure, 0.3 L min ⁻¹ oxidant and fuel flow, 80 °C, 100 % humidity	[454]
(Fe,Co)/N-C	25	505	100% (galvanostatic 0.6 A cm ⁻² , 50 h)	cathode loading 0.77 mg cm ⁻² , home-made Aquivion/ePTFE membrane, 2 bar back pressure, ?? L min ⁻¹ flow, 80 °C, 100 % humidity	[455]
Fe/oPD-Mela	22	270	-	cathode loading 3.0 mg cm ⁻² , N212 membrane, 2 bar back pressure, ?? L min ⁻¹ oxidant and fuel flow, 80 °C, 100 % humidity	[456]
Fe-PANI/C-Mela	13	330	25 % (0.6V, 50h)	cathode loading 4.0 mg cm ⁻² , N212 membrane, 1 bar back pressure, 0.8 L min ⁻¹ oxidant and 0.3 L min ⁻¹ fuel flow, 80 °C, 100 % humidity	[339]
Fe-MBZ	10	330	-	cathode loading 3.5 mg cm ⁻² , N211 membrane, 0.8 bar back pressure, 0.25 L min ⁻¹ oxidant and 0.2 L min ⁻¹ fuel flow, 80 °C, 100 % humidity	[273]
Fe/PI-1000-III-NH₃	10	320	90% (galvanostatic 0.25 A cm ⁻² , 50 h)	cathode loading 4.0 mg cm ⁻² , NR211 membrane, 2 bar back pressure, 0.3 L min ⁻¹ oxidant and 0.3 L min ⁻¹ fuel flow, 80 °C, 100 % humidity	[398]

The best performance is reported for the catalyst labeled as CA#1 [145]. This catalyst was developed by Nisshinbo Holdings Inc. in Japan and is being used in the world's first non-precious metal-based (cathode) fuel cell device. The FCgen®-1040 by Ballard Power Systems. The performance has been achieved after optimization of the catalyst layer and MEA processing. For instance, the peak power density was enhanced from 395 mW cm⁻² to 570 mW cm⁻² just by the optimization of the ionomer content in the catalyst layer (from 40 wt% to 35 wt%) [145]. The stability during a 20 hour constant current hold of 0.5 A cm⁻² increased from 80 % of remaining current to 87 % by lowering the EW of the used ionomer from 1100 to 700 [457]. This thesis was focused on the optimization of the catalyst on the synthesis level. No optimization on the MEA preparation level has been performed so far. Hence, the reported performance of Cat E, which can be ranked among the top third of the listed catalysts looks very promising.

Practicability of the Synthesis Process

The developed synthesis of this work will now briefly be compared with the two, to this date, commercially most advanced non-precious metal-based ORR catalysts. **Figure 100** shows a schematic of the individual synthesis steps for the approach from Pajarito Powder, Nisshinbo Holdings Inc. and the process developed in this work.

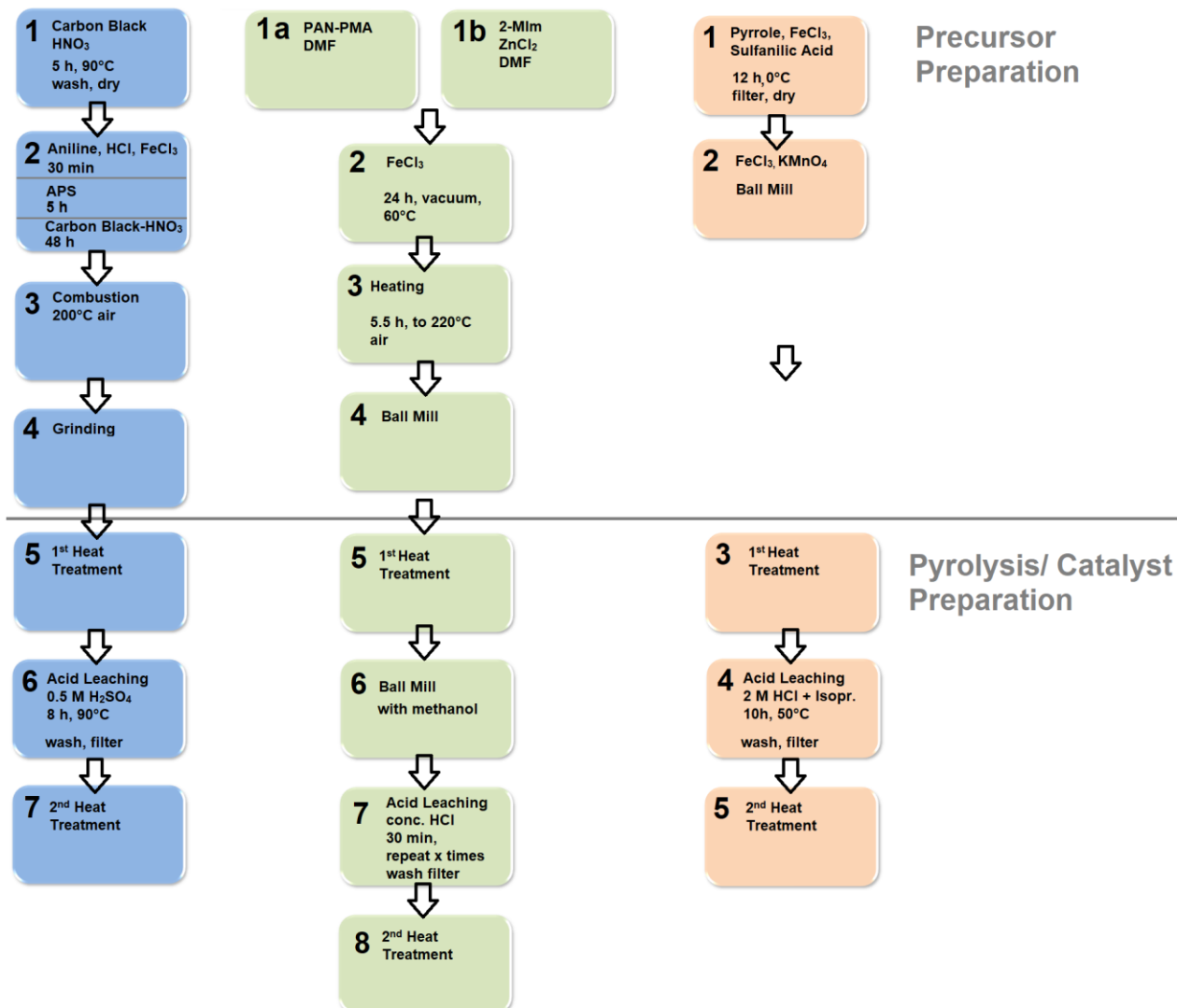


Figure 100: Schematic representation of the particular synthesis steps for the process of making different non-precious metal-based ORR catalysts. Approach developed by Pajarito Powder (left, blue), Nisshinbo Holdings Inc. (middle, green) and the method presented in this work (right, red).

From a standpoint of the overall synthesis steps the approach designed in this work is preferable over the existing commercial products. Indicating that the scale-up of this synthesis is highly feasible and the production costs of this catalysts are indeed very low.

10 Summary and Outlook

This chapter covers the results considering the polypyrrole-based catalysts. The results of the MWCNTs approach are summarized in chapter 7.5.

Within this work, a simple synthesis method for a non-precious metal-based ORR catalyst was developed. The new Me-N-C catalyst is based on doped polypyrrole and was designed towards the application in PEMFCs.

As a result of systematic variation of important synthesis parameters and subsequent physical and electrochemical characterizations, consistent progress in fuel cell performance was made. Further, a deeper understanding of the analyzed synthesis parameters was gained:

(I) A mixture of polypyrrole and iron salt can serve as simple and cheap precursors for the synthesis of Fe-N-C catalysts. However, ^{57}Fe -Mössbauer spectroscopy and TEM showed that the main pyrolysis products of this precursor mixture are highly graphitized carbon and iron carbide particles. These lead to low ORR activity.

(II) If pyrrole is polymerized in the presence of methyl orange, methyl orange doped polypyrrole nanotubes are formed. In contrast to (I), the pyrolysis of these nanotubes together with iron salts gives a highly active catalyst. ^{57}Fe -Mössbauer spectroscopy, TEM and Raman spectroscopy show that the main pyrolysis product of this precursor mixture is an amorphous carbon phase which contains molecular dispersed FeN_xC_y -moieties.

(III) A systematic variation of the synthesis process showed that in order to obtain the effect described in (II), the methyl orange requires to be present during the polymerization of the pyrrole. Only minor enhancement of the ORR activity is observed when methyl orange is added after the polymerization. The low ORR performance of the catalyst obtained from polypyrrole + methyl orange, which was added after polymerization, was again conform with the formation of inactive iron carbide instead of molecular active sites.

(IV) Removing the methyl orange from the methyl orange doped polypyrrole nanotubes after the polymerization through washing, only showed a slight influence on the ORR activity. The washing never removed methyl orange completely. The structural composition of the catalyst from the viewpoint of ^{57}Fe -Mössbauer spectroscopy and TEM did not change. However, an inverse correlation between BET surface area and intensity of the washing (removal of methyl orange) was found.

(V) Based on the findings described in (III) and (IV), one can conclude that the methyl orange is strongly in-cooperated into the polypyrrole network through doping or a similar effect if it is added during the polymerization.

(VI) Other dopants besides methyl orange were systematically tested. The ORR is enhanced only in the case when the dopant molecule holds a phenyl and a sulfonic acid group. From the tested dopants, sulfanilic acid showed the best ORR activity during fuel cell tests. Enhanced mass transport properties were measured for the sulfanilic acid doped polypyrrole catalyst. TEM showed spherical polymer particles of several hundred nanometers. This morphology resembles those of carbon blacks. The latter are known to form catalyst layers with good mass transport properties.

(VII) The type of iron salt inside the precursor mixture plays a crucial role during the synthesis of the polypyrrole-based Fe-N-C catalyst. Oxygen containing iron salts, such as $\text{Fe}(\text{Ac})_2$ or $\text{Fe}(\text{NO}_3)_3$, enhance the BET surface area but also produce inorganic iron phases due to poor iron stabilization. Contrary, FeCl_2 and FeCl_3 showed lower BET surface areas but a purer iron site composition. A mixture of FeCl_3 and $\text{Fe}(\text{NO}_3)_3$ was confirmed to be ideal for high fuel cell performance due to a good trade-off between high surface area and pure active site composition.

(VIII) Synergetic effects were found when iron salts were used in combination with manganese salts. The combination induces an enhancement of BET surface area. A mixture of FeCl_3 and KMnO_4 revealed the best results. A higher fuel cell activity as well as better short term stability (50 h) were established for catalysts prepared with $\text{FeCl}_3/\text{KMnO}_4$ instead of $\text{FeCl}_3/\text{Fe}(\text{NO}_3)_3$.

(IX) BET measurements demonstrated that a second heat treatment in N_2 significantly lowers the surface area of the catalysts. However, a second heat treatment is critical in order to obtain a high performing catalyst. The second heat treatment heals the defects induced by the acid leaching. It was proven that the healing effect can already be achieved after relatively short heat treatment times. However, too short heating times lowered the performance because the defects from the acid leaching were not completely healed. An optimum ORR performance was achieved after heating the catalyst with $800\text{ }^\circ\text{C h}^{-1}$ to $800\text{ }^\circ\text{C}$ and holding that temperature for 15 min. About 83 % of the initial surface area was retained after this treatment.

(X) The absolute temperature of the first heat treatment was varied. The degree of carbonization of the polypyrrole and therefore the catalyst's stability proceeds with higher temperatures. Unfortunately, at the same time active sites are destroyed and inorganic iron phases are formed. A good trade-off between activity and stability was validated at $1000\text{ }^\circ\text{C}$ for the doped polypyrrole approach. More details on this topic are found in the master thesis project of Janik Scharf, who investigated a broader range of temperatures after the first promising results of this work.

(XI) The acid leaching process is significantly enhanced when isopropanol is added during the leaching process. Isopropanol lowers the surface tension of the water-based acid solution. This facilitates to break up particle agglomerates. Hence, the catalyst is dispersed much better in the acid. Otherwise, the agglomerates shield iron particles from getting in contact with the acid. This makes them survive the acid leaching and they leach out during fuel cell operation damaging the MEA. ^{57}Fe -Mössbauer spectroscopy showed 80 - 90 % less iron inside the isopropanol leached sample in comparison to the catalyst leached with just HCl (aq). The fuel cell activity did not decrease, i.e. no active sites were destroyed.

The final catalyst which is presented in this work showed a peak power density of 344 mW cm^{-2} under H_2 -air fuel cell conditions. Considering that no electrode or MEA optimization was performed, this is a very promising result. Moreover, the synthesis process of the presented catalyst is indeed remarkably simple. The use of complex or expensive precursors like MOFs or porphyrins is omitted. The precursor mixture can be prepared within one step by reacting pyrrole, doping agent and transition metal precursor salts. No stability declining NH_3 treatment is necessary.

Future work should focus on the optimization of the electrode and MEA fabrication process. The ink preparation, the amount of binder inside the catalyst layer, as well as the equivalent weight of the binder are crucial factors that influence the fuel cell performance. For evaluation of the stability, CeO_2 particles should be added to the catalyst layer and cerium-ion doped + mechanically reinforced membranes should be adapted as the state-of-the-art in MEA testing. In case of fuel cell activity, power densities of at least $500 - 600 \text{ mW cm}^{-2}$ should be obtained before Me-N-C catalysts can be considered as cost competitive to Pt/C based systems for the automotive application (see chapter 4 **Figure 23**).

Even so the most crucial synthesis parameters have been investigated within this work, several others could still be optimized, to mention some:

(I) The influence of the ball milling parameters, such as frequency, amount or weight of the balls should be studied and optimized.

(II) Further, the amount of doping agent within the polymerization mixture could strongly affect the ORR performance.

(III) Since the improved acid leaching procedure removed significant amount of iron from the catalysts while the activity remained constant, low temperature ^{57}Fe -Mössbauer spectroscopy should be performed. This could clarify if iron or iron oxide nano clusters are present in the "standard acid leached" sample and if the enhanced leaching with isopropanol can indeed remove them. Long term

(100 hours and more) should be performed to inquire the extend of nano clusters effect on the stability.

11 References

- [1] A. Polyzoidis, T. Altenburg, M. Schwarzer, S. Loebbecke, S. Kaskel, Continuous microreactor synthesis of ZIF-8 with high space-time-yield and tunable particle size, *Chem Eng J*, 283 (2016) 971-977.
- [2] M. Hovestadt, J. Vargas Schmitz, T. Weissenberger, F. Reif, M. Kaspereit, W. Schwieger, M. Hartmann, Scale-up of the Synthesis of Zeolitic Imidazolate Framework ZIF-4, *Chem-Ing-Tech*, 89 (2017) 1374-1378.
- [3] T. Johnson, M.M. Lozinska, A.F. Orsi, P.A. Wright, S. Hindocha, S. Poulston, Improvements to the production of ZIF-94; a case study in MOF scale-up, *Green Chem*, 21 (2019) 5665-5670.
- [4] B.p.l. c., BP Energy Outlook: 2019 edition, in, BP Energy, 2019.
- [5] P. Friedlingstein, R.A. Houghton, G. Marland, J. Hackler, T.A. Boden, T.J. Conway, J.G. Canadell, M.R. Raupach, P. Ciais, C. Le Quere, Update on CO₂ emissions, *Nat Geosci*, 3 (2010) 811-812.
- [6] T.A. Boden, G. Marland, R.J. Andres, Global, Regional, and National Fossil-Fuel CO₂ Emissions, Carbon Dioxide Information Analysis Center, Oak Ridge National Laboratory (2010).
- [7] G. El-Montasser, O. Ben-Salha, A new methodology for assessing the energy use-environmental degradation nexus, *Environ Monit Assess*, 191 (2019) 587.
- [8] S. Asongu, G. El Montasser, H. Toumi, Testing the relationships between energy consumption, CO₂ emissions, and economic growth in 24 African countries: a panel ARDL approach, *Environ Sci Pollut R*, 23 (2016) 6563-6573.
- [9] M.A. Khan, M.Z. Khan, K. Zaman, L. Naz, Global estimates of energy consumption and greenhouse gas emissions, *Renew Sust Energ Rev*, 29 (2014) 336-344.
- [10] G. Boluk, M. Mert, Fossil & renewable energy consumption, GHGs (greenhouse gases) and economic growth: Evidence from a panel of EU (European Union) countries, *Energy*, 74 (2014) 439-446.
- [11] S. Jevrejeva, J.C. Moore, A. Grinsted, P.L. Woodworth, Recent global sea level acceleration started over 200 years ago?, *Geophys Res Lett*, 35 (2008).
- [12] M. Hamit-Haggag, Greenhouse gas emissions, energy consumption and economic growth: A panel cointegration analysis from Canadian industrial sector perspective, *Energ Econ*, 34 (2012) 358-364.
- [13] E. Commission, The European Green Deal, Brussel, COM(2019) 640 (2019).
- [14] EuropeanEnvironmentAgency, https://ec.europa.eu/clima/policies/transport_en, in, 2014.
- [15] EuropeanParliament, P7_TA(2014)0117 Ziel für 2020 zur Verringerung der CO₂-Emissionen neuer Personenkraftwagen ***, (2014).
- [16] M. Koers, CO₂-Regulierung bei Pkw und leichten Nutzfahrzeugen, Verband der Automobilindustrie, (2019).
- [17] M. Schweikl, CO₂ EMISSIONS ARE INCREASING CAR MAKERS MUST ACT, PA Knowledge Limited, (2020).
- [18] S. Kreitmair, Hydrogen fuel cell or battery electric vehicles?, UniCredit Research - Sector Report - Automobiles & Parts, (2019).
- [19] D. Papageorgopoulos, Fuel Cell R&D Overview, 2019 DOE Annual Merit Review and Peer Evaluation Meeting, (2019).
- [20] B. James, Cost Projections of PEM Fuel Cell Systems for Automobiles and Medium-Duty Vehicles, in, DOE Fuel Cell Technologies Office Webinar, 2018.
- [21] A. Kongkanand, W.B. Gu, M.F. Mathias, Proton-Exchange Membrane Fuel Cells with Low-Pt Content, in: T. Lipman, A. Weber (Eds.) Fuel Cells and Hydrogen Production. Encyclopedia of Sustainability Science and Technology Series, Springer, New York, NY, 2019.

-
- [22] A. Kongkanand, M.F. Mathias, The Priority and Challenge of High-Power Performance of Low-Platinum Proton-Exchange Membrane Fuel Cells, *Journal of Physical Chemistry Letters*, 7 (2016) 1127-1137.
- [23] D. Bernhardt, J.F. Reilly, MINERAL COMMODITY SUMMARIES 2020, U.S. Department of the Interior and U.S. Geological Survey, Reston, Virginia (2020).
- [24] M. Kübler, U.I. Kramm, Trägerfreier Sauerstoff-Reduktions-Katalysator für die Anwendung in Niedertemperaturbrennstoffzellen und Verfahren zu dessen Herstellung, Antrag auf Erteilung eines Patents, Anmeldenummer 10 2020 111 647.0 (2020).
- [25] E. Proietti, F. Jaouen, M. Lefevre, N. Larouche, J. Tian, J. Herranz, J.P. Dodelet, Iron-based cathode catalyst with enhanced power density in polymer electrolyte membrane fuel cells, *Nat Commun*, 2 (2011) 416.
- [26] H. Meng, N. Larouche, M. Lefevre, F. Jaouen, B. Stansfield, J.P. Dodelet, Iron porphyrin-based cathode catalysts for polymer electrolyte membrane fuel cells: Effect of NH₃ and Ar mixtures as pyrolysis gases on catalytic activity and stability, *Electrochimica Acta*, 55 (2010) 6450-6461.
- [27] G. Wu, K. Artyushkova, M. Ferrandon, A.J. Kropf, D.J. Myers, P. Zelenay, Performance Durability of Polyaniline-derived Non-precious Cathode Catalysts, *ECS Transactions*, 25 (2009).
- [28] K. Lee, L. Zhang, H. Lui, R. Hui, Z. Shi, J.J. Zhang, Oxygen reduction reaction (ORR) catalyzed by carbon-supported cobalt polypyrrole (Co-PPy/C) electrocatalysts, *Electrochimica Acta*, 54 (2009) 4704-4711.
- [29] T.S. Olson, S. Pylypenko, P. Atanassov, K. Asazawa, K. Yamada, H. Tanaka, Anion-Exchange Membrane Fuel Cells: Dual-Site Mechanism of Oxygen Reduction Reaction in Alkaline Media on Cobalt-Polypyrrole Electrocatalysts, *J Phys Chem C*, 114 (2010) 5049-5059.
- [30] W. Wang, J. Luo, W.H. Chen, J. Li, W. Xing, S.L. Chen, Synthesis of mesoporous Fe/N/C oxygen reduction catalysts through NaCl crystallite-confined pyrolysis of polyvinylpyrrolidone, *Journal of Materials Chemistry A*, 4 (2016) 12768-12773.
- [31] D.C. Higgins, G. Wu, H. Chung, U. Martinez, S. Ma, Z. Chen, P. Zelenay, Manganese-Based Non-Precious Metal Catalyst for Oxygen Reduction in Acidic Media, *ECS Transactions*, 61 (2014) 35-42.
- [32] U.I. Kramm, A. Zana, T. Vosch, S. Fiechter, M. Arenz, D. Schmeisser, On the structural composition and stability of Fe-N-C catalysts prepared by an intermediate acid leaching, *J Solid State Electr*, 20 (2016) 969-981.
- [33] C.H. Choi, C. Baldizzone, G. Polymeros, E. Pizzutilo, O. Kasian, A.K. Schuppert, N. Ranjbar Sahraie, M.-T. Sougrati, K.J.J. Mayrhofer, F. Jaouen, Minimizing Operando Demetallation of Fe-N-C Electrocatalysts in Acidic Medium, *ACS Catalysis*, 6 (2016) 3136-3146.
- [34] D.L. Hart, Franz Jones, Stuart, J. Lewis, *The Fuel Cell Industry Review 2019*, E4Tech, (2019).
- [35] F. de Bruijn, The current status of fuel cell technology for mobile and stationary applications, *Green Chem*, 7 (2005) 132-150.
- [36] K.R. Cooper, V. Ramani, J.M. Fenton, H. Russel Kunz, *Experimental Methods and Data Analyses for Polymer Electrolyte Fuel Cells*, Scribner Associates Inc., Southern Pines, North Carolina, USA (2016).
- [37] A. Hermann, T. Chaudhuri, P. Spagnol, Bipolar plates for PEM fuel cells: A review, *Int J Hydrogen Energ*, 30 (2005) 1297-1302.
- [38] J.S. Cooper, Design analysis of PEMFC bipolar plates considering stack manufacturing and environment impact, *Journal of Power Sources*, 129 (2004) 152-169.
- [39] Z.M. Bao, Z.Q. Niu, K. Jiao, Numerical simulation for metal foam two-phase flow field of proton exchange membrane fuel cell, *Int J Hydrogen Energ*, 44 (2019) 6229-6244.
- [40] S.J. Tong, J.C. Bachman, A. Santamaria, J.W. Park, Experimental investigation on a polymer electrolyte membrane fuel cell (PEMFC) parallel flow field design with external two-valve regulation on cathode channels, *Journal of Power Sources*, 242 (2013) 195-201.

-
- [41] G.B. Zhang, K. Jiao, Multi-phase models for water and thermal management of proton exchange membrane fuel cell: A review, *Journal of Power Sources*, 391 (2018) 120-133.
- [42] N. Konno, S. Mizuno, H. Nakaji, Y. Ishikawa, Development of Compact and High-Performance Fuel Cell Stack, *Sae Int J Altern Pow*, 4 (2015) 123-129.
- [43] J.E. Park, J. Lim, S. Kim, I. Choi, C.Y. Ahn, W. Hwang, M.S. Lim, Y.H. Cho, Y.E. Sung, Enhancement of mass transport in fuel cells using three-dimensional graphene foam as flow field, *Electrochimica Acta*, 265 (2018) 488-496.
- [44] S.T. Thompson, B.D. James, J.M. Huya-Kouadio, C. Houchins, D.A. DeSantis, R. Ahluwalia, A.R. Wilson, G. Kleen, D. Papageorgopoulos, Direct hydrogen fuel cell electric vehicle cost analysis: System and high-volume manufacturing description, validation, and outlook, *Journal of Power Sources*, 399 (2018) 304-313.
- [45] J.Y. Wang, H.L. Wang, Y. Fan, Techno-Economic Challenges of Fuel Cell Commercialization, *Engineering-Prc*, 4 (2018) 352-360.
- [46] M. Elyasi, F.A. Khatir, M. Hosseinzadeh, Manufacturing metallic bipolar plate fuel cells through rubber pad forming process, *Int J Adv Manuf Tech*, 89 (2017) 3257-3269.
- [47] M.G. Jung, Y.P. Jeon, C.G. Kang, Metallic Bipolar Plate Fabrication Process of Fuel Cell by Rubber Pad Forming and its Performance Evaluation, *Key Eng Mater*, 535-536 (2013) 310-+.
- [48] Y.X. Liu, L. Hua, Fabrication of metallic bipolar plate for proton exchange membrane fuel cells by rubber pad forming, *Journal of Power Sources*, 195 (2010) 3529-3535.
- [49] Y. Leng, P.W. Ming, D.J. Yang, C.M. Zhang, Stainless steel bipolar plates for proton exchange membrane fuel cells: Materials, flow channel design and forming processes, *Journal of Power Sources*, 451 (2020).
- [50] R.L. Borup, R. Mukundan, T. Rockward, M. Brady, J. Thomson, D. Papadimas, R. Ahluwalia, H. Wang, J. Turner, (Metal) Bipolar Plate Testing, DOE FCTO Distribution for Bipolar Plate Workshop Repo, (2017).
- [51] V.K. Mathur, J. Crawford, Fundamentals of Gas Diffusion Layers in PEM Fuel Cells in: S. Basu (Ed.) *Recent Trends in Fuel Cell Science and Technology*, Anamaya Publishers, New Delhi, India 2007.
- [52] J. Zhou, S. Shukla, A. Putz, M. Secanell, Analysis of the role of the microporous layer in improving polymer electrolyte fuel cell performance, *Electrochimica Acta*, 268 (2018) 366-382.
- [53] A.Z. Weber, J. Newman, Effects of microporous layers in polymer electrolyte fuel cells, *Journal of the Electrochemical Society*, 152 (2005) A677-A688.
- [54] D. Spornjak, A.K. Prasad, S.G. Advani, Experimental investigation of liquid water formation and transport in a transparent single-serpentine PEM fuel cell, *Journal of Power Sources*, 170 (2007) 334-344.
- [55] G.Y. Lin, T. Van Nguyen, Effect of thickness and hydrophobic polymer content of the gas diffusion layer on electrode flooding level in a PEMFC, *Journal of the Electrochemical Society*, 152 (2005) A1942-A1948.
- [56] A.Z. Weber, M.A. Hickner, Modeling and high-resolution-imaging studies of water-content profiles in a polymer-electrolyte-fuel-cell membrane-electrode assembly, *Electrochimica Acta*, 53 (2008) 7668-7674.
- [57] A. Thomas, G. Maranzana, S. Didierjean, J. Dillet, O. Lottin, Thermal and water transfer in PEMFCs: Investigating the role of the microporous layer, *Int J Hydrogen Energ*, 39 (2014) 2649-2658.
- [58] J.H. Nam, M. Kaviany, Effective diffusivity and water-saturation distribution in single- and two-layer PEMFC diffusion medium, *Int J Heat Mass Tran*, 46 (2003) 4595-4611.
- [59] U. Pasaogullari, C.Y. Wang, Two-phase transport and the role of micro-porous layer in polymer electrolyte fuel cells, *Electrochimica Acta*, 49 (2004) 4359-4369.
- [60] Freudenberg, https://fuelcellcomponents.freudenberg-pm.com/-/media/Files/fuelcellcomponents,-d-,freudenbergpm,-d-,com/Finale%20Broschuere_GasDiffusion_RZengl.pdf, in, Gas Diffusion Layers Broschuere.

- [61] K. Scott, Membrane electrode assemblies for polymer electrolyte membrane fuel cells in: J. Kilner, S. Skinner, S. Irvine, P. Edwards (Eds.) *Functional Materials for Sustainable Energy Applications*, Published by Woodhead Publishing Limited, 80 High Street, Sawston, Cambridge CB22 3HJ, UK, 2012.
- [62] S. Banerjee, D.E. Curtin, Nafion (R) perfluorinated membranes in fuel cells, *J Fluorine Chem*, 125 (2004) 1211-1216.
- [63] J. Zhang, H. Zhang, J. Wu, J. Zhang, PEM Fuel Cell Fundamentals, in: J. Zhang, H. Zhang, J. Wu, J. Zhang (Eds.) *Pem Fuel Cell Testing and Diagnosis*, Elsevier B.V., Radarweg 29, PO Box 211, 1000 AE Amsterdam, The Netherland, 2013.
- [64] A. Manthiram, X. Zhao, W. Li, Developments in membranes, catalysts and membrane electrode assemblies for direct methanol fuel cells (DMFCs), in: J. Kilner, S. Skinner, S. Irvine, P. Edwards (Eds.) *Functional Materials for Sustainable Energy Applications*, Woodhead Publishing Limited, 80 High Street, Sawston, Cambridge CB22 3HJ, UK, 2012.
- [65] M. Odgaard, The Use of Per-Fluorinated Sulfonic Acid (PFSA) Membrane as Electrolyte in Fuel Cells, in: T. Nakajima, H. Groult (Eds.) *Advanced Fluoride-Based Materials for Energy Conversion*, Elsevier Inc. , Radarweg 29, PO Box 211, 1000 AE Amsterdam, The Netherlands, 2015.
- [66] G. Dorenbos, Y. Suga, Simulation of equivalent weight dependence of Nafion morphologies and predicted trends regarding water diffusion, *J Membrane Sci*, 330 (2009) 5-20.
- [67] B. Abderezzak, Introduction to Hydrogen Technology, in: A. Dollet (Ed.) *Introduction to Transfer Phenomena in PEM Fuel Cell* Elsevier Ltd., ISTE Press Ltd, 27-37 St George's Road, London SW19 4EU, UK, 2018.
- [68] M. Saito, N. Arimura, K. Hayamizu, T. Okada, Mechanisms of ion and water transport in perfluorosulfonated ionomer membranes for fuel cells, *J Phys Chem B*, 108 (2004) 16064-16070.
- [69] F.A.d. Bruijn, R.C. Makkus, R.K.A.M. Mallant, G.J.M. Janssen, Materials for State-of-the-Art PEM Fuel Cells, and Their Suitability for Operation Above 100°C, in: T.S. Zhao, K.-D. Kreuer, T.V. Nguyen (Eds.) *Advances in Fuel Cells*, Elsevier Ltd., 2007.
- [70] W.Y. Hsu, T.D. Gierke, Ion-Transport and Clustering in Nafion Perfluorinated Membranes, *J Membrane Sci*, 13 (1983) 307-326.
- [71] T.D. Gierke, G.E. Munn, F.C. Wilson, The Morphology in Nafion Perfluorinated Membrane Products, as Determined by Wide-Angle and Small-Angle X-Ray Studies, *J Polym Sci Pol Phys*, 19 (1981) 1687-1704.
- [72] S. Hommura, Y. Kunisa, I. Terada, M. Yoshitake, Characterization of fibril reinforced membranes for fuel cells, *J Fluorine Chem*, 120 (2003) 151-155.
- [73] B.P. Pearman, N. Mohajeri, R.P. Brooker, M.P. Rodgers, D.K. Slattery, M.D. Hampton, D.A. Cullen, S. Seal, The degradation mitigation effect of cerium oxide in polymer electrolyte membranes in extended fuel cell durability tests, *Journal of Power Sources*, 225 (2013) 75-83.
- [74] W. Zheng, J. Kang, K. Moriyama, S.H. Kim, A Multiscale Decomposition Method for Pore-Scale Simulation of Multiphase Transport and Reactions in Cathode Catalyst Layers of Proton Exchange Membrane Fuel Cells, *Journal of The Electrochemical Society*, 167 (2020).
- [75] M.-P.-I.f. Eisenforschung, in.
- [76] S. Mukerjee, J. McBreen, Effect of particle size on the electrocatalysis by carbon-supported Pt electrocatalysts: an in situ XAS investigation, *Journal of Electroanalytical Chemistry*, 448 (1998) 163-171.
- [77] Y. Shao-Horn, W.C. Sheng, S. Chen, P.J. Ferreira, E.F. Holby, D. Morgan, Instability of supported platinum nanoparticles in low-temperature fuel cells, *Top Catal*, 46 (2007) 285-305.
- [78] S. Mukerjee, S. Srinivasan, Enhanced Electrocatalysis of Oxygen Reduction on Platinum Alloys in Proton-Exchange Membrane Fuel-Cells, *Journal of Electroanalytical Chemistry*, 357 (1993) 201-224.

- [79] S. Mukerjee, S. Srinivasan, M.P. Soriaga, J. Mcbreen, Effect of Preparation Conditions of Pt Alloys on Their Electronic, Structural, and Electrocatalytic Activities for Oxygen Reduction-Xrd, Xas, and Electrochemical Studies, *J Phys Chem-Us*, 99 (1995) 4577-4589.
- [80] V. Stamenkovic, T.J. Schmidt, P.N. Ross, N.M. Markovic, Surface composition effects in electrocatalysis: Kinetics of oxygen reduction on well-defined Pt₃Ni and Pt₃Co alloy surfaces, *J Phys Chem B*, 106 (2002) 11970-11979.
- [81] V. Stamenkovic, B.S. Mun, K.J.J. Mayrhofer, P.N. Ross, N.M. Markovic, J. Rossmeisl, J. Greeley, J.K. Norskov, Changing the activity of electrocatalysts for oxygen reduction by tuning the surface electronic structure, *Angew Chem Int Edit*, 45 (2006) 2897-2901.
- [82] M. Oezaslan, P. Strasser, Activity of dealloyed PtCo₃ and PtCu₃ nanoparticle electrocatalyst for oxygen reduction reaction in polymer electrolyte membrane fuel cell, *Journal of Power Sources*, 196 (2011) 5240-5249.
- [83] S. Koh, P. Strasser, Electrocatalysis on bimetallic surfaces: Modifying catalytic reactivity for oxygen reduction by voltammetric surface dealloying, *Journal of the American Chemical Society*, 129 (2007) 12624-+.
- [84] F. Hasche, M. Oezaslan, P. Strasser, Activity, Structure and Degradation of Dealloyed PtNi₃ Nanoparticle Electrocatalyst for the Oxygen Reduction Reaction in PEMFC, *Journal of the Electrochemical Society*, 159 (2012) B25-B34.
- [85] V.R. Stamenkovic, B.S. Mun, M. Arenz, K.J.J. Mayrhofer, C.A. Lucas, G.F. Wang, P.N. Ross, N.M. Markovic, Trends in electrocatalysis on extended and nanoscale Pt-bimetallic alloy surfaces, *Nature Materials*, 6 (2007) 241-247.
- [86] V.R. Stamenkovic, B. Fowler, B.S. Mun, G.F. Wang, P.N. Ross, C.A. Lucas, N.M. Markovic, Improved oxygen reduction activity on Pt₃Ni(111) via increased surface site availability, *Science*, 315 (2007) 493-497.
- [87] J.R. Kitchin, J.K. Norskov, M.A. Barteau, J.G. Chen, Modification of the surface electronic and chemical properties of Pt(111) by subsurface 3d transition metals, *J Chem Phys*, 120 (2004) 10240-10246.
- [88] J.R. Kitchin, J.K. Norskov, M.A. Barteau, J.G. Chen, Role of strain and ligand effects in the modification of the electronic and chemical properties of bimetallic surfaces, *Physical Review Letters*, 93 (2004).
- [89] Q.Y. Jia, K. Caldwell, K. Strickland, J.M. Ziegelbauer, Z.Y. Liu, Z.Q. Yu, D.E. Ramaker, S. Mukerjee, Improved Oxygen Reduction Activity and Durability of Dealloyed PtCo_x Catalysts for Proton Exchange Membrane Fuel Cells: Strain, Ligand, and Particle Size Effects, *Acs Catalysis*, 5 (2015) 176-186.
- [90] P. Strasser, S. Koh, T. Anniyev, J. Greeley, K. More, C.F. Yu, Z.C. Liu, S. Kaya, D. Nordlund, H. Ogasawara, M.F. Toney, A. Nilsson, Lattice-strain control of the activity in dealloyed core-shell fuel cell catalysts, *Nat Chem*, 2 (2010) 454-460.
- [91] W. Vielstich, A. Lamm, H.A. Gasteiger, *Handbook of fuel cells : fundamentals, technology, and applications*, Wiley, Chichester, England ; Hoboken, N.J., 2003.
- [92] S.J. Paddison, H.A. Gasteiger, *Fuel Cells: Selected Entries from the Encyclopedia of Sustainability Science and Technology - Chapter 11 PEM Fuel Cells, Materials and Design/Development Challenges*, Springer Science+Business Media, New York 2013.
- [93] E. Padgett, N. Andrejevic, Z.Y. Liu, A. Kongkanand, W.B. Gu, K. Moriyama, Y. Jiang, S. Kumaraguru, T.E. Moylan, R. Kukreja, D.A. Muller, Connecting Fuel Cell Catalyst Nanostructure and Accessibility Using Quantitative Cryo-STEM Tomography, *Journal of the Electrochemical Society*, 165 (2018) F173-F180.
- [94] A. Kongkanand, W. Gu, M.F. Mathias, *Catalysts for Sustainable Fuel Cell Electric Vehicles*, in, General Motors, Fuel Cell Business, IEA-TCP Advanced Fuel Cells, Berlin, 2017.
- [95] P. Jovanovic, U. Petek, N. Hodnik, F. Ruiz-Zepeda, M. Gatalo, M. Sala, V.S. Selih, T.P. Fellingner, M. Gaberscek, Importance of non-intrinsic platinum dissolution in Pt/C composite fuel cell catalysts, *Physical Chemistry Chemical Physics*, 19 (2017) 21446-21452.

- [96] A. Kongkanand, V. Yarlagadda, M.K. Carpenter, Y. Cai, T.E. Moylan, J.M. Ziegelbauer, W.B. Gu, G. Kleen, Highly Accessible Catalysts for Durable High-Power Performance, FY 2018 Annual Progress Report DOE Hydrogen and Fuel Cells Program, (2018).
- [97] A. Orfanidi, P. Madkikar, H.A. El-Sayed, G.S. Harzer, T. Kratky, H.A. Gasteiger, The Key to High Performance Low Pt Loaded Electrodes, *Journal of the Electrochemical Society*, 164 (2017) F418-F426.
- [98] S. Ott, A. Orfanidi, H. Schmies, B. Anke, H.N. Nong, J. Hubner, U. Gernert, M. Glied, M. Lerch, P. Strasser, Ionomer distribution control in porous carbon-supported catalyst layers for high-power and low Pt-loaded proton exchange membrane fuel cells, *Nature Materials*, 19 (2020) 77-+.
- [99] C. Lim, A.S. Alavijeh, M. Lauritzen, J. Kolodziej, S. Knights, E. Kjeang, Fuel Cell Durability Enhancement with Cerium Oxide under Combined Chemical and Mechanical Membrane Degradation, *Ecs Electrochem Lett*, 4 (2015) F29-F31.
- [100] M. Danilczuk, S. Schlick, F.D. Coms, Cerium(III) as a Stabilizer of Perfluorinated Membranes Used in Fuel Cells: In Situ Detection of Early Events in the ESR Resonator, *Macromolecules*, 42 (2009) 8943-8949.
- [101] V. Prabhakaran, C.G. Arges, V. Ramani, Investigation of polymer electrolyte membrane chemical degradation and degradation mitigation using in situ fluorescence spectroscopy, *P Natl Acad Sci USA*, 109 (2012) 1029-1034.
- [102] P. Mandal, B.K. Hong, J.G. Oh, S. Litster, Understanding the voltage reversal behavior of automotive fuel cells, *Journal of Power Sources*, 397 (2018) 397-404.
- [103] R.T. Atanasoski, L.L. Atanasoska, D.A. Cullen, G.M. Haugen, K.L. More, G.D. Vernstrom, Fuel Cells Catalyst for Start-Up and Shutdown Conditions: Electrochemical, XPS, and STEM Evaluation of Sputter-Deposited Ru, Ir, and Ti on Pt-Coated Nanostructured Thin Film Supports, *Electrocatalysis-Us*, 3 (2012) 284-297.
- [104] C. Gittleman, A. Kongkanand, D. Masten, W. Gu, Materials Research and Development Priorities for Low Cost Automotive PEM Fuel Cells, *Current Opinion in Electrochemistry*, (2019).
- [105] T. Yoshida, K. Kojima, Toyota MIRAI Fuel Cell Vehicle and Progress Toward a Future Hydrogen Society, *Electrochem Soc Inte*, 24 (2015) 45-49.
- [106] B. James, J.M. Huya-Kouadio, C. Houchins, DOE Hydrogen and Fuel Cells Program Review Fuel Cell Systems Analysis, Project ID# FC163, (2017).
- [107] T. Shumsky, L. Clark, Ukraine-Krise treibt den Preis für Palladium, *The Wall Street Journal*, <https://www.wsj.com/articles/ukraine-krise-treibt-den-preis-fur-palladium-1394200482> (2014).
- [108] Palladium Russlands "Geheimwaffe", *Handelsblatt*, <https://www.handelsblatt.com/finanzen/maerkte/devisen-rohstoffe/palladium-russlands-geheimwaffe/9788746-all.html> (2014).
- [109] H. Zipfel, Goldpreis bleibt im Schatten von Palladium, *Finanzmarktwelt*, <https://finanzmarktwelt.de/goldpreis-bleibt-im-schatten-von-palladium-148750/> (2019).
- [110] stooq.com, Historical data: Palladium-NYMEX(PA.F) <https://stooq.com/q/d/?s=pa.f&c=0&i=y>, in.
- [111] European Commission, on the 2017 list of Critical Raw Materials for the EU, Communication from the commission to the European Parliament, the council, the european economic and social committee and the committee of the regions, 490 (2017).
- [112] W. Bernhart, S. Riederle, M. Yoon, Fuel cells - a realistic alternative for zero emission?, Roland Berger Strategy Consultants, (2013).
- [113] V. Beermann, M. Gocyla, S. Kuhl, E. Padgett, H. Schmies, M. Goerlin, N. Erini, M. Shviro, M. Heggen, R.E. Dunin-Borkowski, D.A. Muller, P. Strasser, Tuning the Electrocatalytic Oxygen Reduction Reaction Activity and Stability of Shape-Controlled Pt-Ni Nanoparticles by Thermal Annealing Elucidating the Surface Atomic Structural and Compositional Changes, *Journal of the American Chemical Society*, 139 (2017) 16536-16547.

- [114] C.M. Sanchez-Sanchez, J. Solla-Gullon, F.J. Vidal-Iglesias, A. Aldaz, V. Montiel, E. Herrero, Imaging Structure Sensitive Catalysis on Different Shape-Controlled Platinum Nanoparticles, *Journal of the American Chemical Society*, 132 (2010) 5622-+.
- [115] D. van der Vliet, C. Wang, M. Debe, R. Atanasoski, N.M. Markovic, V.R. Stamenkovic, Platinum-alloy nanostructured thin film catalysts for the oxygen reduction reaction, *Electrochimica Acta*, 56 (2011) 8695-8699.
- [116] A. Bonakdarpour, K. Stevens, G.D. Vernstrom, R. Atanasoski, A.K. Schmoeckel, M.K. Debe, J.R. Dahn, Oxygen reduction activity of Pt and Pt-Mn-Co electrocatalysts sputtered on nano-structured thin film support, *Electrochimica Acta*, 53 (2007) 688-694.
- [117] J. Waldecker, VaporDepositionProcessfor Engineering of Dispersed PEMFC ORR Pt/NbOx/CCatalysts, https://www.hydrogen.energy.gov/pdfs/review18/fc162_waldecker_2018_o.pdf (2019).
- [118] R.R. Adzic, J. Wang, M.B. Vukmirovic, K. Sasaki, Platinum Monolayer Electrocatalysts, DOE Hydrogen and Fuel Cells Annual Merit Review June 14, (2018).
- [119] F. Jaouen, J. Herranz, M. Lefevre, J.P. Dodelet, U.I. Kramm, I. Herrmann, P. Bogdanoff, J. Maruyama, T. Nagaoka, A. Garsuch, J.R. Dahn, T. Olson, S. Pylypenko, P. Atanassov, E.A. Ustinov, Cross-Laboratory Experimental Study of Non-Noble-Metal Electrocatalysts for the Oxygen Reduction Reaction, *Acs Appl Mater Inter*, 1 (2009) 1623-1639.
- [120] U.I. Kramm, I. Herrmann-Geppert, J. Behrends, K. Lips, S. Fiechter, P. Bogdanoff, On an Easy Way To Prepare Metal Nitrogen Doped Carbon with Exclusive Presence of MeN4-type Sites Active for the ORR, *Journal of the American Chemical Society*, 138 (2016) 635-640.
- [121] M. Lefevre, E. Proietti, F. Jaouen, J.P. Dodelet, Iron-Based Catalysts with Improved Oxygen Reduction Activity in Polymer Electrolyte Fuel Cells, *Science*, 324 (2009) 71-74.
- [122] G. Wu, C.M. Johnston, N.H. Mack, K. Artyushkova, M. Ferrandon, M. Nelson, J.S. Lezama-Pacheco, S.D. Conradson, K.L. More, D.J. Myers, P. Zelenay, Synthesis-structure-performance correlation for polyaniline-Me-C non-precious metal cathode catalysts for oxygen reduction in fuel cells, *J Mater Chem*, 21 (2011) 11392-11405.
- [123] A. Ishihara, T. Nagai, K. Ukita, M. Arao, M. Matsumoto, L.W. Yu, T. Nakamura, O. Sekizawa, Y. Takagi, K. Matsuzawa, T.W. Napporn, S. Mitsushima, T. Uruga, T. Yokoyama, Y. Iwasawa, H. Imai, K. Ota, Emergence of Oxygen Reduction Activity in Zirconium Oxide-Based Compounds in Acidic Media: Creation of Active Sites for the Oxygen Reduction Reaction, *J Phys Chem C*, 123 (2019) 18150-18159.
- [124] S. Tominaka, A. Ishihara, T. Nagai, K. Ota, Noncrystalline Titanium Oxide Catalysts for Electrochemical Oxygen Reduction Reactions, *Acs Omega*, 2 (2017) 5209-5214.
- [125] A.K. Mechler, N.R. Sahraie, V. Armel, A. Zitolo, M.T. Sougrati, J.N. Schwammlein, D.J. Jones, F. Jaouen, Stabilization of Iron-Based Fuel Cell Catalysts by Non-Catalytic Platinum, *Journal of the Electrochemical Society*, 165 (2018) F1084-F1091.
- [126] K.A. Kuttiyiel, K. Sasaki, G.G. Park, M.B. Vukmirovic, L.J. Wu, Y.M. Zhu, J.G.G. Chen, R.R. Adzic, Janus structured Pt-FeNC nanoparticles as a catalyst for the oxygen reduction reaction, *Chem Commun*, 53 (2017) 1660-1663.
- [127] L. Chong, J.G. Wen, J. Kubal, F.G. Sen, J.X. Zou, J. Greeley, M. Chan, H. Barkholtz, W.J. Ding, D.J. Liu, Ultralow-loading platinum-cobalt fuel cell catalysts derived from imidazolate frameworks, *Science*, 362 (2018) 1276-+.
- [128] I. Martinaiou, A. Shahraei, F. Grimm, H. Zhang, C. Wittich, S. Klement, S.J. Dolique, H.J. Kleebe, R.W. Stark, U.I. Kramm, Effect of metal species on the stability of Me-N-C catalysts during accelerated stress tests mimicking the start-up and shut-down conditions, *Electrochimica Acta*, 243 (2017) 183-196.
- [129] H. Tributsch, U.I. Koslowski, I. Dorbandt, Experimental and theoretical modeling of Fe-, Co-, Cu-, Mn-based electrocatalysts for oxygen reduction, *Electrochimica Acta*, 53 (2008) 2198-2209.

- [130] C.W.B. Bezerra, L. Zhang, K.C. Lee, H.S. Liu, A.L.B. Marques, E.P. Marques, H.J. Wang, J.J. Zhang, A review of Fe-N/C and Co-N/C catalysts for the oxygen reduction reaction, *Electrochimica Acta*, 53 (2008) 4937-4951.
- [131] H.L. Peng, F.F. Liu, X.J. Liu, S.J. Liao, C.H. You, X.L. Tian, H.X. Nan, F. Luo, H.Y. Song, Z.Y. Fu, P.Y. Huang, Effect of Transition Metals on the Structure and Performance of the Doped Carbon Catalysts Derived From Polyaniline and Melamine for ORR Application, *Acs Catalysis*, 4 (2014) 3797-3805.
- [132] Z.W. Chen, D. Higgins, A.P. Yu, L. Zhang, J.J. Zhang, A review on non-precious metal electrocatalysts for PEM fuel cells, *Energy & Environmental Science*, 4 (2011) 3167-3192.
- [133] P. He, M. Lefevre, G. Faubert, J.P. Dodelet, Oxygen reduction catalysts for polymer electrolyte fuel cells from the pyrolysis of various transition metal acetates adsorbed on 3,4,9,10-perylenetetracarboxylic dianhydride, *J New Mat Electr Sys*, 2 (1999) 243-251.
- [134] D. Ohms, S. Herzog, R. Franke, V. Neumann, K. Wiesener, S. Gamburgcev, A. Kaisheva, I. Iliev, Influence of Metal-Ions on the Electrocatalytic Oxygen Reduction of Carbon Materials Prepared from Pyrolyzed Polyacrylonitrile, *Journal of Power Sources*, 38 (1992) 327-334.
- [135] J.A.R. Vanveen, J.F. Vanbaar, K.J. Kroese, Effect of Heat-Treatment on the Performance of Carbon-Supported Transition-Metal Chelates in the Electrochemical Reduction of Oxygen, *J Chem Soc Farad T 1*, 77 (1981) 2827-2843.
- [136] A. Morozan, V. Goellner, Y. Nedellec, J. Hannauer, F. Jaouen, Effect of the Transition Metal on Metal-Nitrogen-Carbon Catalysts for the Hydrogen Evolution Reaction, *Journal of the Electrochemical Society*, 162 (2015) H719-H726.
- [137] H. Alt, H. Binder, Sandsted.G, Mechanism of Electrocatalytic Reduction of Oxygen on Metal-Chelates, *J Catal*, 28 (1973) 8-19.
- [138] J.L. Shui, C. Chen, L. Grabstanowicz, D. Zhao, D.J. Liu, Highly efficient nonprecious metal catalyst prepared with metal-organic framework in a continuous carbon nanofibrous network, *P Natl Acad Sci USA*, 112 (2015) 10629-10634.
- [139] K. Wiesener, D. Ohms, V. Neumann, R. Franke, N-4 Macrocycles as Electrocatalysts for the Cathodic Reduction of Oxygen, *Mater Chem Phys*, 22 (1989) 457-475.
- [140] G. Wu, K.L. More, C.M. Johnston, P. Zelenay, High-performance electrocatalysts for oxygen reduction derived from polyaniline, iron, and cobalt, *Science*, 332 (2011) 443-447.
- [141] C. Dominguez, F.J. Perez-Alonso, M.A. Salam, J.L.G. de la Fuente, S.A. Al-Thabaiti, S.N. Basahel, M.A. Pena, J.L.G. Fierro, S. Rojas, Effect of transition metal (M: Fe, Co or Mn) for the oxygen reduction reaction with non-precious metal catalysts in acid medium, *Int J Hydrogen Energ*, 39 (2014) 5309-5318.
- [142] P. Zelenay, State of the Art of PGM-free Catalyst Activity and Durability, *ElectroCat Workshop*, Argonne National Laboratory, (2016).
- [143] M. Chokai, T. Daidou, Y. Nabae, Development of Pt-free Carbon-Based Catalyst for PEFC Cathode Prepared from Polyacrylonitrile, *Polymer Electrolyte Fuel Cells* 14, 64 (2014) 261-270.
- [144] X. Yin, L. Lin, H.T. Chung, S.K. Babu, U. Martinez, G.M. Purdy, P. Zelenay, Effects of MEA Fabrication and Ionomer Composition on Fuel Cell Performance of PGM-free ORR Catalyst, *Selected Proceedings from the 231st Ecs Meeting*, 77 (2017) 1273-1281.
- [145] D. Banham, T. Kishimoto, Y.J. Zhou, T. Sato, K. Bai, J. Ozaki, Y. Imashiro, S.Y. Ye, Critical advancements in achieving high power and stable nonprecious metal catalyst-based MEAs for real-world proton exchange membrane fuel cell applications, *Science Advances*, 4 (2018).
- [146] Y. Shao, J.P. Dodelet, G. Wu, P. Zelenay, PGM-Free Cathode Catalysts for PEM Fuel Cells: A Mini-Review on Stability Challenges, *Adv Mater*, 31 (2019) e1807615.
- [147] G. Zhang, R. Chenitz, M. Lefèvre, S. Sun, J.-P. Dodelet, Is iron involved in the lack of stability of Fe/N/C electrocatalysts used to reduce oxygen at the cathode of PEM fuel cells?, *Nano Energy*, 29 (2016) 111-125.
- [148] J.Y. Choi, L.J. Yang, T. Kishimoto, X.G. Fu, S.Y. Ye, Z.W. Chen, D. Banham, Is the rapid initial performance loss of Fe/N/C non precious metal catalysts due to micropore flooding?, *Energy & Environmental Science*, 10 (2017) 296-305.

- [149] G. Liu, X.G. Li, J.W. Lee, B.N. Popov, A review of the development of nitrogen-modified carbon-based catalysts for oxygen reduction at USC, *Catalysis Science & Technology*, 1 (2011) 207-217.
- [150] D. Banham, S. Ye, K. Pei, J. Ozaki, T. Kishimoto, Y. Imashiro, A review of the stability and durability of non-precious metal catalysts for the oxygen reduction reaction in proton exchange membrane fuel cells, *Journal of Power Sources*, 285 (2015) 334-348.
- [151] J. Herranz, F. Jaouen, M. Lefevre, U.I. Kramm, E. Proietti, J.P. Dodelet, P. Bogdanoff, S. Fiechter, I. Abs-Wurmbach, P. Bertrand, T.M. Arruda, S. Mukerjee, Unveiling N-Protonation and Anion-Binding Effects on Fe/N/C Catalysts for O₂ Reduction in Proton-Exchange-Membrane Fuel Cells, *J Phys Chem C*, 115 (2011) 16087-16097.
- [152] G. Liu, X. Li, J.-W. Lee, B.N. Popov, A review of the development of nitrogen-modified carbon-based catalysts for oxygen reduction at USC, *Catalysis Science & Technology*, 1 (2011).
- [153] S. Gupta, D. Tryk, I. Bae, W. Aldred, E. Yeager, Heat-Treated Polyacrylonitrile-Based Catalysts for Oxygen Electroreduction, *J Appl Electrochem*, 19 (1989) 19-27.
- [154] L.L. Pesterfield, J.B. Maddox, M.S. Crocker, G.K. Schweitzer, Pourbaix (E-pH-M) Diagrams in Three Dimensions, *J Chem Educ*, 89 (2012) 891-899.
- [155] S. Baranton, C. Coutanceau, C. Roux, F. Hahn, J.M. Leger, Oxygen reduction reaction in acid medium at iron phthalocyanine dispersed on high surface area carbon substrate: tolerance to methanol, stability and kinetics, *Journal of Electroanalytical Chemistry*, 577 (2005) 223-234.
- [156] H. Meier, U. Tschirwitz, E. Zimmerhackl, W. Albrecht, G. Zeitler, Application of Radioisotope Techniques for Study of Phthalocyanine Catalyzed Electrochemical Processes in Fuel-Cells, *J Phys Chem-Us*, 81 (1977) 712-718.
- [157] C.H. Choi, C. Baldizzone, J.P. Grote, A.K. Schuppert, F. Jaouen, K.J.J. Mayrhofer, Stability of Fe-N-C Catalysts in Acidic Medium Studied by Operando Spectroscopy, *Angew Chem Int Edit*, 54 (2015) 12753-12757.
- [158] R. Chenitz, U.I. Kramm, M. Lefèvre, V. Glibin, G. Zhang, S. Sun, J.-P. Dodelet, A specific demetalation of Fe-N₄ catalytic sites in the micropores of NC_Ar + NH₃ is at the origin of the initial activity loss of the highly active Fe/N/C catalyst used for the reduction of oxygen in PEM fuel cells, *Energy & Environmental Science*, 11 (2018) 365-382.
- [159] H. Li, K. Tsay, H.J. Wang, J. Shen, S.H. Wu, J.J. Zhang, N.Y. Jia, S. Wessel, R. Abouatallah, N. Joos, J. Schrooten, Durability of PEM fuel cell cathode in the presence of Fe³⁺ and Al³⁺, *Journal of Power Sources*, 195 (2010) 8089-8093.
- [160] M. Sulek, J. Adams, S. Kaberline, M. Ricketts, J.R. Waldecker, In situ metal ion contamination and the effects on proton exchange membrane fuel cell performance, *Journal of Power Sources*, 196 (2011) 8967-8972.
- [161] Y.C. Wang, P.F. Zhu, H. Yang, L. Huang, Q.H. Wu, M. Rauf, J.Y. Zhang, J. Dong, K. Wang, Z.Y. Zhou, S.G. Sun, Surface Fluorination to Boost the Stability of the Fe/N/C Cathode in Proton Exchange Membrane Fuel Cells, *Chemelectrochem*, 5 (2018) 1914-1921.
- [162] C.H. Choi, H.-K. Lim, M.W. Chung, G. Chon, N. Ranjbar Sahraie, A. Altin, M.-T. Sougrati, L. Stievano, H.S. Oh, E.S. Park, F. Luo, P. Strasser, G. Dražić, K.J.J. Mayrhofer, H. Kim, F. Jaouen, The Achilles' heel of iron-based catalysts during oxygen reduction in an acidic medium, *Energy & Environmental Science*, 11 (2018) 3176-3182.
- [163] P. Zelenay, D.J. Myers, ElectroCat (Electrocatalysis Consortium), Hydrogen and Fuel Cells Program 2019 Annual Merit Review and Peer Evaluation Meeting, (2019).
- [164] Y. Shao, Highly Active and Durable PGM-free ORR Electrocatalysts through the Synergy of Active Sites, U.S. DOE Fuel Cell Technology Office 2018 Annual Merit Reviews in Environmental Science and Bio-Technology, (2018).
- [165] V. Nallathambi, G. Wu, N. Subramanian, S. Kumaraguru, J. Lee, B.N. Popov, Highly Active Carbon Composite Electrocatalysts for PEM Fuel Cells, *ECS Transactions*, 11 (2007) 241-247.
- [166] J.Z. Li, M.J. Chen, D.A. Cullen, S. Hwang, M.Y. Wang, B.Y. Li, K.X. Liu, S. Karakalos, M. Lucero, H.G. Zhang, C. Lei, H. Xu, G.E. Sterbinsky, Z.X. Feng, D. Su, K.L. More, G.F. Wang, Z.B.

Wang, G. Wu, Atomically dispersed manganese catalysts for oxygen reduction in proton-exchange membrane fuel cells, *Nat Catal*, 1 (2018) 935-945.

[167] A.L. Bouwkamp-Wijnoltz, W. Visscher, J.A.R. van Veen, E. Boellaard, A.M. van der Kraan, S.C. Tang, On active-site heterogeneity in pyrolyzed carbon-supported iron porphyrin catalysts for the electrochemical reduction of oxygen: An in situ Mossbauer study, *J Phys Chem B*, 106 (2002) 12993-13001.

[168] J.A.R. Vanveen, H.A. Colijn, J.F. Vanbaar, On the Effect of a Heat-Treatment on the Structure of Carbon-Supported Metalloporphyrins and Phthalocyanines, *Electrochimica Acta*, 33 (1988) 801-804.

[169] E. Yeager, Electrocatalysts for O₂ reduction, *Electrochimica Acta*, 20 (1984) 1527-1537.

[170] D. Scherson, A.A. Tanaka, S.L. Gupta, D. Tryk, C. Fierro, R. Holze, E.B. Yeager, R.P. Lattimer, Transition-Metal Macrocycles Supported on High Area Carbon - Pyrolysis Mass-Spectrometry Studies, *Electrochimica Acta*, 31 (1986) 1247-1258.

[171] K. Wiesener, N₄-chelates as electrocatalysts for cathodic oxygen reduction, *Electrochimica Acta*, 31 (1986) 1073-1078.

[172] R. Franke, D. Ohms, K. Wiesener, Investigation of the Influence of Thermal-Treatment on the Properties of Carbon Materials Modified by N₄-Chelates for the Reduction of Oxygen in Acidic Media, *Journal of Electroanalytical Chemistry*, 260 (1989) 63-73.

[173] J.P. Dodelet, The Controversial Role of the Metal in Fe- or Co-Based Electrocatalysts for the Oxygen Reduction Reaction in Acid Medium, in: M. Shao (Ed.) *Electroanalysis in Fuel Cells Lecture Notes in Energy* vol. 9, Springer, London, 2013, pp. 271-338.

[174] J. Zhao, W.N. Wang, X.C. Qu, Y.N. Meng, Z.J. Wu, M-porphyrin (M = Mn, Co) carbon materials as oxygen reduction catalysts from density functional studies, *Mol Phys*, (2019).

[175] A. Biloul, F. Coowar, O. Contamin, G. Scarbeck, M. Savy, D. Vandenharm, J. Riga, J.J. Verbist, Oxygen Reduction in Acid-Media on Supported Iron Naphthalocyanine - Effect of Isomer Configuration and Pyrolysis, *Journal of Electroanalytical Chemistry*, 289 (1990) 189-201.

[176] A. Biloul, F. Coowar, O. Contamin, G. Scarbeck, M. Savy, D. Vandenharm, J. Riga, J.J. Verbist, Oxygen Reduction in Acid-Media - Influence of the Heat-Treatment on the Fenpc(1-2) Isomer Mixture Impregnated on Carbon-Blacks and Active Charcoals, *Journal of Electroanalytical Chemistry*, 328 (1992) 219-232.

[177] A. Biloul, F. Coowar, O. Contamin, G. Scarbeck, M. Savy, D. Vandenharm, J. Riga, J.J. Verbist, Oxygen Reduction in an Acid-Medium - Electrocatalysis by Conpc(1,2) Impregnated on a Carbon-Black Support - Effect of Loading and Heat-Treatment, *Journal of Electroanalytical Chemistry*, 350 (1993) 189-204.

[178] S. Gojkovic, S. Gupta, R.F. Savinell, Heat-Treated Iron(III) Tetramethoxyphenyl Porphyrin Supported on High-Area Carbon as an Electrocatalyst for Oxygen Reduction: I. Characterization of the Electrocatalyst, *Journal of The Electrochemical Society*, 145 (1998).

[179] L.T. Weng, P. Bertrand, G. Lalande, D. Guay, J.P. Dodelet, Surface Characterization by Time-of-Flight Sims of a Catalyst for Oxygen Electroreduction - Pyrolyzed Cobalt Phthalocyanine-on-Carbon-Black, *Appl Surf Sci*, 84 (1995) 9-21.

[180] U.I. Kramm, J. Herranz, N. Larouche, T.M. Arruda, M. Lefevre, F. Jaouen, P. Bogdanoff, S. Fiechter, I. Abs-Wurmbach, S. Mukerjee, J.P. Dodelet, Structure of the catalytic sites in Fe/N/C-catalysts for O₂-reduction in PEM fuel cells, *Phys Chem Chem Phys*, 14 (2012) 11673-11688.

[181] U.I. Koslowski, I. Abs-Wurmbach, S. Fiechter, P. Bogdanoff, Nature of the catalytic centers of porphyrin-based electrocatalysts for the ORR: A correlation of kinetic current density with the site density of Fe-N₄ Centers, *J Phys Chem C*, 112 (2008) 15356-15366.

[182] H.T. Chung, D.A. Cullen, D. Higgins, B.T. Sneed, E.F. Holby, K.L. More, P. Zelenay, Direct atomic-level insight into the active sites of a high-performance PGM-free ORR catalyst, *Science*, 357 (2017) 479-483.

- [183] D.A. Cullen, K. More, K.C. Neyerlin, H.T. Chung, P. Zelenay, D.J. Myers, Resolving Active Sites in Atomically Dispersed Electrocatalysts for Energy Conversion Applications, *Microscopy and Microanalysis*, 25 (2019) 2066-2067.
- [184] C.H. Choi, W.S. Choi, O. Kasian, A.K. Mechler, M.T. Sougrati, S. Bruller, K. Strickland, Q. Jia, S. Mukerjee, K.J.J. Mayrhofer, F. Jaouen, Unraveling the Nature of Sites Active toward Hydrogen Peroxide Reduction in Fe-N-C Catalysts, *Angew Chem Int Ed Engl*, 56 (2017) 8809-8812.
- [185] X. Yin, L. Lin, U. Martinez, P. Zelenay, 2,2'-Dipyridylamine as Heterogeneous Organic Molecular Electrocatalyst for Two-Electron Oxygen Reduction Reaction in Acid Media, *Acs Appl Energ Mater*, 2 (2019) 7272-7278.
- [186] A.H. Cook, Catalytic Properties of the Phthalocyanines. Part I. Catalase Properties, *Journal of the Electrochemical Society (Resumed)*, 1761 (1938).
- [187] C. Paquot, The catalytic oxidizing properties of the phthalocyanines, *Comptes rendus de l'Académie des sciences*, 209 (1939) 171-173.
- [188] C. Paquot, F. de Goursac, *Bulletin de la Société Chimique de France*, 172 (1950).
- [189] C. Paquot, *Comptes rendus de l'Académie des sciences Paris*, 214 (1942).
- [190] R. Jasinski, A New Fuel Cell Cathode Catalyst, *Nature*, 201 (1964) 1212-1213.
- [191] H. Jahnke, M. Schönborn, G. Zimmermann, Organic dyestuffs as catalysts for fuel cells, *Topics in Current Chemistry*, 61 (1976) 133-181.
- [192] N. Kobayashi, Y. Nishiyama, Catalytic electroreduction of molecular oxygen at glassy carbon electrodes with immobilized iron porphyrins containing zero, one, or four amino groups, *Journal of Electroanalytical Chemistry and Interfacial Electrochemistry*, 181 (1984) 107-117.
- [193] J.A.R. Vanveen, C. Visser, Oxygen Reduction on Monomeric Transition-Metal Phthalocyanines in Acid Electrolyte, *Electrochimica Acta*, 24 (1979) 921-928.
- [194] M. Savy, P. Andro, C. Bernard, G. Magner, Etude de la réduction de l'oxygène sur les phthalocyanines monomères et polymères—I. principes fondamentaux, choix de l'ion central, *Electrochimica Acta*, 18 (1973) 191-197.
- [195] P. Bogdanoff, I. Herrmann, M. Hilgendorff, I. Dorbandt, S. Fiechter, H. Tributsch, Probing structural effects of pyrolysed CoTMPP-based electrocatalysts for oxygen reduction via new preparation strategies, *J New Mat Electr Sys*, 7 (2004) 85-92.
- [196] S.L. Gupta, D. Tryk, M. Daroux, W. Aldred, E. Yeager, Heat-Treated Pyrrole Black Based Electrocatalysts for Oxygen Reduction, *Journal of the Electrochemical Society*, 133 (1986) C120-C120.
- [197] U.I. Koslowski, I. Herrmann, P. Bogdanoff, C. Barkschat, S. Fiechter, N. Iwata, S. Takahashi, H. Nishikori, Evaluation and Analysis of PEM-FC Performance using Non-Platinum Cathode Catalysts based on Pyrolysed Fe- and Co-Porphyrins -Influence of a Secondary Heat-treatment, *ECS Transactions*, 13 (2008) 125-141.
- [198] N.R. Sahraie, U.I. Kramm, J. Steinberg, Y. Zhang, A. Thomas, T. Reier, J.P. Paraknowitsch, P. Strasser, Quantifying the density and utilization of active sites in non-precious metal oxygen electroreduction catalysts, *Nat Commun*, 6 (2015) 8618.
- [199] H.G. Zhang, H.T. Chung, D.A. Cullen, S. Wagner, U.I. Kramm, K.L. More, P. Zelenay, G. Wu, High-performance fuel cell cathodes exclusively containing atomically dispersed iron active sites, *Energy & Environmental Science*, 12 (2019).
- [200] R. Bashyam, P. Zelenay, A class of non-precious metal composite catalysts for fuel cells, *Nature*, 443 (2006) 63-66.
- [201] Z.K. Jiang, J.M. Yu, T.Z. Huang, M. Sun, Recent Advance on Polyaniline or Polypyrrole-Derived Electrocatalysts for Oxygen Reduction Reaction, *Polymers-Basel*, 10 (2018).
- [202] Z. Shi, J.J. Zhang, Density functional theory study of transitional metal macrocyclic complexes' dioxygen-binding abilities and their catalytic activities toward oxygen reduction reaction, *J Phys Chem C*, 111 (2007) 7084-7090.

- [203] L. Osmieri, A.H.A.M. Videla, P. Ocon, S. Specchia, Kinetics of Oxygen Electroreduction on Me-N-C (Me = Fe, Co, Cu) Catalysts in Acidic Medium: Insights on the Effect of the Transition Metal, *J Phys Chem C*, 121 (2017) 17796-17817.
- [204] J.K. Li, A. Alsudairi, Z.F. Ma, S. Mukerjee, Q.Y. Jia, Asymmetric Volcano Trend in Oxygen Reduction Activity of Pt and Non-Pt Catalysts: In Situ Identification of the Site-Blocking Effect, *Journal of the American Chemical Society*, 139 (2017) 1384-1387.
- [205] S. Gottesfeld, Generation of active sites by potential-driven surface processes: a central aspect of electrocatalysis, *ECS Transactions*, 61 (2014) 1-13.
- [206] J.H. Zagal, M.T.M. Koper, Reactivity Descriptors for the Activity of Molecular MN₄ Catalysts for the Oxygen Reduction Reaction, *Angew Chem Int Edit*, 55 (2016) 14510-14521.
- [207] F. Jaouen, J.P. Dodelet, O₂ Reduction Mechanism on Non-Noble Metal Catalysts for PEM Fuel Cells. Part I: Experimental Rates of O₂ Electroreduction, H₂O₂ Electroreduction, and H₂O₂ Disproportionation, *J Phys Chem C*, 113 (2009) 15422-15432.
- [208] C.H. Choi, H.K. Lim, M.W. Chung, G. Chon, N.R. Sahraie, A. Altin, M.T. Sougrati, L. Stievano, H.S. Oh, E.S. Park, F. Luo, P. Strasser, G. Drazic, K.J.J. Mayrhofer, H. Kim, F. Jaouen, The Achilles' heel of iron-based catalysts during oxygen reduction in an acidic medium, *Energy & Environmental Science*, 11 (2018) 3176-3182.
- [209] L. Lin, Z.K. Yang, Y.F. Jiang, A.W. Xu, Nonprecious Bimetallic (Fe,Mo)-N/C Catalyst for Efficient Oxygen Reduction Reaction, *Acs Catalysis*, 6 (2016) 4449-4454.
- [210] U.I. Kramm, I. Herrmann-Geppert, S. Fiechter, G. Zehl, I. Zizak, I. Dorbandt, D. Schmeißer, P. Bogdanoff, Effect of iron-carbide formation on the number of active sites in Fe-N-C catalysts for the oxygen reduction reaction in acidic media, *J. Mater. Chem. A*, 2 (2014) 2663-2670.
- [211] F. Jaouen, S. Marcotte, J.P. Dodelet, G. Lindbergh, Oxygen reduction catalysts for polymer electrolyte fuel cells from the pyrolysis of iron acetate adsorbed on various carbon supports, *J Phys Chem B*, 107 (2003) 1376-1386.
- [212] G. Faubert, R. Cote, J.P. Dodelet, M. Lefevre, P. Bertrand, Oxygen reduction catalysts for polymer electrolyte fuel cells from the pyrolysis of Fe-II acetate adsorbed 3,4,9,10-perylenetetracarboxylic dianhydride, *Electrochimica Acta*, 44 (1999) 2589-2603.
- [213] M. Lefevre, J.P. Dodelet, P. Bertrand, O₂ reduction in PEM fuel cells: Activity and active site structural information for catalysts obtained by the pyrolysis at high temperature of Fe precursors, *J Phys Chem B*, 104 (2000) 11238-11247.
- [214] H.S. Oh, H. Kim, The role of transition metals in non-precious nitrogen-modified carbon-based electrocatalysts for oxygen reduction reaction, *Journal of Power Sources*, 212 (2012) 220-225.
- [215] S.B. Sinnott, R. Andrews, D. Qian, A.M. Rao, Z. Mao, E.C. Dickey, F. Derbyshire, Model of carbon nanotube growth through chemical vapor deposition, *Chem Phys Lett*, 315 (1999) 25-30.
- [216] J. Hoekstra, A.M. Beale, F. Soulimani, M. Versluijs-Helder, D. van de Kleut, J.M. Koelewijn, J.W. Geus, L.W. Jenneskens, The effect of iron catalyzed graphitization on the textural properties of carbonized cellulose: Magnetically separable graphitic carbon bodies for catalysis and remediation, *Carbon*, 107 (2016) 248-260.
- [217] J. Hoekstra, A.M. Beale, F. Soulimani, M. Versluijs-Helder, J.W. Geus, L.W. Jenneskens, Base Metal Catalyzed Graphitization of Cellulose: A Combined Raman Spectroscopy, Temperature-Dependent X-ray Diffraction and High-Resolution Transmission Electron Microscopy Study, *J Phys Chem C*, 119 (2015) 10653-10661.
- [218] J. Hoekstra, M. Versluijs-Helder, E.J. Vlietstra, J.W. Geus, L.W. Jenneskens, Carbon-Supported Base Metal Nanoparticles: Cellulose at Work, *Chemsuschem*, 8 (2015) 985-989.
- [219] F. Caturla, M. Molinasabio, F. Rodriguezreinoso, Preparation of Activated Carbon by Chemical Activation with ZnCl₂, *Carbon*, 29 (1991) 999-1007.

- [220] S. Ganesan, N. Leonard, S.C. Barton, Impact of transition metal on nitrogen retention and activity of iron-nitrogen-carbon oxygen reduction catalysts, *Physical Chemistry Chemical Physics*, 16 (2014) 4576-4585.
- [221] L. Osmieri, A.H.A.M. Videla, S. Specchia, Optimization of a Fe-N-C electrocatalyst supported on mesoporous carbon functionalized with polypyrrole for oxygen reduction reaction under both alkaline and acidic conditions, *Int J Hydrogen Energy*, 41 (2016) 19610-19628.
- [222] J. Fournier, G. Lalande, R. Cote, D. Guay, J.P. Dodelet, Activation of various Fe-based precursors on carbon black and graphite supports to obtain catalysts for the reduction of oxygen in fuel cells, *Journal of the Electrochemical Society*, 144 (1997) 218-226.
- [223] P.H. Matter, L. Zhang, U.S. Ozkan, The role of nanostructure in nitrogen-containing carbon catalysts for the oxygen reduction reaction, *J Catal*, 239 (2006) 83-96.
- [224] P.H. Matter, E. Wang, J.M.M. Millet, U.S. Ozkan, Characterization of the iron phase in CN_x-based oxygen reduction reaction catalysts, *J Phys Chem C*, 111 (2007) 1444-1450.
- [225] H. Wang, R. Cote, G. Faubert, D. Guay, J.P. Dodelet, Effect of the pre-treatment of carbon black supports on the activity of Fe-based electrocatalysts for the reduction of oxygen, *J Phys Chem B*, 103 (1999) 2042-2049.
- [226] M.J. Park, J.H. Lee, K.P.S.S. Hembram, K.R. Lee, S.S. Han, C.W. Yoon, S.W. Nam, J.Y. Kim, Oxygen Reduction Electrocatalysts Based on Coupled Iron Nitride Nanoparticles with Nitrogen-Doped Carbon, *Catalysts*, 6 (2016).
- [227] Y.S. Zhu, B.S. Zhang, Z.B. Feng, D.S. Su, Synthesis-structure-performance correlation for poly(phenylenediamine)s/iron/carbon non-precious metal catalysts for oxygen reduction reaction, *Catalysis Today*, 260 (2016) 112-118.
- [228] C.Y. Shu, Y.Z. Chen, X.D. Yang, Y. Liu, S.K. Chong, Y. Fang, Y.N. Liu, W.H. Yang, Enhanced Fe dispersion via "pinning" effect of thiocyanate ion on ferric ion in Fe-N-S-doped catalyst as an excellent oxygen reduction reaction electrode, *Journal of Power Sources*, 376 (2018) 161-167.
- [229] S.T. Thompson, A.R. Wilson, P. Zelenay, D.J. Myers, K.L. More, K.C. Neyerlin, D. Papageorgopoulos, ElectroCat: DOE's approach to PGM-free catalyst and electrode R&D, *Solid State Ionics*, 319 (2018) 68-76.
- [230] I. Herrmann, U.I. Kramm, S. Fiechter, P. Bogdanoff, Oxalate supported pyrolysis of CoTMPP as electrocatalysts for the oxygen reduction reaction, *Electrochimica Acta*, 54 (2009) 4275-4287.
- [231] G. Lalande, R. Cote, D. Guay, J.P. Dodelet, L.T. Weng, P. Bertrand, Is nitrogen important in the formulation of Fe-based catalysts for oxygen reduction in solid polymer fuel cells?, *Electrochimica Acta*, 42 (1997) 1379-1388.
- [232] K. Liu, Y. Lei, R. Chen, G. Wang, Oxygen Electroreduction on M-N₄ Macrocyclic Complexes, in: J.H. Zagal, F. Bedioui (Eds.) *Electrochemistry of N₄ Macrocyclic Metal Complexes*, Springer, Cham, 2016.
- [233] P. Gouerec, A. Biloul, O. Contamin, G. Scarbeck, M. Savy, J. Riga, L.T. Weng, P. Bertrand, Oxygen reduction in acid media catalysed by heat treated cobalt tetraazaannulene supported on an active charcoal: Correlations between the performances after longevity tests and the active site configuration as seen by XPS and ToF-SIMS, *Journal of Electroanalytical Chemistry*, 422 (1997) 61-75.
- [234] S.L. Gojkovic, S. Gupta, R.F. Savinell, Heat-treated iron(III) tetramethoxyphenyl porphyrin chloride supported on high-area carbon as an electrocatalyst for oxygen reduction - Part II. Kinetics of oxygen reduction, *Journal of Electroanalytical Chemistry*, 462 (1999) 63-72.
- [235] J.P. Dodelet, Oxygen Reduction in PEM Fuel Cell Conditions: Heat Treated Non Precious Metal N₄ Macrocyclics and Beyond, in: J.H. Zagal, F. Bedioui, J.P. Dodelet (Eds.) *N₄-Macrocyclic Metal Complexes*, Springer Science + Business Media Inc., New York, 2006.

- [236] Y.Y. Liu, X.P. Yue, K.X. Li, J.L. Qiao, D.P. Wilkinson, J.J. Zhang, PEM fuel cell electrocatalysts based on transition metal macrocyclic compounds, *Coordin Chem Rev*, 315 (2016) 153-177.
- [237] S. Dey, B. Mondal, S. Chatterjee, A. Rana, S.K. Amanullah, A. Dey, Molecular electrocatalysts for the oxygen reduction reaction, *Nat Rev Chem*, 1 (2017).
- [238] Z.P. Zhang, J.T. Sun, F. Wang, L.M. Dai, Efficient Oxygen Reduction Reaction (ORR) Catalysts Based on Single Iron Atoms Dispersed on a Hierarchically Structured Porous Carbon Framework, *Angew Chem Int Edit*, 57 (2018) 9038-9043.
- [239] R. Cao, R. Thapa, H. Kim, X. Xu, M.G. Kim, Q. Li, N. Park, M.L. Liu, J. Cho, Promotion of oxygen reduction by a bio-inspired tethered iron phthalocyanine carbon nanotube-based catalyst, *Nature Communications*, 4 (2013).
- [240] M. Hanana, H. Arcostanzo, P.K. Das, M. Bouget, S. Le Gac, H. Okuno, R. Cornut, B. Josselme, V. Dorcet, B. Boitrel, S. Campidelli, Synergic effect on oxygen reduction reaction of strapped iron porphyrins polymerized around carbon nanotubes, *New J Chem*, 42 (2018) 19749-19754.
- [241] N. Zion, D.A. Cullen, P. Zelenay, L. Elbaz, Heat-Treated Aerogel as a Catalyst for the Oxygen Reduction Reaction, *Angew Chem Int Ed Engl*, 59 (2020) 2483-2489.
- [242] M. Bron, S. Fiechter, M. Hilgendorff, P. Bogdanoff, Catalysts for oxygen reduction from heat-treated carbon-supported iron phenantroline complexes, *J Appl Electrochem*, 32 (2002) 211-216.
- [243] L. Tong, Y.C. Wang, M.X. Chen, Z.Q. Chen, Q.Q. Yan, C.L. Yang, Z.Y. Zhou, S.Q. Chu, X. Feng, H.W. Liang, Hierarchically porous carbons as supports for fuel cell electrocatalysts with atomically dispersed Fe-N x moieties, *Chem Sci*, 10 (2019) 8236-8240.
- [244] A. Zitolo, V. Goellner, V. Armel, M.T. Sougrati, T. Mineva, L. Stievano, E. Fonda, F. Jaouen, Identification of catalytic sites for oxygen reduction in iron- and nitrogen-doped graphene materials, *Nat Mater*, 14 (2015) 937-942.
- [245] L. Osmieri, R. Estudero-Cid, M. Armandi, A.H.A.M. Videla, J.L.G. Fierro, P. Ocon, S. Specchia, Fe-N/C catalysts for oxygen reduction reaction supported on different carbonaceous materials. Performance in acidic and alkaline direct alcohol fuel cells, *Appl Catal B-Environ*, 205 (2017) 637-653.
- [246] D. Singh, J. Tian, K. Mamtani, J. King, J.T. Miller, U.S. Ozkan, A comparison of N-containing carbon nanostructures (CNx) and N-coordinated iron-carbon catalysts (FeNC) for the oxygen reduction reaction in acidic media, *J Catal*, 317 (2014) 30-43.
- [247] M. Bron, J. Radnik, M. Fieber-Erdmann, P. Bogdanoff, S. Fiechter, EXAFS, XPS and electrochemical studies on oxygen reduction catalysts obtained by heat treatment of iron phenanthroline complexes supported on high surface area carbon black, *Journal of Electroanalytical Chemistry*, 535 (2002) 113-119.
- [248] F. Roncaroli, E.S. Dal Molin, F.A. Viva, M.M. Bruno, E.B. Halac, Cobalt and Iron Complexes with N-heterocyclic Ligands as Pyrolysis Precursors for Oxygen Reduction Catalysts, *Electrochimica Acta*, 174 (2015) 66-77.
- [249] U.I. Kramm, M. Lefevre, P. Bogdanoff, D. Schmeisser, J.P. Dodelet, Analyzing Structural Changes of Fe-N-C Cathode Catalysts in PEM Fuel Cell by Mossbauer Spectroscopy of Complete Membrane Electrode Assemblies, *J Phys Chem Lett*, 5 (2014) 3750-3756.
- [250] U.I. Kramm, M. Lefevre, N. Larouche, D. Schmeisser, J.P. Dodelet, Correlations between mass activity and physicochemical properties of Fe/N/C catalysts for the ORR in PEM fuel cell via ⁵⁷Fe Mossbauer spectroscopy and other techniques, *J Am Chem Soc*, 136 (2014) 978-985.
- [251] S. Schardt, N. Weidler, W. Wallace, I. Martinaiou, R. Stark, U. Kramm, Influence of the Structure-Forming Agent on the Performance of Fe-N-C Catalysts, *Catalysts*, 8 (2018).
- [252] R. Kothandaraman, V. Nallathambi, K. Artyushkova, S.C. Barton, Non-precious oxygen reduction catalysts prepared by high-pressure pyrolysis for low-temperature fuel cells, *Appl Catal B-Environ*, 92 (2009) 209-216.

- [253] K.C. Heo, K.S. Nahm, S.H. Lee, P. Kim, Heat-treated 2,2'-bipyridine iron complex supported on polypyrrole-coated carbon for oxygen reduction reaction, *J Ind Eng Chem*, 17 (2011) 304-309.
- [254] V. Nallathambi, N. Leonard, R. Kothandaraman, S.C. Barton, Nitrogen Precursor Effects in Iron-Nitrogen-Carbon Oxygen Reduction Catalysts, *Electrochem Solid St*, 14 (2011) B55-B58.
- [255] H. Wang, W. Wang, J.L. Key, S. Ji, Y.Y. Ma, L. Khotseng, W.Z. Lv, R.F. Wang, Sponge-like carbon containing nitrogen and iron provides a non-precious oxygen reduction catalyst, *J Solid State Electr*, 19 (2015) 1181-1186.
- [256] P. Teppor, R. Jager, E. Hark, U. Joost, I. Tallo, P. Paiste, K. Kirsimäe, E. Lust, Oxygen Reduction Reaction on Nitrogen and Cobalt Modified Silicon Carbide Derived Carbon in Acidic Media, *Selected Proceedings from the 233rd Ecs Meeting*, 85 (2018) 855-863.
- [257] R. Jäger, P.E. Kasatkin, E. Härk, P. Teppor, T. Romann, R. Härmas, I. Tallo, U. Mäeorg, U. Joost, P. Paiste, K. Kirsimäe, E. Lust, The effect of N precursors in Fe-N/C type catalysts based on activated silicon carbide derived carbon for oxygen reduction activity at various pH values, *Journal of Electroanalytical Chemistry*, 823 (2018) 593-600.
- [258] L. Zhang, K. Lee, C.W.B. Bezerra, J.L. Zhang, J.J. Zhang, Fe loading of a carbon-supported Fe-N electrocatalyst and its effect on the oxygen reduction reaction, *Electrochimica Acta*, 54 (2009) 6631-6636.
- [259] C.W.B. Bezerra, L. Zhang, K.C. Lee, H.S. Liu, J.L. Zhang, Z. Shi, A.L.B. Marques, E.P. Marques, S.H. Wu, J.J. Zhang, Novel carbon-supported Fe-N electrocatalysts synthesized through heat treatment of iron tripyridyl triazine complexes for the PEM fuel cell oxygen reduction reaction, *Electrochimica Acta*, 53 (2008) 7703-7710.
- [260] S. Li, L. Zhang, H.S. Liu, M. Pan, L. Zan, J.J. Zhang, Heat-treated cobalt-tripyridyl triazine (Co-TPTZ) electrocatalysts for oxygen reduction reaction in acidic medium, *Electrochimica Acta*, 55 (2010) 4403-4411.
- [261] A. Velazquez-Palenzuela, L. Zhang, L.C. Wang, P.L. Cabot, E. Brillas, K. Tsay, J.J. Zhang, Carbon-Supported Fe-N-x Catalysts Synthesized by Pyrolysis of the Fe(II)-2,3,5,6-Tetra(2-pyridyl)pyrazine Complex: Structure, Electrochemical Properties, and Oxygen Reduction Reaction Activity, *J Phys Chem C*, 115 (2011) 12929-12940.
- [262] J. Tian, A. Morozan, M.T. Sougrati, M. Lefevre, R. Chenitz, J.P. Dodelet, D. Jones, F. Jaouen, Optimized synthesis of Fe/N/C cathode catalysts for PEM fuel cells: a matter of iron-ligand coordination strength, *Angew Chem Int Ed Engl*, 52 (2013) 6867-6870.
- [263] A. Serov, K. Artyushkova, P. Atanassov, Fe-N-C Oxygen Reduction Fuel Cell Catalyst Derived from Carbendazim: Synthesis, Structure, and Reactivity, *Advanced Energy Materials*, 4 (2014).
- [264] K. Artyushkova, I. Matanovic, B. Halevi, P. Atanassov, Oxygen Binding to Active Sites of Fe-N-C ORR Electrocatalysts Observed by Ambient-Pressure XPS, *J Phys Chem C*, 121 (2017) 2836-2843.
- [265] A. Serov, P. Atanassov, Carbendazim-based catalytic materials in: S. UNM (Ed.), 2013.
- [266] S. Kabir, K. Artyushkova, A. Serov, B. Kiefer, P. Atanassov, Binding energy shifts for nitrogen-containing graphene-based electrocatalysts - experiments and DFT calculations, *Surf Interface Anal*, 48 (2016) 293-300.
- [267] A. Serov, M.H. Robson, B. Halevi, K. Artyushkova, P. Atanassov, Highly active and durable templated non-PGM cathode catalysts derived from iron and aminoantipyrine, *Electrochemistry Communications*, 22 (2012) 53-56.
- [268] A. Serov, M.J. Workman, K. Artyushkova, P. Atanassov, G. McCool, S. McKinney, H. Romero, B. Halevi, T. Stephenson, Highly stable precious metal-free cathode catalyst for fuel cell application, *Journal of Power Sources*, 327 (2016) 557-564.
- [269] A. Serov, A. Aziznia, P.H. Benhangi, K. Artyushkova, P. Atanassov, E. Gyenge, Borohydride-tolerant oxygen electroreduction catalyst for mixed-reactant Swiss-roll direct borohydride fuel cells, *Journal of Materials Chemistry A*, 1 (2013) 14384-14391.

- [270] A. Serov, M.H. Robson, M. Smolnik, P. Atanassov, Templated bi-metallic non-PGM catalysts for oxygen reduction, *Electrochimica Acta*, 80 (2012) 213-218.
- [271] M.H. Robson, A. Serov, K. Artyushkova, P. Atanassov, A mechanistic study of 4-aminoantipyrine and iron derived non-platinum group metal catalyst on the oxygen reduction reaction, *Electrochimica Acta*, 90 (2013) 656-665.
- [272] D. Sebastian, V. Baglio, A.S. Arico, A. Serov, P. Atanassov, Performance analysis of a non-platinum group metal catalyst based on iron-aminoantipyrine for direct methanol fuel cells, *Appl Catal B-Environ*, 182 (2016) 297-305.
- [273] S. Stariha, K. Artyushkova, M.J. Workman, A. Serov, S. Mckinney, B. Halevi, P. Atanassov, PGM-free Fe-N-C catalysts for oxygen reduction reaction: Catalyst layer design, *Journal of Power Sources*, 326 (2016) 43-49.
- [274] J. Maruyama, N. Fukui, M. Kawaguchi, I. Abe, Use of purine and pyrimidine bases as nitrogen sources of active site in oxygen reduction catalyst, *Journal of Power Sources*, 194 (2009) 655-661.
- [275] N.P. Subramanian, X.G. Li, V. Nallathambi, S.P. Kumaraguru, H. Colon-Mercado, G. Wu, J.W. Lee, B.N. Popov, Nitrogen-modified carbon-based catalysts for oxygen reduction reaction in polymer electrolyte membrane fuel cells, *Journal of Power Sources*, 188 (2009) 38-44.
- [276] N. Leonard, V. Nallathambi, S.C. Barton, Carbon Supports for Non-Precious Metal Oxygen Reducing Catalysts, *Journal of the Electrochemical Society*, 160 (2013) F788-F792.
- [277] S. Gupta, S. Zhao, O. Ogoke, Y. Lin, H. Xu, G. Wu, Engineering Favorable Morphology and Structure of Fe-N-C Oxygen-Reduction Catalysts through Tuning of Nitrogen/Carbon Precursors, *ChemSusChem*, 10 (2017) 774-785.
- [278] T.E. Wood, Z. Tan, A.K. Schmoedel, D. O'Neill, R. Atanasoski, Non-precious metal oxygen reduction catalyst for PEM fuel cells based on nitroaniline precursor, *Journal of Power Sources*, 178 (2008) 510-516.
- [279] Z.-l. Deng, Q.-f. Yi, M. Lei, Preparation of Co Doped Nitroaniline Composites and Their Electrochemical Activities for Oxygen Reduction Reaction, *Chinese Journal Of Synthetic Chemistry*, (2018).
- [280] Y. Li, C.S. Mo, J. Li, D.S. Yu, Pyrazine?nitrogen?rich exfoliated C 4 N nanosheets as efficient metal?free polymeric catalysts for oxygen reduction reaction, *J Energy Chem*, 49 (2020) 243-247.
- [281] Y.J. Chen, S.F. Ji, S. Zhao, W.X. Chen, J.C. Dong, W.C. Cheong, R.A. Shen, X.D. Wen, L.R. Zheng, A.I. Rykov, S.C. Cai, H.L. Tang, Z.B. Zhuang, C. Chen, Q. Peng, D.S. Wang, Y.D. Li, Enhanced oxygen reduction with single-atomic-site iron catalysts for a zinc-air battery and hydrogen-air fuel cell, *Nature Communications*, 9 (2018).
- [282] X.L. Xu, Z.X. Xia, X.M. Zhang, H.Q. Li, S.L. Wang, G.Q. Sun, Size-dependence of the electrochemical performance of Fe-N-C catalysts for the oxygen reduction reaction and cathodes of direct methanol fuel cells, *Nanoscale*, 12 (2020) 3418-3423.
- [283] B. Ni, C. Ouyang, X.B. Xu, J. Zhuang, X. Wang, Modifying Commercial Carbon with Trace Amounts of ZIF to Prepare Derivatives with Superior ORR Activities, *Advanced Materials*, 29 (2017).
- [284] H.G. Zhang, S. Hwang, M.Y. Wang, Z.X. Feng, S. Karakalos, L.L. Luo, Z. Qiao, X.H. Xie, C.M. Wang, D. Su, Y.Y. Shao, G. Wu, Single Atomic Iron Catalysts for Oxygen Reduction in Acidic Media: Particle Size Control and Thermal Activation, *Journal of the American Chemical Society*, 139 (2017) 14143-14149.
- [285] R. Gokhale, L.K. Tsui, K. Roach, Y.C. Chen, M.M. Hossen, K. Artyushkova, F. Garzon, P. Atanassov, Hydrothermal Synthesis of Platinum-Group-Metal-Free Catalysts: Structural Elucidation and Oxygen Reduction Catalysis, *Chemelectrochem*, 5 (2018) 1848-1853.
- [286] X.J. Wang, J.W. Zhou, H. Fu, W. Li, X.X. Fan, G.B. Xin, J. Zheng, X.G. Li, MOF derived catalysts for electrochemical oxygen reduction, *Journal of Materials Chemistry A*, 2 (2014) 14064-14070.

- [287] T. Al-Zoubi, Y. Zhou, X. Yin, B. Janicek, C.J. Sun, C.E. Schulz, X.H. Zhang, A.A. Gewirth, P. Huang, P. Zelenay, H. Yang, Preparation of Nonprecious Metal Electrocatalysts for the Reduction of Oxygen Using a Low-Temperature Sacrificial Metal, *Journal of the American Chemical Society*, 142 (2020) 5477-5481.
- [288] M. Sun, D. Davenport, H.J. Liu, J.H. Qu, M. Elimelech, J.H. Li, Highly efficient and sustainable non-precious-metal Fe-N-C electrocatalysts for the oxygen reduction reaction, *Journal of Materials Chemistry A*, 6 (2018) 2527-2539.
- [289] C. Lo Vecchio, A.S. Arico, G. Monforte, V. Baglio, EDTA-derived Co-N-C and Fe-N-C electro-catalysts for the oxygen reduction reaction in acid environment, *Renew Energ*, 120 (2018) 342-349.
- [290] C. Lo Vecchio, A.S. Arico, V. Baglio, Application of Low-Cost Me-N-C (Me = Fe or Co) Electrocatalysts Derived from EDTA in Direct Methanol Fuel Cells (DMFCs), *Materials*, 11 (2018).
- [291] Z.W. Chang, F.L. Meng, H.X. Zhong, X.B. Zhang, Anchoring Iron-EDTA Complex on Graphene toward the Synthesis of Highly Efficient Fe-N-C Oxygen Reduction Electrocatalyst for Fuel Cells, *Chinese J Chem*, 36 (2018) 287-292.
- [292] L. Wang, P. Liang, J. Zhang, X. Huang, Activity and stability of pyrolyzed iron ethylenediaminetetraacetic acid as cathode catalyst in microbial fuel cells, *Bioresource Technol*, 102 (2011) 5093-5097.
- [293] Z. Chen, D. Higgins, H.S. Tao, R.S. Hsu, Z.W. Chen, Highly Active Nitrogen-Doped Carbon Nanotubes for Oxygen Reduction Reaction in Fuel Cell Applications, *J Phys Chem C*, 113 (2009) 21008-21013.
- [294] G. Liu, X. Li, B.N. Popov, Stability Study of Nitrogen-Modified Carbon Composite Catalysts for Oxygen Reduction Reaction in Polymer Electrolyte Membrane Fuel Cells, *ECS Transactions*, 25 (2009) 1251-1259.
- [295] G. Liu, X.G. Li, P. Ganesan, B.N. Popov, Studies of oxygen reduction reaction active sites and stability of nitrogen-modified carbon composite catalysts for PEM fuel cells, *Electrochimica Acta*, 55 (2010) 2853-2858.
- [296] N.P. Subramanian, S.P. Kumaraguru, H. Colon-Mercado, H. Kim, B.N. Popov, T. Black, D.A. Chen, Studies on Co-based catalysts supported on modified carbon substrates for PEMFC cathodes, *Journal of Power Sources*, 157 (2006) 56-63.
- [297] V. Nallathambi, J.W. Lee, S.P. Kumaraguru, G. Wu, B.N. Popov, Development of high performance carbon composite catalyst for oxygen reduction reaction in PEM Proton Exchange Membrane fuel cells, *Journal of Power Sources*, 183 (2008) 34-42.
- [298] A. Serov, M.H. Robson, K. Artyushkova, P. Atanassov, Templated non-PGM cathode catalysts derived from iron and poly(ethyleneimine) precursors, *Appl Catal B-Environ*, 127 (2012) 300-306.
- [299] J. Maruyama, I. Abe, Fuel Cell Cathode Catalyst with Heme-Like Structure Formed from Nitrogen of Glycine and Iron, *Journal of The Electrochemical Society*, 154 (2007).
- [300] J. Zhang, Q.D. Li, H. Wu, C.Y. Zhang, K. Cheng, H. Zhou, M. Pan, S.C. Mu, Nitrogen-self-doped carbon with a porous graphene-like structure as a highly efficient catalyst for oxygen reduction, *Journal of Materials Chemistry A*, 3 (2015) 10851-10857.
- [301] J.Y. Liu, Y. Liu, P. Li, L.H. Wang, H.R. Zhang, H. Liu, J.L. Liu, Y.X. Wang, W. Tian, X.B. Wang, Z.T. Li, M.B. Wu, Fe-N-doped porous carbon from petroleum asphalt for highly efficient oxygen reduction reaction, *Carbon*, 126 (2018) 1-8.
- [302] S. Son, D. Lim, D. Nam, J. Kim, S.E. Shim, S.H. Baeck, N, S-doped nanocarbon derived from ZIF-8 as a highly efficient and durable. electro-catalyst for oxygen reduction reaction, *J Solid State Chem*, 274 (2019) 237-242.
- [303] K. Hu, L. Tao, D.D. Liu, J. Huo, S.Y. Wang, Sulfur-Doped Fe/N/C Nanosheets as Highly Efficient Electrocatalysts for Oxygen Reduction Reaction, *Acs Appl Mater Inter*, 8 (2016) 19379-19385.

- [304] D.B. Liu, C.Q. Wu, S.M. Chen, S.Q. Ding, Y.F. Xie, C.D. Wang, T. Wang, Y.A. Haleem, Z.U. Rehman, Y. Sang, Q. Liu, X.S. Zheng, Y. Wang, B.H. Ge, H.X. Xu, L. Song, In situ trapped high-density single metal atoms within graphene: Iron-containing hybrids as representatives for efficient oxygen reduction, *Nano Res*, 11 (2018) 2217-2228.
- [305] H.T. Chung, J.H. Won, P. Zelenay, Active and stable carbon nanotube/nanoparticle composite electrocatalyst for oxygen reduction, *Nat Commun*, 4 (2013) 1922.
- [306] L.J. Zhong, Y. Hu, L.N. Cleemann, C. Pan, J. Svaerke, J.O. Jensen, Q.F. Li, Encapsulated iron-based oxygen reduction electrocatalysts by high pressure pyrolysis, *Int J Hydrogen Energy*, 42 (2017) 22887-22896.
- [307] H.T. Chung, C.M. Johnston, P. Zelenay, Synthesis and Evaluation of Heat-treated, Cyanamide-derived Nonprecious Catalysts for Oxygen Reduction, *ECS Transactions*, 25 (2009) 485-492.
- [308] W. Kicinski, M. Szala, M. Bystrzejewski, Sulfur-doped porous carbons: Synthesis and applications, *Carbon*, 68 (2014) 1-32.
- [309] W. Kicinski, B. Dembinska, M. Norek, B. Budner, M. Polanski, P.J. Kulesza, S. Dyjak, Heterogeneous iron-containing carbon gels as catalysts for oxygen electroreduction: Multifunctional role of sulfur in the formation of efficient systems, *Carbon*, 116 (2017) 655-669.
- [310] J. Pampel, A. Mehmood, M. Antonietti, T.P. Fellingner, Ionothermal template transformations for preparation of tubular porous nitrogen doped carbons, *Mater Horizons*, 4 (2017) 493-501.
- [311] A. Serov, K. Artyushkova, P. Atanassov, Sacrificial support method: Design of open-frame non-PGM catalysts, *Abstr Pap Am Chem S*, 245 (2013).
- [312] (!!! INVALID CITATION !!! {Artyushkova, 2013 #989;Serov, 2012 #988;Stariha, 2016 #950;Serov, 2015 #872;Artyushkova, 2017 #949;Serov, 2014 #948;Kabir, 2016 #952;Serov, 2012 #956;Robson, 2013 #957;Serov, 2013 #955;Artyushkova, 2017 #949}).
- [313] D. Sebastian, A. Serov, K. Artyushkova, P. Atanassov, A.S. Arico, V. Baglio, Performance, methanol tolerance and stability of Fe-aminobenzimidazole derived catalyst for direct methanol fuel cells, *Journal of Power Sources*, 319 (2016) 235-246.
- [314] A. Serov, K. Artyushkova, E. Niangar, C. Wang, N. Dale, F. Jaouen, M.-T. Sougrati, Q. Jia, S. Mukerjee, P. Atanassov, Nano-structured non-platinum catalysts for automotive fuel cell application, *Nano Energy*, 16 (2015) 293-300.
- [315] S.Q. Ma, G.A. Goenaga, A.V. Call, D.J. Liu, Cobalt Imidazolate Framework as Precursor for Oxygen Reduction Reaction Electrocatalysts, *Chem-Eur J*, 17 (2011) 2063-2067.
- [316] G.A. Goenaga, S. Ma, S. Yuan, D.J. Liu, New Approaches to Non-PGM Electrocatalysts Using Porous Framework Materials, *ECS Transactions*, 33 (2010) 579-586.
- [317] B. You, N. Jiang, M.L. Sheng, W.S. Drisdell, J. Yano, Y.J. Sun, Bimetal-Organic Framework Self-Adjusted Synthesis of Support-Free Nonprecious Electrocatalysts for Efficient Oxygen Reduction, *Acs Catalysis*, 5 (2015) 7068-7076.
- [318] X.J. Wang, H.G. Zhang, H.H. Lin, S. Gupta, C. Wang, Z.X. Tao, H. Fu, T. Wang, J. Zheng, G. Wu, X.G. Li, Directly converting Fe-doped metal organic frameworks into highly active and stable Fe-N-C catalysts for oxygen reduction in acid, *Nano Energy*, 25 (2016) 110-119.
- [319] U.I. Kramm, I. Abs-Wurmbach, I. Herrmann-Geppert, J. Radnik, S. Fiechter, P. Bogdanoff, Influence of the Electron-Density of FeN₄-Centers Towards the Catalytic Activity of Pyrolyzed FeTMPPCI-Based ORR-Electrocatalysts, *Journal of The Electrochemical Society*, 158 (2011).
- [320] H.F. Wang, L.Y. Chen, H. Pang, S. Kaskel, Q. Xu, MOF-derived electrocatalysts for oxygen reduction, oxygen evolution and hydrogen evolution reactions, *Chem Soc Rev*, 49 (2020) 1414-1448.
- [321] Y.Z. Chen, R. Zhang, L. Jiao, H.L. Jiang, Metal-organic framework-derived porous materials for catalysis, *Coordin Chem Rev*, 362 (2018) 1-23.

- [322] H.M. Barkholtz, D.J. Liu, Advancements in rationally designed PGM-free fuel cell catalysts derived from metal-organic frameworks, *Mater Horizons*, 4 (2017) 20-37.
- [323] H.G. Zhang, H. Osgood, X.H. Xie, Y.Y. Shao, G. Wu, Engineering nanostructures of PGM-free oxygen-reduction catalysts using metal-organic frameworks, *Nano Energy*, 31 (2017) 331-350.
- [324] S. Gonen, L. Elbaz, Metal organic frameworks as catalysts for oxygen reduction, *Current Opinion in Electrochemistry*, 9 (2018) 179-188.
- [325] H.T. Chung, P. Zelenay, A simple synthesis of nitrogen-doped carbon micro- and nanotubes, *Chem Commun*, 51 (2015) 13546-13549.
- [326] F. Jaouen, M. Lefevre, J.P. Dodelet, M. Cai, Heat-treated Fe/N/C catalysts for O₂ electroreduction: Are active sites hosted in micropores?, *J Phys Chem B*, 110 (2006) 5553-5558.
- [327] F. Jaouen, A.M. Serventi, M. Lefevre, J.P. Dodelet, P. Bertrand, Non-noble electrocatalysts for O₂ reduction: How does heat treatment affect their activity and structure? Part II. Structural changes observed by electron microscopy, Raman, and mass spectroscopy, *J Phys Chem C*, 111 (2007) 5971-5976.
- [328] F. Jaouen, F. Charreteur, J.P. Dodelet, Fe-based catalysts for oxygen reduction in PEMFCs - Importance of the disordered phase of the carbon support, *Journal of the Electrochemical Society*, 153 (2006) A689-A698.
- [329] F. Jaouen, J.P. Dodelet, Non-noble electrocatalysts for O₂ reduction: How does heat treatment affect their activity and structure? Part I. Model for carbon black gasification by NH₃: Parametric calibration and electrochemical validation, *J Phys Chem C*, 111 (2007) 5963-5970.
- [330] F. Jaouen, E. Proietti, M. Lefèvre, R. Chenitz, J.-P. Dodelet, G. Wu, H.T. Chung, C.M. Johnston, P. Zelenay, Recent advances in non-precious metal catalysis for oxygen-reduction reaction in polymer electrolyte fuelcells, *Energy Environ. Sci.*, 4 (2011) 114-130.
- [331] M. Lefevre, J.P. Dodelet, Fe-based electrocatalysts made with microporous pristine carbon black supports for the reduction of oxygen in PEM fuel cells, *Electrochimica Acta*, 53 (2008) 8269-8276.
- [332] K. Mamtani, D. Singh, J. Tian, J.-M.M. Millet, J.T. Miller, A.C. Co, U.S. Ozkan, Evolution of N-Coordinated Iron–Carbon (FeNC) Catalysts and Their Oxygen Reduction (ORR) Performance in Acidic Media at Various Stages of Catalyst Synthesis: An Attempt at Benchmarking, *Catal Lett*, 146 (2016) 1749-1770.
- [333] X.H. Tang, H.R. Li, Z.W. Du, H.Y. Ng, Polyaniline and iron based catalysts as air cathodes for enhanced oxygen reduction in microbial fuel cells, *Rsc Adv*, 5 (2015) 79348-79354.
- [334] Y.F. Zhan, X. Yu, L.M. Cao, B.D. Zhang, X.X. Wu, F.Y. Xie, W.H. Zhang, J. Chen, W.G. Xie, W.J. Mai, H. Meng, The influence of nitrogen source and doping sequence on the electrocatalytic activity for oxygen reduction reaction of nitrogen doped carbon materials, *Int J Hydrogen Energ*, 41 (2016) 13493-13503.
- [335] U.I. Kramm, I. Herrmann-Geppert, P. Bogdanoff, S. Fiechter, Effect of an Ammonia Treatment on Structure, Composition, and Oxygen Reduction Reaction Activity of Fe–N–C Catalysts, *The Journal of Physical Chemistry C*, 115 (2011) 23417-23427.
- [336] N. Ramaswamy, U. Tylus, Q.Y. Jia, S. Mukerjee, Activity Descriptor Identification for Oxygen Reduction on Nonprecious Electrocatalysts: Linking Surface Science to Coordination Chemistry, *Journal of the American Chemical Society*, 135 (2013) 15443-15449.
- [337] N.D. Leonard, S. Wagner, F. Luo, J. Steinberg, W. Ju, N. Weidler, H. Wang, U.I. Kramm, P. Strasser, Deconvolution of Utilization, Site Density, and Turnover Frequency of Fe Nitrogen Carbon Oxygen Reduction Reaction Catalysts Prepared with Secondary N-Precursors, *Acs Catalysis*, 8 (2018) 1640-1647.
- [338] X.J. Wang, L.R. Zou, H. Fu, Y.F. Xiong, Z.X. Tao, J. Zheng, X.G. Li, Noble Metal-Free Oxygen Reduction Reaction Catalysts Derived from Prussian Blue Nanocrystals Dispersed in Polyaniline, *Acs Appl Mater Inter*, 8 (2016) 8436-8444.

- [339] H.L. Peng, Z.Y. Mo, S.J. Liao, H.G. Liang, L.J. Yang, F. Luo, H.Y. Song, Y.L. Zhong, B.Q. Zhang, High Performance Fe- and N- Doped Carbon Catalyst with Graphene Structure for Oxygen Reduction, *Sci Rep-Uk*, 3 (2013).
- [340] C.W. Roh, H. Lee, Fe/N/C catalysts synthesized using graphene aerogel for electrocatalytic oxygen reduction reaction in an acidic condition, *Korean J Chem Eng*, 33 (2016) 2582-2588.
- [341] R. Wu, S.G. Chen, Y.L. Zhang, Y. Wang, W. Ding, L. Li, X.Q. Qi, X. Shen, Z.D. Wei, Template-free synthesis of hollow nitrogen-doped carbon as efficient electrocatalysts for oxygen reduction reaction, *Journal of Power Sources*, 274 (2015) 645-650.
- [342] C.Z. Guo, B.X. Wen, W.L. Liao, Z.B. Li, L.T. Sun, C. Wang, Y.C. Wu, J. Chen, Y.Q. Nie, J.L. Liao, C.G. Chen, Template-assisted conversion of aniline nanopolymers into non-precious metal FeN/C electrocatalysts for highly efficient oxygen reduction reaction, *J Alloy Compd*, 686 (2016) 874-882.
- [343] V.A. Setyowati, H.C. Huang, C.C. Liu, C.H. Wang, Effect of Iron Precursors on the Structure and Oxygen Reduction Activity of Iron-Nitrogen-Carbon Catalysts, *Electrochimica Acta*, 211 (2016) 933-940.
- [344] G. Wu, P. Zelenay, Nanostructured Nonprecious Metal Catalysts for Oxygen Reduction Reaction, *Accounts Chem Res*, 46 (2013) 1878-1889.
- [345] Y. Zhang, Improving ORR Activity of Nitrogen-Doped Carbon Catalysts via Washing PANI-iron Coordination Precursor with ethanol, *International Journal of Electrochemical Science*, (2019) 2476-2488.
- [346] X. Yin, H.T. Chung, U. Martinez, L. Lin, K. Artyushkova, P. Zelenay, PGM-Free ORR Catalysts Designed by Templating PANI-Type Polymers Containing Functional Groups with High Affinity to Iron, *Journal of the Electrochemical Society*, 166 (2019) F3240-F3245.
- [347] J. Quilez-Bermejo, C. Gonzalez-Gaitan, E. Morallon, D. Cazorla-Amoros, Effect of carbonization conditions of polyaniline on its catalytic activity towards ORR. Some insights about the nature of the active sites, *Carbon*, 119 (2017) 62-71.
- [348] G.H. Wang, K.Z. Jiang, M.L. Xu, C.G. Min, B.H. Ma, X.K. Yang, A high activity nitrogen-doped carbon catalyst for oxygen reduction reaction derived from polyaniline-iron coordination polymer, *Journal of Power Sources*, 266 (2014) 222-225.
- [349] A. Garsuch, K. MacIntyre, X. Michaud, D.A. Stevens, J.R. Dahn, Fuel cell studies on a non-noble metal catalyst prepared by a template-assisted synthesis route, *Journal of the Electrochemical Society*, 155 (2008) B953-B957.
- [350] X.X. Yuan, X. Zeng, H.J. Zhang, Z.F. Ma, C.Y. Wang, Improved Performance of Proton Exchange Membrane Fuel Cells with p-Toluenesulfonic Acid-Doped Co-PPy/C as Cathode Electrocatalyst, *Journal of the American Chemical Society*, 132 (2010) 1754-+.
- [351] T.N. Tran, M.Y. Song, K.P. Singh, D.S. Yang, J.S. Yu, Iron-polypyrrole electrocatalyst with remarkable activity and stability for ORR in both alkaline and acidic conditions: a comprehensive assessment of catalyst preparation sequence, *Journal of Materials Chemistry A*, 4 (2016) 8645-8657.
- [352] F.L. Meng, Z.L. Wang, H.X. Zhong, J. Wang, J.M. Yan, X.B. Zhang, Reactive Multifunctional Template-Induced Preparation of Fe-N-Doped Mesoporous Carbon Microspheres Towards Highly Efficient Electrocatalysts for Oxygen Reduction, *Advanced Materials*, 28 (2016) 7948-7955.
- [353] W.H. Niu, L.G. Li, N. Wang, S.B. Zeng, J. Liu, D.K. Zhao, S.W. Chen, Volatilizable template-assisted scalable preparation of honeycomb-like porous carbons for efficient oxygen electroreduction, *Journal of Materials Chemistry A*, 4 (2016) 10820-10827.
- [354] G.A. Ferrero, K. Preuss, A. Marinovic, A.B. Jorge, N. Mansor, D.J. Brett, A.B. Fuertes, M. Sevilla, M.M. Titirici, Fe-N-Doped Carbon Capsules with Outstanding Electrochemical Performance and Stability for the Oxygen Reduction Reaction in Both Acid and Alkaline Conditions, *Acs Nano*, 10 (2016) 5922-5932.

- [355] Y. Meng, J. Yin, T. Jiao, J. Bai, L. Zhang, J. Su, S. Liu, Z. Bai, M. Cao, Q. Peng, Self-assembled copper/cobalt-containing polypyrrole hydrogels for highly efficient ORR electrocatalysts, *J Mol Liq*, 298 (2020).
- [356] S. Zeng, F. Lyu, H. Nie, Y. Zhan, H. Bian, Y. Tian, Z. Li, A. Wang, J. Lu, Y.Y. Li, Facile fabrication of N/S-doped carbon nanotubes with Fe₃O₄ nanocrystals enmeshed for lasting synergy as efficient oxygen reduction catalysts, *Journal of Materials Chemistry A*, 5 (2017) 13189-13195.
- [357] R. Sulub, W. Martinez-Millan, M.A. Smit, Study of the Catalytic Activity for Oxygen Reduction of Polythiophene Modified with Cobalt or Nickel, *International Journal of Electrochemical Science*, 4 (2009) 1015-1027.
- [358] S.J. Han, H.J. Jung, J.H. Shim, H.C. Kim, S.J. Sung, B. Yoo, D.H. Lee, C. Lee, Y. Lee, Non-platinum oxygen reduction electrocatalysts based on carbon-supported metal-polythiophene composites, *Journal of Electroanalytical Chemistry*, 655 (2011) 39-44.
- [359] J.X. Guo, Q.J. Niu, Y.C. Yuan, I. Maitlo, J. Nie, G.P. Ma, Electrospun core-shell nanofibers derived Fe-S/N doped carbon material for oxygen reduction reaction, *Appl Surf Sci*, 416 (2017) 118-123.
- [360] W.M. Millan, T.T. Thompson, L.G. Arriaga, M.A. Smit, Characterization of composite materials of electroconductive polymer and cobalt as electrocatalysts for the oxygen reduction reaction, *Int J Hydrogen Energy*, 34 (2009) 694-702.
- [361] L. Zhang, H. Wang, H. Wang, X.P. Liu, L. Su, L. Yu, P. Chen, Bulk Production of N, Fe-Doped Carbon with High Surface Area and Big Pore Volume and Its Excellent Activity for Oxygen Reduction in Acidic Media, *Journal of the Electrochemical Society*, 163 (2016) H738-H743.
- [362] Q. Wang, Z.Y. Zhou, Y.J. Lai, Y. You, J.G. Liu, X.L. Wu, E. Terefe, C. Chen, L. Song, M. Rauf, N. Tian, S.G. Sun, Phenylenediamine-Based Fe_{Nx}/C Catalyst with High Activity for Oxygen Reduction in Acid Medium and Its Active-Site Probing, *Journal of the American Chemical Society*, 136 (2014) 10882-10885.
- [363] Y.C. Wang, Y.J. Lai, L. Song, Z.Y. Zhou, J.G. Liu, Q. Wang, X.D. Yang, C. Chen, W. Shi, Y.P. Zheng, M. Rauf, S.G. Sun, S-Doping of an Fe/N/C ORR Catalyst for Polymer Electrolyte Membrane Fuel Cells with High Power Density, *Angew Chem Int Ed Engl*, 54 (2015) 9907-9910.
- [364] S.A. Gharaibeh, V.I. Birss, Phenylenediamine as a Promising Ligand for Non-Noble Metal ORR Catalysts, *Polymer Electrolyte Fuel Cells 13 (Pefc 13)*, 58 (2013) 1701-1712.
- [365] D. Malko, T. Lopes, E. Symianakis, A.R. Kucernak, The intriguing poison tolerance of non-precious metal oxygen reduction reaction (ORR) catalysts, *Journal of Materials Chemistry A*, 4 (2016) 142-152.
- [366] T. Najam, S.S.A. Shah, W. Ding, J.X. Jiang, L. Jia, W. Yao, L. Li, Z.D. Wei, An Efficient Anti-poisoning Catalyst against SO_x, NO_x, and PO_x: P, N-Doped Carbon for Oxygen Reduction in Acidic Media, *Angew Chem Int Edit*, 57 (2018) 15101-15106.
- [367] L.L. Cui, M. Wu, J.B. Xiang, Iron and nitrogen co-functionalized porous 3D graphene frameworks as an efficient oxygen reduction catalyst, *Rsc Adv*, 6 (2016) 74886-74894.
- [368] Z.Y. Guo, C.C. Jiang, C. Teng, G.Y. Ren, Y. Zhu, L. Jiang, Sulfur, Trace Nitrogen and Iron Codoped Hierarchically Porous Carbon Foams as Synergistic Catalysts for Oxygen Reduction Reaction, *Acs Appl Mater Inter*, 6 (2014) 21454-21460.
- [369] J.A. Vigil, T.N. Lambert, K. Eldred, Electrodeposited MnO_x/PEDOT Composite Thin Films for the Oxygen Reduction Reaction, *Acs Appl Mater Inter*, 7 (2015) 22745-22750.
- [370] S.N. Bhande, S.M. Unni, S. Kurungot, Nitrogen and sulphur co-doped crumbled graphene for the oxygen reduction reaction with improved activity and stability in acidic medium, *Journal of Materials Chemistry A*, 4 (2016) 6014-6020.
- [371] T. Kangkamano, M. Vagin, L. Meng, P. Thavarungkul, P. Kanatharana, X. Crispin, C.W. Mak, Product-to-Intermediate Relay Achieving Complete Oxygen Reduction Reaction (cORR) with Prussian Blue Integrated Nanoporous Polymer Cathode in Fuel Cells, *Nano Energy*, pre-proof (2020).

- [372] M. Yang, H.B. Chen, D.G. Yang, Y. Gao, H.M. Li, Using nitrogen-rich polymeric network and iron(II) acetate as precursors to synthesize highly efficient electrocatalyst for oxygen reduction reaction in alkaline media, *Journal of Power Sources*, 307 (2016) 152-159.
- [373] M. Yang, H.B. Chen, D.G. Yang, Y. Gao, H.M. Li, High-performance electrocatalyst for oxygen reduction reaction derived from copolymer networks and iron(II) acetate, *Rsc Adv*, 6 (2016) 97259-97265.
- [374] X.L. Yan, Y.C. Yao, Y. Chen, Highly Active and Stable Fe-N-C Oxygen Reduction Electrocatalysts Derived from Electrospinning and In Situ Pyrolysis, *Nanoscale Res Lett*, 13 (2018).
- [375] X.X. Yan, L. Gan, F. Fang, K.X. Liu, J. Luo, J. Zhu, Controllable synthesis of porous iron-nitrogen-carbon nanofibers with enhanced oxygen reduction electrocatalysis in acidic medium, *Rsc Adv*, 5 (2015) 50324-50327.
- [376] G.M. Kim, S. Baik, J.W. Lee, Enhanced oxygen reduction from the insertion of cobalt into nitrogen-doped porous carbons, *Rsc Adv*, 5 (2015) 87971-87980.
- [377] J.L. Chen, W.B. Li, B.Q. Xu, Nitrogen-rich Fe-N-C materials derived from polyacrylonitrile as highly active and durable catalysts for the oxygen reduction reaction in both acidic and alkaline electrolytes, *J Colloid Interf Sci*, 502 (2017) 44-51.
- [378] N. Nakagawa, M.A. Abdelkareem, D. Takino, T. Ishikawa, T. Tsujiguchi, PAN Based Carbon Nanofibers as an Active ORR Catalyst for DMFC, *ECS Transactions*, 41 (2011) 2219-2229.
- [379] J. Wu, D. Higgins, Z. Chen, Electrospun Iron/Polyacrylonitrile Derived Nanofibrous Catalysts for Oxygen Reduction Reaction, *ECS Transactions*, 50 (2013) 1807-1812.
- [380] P. Zamani, D. Higgins, F. Hassan, G.P. Jiang, J. Wu, S. Abureden, Z.W. Chen, Electrospun Iron-Polyaniline-Polyacrylonitrile Derived Nanofibers as Non-Precious Oxygen Reduction Reaction Catalysts for PEM Fuel Cells, *Electrochimica Acta*, 139 (2014) 111-116.
- [381] A. Serov, U. Tylus, K. Artyushkova, S. Mukerjee, P. Atanassov, Mechanistic studies of oxygen reduction on Fe-PEI derived non-PGM electrocatalysts, *Appl Catal B-Environ*, 150 (2014) 179-186.
- [382] U. Tylus, Q. Jia, H. Hafiz, R.J. Allen, B. Barbiellini, A. Bansil, S. Mukerjee, Engendering anion immunity in oxygen consuming cathodes based on Fe-N-x electrocatalysts: Spectroscopic and electrochemical advanced characterizations, *Appl Catal B-Environ*, 198 (2016) 318-324.
- [383] J.Y. Choi, R.S. Hsu, Z.W. Chen, Highly Active Porous Carbon-Supported Nonprecious Metal-N Electrocatalyst for Oxygen Reduction Reaction in PEM Fuel Cells, *J Phys Chem C*, 114 (2010) 8048-8053.
- [384] X.G. Li, G. Liu, B.N. Popov, Activity and stability of non-precious metal catalysts for oxygen reduction in acid and alkaline electrolytes, *Journal of Power Sources*, 195 (2010) 6373-6378.
- [385] R. Kobayashi, J. Ozaki, Novel N-Doped Carbon Cathode Catalyst for Polymer Electrolyte Membrane Fuel Cells Formed on Carbon Black, *Chem Lett*, 38 (2009) 396-397.
- [386] Z.J. Zhang, Q. Shu, C. Chen, T.C. Xiao, Z.Y. Hu, S.C. Wu, J.S. Li, Nitrogen Doped Carbon Wrapped Fe₃O₄ as an Efficient Bifunctional Oxygen Electrocatalyst, *International Journal of Electrochemical Science*, 12 (2017) 6129-6136.
- [387] Z.Z. Liang, C.C. Zhang, H.T. Yuan, W. Zhang, H.Q. Zheng, R. Cao, PVP-assisted transformation of a metal-organic framework into Co-embedded N-enriched meso/microporous carbon materials as bifunctional electrocatalysts, *Chem Commun*, 54 (2018) 7519-7522.
- [388] M.T. Nguyen, B. Mecheri, A. Iannaci, A. D'Epifanio, S. Licocchia, Iron/Polyindole-based Electrocatalysts to Enhance Oxygen Reduction in Microbial Fuel Cells, *Electrochimica Acta*, 190 (2016) 388-395.
- [389] W. Shi, Y.C. Wang, C. Chen, X.D. Yang, Z.Y. Zhou, S.G. Sun, A mesoporous Fe/N/C ORR catalyst for polymer electrolyte membrane fuel cells, *Chinese Journal of Catalysis*, 37 (2016) 1103-1108.

- [390] J. Liebscher, R. Mrowczynski, H.A. Scheidt, C. Filip, N.D. Hadade, R. Turcu, A. Bende, S. Beck, Structure of Polydopamine: A Never-Ending Story?, *Langmuir*, 29 (2013) 10539-10548.
- [391] D. Zhou, L.P. Yang, L.H. Yu, J.H. Kong, X.Y. Yao, W.S. Liu, Z.C. Xu, X.H. Lu, Fe/N/C hollow nanospheres by Fe(III)-dopamine complexation-assisted one-pot doping as nonprecious-metal electrocatalysts for oxygen reduction, *Nanoscale*, 7 (2015) 1501-1509.
- [392] W.L. Gu, L.Y. Hu, J. Li, E.K. Wang, Iron and nitrogen co-doped hierarchical porous graphitic carbon for a high-efficiency oxygen reduction reaction in a wide range of pH, *Journal of Materials Chemistry A*, 4 (2016) 14364-14370.
- [393] Y. Zhao, K. Kamiya, K. Hashimoto, S. Nakanishi, Efficient Bifunctional Fe/C/N Electrocatalysts for Oxygen Reduction and Evolution Reaction, *J Phys Chem C*, 119 (2015) 2583-2588.
- [394] L. Huang, C.Y. Zhao, Y.F. Yao, Y. You, Z.W. Wang, C.P. Wu, Y. Sun, J. Tian, J.G. Liu, Z.G. Zou, Fe/N/C catalyst with high activity for oxygen reduction reaction derived from surfactant modified porous carbon-supported melamine-formaldehyde resin, *Int J Hydrogen Energy*, 41 (2016) 11090-11098.
- [395] W.H. Lee, D.W. Lee, H. Kim, Development of Nitrogen-Doped Carbon Catalysts Using Melamine-Based Polymer as a Nitrogen Precursor for the Oxygen Reduction Reaction, *Journal of the Electrochemical Society*, 162 (2015) F744-F749.
- [396] M. Chokai, M. Taniguchi, S. Moriya, K. Matsubayashi, T. Shinoda, Y. Nabae, S. Kuroki, T. Hayakawa, M.A. Kakimoto, J. Ozaki, S. Miyata, Preparation of Carbon Alloy Catalysts from a Polyhydroxyamide with Iron Phthalocyanine via a Poly-biphenylenebisoxazole Composite, *J Photopolym Sci Tec*, 23 (2010) 459-464.
- [397] M. Chokai, M. Taniguchi, S. Moriya, K. Matsubayashi, T. Shinoda, Y. Nabae, S. Kuroki, T. Hayakawa, M. Kakimoto, J. Ozaki, S. Miyata, Preparation of carbon alloy catalysts for polymer electrolyte fuel cells from nitrogen-containing rigid-rod polymers, *Journal of Power Sources*, 195 (2010) 5947-5951.
- [398] Y. Nabae, Y.B. Kuang, M. Chokai, T. Ichihara, A. Isoda, T. Hayakawa, T. Aoki, High performance Pt-free cathode catalysts for polymer electrolyte membrane fuel cells prepared from widely available chemicals, *Journal of Materials Chemistry A*, 2 (2014) 11561-11564.
- [399] L. Lin, Q. Zhu, A.W. Xu, Noble-Metal-Free Fe-N/C Catalyst for Highly Efficient Oxygen Reduction Reaction under Both Alkaline and Acidic Conditions, *Journal of the American Chemical Society*, 136 (2014) 11027-11033.
- [400] Z. Ding, C.M. Johnston, P. Zelenay, A Simple Synthesis Method of Sulfur-Free Fe-N/C Catalyst with High ORR Activity, *ECS Transactions*, 33 (2010) 565-577.
- [401] C.M. Johnston, G. Wu, M. Ferrandon, D.J. Myers, K. More, K. Artyushkova, P. Zelenay, Factors Correlating to the Activity and Durability of PANI-derived ORR Catalysts, *ECS Meeting Abstracts*, 218th ECS Meeting (2010).
- [402] G. Wu, M.A. Nelson, N.H. Mack, S.G. Ma, P. Sekhar, F.H. Garzon, P. Zelenay, Titanium dioxide-supported non-precious metal oxygen reduction electrocatalyst, *Chem Commun*, 46 (2010) 7489-7491.
- [403] W. Feng, H.Y. Li, X. Cheng, T.C. Jao, F.B. Weng, A. Su, Y.C. Chiang, A comparative study of pyrolyzed and doped cobalt-polypyrrole electrocatalysts for oxygen reduction reaction, *Appl Surf Sci*, 258 (2012) 4048-4053.
- [404] B. Jeong, D. Shin, H. Jeon, J.D. Ocon, B.S. Mun, J. Baik, H.J. Shin, J. Lee, Excavated Fe-N-C sites for enhanced electrocatalytic activity in the oxygen reduction reaction, *ChemSusChem*, 7 (2014) 1289-1294.
- [405] J. Tian, L. Birry, F. Jaouen, J.P. Dodelet, Fe-based catalysts for oxygen reduction in proton exchange membrane fuel cells with cyanamide as nitrogen precursor and/or pore-filler, *Electrochimica Acta*, 56 (2011) 3276-3285.
- [406] F. Jaouen, F. Charretre, J.P. Dodelet, Fe-Based Catalysts for Oxygen Reduction in PEMFCs: Importance of the Disordered Phase of the Carbon Support, *ECS Meeting Abstracts*, 153 (2006) A689-A698.

- [407] F. Charreteur, F. Jaouen, S. Ruggeri, J.P. Dodelet, Fe/N/C non-precious catalysts for PEM fuel cells: Influence of the structural parameters of pristine commercial carbon blacks on their activity for oxygen reduction, *Electrochimica Acta*, 53 (2008) 2925-2938.
- [408] F. Charreteur, S. Ruggeri, F. Jaouen, J.P. Dodelet, Increasing the activity of Fe/N/C catalysts in PEM fuel cell cathodes using carbon blacks with a high-disordered carbon content, *Electrochimica Acta*, 53 (2008) 6881-6889.
- [409] G. Wu, K.L. More, P. Xu, H.L. Wang, M. Ferrandon, A.J. Kropf, D.J. Myers, S. Ma, C.M. Johnston, P. Zelenay, A carbon-nanotube-supported graphene-rich non-precious metal oxygen reduction catalyst with enhanced performance durability, *Chem Commun (Camb)*, 49 (2013) 3291-3293.
- [410] N. Larouche, R. Chenitz, M. Lefèvre, E. Proietti, J.-P. Dodelet, Activity and stability in proton exchange membrane fuel cells of iron-based cathode catalysts synthesized with addition of carbon fibers, *Electrochimica Acta*, 115 (2014) 170-182.
- [411] H.R. Byon, J. Suntivich, Y. Shao-Horn, Graphene-Based Non-Noble-Metal Catalysts for Oxygen Reduction Reaction in Acid, *Chem Mater*, 23 (2011) 3421-3428.
- [412] H.T. Chung, G. Wu, Q. Li, P. Zelenay, Role of two carbon phases in oxygen reduction reaction on the Co-PPy-C catalyst, *Int J Hydrogen Energ*, 39 (2014) 15887-15893.
- [413] M. Kubler, S. Wagner, T. Jurzinsky, S. Paul, N. Weidler, E.D.G. Villa, C. Cremers, U.I. Kramm, Impact of Surface Functionalization on the Intrinsic Properties of the Resulting Fe-N-C Catalysts for Fuel Cell Applications, *Energy Technol-Ger*, (2020).
- [414] C. Niether, M.S. Rau, C. Cremers, D.J. Jones, K. Pinkwart, J. Tübke, Development of a novel experimental DEMS set-up for electrocatalyst characterization under working conditions of high temperature polymer electrolyte fuel cells, *Journal of Electroanalytical Chemistry*, 747 (2015) 97-103.
- [415] X. Wang, W. Li, Z. Chen, M. Waje, Y. Yan, Durability investigation of carbon nanotube as catalyst support for proton exchange membrane fuel cell, *Journal of Power Sources*, 158 (2006) 154-159.
- [416] F. Hasche, M. Oezaslan, P. Strasser, Activity, stability and degradation of multi walled carbon nanotube (MWCNT) supported Pt fuel cell electrocatalysts, *Phys Chem Chem Phys*, 12 (2010) 15251-15258.
- [417] F. Gao, G.-L. Zhao, Z. Wang, D. Bagayoko, D.-J. Liu, Catalytic reaction on FeN₄/C site of nitrogen functionalized carbon nanotubes as cathode catalyst for hydrogen fuel cells, *Catalysis Communications*, 62 (2015) 79-82.
- [418] H. Jia, Z. Sun, D. Jiang, S. Yang, P. Du, An iron porphyrin-based conjugated network wrapped around carbon nanotubes as a noble-metal-free electrocatalyst for efficient oxygen reduction reaction, *Inorganic Chemistry Frontiers*, 3 (2016) 821-827.
- [419] I. Hijazi, T. Bourgeteau, R. Cornut, A. Morozan, A. Filoramo, J. Leroy, V. Derycke, B. Josselme, S. Campidelli, Carbon nanotube-templated synthesis of covalent porphyrin network for oxygen reduction reaction, *J Am Chem Soc*, 136 (2014) 6348-6354.
- [420] T. Jurzinsky, E.D. Gomez-Villa, M. Kübler, M. Bruns, P. Elsässer, J. Melke, F. Scheiba, C. Cremers, Functionalization of multi-walled carbon nanotubes with indazole, *Electrochimica Acta*, 298 (2019) 884-892.
- [421] D. Priftis, G. Sakellariou, D. Baskaran, J.W. Mays, N. Hadjichristidis, Polymer grafted Janus multi-walled carbon nanotubes, *Soft Matter*, 5 (2009).
- [422] B.H.R. Suryanto, T. Fang, S. Cheong, R.D. Tilley, C. Zhao, From the inside-out: leached metal impurities in multiwall carbon nanotubes for purification or electrocatalysis, *Journal of Materials Chemistry A*, 6 (2018) 4686-4694.
- [423] Nanocyl, Technical Data Sheet: NC7000TM, in: T.D.S. NC7000TM (Ed.), 2016.
- [424] U.I. Kramm, L. Ni, S. Wagner, (57) Fe Mossbauer Spectroscopy Characterization of Electrocatalysts, *Adv Mater*, 31 (2019) e1805623.
- [425] S. Wagner, H. Auerbach, C.E. Tait, I. Martinaiou, S.C.N. Kumar, C. Kubel, I. Sergeev, H.C. Wille, J. Behrends, J.A. Wolny, V. Schunemann, U.I. Kramm, Elucidating the Structural

Composition of a Fe-N-C Catalyst by Nuclear- and Electron-Resonance Techniques, *Angew Chem Int Edit*, 58 (2019) 10486-10492.

[426] I. Martinaiou, A. Shahraei, F. Grimm, H. Zhang, C. Wittich, S. Klemenz, S.J. Dolique, H.-J. Kleebe, R.W. Stark, U.I. Kramm, Effect of metal species on the stability of Me-N-C catalysts during accelerated stress tests mimicking the start-up and shut-down conditions, *Electrochimica Acta*, 243 (2017) 183-196.

[427] A. Bonakdarpour, M. Lefevre, R. Yang, F. Jaouen, T. Dahn, J.-P. Dodelet, J.R. Dahn, Impact of Loading in RRDE Experiments on Fe-N-C Catalysts: Two- or Four-Electron Oxygen Reduction?, *Electrochemical and Solid-State Letters*, 11 (2008).

[428] T. Jurzinsky, P. Kurzahls, C. Cremers, A novel differential electrochemical mass spectrometry method to determine the product distribution from parasitic Methanol oxidation reaction on oxygen reduction reaction catalysts, *Journal of Power Sources*, 389 (2018) 61-69.

[429] Q. Wang, C.S. Cha, J. Lu, L. Zhuang, The electrochemistry of "solid/water" interfaces involved in PEM-H₂O reactors: part I. The "Pt/water" interfaces, *Phys Chem Chem Phys*, 11 (2009) 679-687.

[430] U.A. Paulus, Z. Veziridis, B. Schnyder, M. Kuhnke, G.G. Scherer, A. Wokaun, Fundamental investigation of catalyst utilization at the electrode/solid polymer electrolyte interface - Part I. Development of a model system, *Journal of Electroanalytical Chemistry*, 541 (2003) 77-91.

[431] N. Linse, L. Gubler, G.G. Scherer, A. Wokaun, The effect of platinum on carbon corrosion behavior in polymer electrolyte fuel cells, *Electrochimica Acta*, 56 (2011) 7541-7549.

[432] A. Zana, J. Speder, N.E.A. Reeler, T. Vosch, M. Arenz, Investigating the corrosion of high surface area carbons during start/stop fuel cell conditions: A Raman study, *Electrochimica Acta*, 114 (2013) 455-461.

[433] F. Maillard, O.S. W, L. Castanheira, L. Dubau, F.H.B. Lima, Carbon Corrosion in Proton-Exchange Membrane Fuel Cells: Spectrometric Evidence for Pt-Catalysed Decarboxylation at Anode-Relevant Potentials, *Chemphyschem*, 20 (2019) 3106-3111.

[434] F. Jaouen, V. Goellner, M. Lefevre, J. Herranz, E. Proietti, J.P. Dodelet, Oxygen reduction activities compared in rotating-disk electrode and proton exchange membrane fuel cells for highly active Fe-N-C catalysts, *Electrochimica Acta*, 87 (2013) 619-628.

[435] Y.Y. Shao, J.P. Dodelet, G. Wu, P. Zelenay, PGM-Free Cathode Catalysts for PEM Fuel Cells: A Mini-Review on Stability Challenges, *Advanced Materials*, 31 (2019).

[436] Y. Li, P. Bober, M. Trchova, J. Stejskal, Polypyrrole prepared in the presence of methyl orange and ethyl orange: nanotubes versus globules in conductivity enhancement, *J Mater Chem C*, 5 (2017) 4236-4245.

[437] J. Kopecka, D. Kopecky, M. Vrnata, P. Fitl, J. Stejskal, M. Trchova, P. Bober, Z. Moravkova, J. Prokes, I. Sapurina, Polypyrrole nanotubes: mechanism of formation, *Rsc Adv*, 4 (2014) 1551-1558.

[438] D. Kopecky, M. Varga, J. Prokes, M. Vrnata, M. Trchova, J. Kopecka, M. Vaclavik, Optimization routes for high electrical conductivity of polypyrrole nanotubes prepared in presence of methyl orange, *Synthetic Met*, 230 (2017) 89-96.

[439] S. Valtera, J. Prokes, J. Kopecka, M. Vrnata, M. Trchova, M. Varga, J. Stejskal, D. Kopecky, Dye-stimulated control of conducting polypyrrole morphology, *Rsc Adv*, 7 (2017) 51495-51505.

[440] X.M. Yang, Z.X. Zhu, T.Y. Dai, Y. Lu, Facile fabrication of functional polypyrrole nanotubes via a reactive self-degraded template, *Macromol Rapid Comm*, 26 (2005) 1736-1740.

[441] M. Trchova, J. Stejskal, Resonance Raman Spectroscopy of Conducting Polypyrrole Nanotubes: Disordered Surface versus Ordered Body, *J Phys Chem A*, 122 (2018) 9298-9306.

[442] A. Janssen, I. Martinaiou, S. Wagner, N. Weidler, A. Shahraei, U.I. Kramm, Influence of sulfur in the precursor mixture on the structural composition of Fe-N-C catalysts, *Hyperfine Interact*, 239 (2018).

-
- [443] A.C. Ferrari, J. Robertson, Interpretation of Raman spectra of disordered and amorphous carbon, *Phys Rev B*, 61 (2000) 14095-14107.
- [444] M.J. Matthews, M.A. Pimenta, G. Dresselhaus, M.S. Dresselhaus, M. Endo, Origin of dispersive effects of the Raman D band in carbon materials, *Phys Rev B*, 59 (1999) R6585-R6588.
- [445] F. Tuinstra, J.L. Koenig, Raman Spectrum of Graphite, *J Chem Phys*, 53 (1970) 1126-&.
- [446] J. Blomquist, H. Lang, R. Larsson, A. Widelov, Pyrolysis Behavior of Metalloporphyrins .2. A Mossbauer Study of Pyrolyzed Fe(III) Tetraphenylporphyrin Chloride, *J Chem Soc Faraday T*, 88 (1992) 2007-2011.
- [447] A. Morozan, P. Jegou, S. Campidelli, S. Palacin, B. Jusselme, Relationship between polypyrrole morphology and electrochemical activity towards oxygen reduction reaction, *Chem Commun*, 48 (2012) 4627-4629.
- [448] H. Zhang, H.T. Chung, D.A. Cullen, S. Wagner, U.I. Kramm, K.L. More, P. Zelenay, G. Wu, High-performance fuel cell cathodes exclusively containing atomically dispersed iron active sites, *Energy & Environmental Science*, 12 (2019) 2548-2558.
- [449] J. Li, S. Ghoshal, W. Liang, M.-T. Sougrati, F. Jaouen, B. Halevi, S. McKinney, G. McCool, C. Ma, X. Yuan, Z.-F. Ma, S. Mukerjee, Q. Jia, Structural and mechanistic basis for the high activity of Fe–N–C catalysts toward oxygen reduction, *Energy & Environmental Science*, 9 (2016) 2418-2432.
- [450] S. Wagner, H. Auerbach, C.E. Tait, I. Martinaiou, S.C.N. Kumar, C. Kubel, I. Sergeev, H.C. Wille, J. Behrends, J.A. Wolny, V. Schunemann, U.I. Kramm, Elucidating the Structural Composition of an Fe-N-C Catalyst by Nuclear- and Electron-Resonance Techniques, *Angew Chem Int Ed Engl*, 58 (2019) 10486-10492.
- [451] X. Wan, X. Liu, Y. Li, R. Yu, R. Zheng, W. Yan, H. Wang, J. Shui, Fe–N–C electrocatalyst with dense active sites and efficient mass transport for high-performance proton exchange membrane fuel cells, *Nat Catal*, 2 (2019) 259-268.
- [452] X.G. Fu, P. Zamani, J.Y. Choi, F.M. Hassan, G.P. Jiang, D.C. Higgins, Y.N. Zhang, M.A. Hoque, Z.W. Chen, In Situ Polymer Graphenization Ingrained with Nanoporosity in a Nitrogenous Electrocatalyst Boosting the Performance of Polymer-Electrolyte-Membrane Fuel Cells, *Advanced Materials*, 29 (2017).
- [453] K. Strickland, M.W. Elise, Q.Y. Jia, U. Tylus, N. Ramaswamy, W.T. Liang, M.T. Sougrati, F. Jaouen, S. Mukerjee, Highly active oxygen reduction non-platinum group metal electrocatalyst without direct metal-nitrogen coordination, *Nature Communications*, 6 (2015).
- [454] F. Afsahi, S. Kaliaguine, Non-precious electrocatalysts synthesized from metal-organic frameworks, *Journal of Materials Chemistry A*, 2 (2014) 12270-12279.
- [455] J. Wang, Z.Q. Huang, W. Liu, C.R. Chang, H.L. Tang, Z.J. Li, W.X. Chen, C.J. Jia, T. Yao, S.Q. Wei, Y. Wu, Y.D. Lie, Design of N-Coordinated Dual-Metal Sites: A Stable and Active Pt-Free Catalyst for Acidic Oxygen Reduction Reaction, *Journal of the American Chemical Society*, 139 (2017) 17281-17284.
- [456] H.L. Peng, S.Y. Hou, D. Dang, B.Q. Zhang, F.F. Liu, R.P. Zheng, F. Luo, H.Y. Song, P.Y. Huang, S.J. Liao, Ultra-high-performance doped carbon catalyst derived from o-phenylenediamine and the probable roles of Fe and melamine, *Appl Catal B-Environ*, 158 (2014) 60-69.
- [457] D. Banham, T. Kishimoto, T. Sato, Y. Kobayashi, K. Narizuka, J.-i. Ozaki, Y. Zhou, E. Marquez, K. Bai, S. Ye, New insights into non-precious metal catalyst layer designs for proton exchange membrane fuel cells: Improving performance and stability, *Journal of Power Sources*, 344 (2017) 39-45.

12 Appendix

^{57}Fe -Mössbauer spectra and assigned iron species of the $\text{FeCl}_3 + \text{Mn}$ catalysts of chapter 8.4 are given in Figure S1 and Table S1.

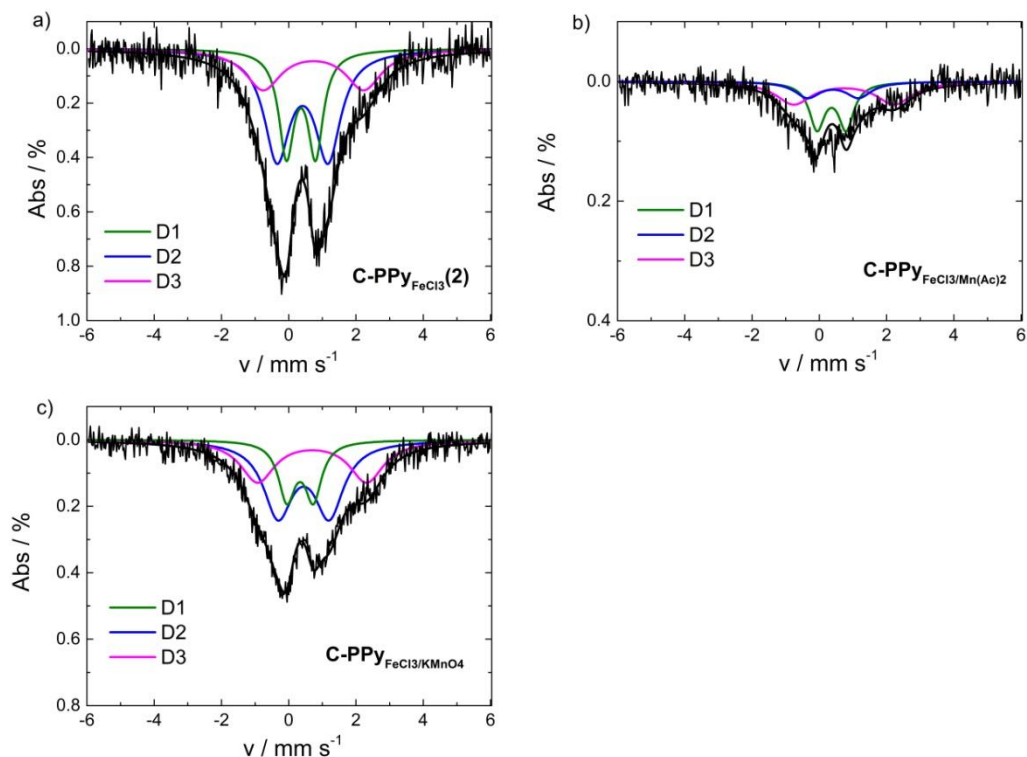


Figure S1: Mössbauer spectra of polypyrrole methyl orange nanotube catalysts prepared with different Fe and Fe + Mn salt mixtures.

Table S1: Mössbauer parameters and assignment of iron species for the polypyrrole methyl orange-based catalysts which were prepared with different iron and manganese salts.

	C-PPy_{FeCl₂}(2)		C-PPy_{FeCl₃/Mn(Ac)₂}		C-PPy_{FeCl₃/KMnO₄}	
	population / %		population / %		population / %	
	$\delta_{\text{iso}} / \text{mm s}^{-1}$	$\Delta E_{\text{q}} / \text{mm s}^{-1}$	$\delta_{\text{iso}} / \text{mm s}^{-1}$	$\Delta E_{\text{q}} / \text{mm s}^{-1}$	$\delta_{\text{iso}} / \text{mm s}^{-1}$	$\Delta E_{\text{q}} / \text{mm s}^{-1}$
D1 L_2FeN_4 (2+, S = 0), LFeN_4 (3+, S = 5/2), cluster	27.6	0.36	37.0	0.36	21.3	0.34
D2 FeN_4 (2+, S = 1)	47.6	0.41	21.0	0.41	47.1	0.44
D3 FeN_4 (2+, S = 2)	24.9	0.73	42.0	0.73	31.6	0.70

Table S2: Mössbauer parameters and assignment of iron species for the polypyrrole methyl orange based catalysts which were prepared at different temperatures and with an isopropanol assisted acid leaching, see chapter 8.5.2, Figure 82 and chapter 8.6, Figure 89.

	C-2htm-PPy _{+FeCl₃/-KMnO₄}		C-2htm-PPy _{+FeCl₃/-KMnO₄} _1000 same as C-PPy-100		C-PPy-100-IsoAL	
	population / %		population / %		population / %	
	$\delta_{iso} / \text{mm s}^{-1}$	$\Delta E_q / \text{mm s}^{-1}$	$\delta_{iso} / \text{mm s}^{-1}$	$\Delta E_q / \text{mm s}^{-1}$	$\delta_{iso} / \text{mm s}^{-1}$	$\Delta E_q / \text{mm s}^{-1}$
D1 L ₂ FeN ₄ (2+, S = 0), LFeN ₄ (3+, S = 5/2), cluster	39		16.4		67.3	
	0.34	1.02	0.48	1.12	0.28	1.17
D2	45		22.9		-	
	0.27	1.77	0.97	0.49	-	-
D3	15.7		-		32.7	
	1.1	2.77	-	-	0.93	1.83
Sext 1 site A in Fe ₃ O ₄	-		29.3		-	
	-		0.32	H =49.0 T	-	
Sext 2 site B in Fe ₃ O ₄	-		10.8		-	
	-		0.72	H =46.0 T	-	
Sext 3 alpha iron	-		20.7		-	
	-		0.00	H =33.0 T	-	

Reproducibility of the Preparation Process

To validate the reproducibility of the overall synthesis process, C-PPy_{FeCl₃} (chapter 8.3) and C-PPy_{FeCl₃}(2) (chapter 8.4) were prepared according to an identical protocol. Likewise, C-PPy-1000 was re-prepared, it is denoted as VGC21 and was used for tests in the fuel cell. It should be emphasized that the reproducibility of the electrochemical measurements, such as RRDE and FC, was already monitored within the overall course of this work. RRDE experiments were always conducted twice and the error bars were included to the figures. Because FC measurements are much more time and material consuming, 40 - 50 % of the samples were chosen randomly and re-measured, see **Table 11**. **Table S3** shows the four samples that will be discussed.

Table S3: Catalysts that were prepared twice to validate the reproducibility.

Sample Name	Polypyrrole Tube Type	Polypyrrole Tube / mg	FeCl ₃ / mg	KMnO ₄ / mg	1 st HT	2 nd HT
C-PPy _{FeCl₃}	washed	350	350	-	800 °C	-
C-PPy _{FeCl₃} (2)	washed	350	350	-	800 °C	-
C-PPy-1000	unwashed	350	590	176	1000 °C	800 °C
VGC21	unwashed	350	590	176	1000 °C	800 °C

The BET surface area of C-PPy_{FeCl₃} is 545 m² g⁻¹. For C-PPy_{FeCl₃}(2) it is 512 m² g⁻¹. A total deviation of about 6 % is observed. No difference in morphology was found for the two catalysts during TEM analysis, the results are shown in **Figure S2**.

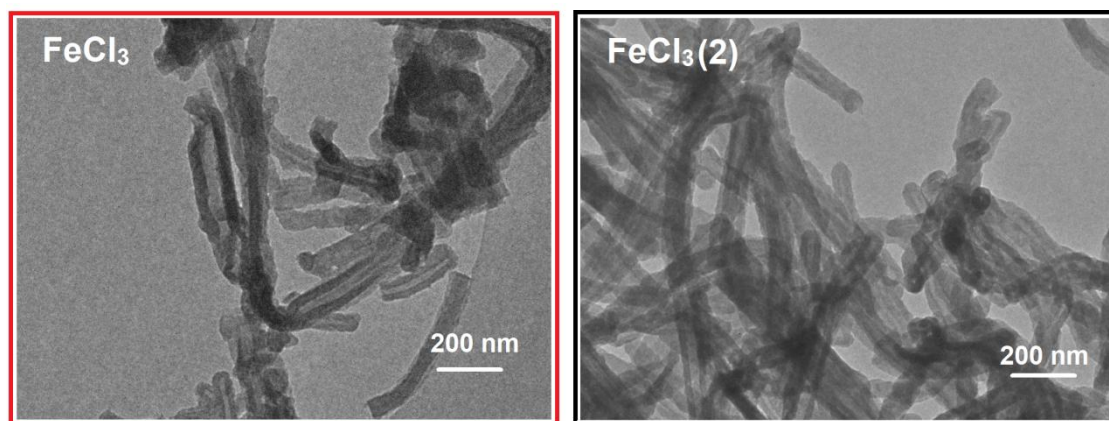


Figure S2: TEM pictures of two identically prepared catalysts, no difference in morphology is seen.

The electrochemical activity and selectivity of C-PPy_{FeCl₃} and C-PPy_{FeCl₃}(2) was measured with a RRDE, the results are displayed in **Figure S3**. The RRDE measurements for both catalysts were conducted twice, the error bars are included. The ORR activity of the two identically prepared catalysts is indeed very reproducible. No difference in onset potential and only minor divergence for the diffusion limited current is detectable. The H₂O₂ yield of C-PPy_{FeCl₃} is 1.5 % and 0.8 % was found for C-PPy_{FeCl₃}(2). However, as indicated by the error bars of C-PPy_{FeCl₃}, the reproducibility of the selectivity experiments is more likely limited by the RRDE experimental setup itself than by the catalysts or the synthesis of the catalysts. The high electrode loadings that are required for RRDE experiments with Fe-N-C catalysts are responsible for this behavior.

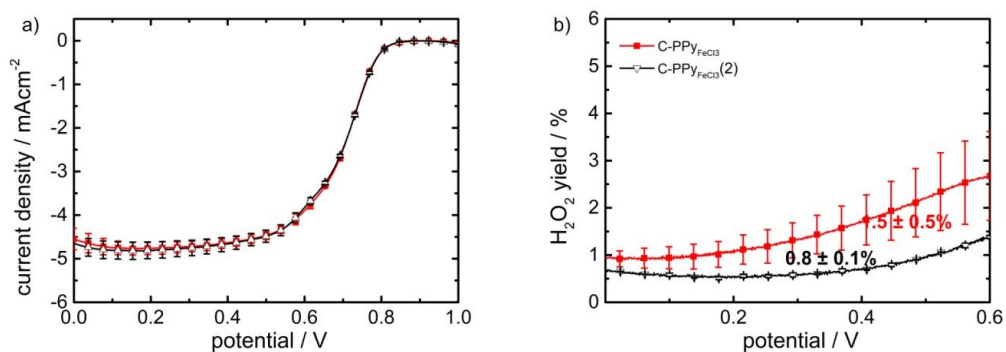


Figure S3: Reductive scans of the polarization curves obtained in 0.1 M H₂SO₄ saturated with O₂, rotation rate of 1500 rpm, 10 mV s⁻¹ and a disc loading of 0.5 mg cm⁻². The disc current density is given in (a) and the H₂O₂ yield in (b).

Figure S4 gives the Mössbauer spectra of the two identically prepared catalysts. **Table S4** shows the assigned iron species and Mössbauer parameters. From the iron composition the preparation seems quite reproducible, the same doublet species can be found both catalysts. However, the population of the different species is slightly different as seen from **Table S4**.

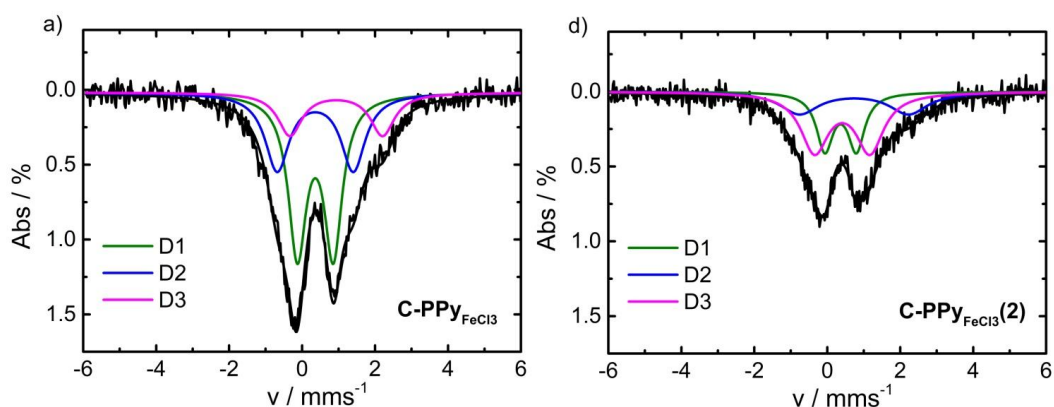


Figure S4: ⁵⁷Fe Mössbauer spectra of two identically prepared catalysts, C-PPy_{FeCl3} and C-PPy_{FeCl3}(2).

Table S4: Mössbauer parameters of the samples C-PPy_{FeCl3} and C-PPy_{FeCl3}(2).

Sites	Parameter	C-PPy _{FeCl3}	C-PPy _{FeCl3} (2)
D1, Fe^{II}N₄, low spin	$\Delta_{\text{iso}} / \text{mm s}^{-1}$	0.362	0.365
	$\Delta E_{\text{Q}} / \text{mm s}^{-1}$	0.984	0.864
	hwhm / mm s^{-1}	0.3	0.3
	Population / %	49.8	27.6
D2, Fe^{II}N₄, middle spin	$\Delta_{\text{iso}} / \text{mm s}^{-1}$	0.361	0.401
	$\Delta E_{\text{Q}} / \text{mm s}^{-1}$	2.086	1.52
	hwhm / mm s^{-1}	0.4	0.4
	Population / %	32.2	47.6
D3, Fe^{II}N₄, High spin	$\Delta_{\text{iso}} / \text{mm s}^{-1}$	0.936	0.734
	$\Delta E_{\text{Q}} / \text{mm s}^{-1}$	2.54	2.99
	hwhm / mm s^{-1}	0.4	0.6
	Population / %	17.9	24.9

The reproducibility considering fuel cell activity was examined by re-preparing C-PPy-1000. VGC21 was prepared according to the same procedure as C-PPy-1000. While the complete procedure of catalyst synthesis, electrode and MEA fabrication as well as the execution of the fuel cell measurements was conducted by another PhD student. The results are shown in **Figure S5**. Despite minor variance in the mass transport region the measurements give almost identical results.

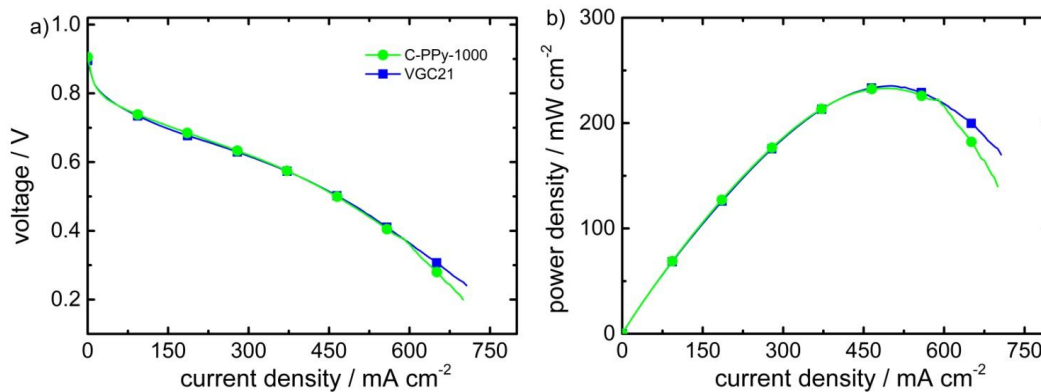


Figure S5: PEMFC polarization curves of two identically prepared catalysts, C-PPy-1000 and VGC21, (experiment conditions: H₂-air, cathode loading 3.4 mg cm⁻², N212 membrane, 1 bar gauge back pressure, 0.2 L min⁻¹ oxidant and fuel flow, 80 °C, 96 % humidity).

TEM Pictures

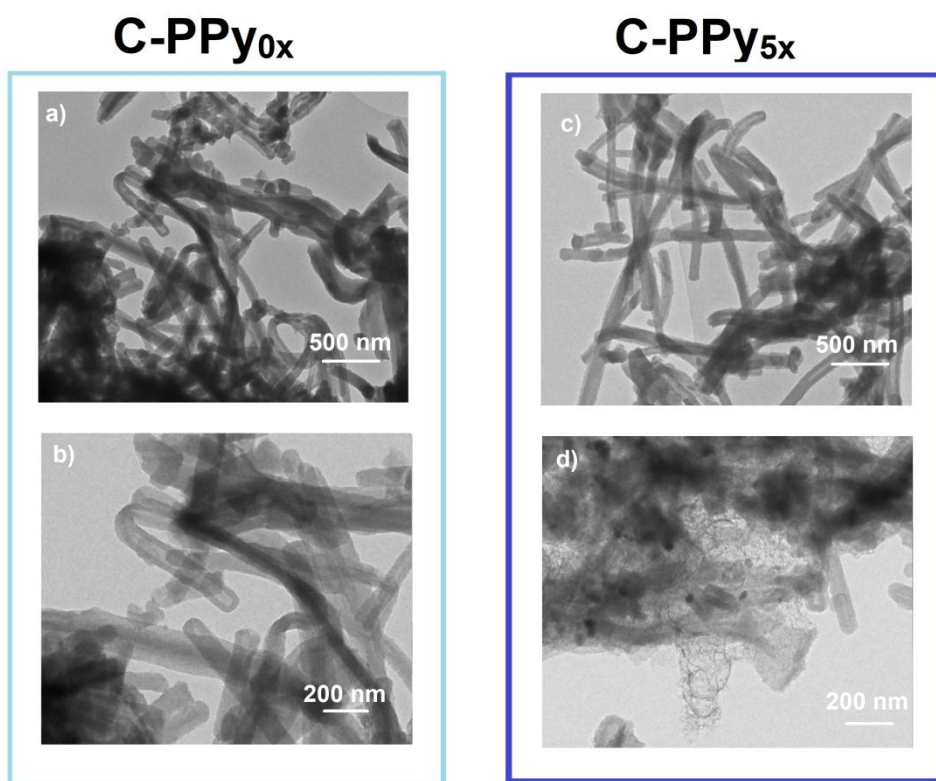


Figure S6: TEM photographs of the catalysts C-PPy_{0x} and C-PPy_{5x}.

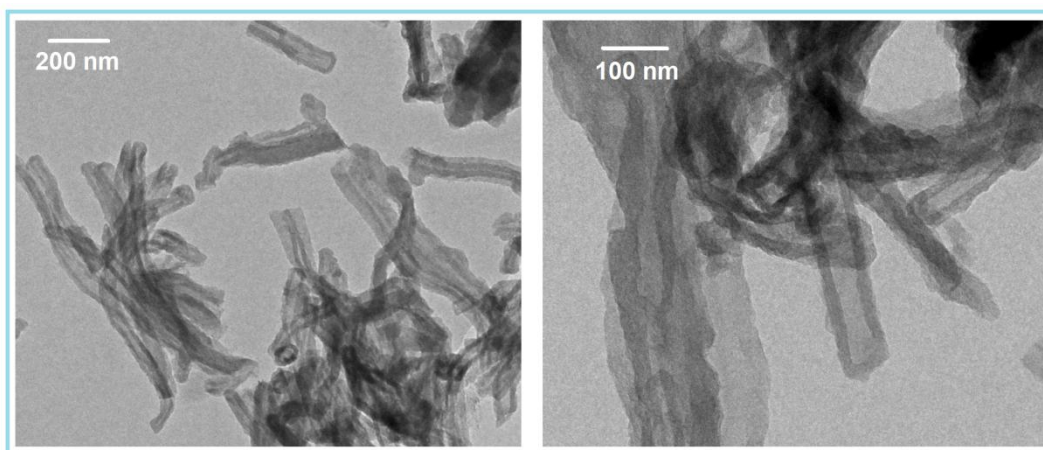


Figure S7: TEM pictures of the catalyst C-2ht-PPy_{FeC3/KMnO4}.

Washing Water of Polypyrrole-Methyl Orange Nanotubes



Figure S8: Filtrate after #number of washing steps. The polypyrrole nanotubes were washed according to the mentioned procedure in the experimental part. The red color indicates the removal of FeCl_3 and methyl orange. The yellow color indicates the removal of methyl orange.

Fuel Cell

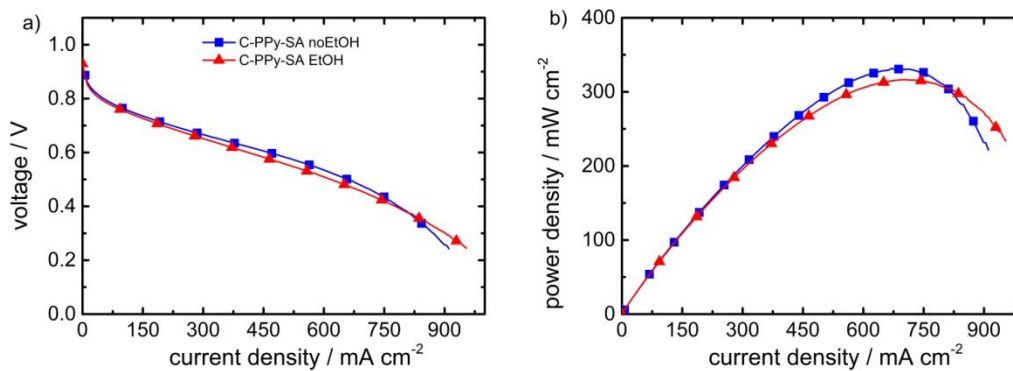


Figure S9: FC polarization curves of catalysts prepared with and without an ethanol washing step of the polypyrrole precursor, the FC performance is not affected. The standard experiment conditions as mentioned before were used.